ABSTRACT

Title of dissertation: A SEARCH FOR MUON NEUTRINOS IN COINCIDENCE WITH GAMMA-RAY BURSTS IN THE SOUTHERN HEMISPHERE SKY USING THE ICECUBE NEUTRINO OBSERVATORY

Ryan Edward Maunu, Doctor of Philosophy, 2016

Dissertation directed by: Professor Kara Hoffman
Department of Physics

The origin of observed ultra-high energy cosmic rays (UHECRs, energies in excess of $10^{18.5}$ eV) remains unknown, as extragalactic magnetic fields deflect these charged particles from their true origin. Interactions of these UHECRs at their source would invariably produce high energy neutrinos. As these neutrinos are chargeless and nearly massless, their propagation through the universe is unimpeded and their detection can be correlated with the origin of UHECRs.

Gamma-ray bursts (GRBs) are one of the few possible origins for UHECRs, observed as short, immensely bright outbursts of gamma-rays at cosmological distances. The energy density of GRBs in the universe is capable of explaining the measured UHECR flux, making them promising UHECR sources. Interactions between UHECRs and the prompt gamma-ray emission of a GRB would produce neutrinos that would be detected in coincidence with the GRB's gamma-ray emission.

The IceCube Neutrino Observatory can be used to search for these neutrinos in coincidence with GRBs, detecting neutrinos through the Cherenkov radiation emitted by secondary charged particles produced in neutrino interactions in the South Pole glacial ice. Restricting these searches to be in coincidence with GRB gamma-ray emission, analyses can be performed with very little atmospheric background. Previous searches have focused on detecting muon tracks from muon neutrino interactions from

the Northern Hemisphere, where the Earth shields IceCube's primary background of atmospheric muons, or spherical cascade events from neutrinos of all flavors from the entire sky, with no compelling neutrino signal found.

Neutrino searches from GRBs with IceCube have been extended to a search for muon tracks in the Southern Hemisphere in coincidence with 664 GRBs over five years of IceCube data in this dissertation. Though this region of the sky contains IceCube's primary background of atmospheric muons, it is also where IceCube is most sensitive to neutrinos at the very highest energies as Earth absorption in the Northern Hemisphere becomes relevant. As previous neutrino searches have strongly constrained neutrino production in GRBs, a new per-GRB analysis is introduced for the first time to discover neutrinos in coincidence with possibly rare neutrino-bright GRBs. A stacked analysis is also performed to discover a weak neutrino signal distributed over many GRBs.

Results of this search are found to be consistent with atmospheric muon backgrounds. Combining this result with previously published searches for muon neutrino tracks in the Northern Hemisphere, cascade event searches over the entire sky, and an extension of the Northern Hemisphere track search in three additional years of IceCube data that is consistent with atmospheric backgrounds, the most stringent limits yet can be placed on prompt neutrino production in GRBs, which increasingly disfavor GRBs as primary sources of UHECRs in current GRB models.

A SEARCH FOR MUON NEUTRINOS IN COINCIDENCE WITH GAMMA-RAY BURSTS IN THE SOUTHERN HEMISPHERE SKY USING THE ICECUBE NEUTRINO OBSERVATORY

by

Ryan Edward Maunu

Dissertation submitted to the Faculty of the Graduate School of the
University of Maryland, College Park in partial fulfillment
of the requirements for the degree of
Doctor of Philosophy
2016

Advisory Committee:
Dr. Kara Hoffman, Chair/Adviser
Dr. Gregory Sullivan
Dr. Erik Blaufuss
Dr. Julie McEnery
Dr. Richard Mushotzsky

Acknowledgments

To complete this dissertation and reach this point after so many years of work, there have been innumerable people who have assisted me, and it would be impossible to acknowledge everyone here. To everyone that helped me in my pursuit of a degree in science and physics who are not named here, a big thank you!

First, I would like to thank my family for their constant support. They have always been there to offer encouragement and advice as I made my slow transition from the biomedical sciences to physics, and then into and through graduate school. It hasn't been easy with some of the medical issues I've had, but with them I knew I'd always find support and guidence in whatever I pursued.

Next, I'd like to thank Megan Perez, my fiancée, and constant editor for all my graduate projects. Her constant help and love have been invaluble as I've moved from student to researcher at Maryland. She did this regardless of all the times I annoyed her by excusing myself to run "just one more calculation," and there's no way I would have finished my degree at this point without her patience. I'd also like to extend my gratitude and love to the entire Perez-Zientek family clan, who welcomed me to Maryland with open arms and made Maryland feel like home, despite being so far from my native Minnesota.

Working on IceCube has been absolutely wonderful experience, and I'd like to thank my adviser Kara Hoffman for inviting me to work on the project. Through both my work on the Askaryan Radio Array and IceCube, she has been a steady source of guidence from being a new student with no experience in neutrino astrophysics until now. I would also like to thank Greg Sullivan for co-advising my dissertation work. In group discussions, his prodding forced me to understand neutrino searches from GRBs more thoroughly and defend the work I had done. For all the coordination that it took to work with IceCube, between collaboration meetings and conferences, I have to thank Naomi Russo, our program administrator.

Many thanks to Erik Blaufuss, who was always available to discuss the analysis work I was doing. Also, a thank you to Don La Dieu and Alex Olivas for their responsiveness to any coding or computer complications I ran into. A huge thank you to my GRB-search predecessors, Mike Richman and Robert Hellauer, both of whom helped get me started and work through any problems I had performing my own GRB analysis. I especially have to thank Mike for convincing me that IceCube would be the right fit when I met him at a party at my house—I may not have joined IceCube without him! And of course, a thank you to my fellow IceCube graduate students Elim Cheung, Ming Song, and Liz Friedman who I've shared an office with over the last couple years along with Josh Wood, as well as John Felde, our IceCube post-doc. I've had so much fun with all of you between the happy hours, collaboration meetings, and just shooting the shit around the office, that graduate school has never felt like much of a drag. I'll definitely miss my time with IceCube because of you, as well as all the IceCubers who are too many to name here! Of special mention are Martin Cassier, Kevin Meagher, and Aya Ishihara, who served as collaboration reviewers on my analysis and with their feedback ensured that my work was up to collaboration standards.

Beyond IceCube, I'd like to thank all my fellow University of Maryland physics graduate students, especially Chris Schroeder, Nat Steinsultz, George Hine, Kevin Pedro, Joe Garrett, Jack Wimberley, Young Shin, and Richard Knoche. Whether it was studying for classes or quals, going out to DC, hanging out to watch bad movies or have game nights, or doing potlucks, your friendship has meant so much to me. It would have been hard to finish graduate without you all!

Finally, I would like to thank and acknowledge the University of Maryland and the National Science Foundation for their financial support of my graduate studies and research.

Contents

List of Tables

List of Figures

Chapter 1

Introduction

Charged particles known as cosmic rays constantly bombard the Earth's atmosphere from space. Victor Hess discovered these alien particles in hot air balloon flights in 1912 [1]. He had observed an anamolous radiative signature that increased with altitude, establishing the source to be extraterrestrial. Experiments since then have found their composition to be atomic nuclei with traces of electrons, and their energy spectrum follows a steeply falling power law over many decades of energy, shown in Figure 1.1 Though this spectral index appears to be constant, there is actually a clear structure, shown in Figure 1.2, where the flux has been scaled to $E^{2.5} \times dN/dE$. The cosmic ray spectrum is directly detected by satellites up to around 10^{15} eV, while above this energy extensive air-shower detectors on the surface of the Earth observe secondary particles that are produced when the cosmic rays strike the atmosphere.

The spectrum above $\sim 10^9$ eV is charcterized by a $dN/dE \sim E^{-2.7}$ power law spectrum up to the so-called *knee* around 10^{15} eV, and has been established to be of galactic origin from supernova remnants (SNRs) [3]. Above the knee, the spectrum steepens to $dN/dE \sim E^{-3}$ until the feature know as the *ankle* at $10^{18.6}$ eV. This portion of the cosmic ray spectrum is hypothesized to be a transition between galactic and extragalactic components, where the galactic sources reach their maximal containment energies. Above the ankle, the spectrum hardens again to $dN/dE \sim E^{-2.7}$, likely at the transition to extragalactic sources. The spectrum then falls above energies of 10^{20} eV.

The origin of this spectral softening at the highest energies has not been established. Though it is consistent with the energy where proton primaries in cosmic rays can interact with the cosmic microwave background (CMB) to produce pions through

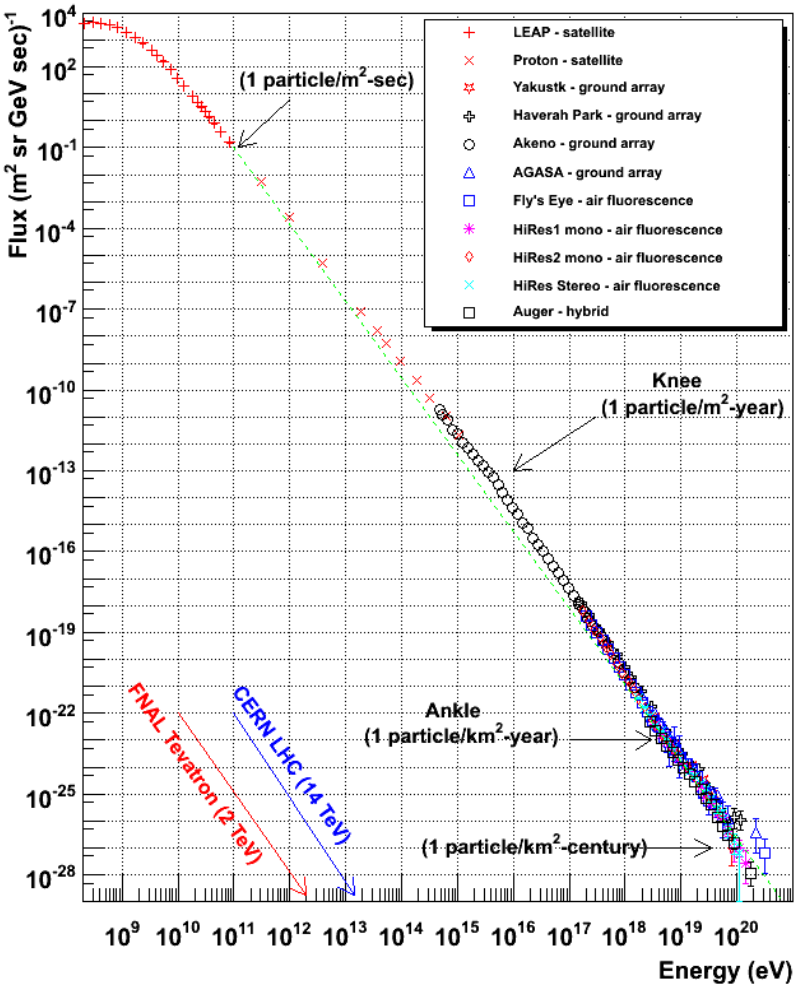

Figure 1.1: The cosmic ray flux spectrum as a function of primary energy for a number of cosmic ray experiments. Rough estimates of event rates at notable regions of the spectrum are indicated, as well as the particle beam center of mass energies for reference. Figure from William Hanlon, University of Utah.

to the Δ^+ resonance, called the GZK mechanism (after Greisen, and Zatsepin and Kuzmin) [4], it could also be a result of cosmic ray accelerators reaching their maximal energies. The composition of these ultra-high energy cosmic rays (UHECRs, $E_{CR} \gtrsim 10^{18.5}\,\text{eV}$) is still in dispute with the Pierre Auger Observatory favoring a transition to iron nuclei primaries [5], and the HiRes experiment and its successor Telescope Array (TA) favoring proton primaries [6, 7]. The composition of these UHECRs could be resolved through the discovery and spectral measurement of neutrinos produced through the GZK mechanism.

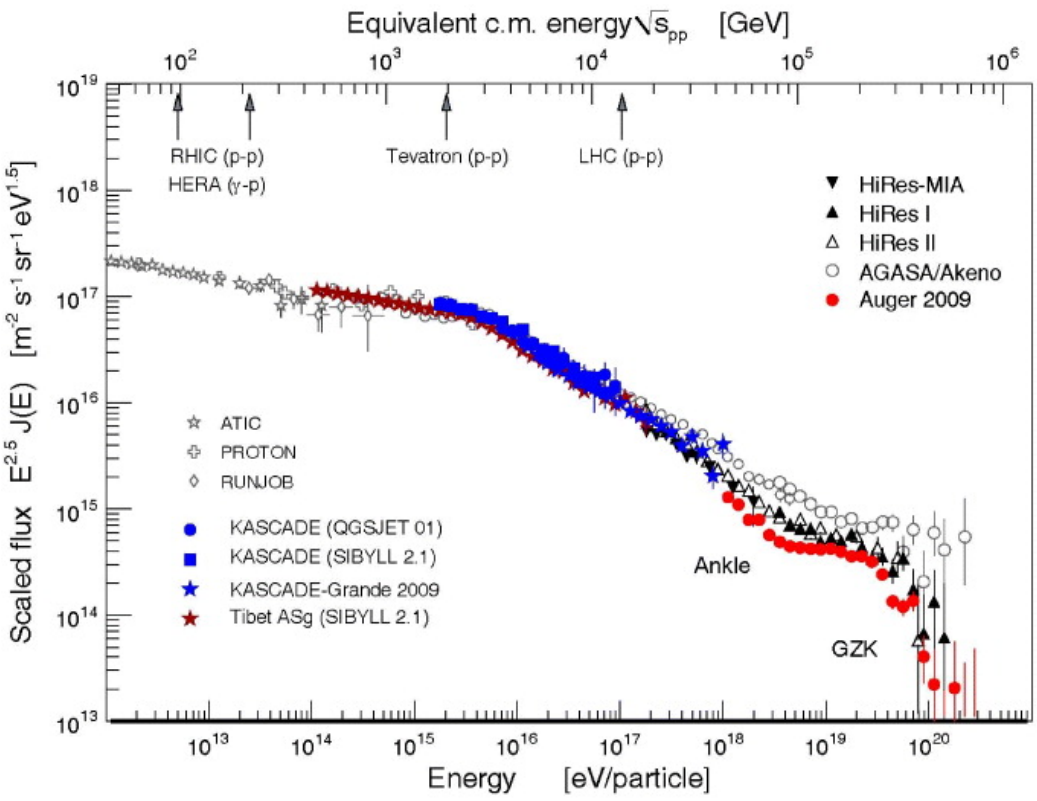

Figure 1.2: The cosmic ray flux spectrum scaled to an $E^{2.5} \times dN/dE$ spectrum, displaying the detailed structure of the steeply falling power-law spectrum. Center-of-mass equivalent energy scales for cosmic ray collisions in the atmosphere are provided. Figure from [2].

Moreover, the accelerators that produce UHECRs have not yet been identified. Intergalactic magnetic fields bend the paths of these charged particles, making it difficult to correlate arrival directions of the UHECRs at Earth to their true origin. Using simple energy considerations, Hillas narrowed the field of possible sources by requiring that the magnetic field of the accelerator must be sufficient to confine the UHECRs within the size of the source [8]. The updated Hillas plot of Figure 1.3 shows such sources—notably compact sources like neutron stars, gamma-ray bursts, and SNRs, or galactic sources such as active galactic nuclei (AGNs)—compared to the energy requirements of accelerating UHECR proton and iron nuclei primaries [9].

Gamma-ray bursts (GRBs) have long been considered promising sources of UHECRs. These events are some of the most violent in the universe, releasing im-

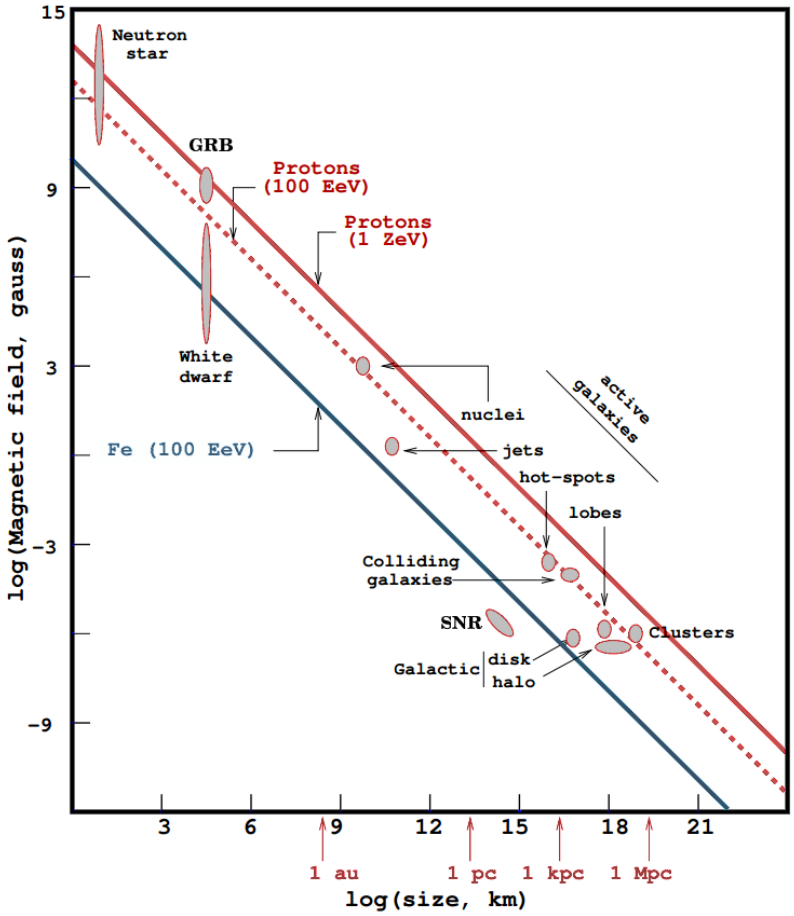

Figure 1.3: The Hillas plot, showing the acceleration capabilities of astrophysical objects as a function of size and magnetic field strength. The solid and dashed red lines represent the conditions required for proton acceleration to 10^{21} eV and 10^{20} eV, respectively, while the blue line is for iron nuclei acceleration to 10^{20} eV. Figure from [9].

mense gamma-ray radiation for between 10^{-3} s and 1000 s, becoming the brightest objects in the gamma-ray sky during that time. *Long* GRBs ($\gtrsim 2$ s in duration) are associated with the catastrophic collapses of supermassive stars into a black hole [10–12], while *short* GRBs ($\lesssim 2$ s in duration) are theorized to be the result of mergers of compact binary systems (i.e. two neutron stars, or a neutron star-black hole binary) [13]. Both classes of GRBs are extragalactic events that have been observed to be isotropically distributed in the sky and have been established to be visible at large cosmological distances, as GRB host galaxies have measured redshifts of

$0.033 \lesssim z \lesssim 8$ [12, 14–19]. The large amounts of energy released so quickly puts GRBs as a class at the top left of the Hillas plot in Figure 1.3, capable of accelerating UHECRs. Given their transient nature and that they can be well localized, GRBs allow for low background searches for UHECRs production during their initial, high fluence gamma-ray emission (called the *prompt* emission).

Though UHECRs themselves are difficult to correlate with GRBs due to deflection by intergalactic magnetic fields, observation of neutral particles produced concurrently with the UHECRs would constitute evidence of hadronic acceleration. At their source, accelerated hadrons would interact with photons to produce pions through the Δ^+ resonance to first order:

$$p + \gamma \rightarrow \Delta^+ \rightarrow \begin{cases} p + \pi^0 \rightarrow p + 2\gamma \\ \\ n + \pi^+ \rightarrow n + \mu^+ + \nu_\mu \rightarrow n + e^+ + \nu_e + \bar{\nu}_\mu + \nu_\mu \end{cases} \tag{1.1}$$

Both the gamma-rays and high energy neutrinos produced in the decays of the neutral and charged pions, respectively, are detectable and are the signature of hadronic acceleration in a cosmic accelerator.

The gamma-rays produced in these pion decays would have sufficient energy to pair-produce in interactions with the CMB and extragalactic infrared light, attenuating the highest energy photons observable from sources beyond the local group. The surviving pion-decay gamma-ray flux at Earth would then be hard to distinguish from other gamma-ray production mechanisms at the source. The observable distance of gamma-rays and cosmic ray protons are shown in Figure 1.4 as a function of energy.

The high energy neutrinos produced in these pion decays, however, would be an unambiguous signal of hadronic acceleration in a UHECR source. These chargeless, nearly massless leptons interact only through the weak force, giving them extremely small interaction cross sections at all energies. As such, neutrinos can escape from the source and propagate through the known universe completely unimpeded, making

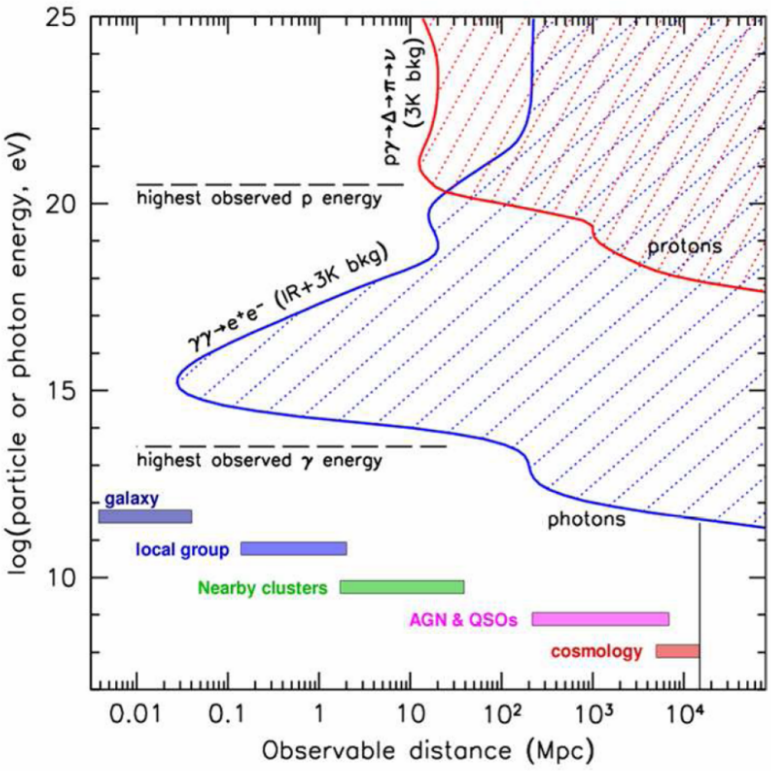

Figure 1.4: Astrophysics messenger particle observable distances as a function of messenger energy. Note that the universe is transparent to neutrinos at all distances and energies shown here. Figure from [20].

them ideal cosmic messengers to probe currently unobservable astrophysical phenomena. The property that makes neutrinos ideal astrophysical messenger particles also make them difficult to detect, requiring large bodies of a dense material to observe a neutrino interaction as well as a material that allows observation of the secondary particles produced in the interactions.

The IceCube Neutrino Observatory is currently the best detector for such a search of neutrino production in GRBs. It consists of 5160 optical modules that instrument more than one billion tons of natural ice at the South Pole, which detect the Cherenkov radiation emitted by the charged secondary particles produced in neutrino interactions in the ice. Muons produced in charged current interactions of muon neutrinos can travel for kilometers in the ice before decaying, greatly increasing the effective volume of the detector; these muons appear as well-localized *tracks* of light

in the detector. Neutrino interactions can also appear as nearly spherical *cascades* from the electromagnetic and hadronic particle showers produced in electron and tau neutrino charged current interactions, as well as in neutral current interactions of all neutrino flavors. By searching for neutrinos whose interaction is contained within the detector [21, 22], IceCube successfully discovered a high-energy astrophysical neutrino flux with unknown origin. This was later confirmed in an independent search for high energy muon neutrino-induced tracks from the Northern Hemisphere [23]

Past searches in IceCube for neutrino production in GRBs have primary focused on the muon neutrino tracks from GRBs in the Northern Hemisphere sky, where the Earth is used to shield IceCube's primary background of muons produced in cosmic ray air showers. In four years of searches with both the fully and partially completed detector, no muon neutrino signal was detected from GRBs [24–26]. Recently, this search was extended to cascade events from all GRBs in the sky. This search also failed to find a compelling neutrino signal from GRBs [27].

The previous null results impel a further expansion of the neutrino search window in IceCube to muon neutrino tracks from GRBs in the Southern Hemisphere sky. Though this region of the sky contains IceCube's primary background of atmospheric muons—recorded by the detector at a rate of $\gtrsim 2\,\mathrm{kHz}$—their spectrum is relatively soft compared to the expected neutrino signal from GRBs. Further, IceCube is most sensitive to the highest energy neutrino signal in this portion of the sky, as the Earth becomes opaque to neutrinos with energies $E_\nu \gtrsim 1\,\mathrm{PeV}$. A search for muon neutrino tracks from GRBs in the Southern Hemisphere sky is therefore possible and complementary to previous neutrino searches from GRBs with IceCube.

This dissertation is organized as follows. Chapter 2 describes GRBs and their expected neutrino production. The IceCube detector and event processing is then outlined in Chapter 3, followed by event reconstruction and simulation in Chapter 4. The Southern Hemisphere muon neutrino track event selection and unbinned likeli-

hood analysis are then discussed in Chapter 5 and Chapter 6, respectively. Finally, Chapter 7 presents the results of the muon neutrino search from GRBs in the Southern Hemisphere sky in combination with previous Northern Hemisphere muon neutrino and all-sky cascade searches, with Chapter 8 offering conclusions and a discussion of the future of neutrino searches from GRBs with IceCube.

Chapter 2

Gamma-Ray Bursts

GRBs are extremely violent cosmological events that emit condensed gamma-ray radiation in the span of a few milliseconds to thousands of seconds. In that brief time, the GRB is the brightest object in the gamma-ray sky. These events are detected several times per day isotropically in the sky by gamma-ray detecting satellites. As the brightest electromagnetic outbursts ever detected, GRBs are promising sources of UHECRs and high-energy neutrinos.

2.1 Historical Observations

The Vela satellites deployed by the United States Department of Defense discovered GRBs in 1967 [28]. These satellites consisted of omni-directional gamma-ray detectors with a primary mission of surveilling countries for possible violations of the 1963 Nuclear Test-Ban Treaty. They observed anamolous gamma-ray flashes which were established to have not originated from the Earth through triangulation. The discovery was confirmed by Russian IMP-6 satellites [29] and ground-based observatories [30] in 1973, when the Vela data, initially classified, was finally released to the public. Hundreds of possible progenitors were proposed to explain the origin of the GBRs, but, given the brevity of the events and the unpredictability of their occurence, little progress was made for more than 25 years.

It was only when the Burst and Transient Search Experiment (BATSE) aboard the Compton Gamma Ray Observatory (CGRO) was launched in 1991 that the nature of GRBs began to be revealed. Over nine years of operation, BATSE discovered an isotropic distribution of 2704 GRBs with little spatial dependence in the gamma-ray

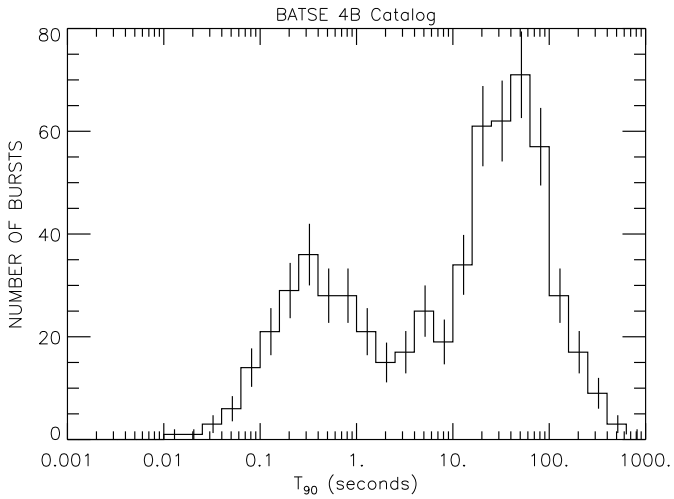

Figure 2.1: Duration distribution of BATSE GRBs, showing both short and long classes. T90 refers to the time window length that contains 90% of the measure gamma-ray fluence of a given GRB [31].

intensity measured [31], providing the first evidence of the the extragalactic origin of GRBs. The directional resolution of the detector of a few degrees was insufficient for source identification, however. Duration information of the GRBs revealed two classes of GRBs, a *long* class that lasted for $\gtrsim 2\,\mathrm{s}$ and a *short* class lasting $\lesssim 2\,\mathrm{s}$, the distribution of which is shown in Figure 2.1. Temporal lightcurves of the BATSE GRBs also revealed temendous variability and irregularity in the GRB gamma-ray emission.

The BeppoSAX satellite, launched in 1996, observed the fading afterglow of long GRBs in x-rays for the first time in 1997 [32]. The directional resolution of this satellite was sufficient to allow ground based optical observatories to search for possible progenitors of these long GRBs [33, 34]. From these measurements, many long GRB progenitors were found to have redshifts of $z \gtrsim 1$ based on optical measurements of their host galaxies, establishing long GRBs to be extragalactic events.

For GRBs to appear so bright at such distances—brighter than their host galaxies, albeit on short time scales—tremendous energies on the order of a solar rest mass $M_\odot c^2 \sim 2 \times 10^{54}\,\mathrm{erg}$ would have to be released during the gamma-ray emission if

radiated isotropically. Such energies would be particularly prohibitive for theories of GRBs involving stellar progenitors, as supernovae only radiate on the order of 10^{51} erg over the span of weeks. Analysis of the afterglow light curves of a number of BeppoSAX localized GRBs, however, found breaks in their decay [35–37], suggesting that the emission of GRBs is beamed in a collimated jet. The energy requirement for gamma-ray radiation in such a jet is reduced to $\sim 10^{54} \times \Omega/4\pi$ erg, where Ω is the solid angle into which the jet is beamed, making the energy constraints for a stellar origin to GRBs much less severe.

The High Energy Transient Explorer (HETE-2) was launched in 2000, consisting of gamma-ray, x-ray, and ultraviolet (UV) light detectors capable of near real-time localization of GRBs and localization of afterglows with arcsecond precision. The HETE-2 rapid response program led to the first unambiguous association of a long GRB with a supernova (SN) [10, 11], establishing the stellar origin of this class of GRBs. HETE-2 also detected the first afterglow associated with a short GRB [38], leading to the first redshift localization of the short GRB population.

2.2 Modern Detection

The modern era of GRB detection was heralded with the launch of the Swift and Fermi satellite experiments. These detectors and their key discoveries are discussed here. Other experiments contributing to the sample of GRBs examined in this dissertation are also briefly described. The characteristics of all detectors used in this analysis are summarized in Table 2.1.

2.2.1 The Swift Experiment

The Swift experiment consists of a wide-field Burst Alert Telescope (BAT) [39], X-Ray Telescope (XRT) [40], and UV-Optical Telescope (UVOT) [41], and was launched

Table 2.1: Characteristics of GRB satellite detectors used in this dissertation.

Detector	Field of View	GRB Localization	Energy Range
Fermi-GBM	$\geq 2.5\pi$ sr	$1 - 15^\circ$	$8\,\mathrm{keV} - 40\,\mathrm{MeV}$
Fermi-LAT	0.8π sr	$\lesssim 1^\circ$	$20\,\mathrm{MeV} - 300\,\mathrm{GeV}$
INTEGRAL	$12^\circ \times 12^\circ$	$1 - 15'$	$15\,\mathrm{keV} - 10\,\mathrm{MeV}$
IPN	4π sr	$0.1 - 5^\circ$	—
Konus-Wind	4π sr	—	$10\,\mathrm{keV} - 10\,\mathrm{MeV}$
MAXI	$1.5^\circ \times 160^\circ$	$0.1 - 0.2^\circ$	$0.5 - 30\,\mathrm{keV}$
SuperAGILE	$107^\circ \times 68^\circ$	$1 - 2'$	$15 - 45\,\mathrm{keV}$
Suzaku-WAM	$\sim 2\pi$ sr	—	$50\,\mathrm{keV} - 5\,\mathrm{MeV}$
Swift-BAT	1.4 sr	$1 - 4'$	$15 - 150\,\mathrm{keV}$
Swift-XRT	$23.6' \times 23.6'$	$18''$	$0.2 - 10\,\mathrm{keV}$
Swift-UVOT	$17' \times 17'$	$0.9''$	optical $(170 - 600\,\mathrm{nm})$

into orbit around Earth in 2004. Swift-BAT scans the sky with a 1.4 sr field of view (FOV) to detect GRBs over the $15 - 150\,\mathrm{keV}$ hard x-ray and gamma-ray energy range using a $5200\,\mathrm{cm}^2$ coded-aperture panel of $4 \times 4\,\mathrm{mm}^2$ CdZnTe elements. The satellite is capable of determining the burst location to $1 - 4'$ and quickly slews to that location in under 100 s. The Swift-XRT and UVOT detectors can then observe GRB afterglows, resulting in GRB localizations of arcsec (XRT) to sub-arcsec (UVOT) precision as well as redshift determination.

Swift has made a number of key contributions to our understanding of GRB progenitors. It was significantly more prolific than its predecessors in yielding well-localized GRBs, detecting ∼100 GRB per year, with ∼90% having XRT and ∼30% having UVOT follow-up observations. The long GRBs in this sample had average redshifts of $z \gtrsim 2$ [14], a factor of ∼2 higher than those measured in BeppoSAX and HETE-2 bursts. This was largely a result of both Swift's greater gamma-ray sensitivity and faster localizations for ground-based observatory follow-ups. Further, Swift measured GRB redshifts up to $6 \lesssim z \lesssim 8$ [16–19], placing these GRB progenitors amongst the earliest stars in the universe. Swift also detected the nearest GRB ever observed at $z = 0.033$ [12], which was shortly associated with SN 2006aj.

Following the work of HETE-2, Swift detected a number of short GRB afterglows, resulting in the first measurement of short GRB redshifts. They found that the redshift of these bursts was on average a factor of $1/3 - 1/2$ less than that of long GRBs [15]. The galaxies that these short GRBs were associated with, typically early-type elliptical galaxies, showed little significant star-formation. Coupled with the low-luminousity of short GRBs compared to long GRBs, these observations are consistent with the interpretation that an old population of compact binary systems (i.e. binary neutrons star or neutron star–black hole binary systems) are the progenitors of short GRBs through a catastrophic merger due to systematic loss of angular momentum of the system.

2.2.2 The Fermi Experiment

The Fermi Gamma-Ray Space Telescope (Fermi) is a large FOV gamma-ray detector that was launched into orbit around Earth in 2008, consisting of the Gamma-ray Burst Monitor (GBM) [42] and Large Area Telescope (LAT) [43] detectors. Combined, these detectors measure high energy gamma-ray emission over the broadest energy range of any gamma-ray detector in operation.

The GBM detector consists of 12 activated sodium iodide (NaI) scintillation detectors placed at the corners of the satellite operating in the $8\,\mathrm{keV} - 1\,\mathrm{MeV}$ gamma-ray energy range and 2 bismuth germanate (BGO) scintillation detectors operating in the $200\,\mathrm{keV} - 40\,\mathrm{MeV}$ energy range; a basic diagram of these detector elements are shown in Figure 2.2. Taken together, Fermi-GBM observes the entire sky not occulted by the Earth ($\geq 8\,\mathrm{sr}$). Burst positions are determined to $1 - 15^\circ$ precision through the measured gamma-ray fluence at each NaI scintillation detector and accounting for their expected angular response. Through comparison of GRB positions with Swift measurements, the systematic uncertainty of the GBM burst positions can be parameterized as a weighted sum of Gaussian distributions with the following

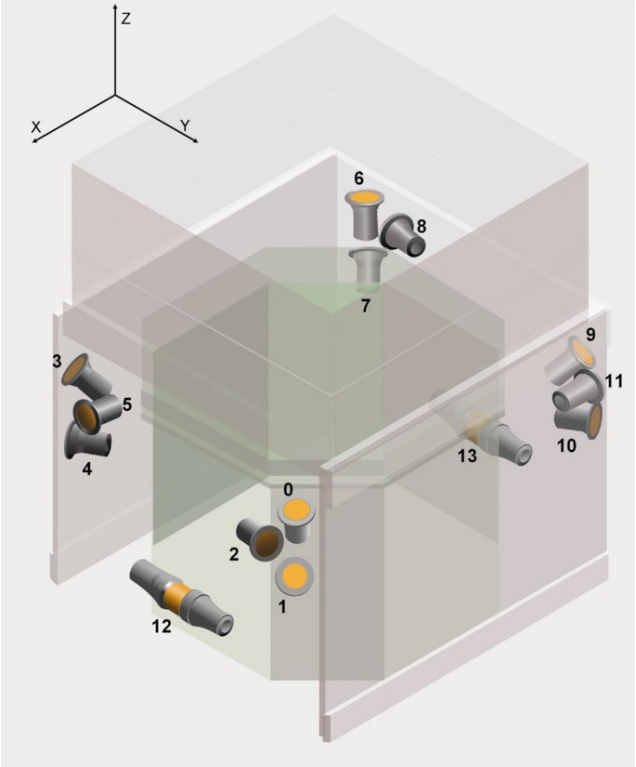

Figure 2.2: Diagram of the Fermi-GBM detector. Elements 0-11 show positions and orientations of the 12 NaI detectors, and elements 12 and 13 show the BGO detectors. Figure from [42].

parameters: $\sigma_1 = 2.6°$ with weight $w_1 = 0.72$, and $\sigma_2 = 10.4°$ with weight $w_2 = 0.28$ [44]. The Fermi-GBM detector is currently the most prolific GRB detector in operation, yielding catalogs of $\gtrsim 200$ GRBs per-year [45, 46].

The LAT detector is composed of a 4×4 array of tracker silicon strip detector towers interleaved with a high-Z material (tungsten) to induce e^+e^- pair-production from incident gamma-rays, with energy sensitivity between $20\,\mathrm{MeV} - 300\,\mathrm{GeV}$. Cosmic ray backgrounds are reduced through an anticoincidence shield consisting of tiles of plastic scintillator that surround the silicon tracker array. The FOV of the detector is $\gtrsim 2.4\,\mathrm{sr}$, while its angular resolution is strongly energy dependent, with a resolution of $5°$ at $100\,\mathrm{MeV}$ decreasing to $\lesssim 1°$ above $1\,\mathrm{GeV}$. Though its reduced FOV and higher energy threshold make the Fermi-LAT detector less useful than Fermi-GBM

at detecting GRBs, the LAT detector can continue observation of GRBs into the high energy gamma-ray band.

2.2.3 Other Current GRB Detectors

Though Swift and Fermi contribute the majority of GRB detections to this analysis, a number of other experiments can detect or contribute information to GRBs in the final sample:

INTEGRAL: The International Gamma-Ray Astrophysics Laboratory (INTEGRAL) experiment was launched into a highly eccentric orbit around Earth in 2002 [47]. The satellite contains several complimentary detectors that are co-aligned with overlapping FOVs: the SPI spectrometer with sensitivity between $20\,\mathrm{keV} - 8\,\mathrm{MeV}$ (capable of good spectral and temporal resolution on gamma-ray sources), the IBIS imager optimized for arcmin angular precision imaging between $15\,\mathrm{keV} - 10\,\mathrm{MeV}$, the JEB-X x-ray band monitor, and the OMC V-band optical monitor. The IBIS imager is capable of $12'$ angular precision, though due to its small FOV, contribute very few GRB localizations that are better than Swift localizations.

Konus-Wind: The Konus detector [48] is mounted on the GSS-Wind spacecraft, which was launched in 1994 and was inserted into orbit around the Sun at the Sun-Earth L_1 Lagrangian point in 2004. The detector consists of two NaI scintillation detectors with gamma-ray sensitivity between $10\,\mathrm{keV} - 10\,\mathrm{MeV}$ and a full-sky $4\pi\,\mathrm{sr}$ field of view. The detector's primary mission is to provide temporal and spectral measurements of gamma-ray flares including GRBs.

MAXI: The Monitoring All-sky X-ray Image (MAXI) [49] is an x-ray band detector, which was installed on the International Space Station in 2004. The detector consists of two wide FOV x-ray slit cameras: a gas-proportional counter

slit camera with sensitivity between $2 - 30\,\mathrm{keV}$ and an x-ray CCD slit camera with sensitivity between $0.5 - 12\,\mathrm{keV}$. These cameras have $0.1 - 0.2^\circ$ angular resolution in measuring GRB afterglows.

AGILE and SuperAGILE: The AGILE satellite [50] launched in 2007 into low-Earth orbit, composed of the Gamma-Ray Imaging Detector (GRID), a CsI mini-calorimeter, a plastic scintillator anticoincidence shield, and the SuperAGILE x-ray monitor [51]. The GRID consists of four independent silicon-tungsten tracker arrays sensitive to the $30\,\mathrm{MeV} - 50\,\mathrm{GeV}$ energy range capable of resolving gamma-ray sources to $15'$ angular precision within a large $\sim$2.5 sr FOV. SuperAGILE consists of four further silicon trackers with a tungsten coded mask sensitive to the $15 - 45\,\mathrm{keV}$ energy range. The SuperAGILE detector has a $107^\circ \times 68^\circ$ rectangular total FOV overlapping that of the GRID and is capable of resolving sources to $6'$ angular precision, allowing simulataneous measurement of GRBs in both gamma-rays and hard x-rays.

Suzaku-WAM: The Suzaku satellite's Wide-band All-sky Monitor (WAM) [52] has been in operation since 2005 in a low-Earth orbit. The WAM detector consists of the Hard X-ray Detector (HXD) [53] and its four BGO anticoincidence shields. Though it has no imaging capabilities, Suzaku-WAM provides good temporal and spectral measurements of GRBs in energies between $50\,\mathrm{keV} - 5\,\mathrm{MeV}$.

IPN: The Third Interplanetary Network (IPN) is a network of satellites that can localize GRBs to roughly degree precision through triangulation from gamma-ray emission arrival timing [54]. The current IPN consists of Swift, Fermi, Suzaku, AGILE, and RHESSI in low-Earth orbit; INTEGRAL in its highly-eccentric Earth orbit; Konus-Wind at the Sun-Earth L_1 Lagrangian point; MESSENGER, which entered orbit around Mercury in 2011, and used the last of its propellant to deorbit by crashing to the surface of Mercury in 2015; and Mars-

Odyssey in orbit around Mars. Given the large number of satellites, the nearly isotropic sensitivity of the many of these satellites, and that several of the satellites are not occulted by any planets, the IPN is an all-sky, all-time GRB monitor.

2.2.4 Gamma-Ray Burst Coordinates Network

GRB observations are reported to the NASA Gamma-ray burst Coordinates Network (GCN) [55], part of the Transient Astronomy Network (TAN). Observations are circulated by email to the GCN community through notices, circulars, and reports, and are permanently archived. Notices relay the spatial coordinates of GRBs or transients in near real-time to ground-based or space-based follow-up observatories. Circulars are prose-style emails reporting follow-up observation with refined timing, localization, and spectral measurement results, or calls for coordination with other observatories. Reports are prose-style write-ups of observations issued at a later time, allowing observatories to distribute results of full analyses and corrections to previous notices or circulars.

2.2.5 GRBweb

Though all spacecrafts summarized in Table 2.1 publish observations to the GCN, the infomation is archived in email form, making compilation of GRB information from multiple detectors difficult. A set of PHP scripts read the temporal, spatial, and spectral information from these emails and store it in a MySQL database. Fermi-GBM publishes GRB information to a separate archive—later in catalogs as well [45, 46]—which is also extracted and included in the MySQL database. The compiled database is tabulated on a publicly available website, called GRBweb, into a summary table for all GRBs observed, as well as into per-GRB, per-detector tables [56,

57]. The GRBweb summary table compiles all temporal, spatial, and spectral information used in this dissertation.

The temporal information of a GRB is used to correlate neutrino candidate events with the prompt gamma-ray emission of a GRB. Should more than one detector observe a GRB in gamma-rays, the most inclusive prompt gamma-ray time window is calculated and denoted as $T_{100} = T_2 - T_1$, where T_1 and T_2 are the earliest and latest gamma-ray detection times, respectively. The GRB start time taken to be T_1.

Localization information of GRBs is used to correlate neutrino candidate events spatially with a GRB. The GRB localization and angular uncertainty (scaled to a 1σ error circle) is taken preferentially from the most accurate satellites in roughly the following order: Swift-UVOT, Swift-XRT, Swift-BAT, SuperAGILE, INTEGRAL, Maxi, Fermi-LAT, IPN, and then Fermi-GBM. Redshift measurements for GRBs are also recorded when available; when no redshift is measured, z is taken to be 0.5 for short GRBs and 2.15 for long GRBs.

Spectral measurements of a GRB's gamma-ray fluence are used to constrain neutrino production in certain GRB models. Fluence measurements are taken preferentially from the detector with the widest reported energy bandwidth in its GCN, roughly in the following order: Fermi-GBM, Konus-Wind, Suzaku-WAM, INTEGRAL, and then Swift-BAT. Spectral fits as a function of energy are reported as a power law, a power law with an exponential energy cut-off, or a Band function [58] of the form:

$$F_\gamma(E_\gamma) = f_\gamma \times \begin{cases} \left(\frac{E_\gamma}{100\,\mathrm{keV}}\right)^{-\alpha_\gamma} \exp\left[-\frac{(\beta_\gamma-\alpha_\gamma)E_\gamma}{\varepsilon_0}\right], & E_\gamma \leq \varepsilon_0 \\ \left(\frac{\varepsilon_0}{100\,\mathrm{keV}}\right)^{\beta_\gamma-\alpha_\gamma} \exp\left(\alpha_\gamma-\beta_\gamma\right)\left(\frac{E_\gamma}{100\,\mathrm{keV}}\right)^{-\beta_\gamma}, & \varepsilon_0 < E_\gamma. \end{cases} \tag{2.1}$$

For use in GRB neutrino production model calculations, these fits are reinterpreted as a broken power law of the form:

$$F_\gamma(E_\gamma) = f_\gamma \times \begin{cases} \varepsilon_\gamma^{(\alpha_\gamma-\beta_\gamma)} E_\gamma^{-\alpha_\gamma}, & E_\gamma \leq \varepsilon_\gamma \\ E_\gamma^{-\beta_\gamma}, & \varepsilon_\gamma < E_\gamma \end{cases} \tag{2.2}$$

where ε_γ is the gamma-ray break energy. For power law spectral fits, α_γ is set to the fit spectral index, and $\beta_\gamma = \alpha_\gamma + 1$; the break energy ε_γ is set to 1 MeV for short GRBs, and 200 keV for long GRBs. For a power law with an exponential energy cutoff fit, ε_γ is set to the cutoff energy $E_{\rm cutoff}$, while α_γ is set to the fit spectral index and $\beta_\gamma = \alpha_\gamma + 2$. For a Band function fit, α_γ and β_γ are set to the spectral indices of the Band function, with a break energy of $\varepsilon_\gamma = \varepsilon_0$. Where spectral measurements have been quoted, the broken power law fluence normalization f_γ is take to be that given in the GCN. For GRBs without reported spectral fits, α_γ , β_γ, and ε_γ are set to average values from the Fermi-GBM catalog: $\alpha_\gamma = 1$, $\beta_\gamma = \alpha_\gamma + 1 = 2$, and $f_\gamma = 10^{-5}\,\mathrm{erg\,cm^{-2}}$, with $\varepsilon_\gamma = 1\,\mathrm{MeV}$ for short GRBs and $\varepsilon_\gamma = 200\,\mathrm{keV}$ for long GRBs. Should the GRB only be measured by Fermi GBM, the spectral parameters are set to average values from the Fermi GBM two-year catalog [44], which are consistent within the errors of the four-year catalog [45]: $\alpha_\gamma = 1.05$, $\beta_\gamma = 2.25$, and $\varepsilon_\gamma = 205\,\mathrm{keV}$.

Only GRBs in the Southern Hemisphere sky occuring during good operation of the IceCube Neutrino Observatory are analyzed in this dissertation. Over four years of operation with the full IceCube detector and one year of a nearly complete IceCube detector with 79-strings (May 2010 through May 2015 in total), 664 GRBs are analyzed, with the detectors yielding the temporal, spatial, and spectral measurements of these GRBs summarized in Table 2.2. The measured T_{100} and spatial distributions are shown in Figures 2.3 and 2.4, respectively, while more detailed information of the analyzed GRB sample is provided in Appendix A.

Table 2.2: Fraction of GRB measurements made by each detector contributing to the GCN.

Detector	T_1	T_2	Position	Fluence
Fermi-GBM	434 (65.4%)	416 (62.7%)	377 (56.8%)	464 (69.9%)
Fermi-LAT	0 (0%)	0 (0%)	22 (3.3%)	0 (0%)
INTEGRAL	10 (1.5%)	11 (1.7%)	10 (1.7%)	7 (1.1%)
IPN	0 (0%)	0 (0%)	44 (6.6%)	0 (0%)
Konus-Wind	44 (6.6%)	56 (8.4%)	0 (0%)	61 (9.2%)
Maxi	6 (0.9%)	5 (0.8%)	13 (2.0%)	0 (0%)
SuperAGILE	0 (0%)	0 (0%)	0 (0%)	0 (0%)
Suzaku-WAM	18 (2.7%)	9 (1.4%)	0 (0%)	1 (0.2%)
Swift-BAT	151 (22.7%)	166 (25.0%)	63 (9.5%)	101 (15.2%)
Swift-XRT	0 (0%)	0 (0%)	122 (18.4%)	0 (0%)
Swift-UVOT	0 (0%)	0 (0%)	13 (2.0%)	0 (0%)

2.3 Models of Neutrino Production

The principal model to describe the observed gamma-ray emission involves a highly relativistic outflow of matter (called the *fireball*) created through rapid accretion onto a black hole central engine and emitted along the axis of rotation of the progenitor. This process is initiated by a stellar collapse into a black hole or compact binary merger that releases on the order of a few solar masses of gravitational energy in the form of kinetic energy. The outflow is composed of many relativistic shells with differing Lorentz factors, each made of a plasma of electrons, photons, and protons. These shells of differing speeds collide and produce shocks in the plasma (called *internal* shocks). By reflecting the charged particles across the edge of this shock through chaotic electric and magnetic fields, these particles are accelerated through first order Fermi acceleration. Synchrotron radiation and inverse-Compton scattering by accelerated electrons in the shock yield the observed gamma-ray emission.

The internal shock fireball model naturally explains a number of characteristics observed in GRB emission. The plasma outflow is produced in the form of a relativistic jet, which beams the produced radiation in the direction of an observer

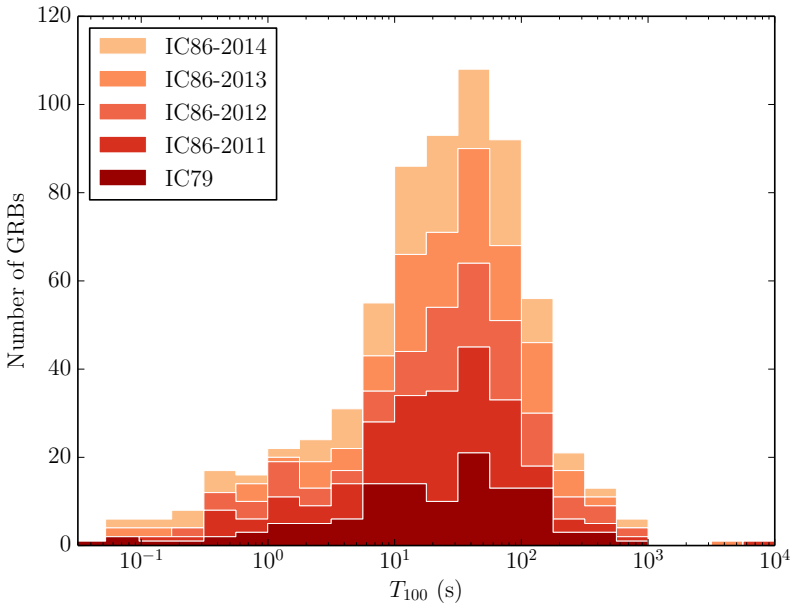

Figure 2.3: T_{100} distribution of GRBs analyzed in this dissertation, with contributions from each IceCube year highlighted.

and reduces the required energy inferred from the GRB observation. Collisions of many shells in the fireball, further, can yield the rapid temporal variability that is observed in GRB emission. As the fireball adiabatically expands in the outflow, the plasma transitions from optically thick to optically thin, resulting in thermal and non-thermal spectral components that have been observed in some GRBs [59, 60]. After further expansion and cooling, the fireball collides with the surrounding interstellar medium, which creates additional shocks (*external* shocks), resulting in the observed broadband GRB afterglows.

The internal shocks of the fireball are also capable of accelerating protons or other heavier nuclei present in the outflow up to energies of $\gtrsim 10^{20}\,\mathrm{eV}$, the energies required in the observed UHECR spectrum [61]. Moreover, the average energy generation rate in measured GRBs is capable of explaining the observed UHECR flux, making GRBs promising sources of UHECRs [62]. The strong magnetic fields of the shocks would, however, tend to confine the accelerated protons, requiring UHECRs

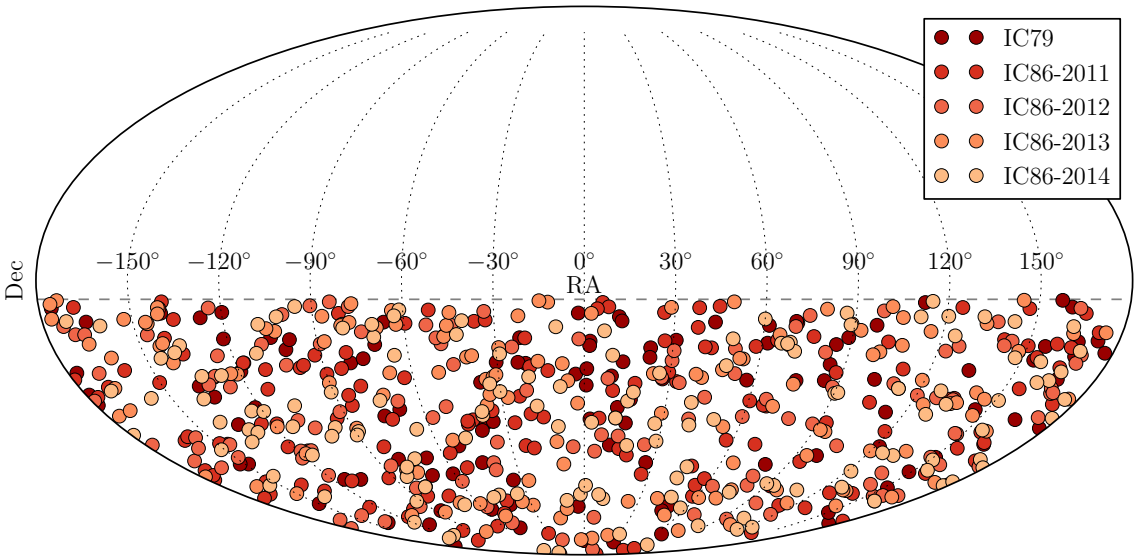

Figure 2.4: Spatial distribution of GRBs in each IceCube year analyzed in this dissertation, in equatorial coordinates. The IceCube overburden *horizon* is indicated with the dashed line.

to escape the fireball as neutrons, through direct escape of protons near the edge of the fireball, or through diffusive processes [63].

The accelerated protons within the fireball would interact with the gamma-ray field present in the fireball to produce neutrinos. As a simplifying assumption, gamma-ray production—through synchrotron radiation and inverse-Compton scattering of accelerated electrons—and proton acceleration are presumed to occur at the same locations in the relativistic fireball, though this assumption does not necessarily hold in multi-zone dynamic internal shock models [64]. This section describes this neutrino production under two paradigms: one where neutrino production is derived from measured GRB characteristics assuming GRBs are one possible source of UHECRs, and one in which the neutrino production is scaled directly to the UHECR spectrum under the hypothesis that UHECRs are produced solely by GRBs.

2.3.1 Internal Shock Fireball Model

The gamma-ray radiation and UHECR production in the relativistic fireball model is contingent on acceleration of charged particles in the fireball. The internal shock model conveniently achieves this through collisions of many comoving plasma shells in the fireball, which can explain the extreme temporal variability in observed GRBs and the measured non-thermal power law gamma-ray spectrum through the synchrotron radiation and inverse Compton scattering of accelerated electrons in the shocks.

Collisions between plasma shells accelerate the charged particles in the fireball through Fermi acceleration at the shock that forms in a collision. The expected spectrum of particles resulting from Fermi acceleration is derived following [65]. Charged particles that move across the shock front gain an amount of energy proportional to the particle's energy for each pair of *in–out* crossings:

$$\Delta E = \xi E. \tag{2.3}$$

Here, ξ is the fractional energy gain the particle obtains per crossing. This acceleration is achieved through *collisionless* scattering of the particle by magnetic fields near the relativistic shock front. The energy of the particle after n such crossings is then

$$E_n = E_0 \left(1 + \xi\right)^n . \tag{2.4}$$

Inverting this equation, the number of crossings required to reach an energy E is

$$n = \frac{\ln\left(E/E_0\right)}{\ln\left(1 + \xi\right)}. \tag{2.5}$$

If the probability of the particle escaping the acceleration region is $P_{\rm esc}$, the number of particles that attain an energy E or higher is proportional to

$$N(\geq E) \propto \sum_{m=n}^{\infty} (1 - P_{\rm esc})^m = \frac{(1 - P_{\rm esc})^n}{P_{\rm esc}}. \tag{2.6}$$

By inserting (2.5) into (2.6), taking the logarithm, and re-exponentiating, the number of particles above an energy E is found as

$$N(\geq E) \propto \frac{1}{P_{\rm esc}} \left(\frac{E}{E_0}\right)^{\frac{\ln(1-P_{\rm esc})}{\ln(1+\xi)}}. \tag{2.7}$$

Noting the exponential is constant, one can write

$$\gamma = \frac{\ln\left[1/(1 - P_{\rm esc})\right]}{\ln(1 + \xi)} \approx \frac{P_{\rm esc}}{\xi} \tag{2.8}$$

assuming $P_{\rm esc}$ and ξ are small, leaving

$$N(\geq E) \propto \frac{1}{P_{\rm esc}} \left(\frac{E}{E_0}\right)^{-\gamma}. \tag{2.9}$$

Typically, the spectrum of particles is written as a differential flux. Differentiating (2.9) gives

$$\frac{dN}{dE} \propto E^{-(\gamma+1)}. \tag{2.10}$$

For shocks in an ideal monotonic gas, the integral spectral index can be shown to be $\gamma = 1$, giving a differential flux of $dN/dE \propto E^{-2}$. This ideal spectrum is consistent with the electron spectrum inferred from the measured gamma-ray flux of $dN_e/dE_e \propto E_e^{-p}$ with $p \sim 2 - 2.5$. Fermi acceleration would yield a similar power law spectrum for heavier charged particles in the plasma like protons or nuclei, consistent with the measured UHECR flux.

The type of Fermi acceleration discussed here is known as first-order Fermi acceleration, as ξ is proportional to the velocity of the planar shock front $\beta = v/c$. Fermi's original proposal of particle acceleration through collisionless scattering of charged particles with a magnetic field involved a moving magnetic cloud with velocity β. The energy gain factor ξ in this case is only proportional to β^2, giving this process the name second-order Fermi acceleration. Both processes achieve efficient charged particle acceleration capable of producing UHECRs.

Protons accelerated in the fireball interact with the gamma-ray radiation field to produce pions to first order through the Δ^+ resonance:

$$p + \gamma \rightarrow \Delta^+ \rightarrow \begin{cases} p + \pi^0 \\ \\ n + \pi^+ \end{cases} \tag{2.11}$$

The energy required for this process to occur, in the comoving (primed) fireball frame is

$$E'_p E'_\gamma \geq \frac{m_\Delta^2 - m_p^2}{4}, \tag{2.12}$$

which in the observer frame is

$$E_p \geq \left(\frac{\Gamma}{1+z}\right)^2 \frac{m_\Delta^2 - m_p^2}{4E_\gamma}, \tag{2.13}$$

where Γ is the bulk Lorentz factor of the expanding fireball. The pions produced here decay, yielding gamma-rays and neutrinos:

$$\begin{aligned} \pi^0 &\rightarrow \gamma + \gamma \\ \pi^+ &\rightarrow \mu^+ + \nu_\mu \rightarrow e^+ + \nu_e + \bar{\nu}_\mu + \nu_\mu. \end{aligned} \tag{2.14}$$

Though the initial ratio of neutrino flavors produced at the GRB progenitor is

$$(\nu_e : \nu_\mu : \nu_\tau)_{\text{source}} \approx (1 : 2 : 0)\,, \tag{2.15}$$

these neutrinos will oscillate between flavors over cosmological baselines, giving an approximate flavor ratio at Earth of

$$(\nu_e : \nu_\mu : \nu_\tau)_{\text{Earth}} \approx (1 : 1 : 1)\,. \tag{2.16}$$

The neutrinos produced here would propagate at nearly the speed of light, making them detectable concurrently with the prompt gamma-ray emission of a GRB.

2.3.2 Neutrino Production Scaled to Gamma-Ray Spectrum

The measured neutrino flux of the internal shock fireball model is calculable assuming an ideal proton source spectrum of $dN_p/dE_p \propto E_p^{-2}$ and a photon interaction field derived directly from that measured at Earth. Under these assumptions, GRBs would be a possible source of UHECRs, though not necessarily the only source as the proton spectrum has no explicit scaling to that measured at Earth, requiring an assumed baryonic loading in the GRBs, an assumed number of GRBs, and an assumed efficiency of proton escape.

To obtain the expected neutrino spectrum, the analytical approach of Guetta et al. is followed [66], with modifications of Hümmer, Baerwald, and Winter [67] discussed. Given a proton with energy E_p, the energy per-neutrino in (2.14) is

$$E_\nu = \frac{1}{4}\langle x_{p\to\pi}\rangle E_p \geq 7\times 10^5\,\text{GeV}\frac{1}{(1+z)^2}\left(\frac{\Gamma}{10^{2.5}}\right)^2\left(\frac{E_\gamma}{1\,\text{MeV}}\right)^{-1}. \tag{2.17}$$

Here, the 1/4 factor is a result of the four leptons of (2.14) obtaining roughly the same fraction of the pion's energy, $\langle x_{p\to\pi}\rangle \simeq 0.2$ is the average fraction of the proton's

energy deposited in the pion per interaction, and the result has been placed in the inequality of (2.13). From (2.17), it is clear that at each proton energy, the neutrino spectrum will follow the gamma-ray field spectrum. The photon interaction field is taken to be a broken power law as parameterized in (2.2), meaning the first neutrino break energy is therefore simply

$$\varepsilon_\nu^b = 7 \times 10^5 \,\mathrm{GeV} \frac{1}{(1+z)^2} \left(\frac{\Gamma}{10^{2.5}}\right)^2 \left(\frac{\varepsilon_\gamma}{1\,\mathrm{MeV}}\right)^{-1}. \tag{2.18}$$

The highest energy pions and muons cool through synchrotron radiation before decaying, introducing additional neutrino break energies. This effect occurs where the lifetime of the pion (or muon) is comparable to its synchrotron loss time in the comoving frame:

$$t'_{\mathrm{syn}} = \frac{3 m_{\pi(\mu)}^4 c^3}{4 \sigma_T m_e^2 E'_{\pi(\mu)} U'_B} \approx \tau'_{\pi(\mu)} = \tau^0_{\pi(\mu)} \frac{E'_{\pi(\mu)}}{m_{\pi(\mu)} c^2} \tag{2.19}$$

where $U'_B = B'^2/8\pi$ is the energy density of the shocked plasma magnetic field, $\sigma_T = 6.65 \times 10^{-25}\,\mathrm{cm}$ is the Thompson scattering length, $\tau^0_\pi = 2.6 \times 10^{-8}\,\mathrm{s}$ is the rest frame decay time of the pion, and $\tau^0_\mu = 2.2 \times 10^{-6}\,\mathrm{s}$ is the rest frame decay time of the muon. The fraction of energy in the magnetic field ϵ_B can be related to the shell collision radius R through

$$\epsilon_B L_{\mathrm{int}} = \frac{4\pi R^2 c \Gamma^2 B'^2}{8\pi}. \tag{2.20}$$

The internal plasma energy L_{int} here can also be related to the measured isotropic photon luminousity by $\epsilon_e L_{\mathrm{int}} = L_\gamma^{\mathrm{iso}}$, with ϵ_e being the fraction of accelerated electron energy converted to photons. Further, the collision radius R can be related to the velocity of the plasma shells and the GRB variability time scale t_v. The average difference of velocity in shells is approximately $\Delta v \sim c^2/2\Gamma^2$. The time of collision is

therefore approximately $t_c \sim ct_v/\Delta v$, meaning the collision radius is approximately

$$R = ct_c \simeq 2\Gamma^2 ct_v. \tag{2.21}$$

With these relations, the ratio of synchrotron loss time to pion decay time of (2.19) becomes

$$\frac{t'_{\rm syn}}{\tau'_{\pi(\mu)}} = \frac{1}{(1+z)^4}\frac{12\pi m^5_{\pi(\mu)} c^8 \epsilon_e \Gamma^8 t_v^2}{\sigma_T m_e^2 \tau^0_{\pi(\mu)} \epsilon_B E^2_{\pi(\mu)} L^{\rm iso}_\gamma} \tag{2.22}$$

where the measured variability time scale t_v at Earth is converted to that at the progenitor with a $(1+z)$ factor from cosmological expansion, and the pion (muon) energy $E_{\pi(\mu)}$ is in the Earth frame. The neutrino break energy from pion decay is then determined where $t'_{\rm syn}/\tau'_\pi \sim 1$:

$$\begin{aligned} \varepsilon^s_{\nu_\mu} &= \frac{1}{4}\frac{1}{(1+z)^2}\sqrt{\frac{12\pi m^5_{\pi(\mu)} c^8 \epsilon_e \Gamma^8 t_v^2}{\sigma_T m_e^2 \tau^0_{\pi(\mu)} \epsilon_B E^2_{\pi(\mu)} L^{\rm iso}_\gamma}} \\ &= 10^8\,{\rm GeV}\frac{1}{(1+z)^2}\sqrt{\frac{\epsilon_e}{\epsilon_B}}\left(\frac{\Gamma}{10^{2.5}}\right)^4\left(\frac{t_v}{10^{-2}\,{\rm s}}\right)\left(\frac{L^{\rm iso}_\gamma}{10^{52}\,{\rm erg\,s^{-1}}}\right)^{-1/2}, \end{aligned} \tag{2.23}$$

recognizing on average the pion evenly distributes is energy among its four lepton decay products. Because the decay time of the muon is 100 times that of the pion, the neutrino break energy from muon synchrotron cooling is 10 times smaller through the proportionality $t'_{\rm syn}/\tau' \propto E_\nu^{-2}$, giving

$$\varepsilon^s_{\nu_e,\bar\nu_\mu} = \varepsilon^s_\nu = 10^7\,{\rm GeV}\frac{1}{(1+z)^2}\sqrt{\frac{\epsilon_e}{\epsilon_B}}\left(\frac{\Gamma}{10^{2.5}}\right)^4\left(\frac{t_v}{10^{-2}\,{\rm s}}\right)\left(\frac{L^{\rm iso}_\gamma}{10^{52}\,{\rm erg\,s^{-1}}}\right)^{-1/2}. \tag{2.24}$$

Additionally, the $t'_{\rm syn}/\tau' \propto E_\nu^{-2}$ relationship results in a steeping of the original spectrum above this break energy by a factor of 2.

Accounting for only the muon cooling break energy, the final neutrino spectrum will be a double broken power law of the form

$$F_\nu(E_\nu) = f_\nu \times \begin{cases} \left(\varepsilon_\nu^b\right)^{\alpha_\nu-\beta_\nu} E_\nu^{-\alpha_\nu}, & E_\nu \le \varepsilon_\nu^b \\ E_\nu^{-\beta_\nu}, & \varepsilon_\nu^b < E_\nu \le \varepsilon_\nu^s \\ \left(\varepsilon_\nu^s\right)^{\gamma_\nu-\beta_\nu} E_\nu^{-\gamma_\nu}, & \varepsilon_\nu^s < E_\nu, \end{cases} \tag{2.25}$$

where the neutrino spectral indices are related to the gamma-ray spectral indices by

$$\alpha_\nu = 3 - \beta_\gamma,\ \beta_\nu = 3 - \alpha_\gamma,\ \gamma_\nu = \beta_\nu + 2. \tag{2.26}$$

The scaling of the neutrino spectrum f_ν is determined assuming that the total energy in neutrinos is proportional to the total energy in gamma-rays, that is

$$\int_0^\infty dE_\nu E_\nu F_\nu\left(E_\nu\right) = \frac{1}{8}\frac{1}{f_e} f_\pi \int_{1\,\mathrm{keV}}^{10\,\mathrm{MeV}} dE_\gamma E_\gamma F_\gamma\left(E_\gamma\right), \tag{2.27}$$

where the factor of 1/8 accounts for the roughly equal energy of the proton deposited in neutral and charged pions, and that the charged pion distributes its energy to each of the four lepton decay products equally; f_e is the fraction of energy in the fireball carried by electrons compared to that in protons, that is $f_e = 1/f_p$. The total fraction of the proton energy deposited in pions is denoted by f_π . The gamma-ray spectrum integral is truncted as some spectral fits may give divergent integrals with infinite bounds.

The fraction of energy deposited in pions is

$$f_\pi = 1 - \left(1 - \langle x_{p\to\pi}\rangle\right)^{\tau_{p\gamma}}, \tag{2.28}$$

where the optical depth $\tau_{p\gamma}$ can be estimated by the approximate size of the shock region $\Delta R'$ and proton-photon mean free path $\lambda_{p\gamma}$ by $\tau_{p\gamma} = \Delta R'/\lambda_{p\gamma}$. The mean free path can be rewritten using the number density of photons n_γ in the shock region, and the Δ^+ interaction cross section σ_Δ as $\lambda_{p\gamma} = 1/n_\gamma \sigma_\Delta$. Further, the number density of photons can be estimated using geometric considerations by

$$n_\gamma \simeq \frac{U'_\gamma}{\varepsilon'_\gamma} = \left(\frac{L_\gamma^{\rm iso} t_v/\Gamma}{4\pi R^2 \Delta R'}\right) \Big/ \left(\frac{\varepsilon_\gamma}{\Gamma}\right) \tag{2.29}$$

where all photons are estimated to be at the break energy ε_γ. Using the relation of (2.21), this becomes

$$n_\gamma \simeq \frac{L_\gamma^{\rm iso}}{16\pi c^2 t_v \Gamma^4 \Delta R' \varepsilon_\gamma}, \tag{2.30}$$

allowing the optical depth to be written as

$$\tau_{p\gamma} = \Delta R' n_\gamma \sigma_\Delta \simeq \left(\frac{L_\gamma^{\rm iso}}{10^{52}\,{\rm erg\,s^{-1}}}\right) \left(\frac{t_v}{10^{-2}\,{\rm s}}\right)^{-1} \left(\frac{\Gamma}{10^{2.5}}\right)^{-4} \left(\frac{\varepsilon_\gamma}{1\,{\rm MeV}}\right). \tag{2.31}$$

Though one can measure ε_γ and $L_\gamma^{\rm iso}$ on a per-GRB basis, the rest of the model is largely unconstrained. For bursts with no measured redshift, $L_\gamma^{\rm iso}$ is determined based on average z values. For simplicity, it is assumed there is an equipartition of energy in electrons and the magnetic fields, with $\epsilon_e = \epsilon_B = 0.1$. The GRB variability time scale is estimated based on the smallest variability seen in observed GRBs, taken to be $t_v = 10^{-3}\,{\rm s}$ for short GRBs and $t_v = 10^{-2}\,{\rm s}$ for long GRBs. The fireball bulk Lorentz factor Γ and the baryonic loading fraction f_p remain free, though they are estimated in the range $100 \lesssim \Gamma \lesssim 1000$ and $f_p \sim 10$, which are roughly consistent with GRBs being UHECR progenitors.

The model derived here was presented by Guetta et al. in [66], and was strongly constrained in an analysis of two years of IceCube data with a partially completed detector [25]. This was not altogether surprising as several omissions were noted

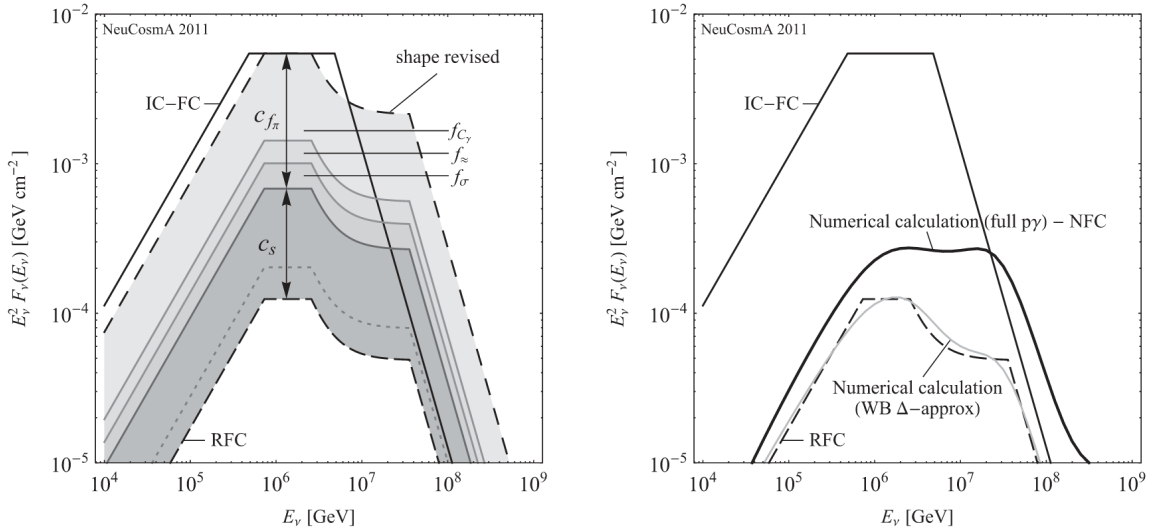

Figure 2.5: Revisions made to the analytical model of Guetta et al. in [66], referred to in these plots as IC-FC. The left plot shows the step-by-step revisions in terms of shape and scale of the analytical model, resulting in the revised analytical model RFC. The right plot compares these model to numerical simulation. Figure from [67].

by Hümmer et al. in the original Guetta et al. model [67]. The total effect of these changes are summarized in Figure 2.5. First, Hümmer et al. note several changes that should be made to the shape of the neutrino spectrum, namely the photohadronic interaction threshold of (2.18) is increased by a factor of 2 accounting for average interactions not occuring *head-on*, and that both muon and pion cooling breaks can be included. Further, several corrections can be made to the estimated value of f_π presented: (1) the entire photon spectrum is used rather than just considering all photons to be at the break energy in (2.29) (f_{C_γ} in Figure 2.5), (2) a rounding error is corrected in the expansion of (2.28) with (2.31) ($f_\approx$ in Figure 2.5), and (3) the accounting for the width of the Δ^+ resonance in (2.31) (f_σ in Figure 2.5). Lastly the energy dependence of the proton's mean free path and energy losses of secondaries in the fireball can be included (c_s in Figure 2.5). These corrections result in over an order of magnitude lower predicted neutrino fluence compared to the original Guetta et al. model.

Neutrino spectra based on GRB gamma-ray measurements are now calculated numerically by generating Monte Carlo particle interactions according to the standard model with SOPHIA [68]. An ensemble of protons is propagated in a gamma-ray field derived from that measured at Earth, and $p-\gamma$ interactions are generated, even those beyond the simple Δ^+ resonance approximation of the Guetta et al. model. The magnetic fields in the fireball are accounted for in this simulation to account for synchrotron losses of all intermediate mesons before they decaying. Results of these numerical spectrum calculations are comparable to those presented by Hümmer et al. shown in Figure 2.5.

Beyond the standard internal shock fireball model, two alternative models are also considered: (1) a model that pushes the neutrino and gamma-ray production to a dissipative photosphere, where the fireball transitions from optically thick to thin in $\gamma-\gamma$ interactions, and (2) a Poynting-dominated model, which generates gamma-ray radiation through dissipation of energy in the fireball's magnetic fields at a much larger radius than that in the internal shock model. The primary difference in these models compared to the internal shock model is the radius of neutrino and gamma-ray production, which affects the gamma-ray number density from (2.29) and therefore the $p-\gamma$ optical depth of the fireball.

In the dissipative photosphere (photospheric) model [69, 70], the prompt gamma-ray emission is proposed to occur at Thompson photosphere with radius

$$R_{\rm ph} \simeq \frac{3.7\times10^{11}\,{\rm m}}{\epsilon_e}\left(\frac{L_\gamma^{\rm iso}}{10^{52}\,{\rm erg\,s^{-1}}}\right)\left(\frac{\Gamma}{10^{2.5}}\right)^{-3}. \tag{2.32}$$

Under standard assumptions for values of the GRB variability time scale and a bulk Lorentz factor $\Gamma\sim10^{2.5}$, the internal shock model places the plasma shell collision radius at $R_{\rm IS}\sim10^{13}-10^{14}\,{\rm m}$. The optical depth is roughly increased by a factor of $R_{\rm IS}/R_{\rm ph}$, while the second neutrino break energy ε_ν^s is decreased by the same

factor. The overall affect is increased neutrino production, primarily at lower energies compared to the internal shock model.

The magnetic dissipation model considered is the Internal Collision MAgnetic Reconnection and Turbulence (ICMART) model [70, 71], which postulates ordered magnetic fields in the fireball are disrupted through internal shock collisions, inducing magnetic reconnection events that result in gamma-ray emission at a radius of $R_{\rm ICMART} \sim 10^{15}\,{\rm m}$. By the same argument presented in the photospheric case, the $p-\gamma$ optical depth is roughly decreased by a factor of $R_{\rm IS}/R_{\rm ICMART}$, while the second neutrino break energy increase by the same factor. The net effect is an overall reduction in the total neutrino production, but with production at higher neutrino energies, compared to the internal shock model.

The predicted neutrino spectra from the photospheric and ICMART models can be numerically calculated with the same particle interaction Monte Carlo as the internal shock model, with slightly different simulated radii. The predicted neutrino spectra for the GRBs analyzed in this dissertation with a variety of Γ-factors and $f_p = 10$ for the internal shock fireball model, photospheric, and ICMART models are shown in Figure 2.6.

2.3.3 Neutrino Production Scaled to UHECR Spectrum

Though the models of Section 2.3.2 contain assumptions relating the bulk Lorentz factor Γ and baryonic loading f_p to possible UHECR generation, there is no explicit relation of these models to the UHECR flux measured at Earth. One can, however, make that explicit connection and calculate the resulting neutrino flux observed at Earth assuming GRBs are the progenitors of the entire UHECR flux.

Assuming protons freely escape the GRB fireball to result in the UHECR flux $> 10^{19}\,{\rm eV}$, Waxman and Bahcall [72] calculated the resulting neutrino flux. Their derivation of the expected neutrino spectrum roughly follows the derivation presented

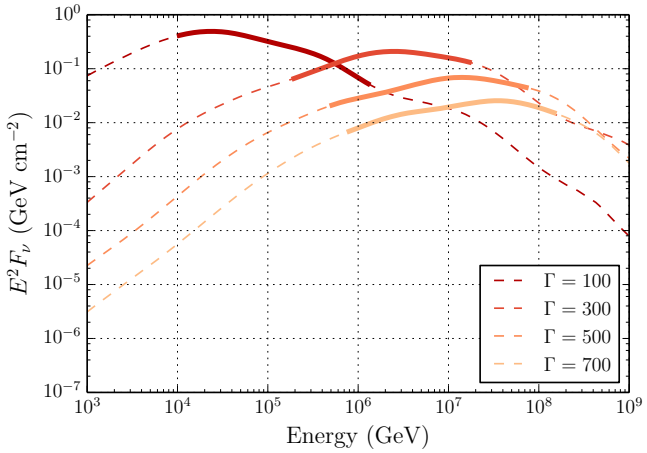

(a) Internal shock fireball model.

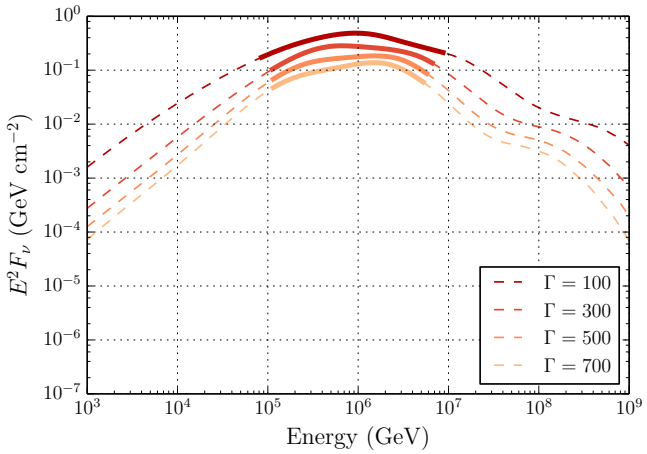

(b) Photospheric fireball model.

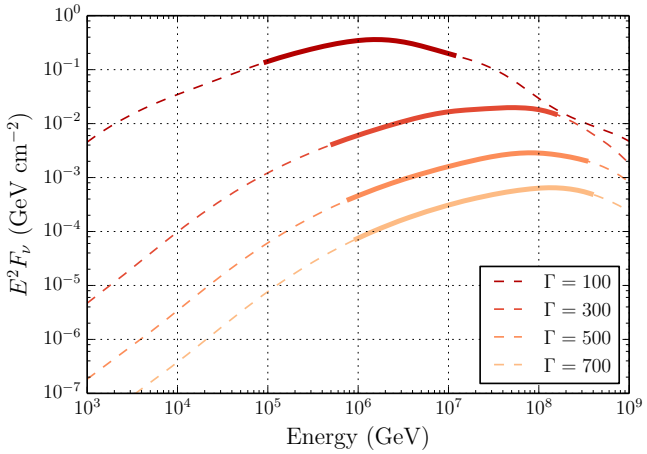

(c) ICMART model.

Figure 2.6: Predicted total neutrino fluence from the 664 GRBs investigated in this dissertation for a number of Γ factors and $f_p = 10$. Solid lines indicate the energy interval over which 90% of neutrino events are detected in the final analysis.

in Guetta et al. as they take neutrino production to occur only through the Δ^+ resonance. Gamma-ray spectral fits are taken to be broken power laws with average fit values from the BATSE catalog: spectral indices of $\alpha_\gamma = 1$ and $\beta_\gamma = 2$, and a break energy of $\varepsilon_\gamma = 1\,\mathrm{MeV}$. The neutrino spectrum then takes the form

$$\Phi_\nu(E_\nu) = \Phi_0 \times \begin{cases} E_\nu^{-1}\varepsilon_b^{-1}, & E_\nu \leq \varepsilon_b \\ E_\nu^{-2}, & \varepsilon_b < E_\nu \leq 10\varepsilon_b \\ E_\nu^{-4}\left(10\varepsilon_b\right)^2, & 10\varepsilon_b < E_\nu \end{cases} \tag{2.33}$$

where the break energy is $\varepsilon_b \sim 10^6\,\mathrm{GeV}$. The break energy is obtained assuming a variability time scale of $t_v = 10^{-3}\,\mathrm{s}$, a bulk Lorentz factor of $\Gamma = 300$, and a gamma-ray isotropic luminousity of $L_\gamma^{\mathrm{iso}} = 10^{51}\,\mathrm{erg\,s^{-1}}$. The cosmological neutrino energy production rate is then directly related to the cosmological UHECR production rate above the proton break energy of $\varepsilon_p \sim 10^{16}\,\mathrm{eV}$, calculated from the measured UHECR flux and assuming a proton injection spectrum of $dN_p/dE_p \propto E_p^{-2}$. Taking a pion production efficiency of approximately

$$f_\pi \simeq 0.2\left(\frac{L_\gamma^{\mathrm{iso}}}{10^{52}\,\mathrm{erg\,s^{-1}}}\right)\left(\frac{t_v}{10^{-2}\,\mathrm{s}}\right)^{-1}, \tag{2.34}$$

and using an updated measurement of the UHECR flux [73], the per-flavor flux normalization required is $\varepsilon_b^2\Phi_0 \simeq 2.2\times10^{-9}\,\mathrm{GeV\,cm^{-2}\,s^{-1}\,sr^{-1}}$.

Alternatively, Ahlers, et. al. [74] postulated protons are completely confined to the fireball and UHECRs are derived from the neutrons produced in the photo-pion interactions of (2.11) escaping the fireball, which later decay to protons. This model guarantees three neutrinos per UHECR, meaning the resulting neutrino flux is much more optimistic than that expected by the proton direct escape model. From the measured UHECR flux $> 10^{19}\,\mathrm{eV}$, the expected neutrino flux normalization under similar assumptions as Waxman and Bahcall is $\varepsilon_b^2\Phi_0 \simeq 6\times10^{-8}\,\mathrm{GeV\,cm^{-2}\,s^{-1}\,sr^{-1}}$. As

Ahlers et al. noted, this was strongly excluded by an analysis of events in coincidence with GRBs using the partially completed, 40-string detector [24, 74].

2.3.4 Neutrino Production Model Tests

Searches for prompt neutrino production from GRBs typically calculate a test statistic related to the number of observed neutrino candidate events consistent with the analyzed GRBs spatially and temporally. Should this test statistic be consistent with the background-only expectation of the experiment in the frequentist formulation, one can produce limits to a given neutrino production model at a desired confidence level. Conversely, should a statistically significant signal be observed, one can produce confidence intervals for neutrino model spectral normalizations. This methodology as applied to the maximized unbinned likelihood employed in this dissertation is discussed in Chapter 6.

The models of Section 2.3.2 and Section 2.3.3 are tested in this dissertation with several simplifying assumptions. For the numerical models of Section 2.3.2, models are tested on a per bulk Lorentz factor Γ and baryonic loading factor f_p basis, that is every GRB in the analyzed sample is assumed to be modeled by the same average values of Γ and f_p with no GRB-to-GRB variability. Per-GRB predicted neutrino fluences are then calculated with these burst parameters, and measured GRB characteristics.

Should GRBs produce neutrinos during their prompt gamma-ray emission phase, these neutrinos could be visible as a *quasi*-diffuse flux as GRBs occur isotropically over the entire sky at a constant rate. When measured and averaged over long exposures, this quasi-diffuse flux would simulate a true diffuse neutrino flux. An effective per-flavor quasi-diffuse neutrino flux can be determined from model fluences assuming the observed GRBs are representative of the yearly ensemble of GRBs that occur, but are not necessarily observed at Earth due to the limited sensitivity of current gamma-ray detectors. The canonical value for the number of GRBs

which occur over the entire sky per-year which are detectable by current observatories is $\dot{N}_{\rm GRB} = 667\,{\rm yr}^{-1}$. If the per-flavor neutrino fluence for GRB g is $F_{g;\Gamma,f_p}(E_\nu)$ for given values of Γ and f_p, the per-flavor quasi-diffuse flux is calculated to be $\Phi_{\Gamma,f_p}(E_\nu) = \left[\sum_g F_{g;\Gamma,f_p}(E_\nu)\right] \times \left(\dot{N}_{\rm GRB}/N_{\rm obs}\right) \times (4\pi\,{\rm sr})^{-1}$, where $N_{\rm obs}$ is the number of actual GRBs observed. Similarly, the UHECR scaled models of Section 2.3.3 are tested assuming eached GRB analyzed contributes an equal average neutrino fluence to the per-flavor quasi-diffuse flux spectrum of (2.33), where the quasi-diffuse flux is determined identically to the numerical models.

Chapter 3

IceCube Neutrino Observatory

The small interaction cross-section that allows neutrinos to propagate through the universe unimpeded, making them ideal astrophysical messenger particles, also prevents them from being easily studied. Detectors consisting of large bodies of dense materials are required. Detection of neutrinos emitted by SN1987A [75–77] and solar neutrinos [78] in large man-made neutrino interaction targets established that neutrino astrophysics was possible. The detection of neutrinos at higher energies produced in hadronic interactions at cosmic ray sources, however, requires a much larger detection volume, predicted to be on the order of a cubic kilometer using water or ice as a detector medium [79].

The IceCube Neutrino Observatory (typically called IceCube) is the first neutrino detector that reaches the cubic kilometer fiducial volume benchmark. The detector consists of over 5000 photomultiplier tubes (PMTs) that instrument a gigaton of ice in a hexagonal array beneath the South Pole. A schematic of the detector is shown in Figure 3.1. Neutrinos interacting in the ice or nearby bed-rock induce a shower of secondary charged particles, which emit Cherenkov radiation that is subsequently detected by the PMT array. The array is placed $\gtrsim 1.4\,\mathrm{km}$ below the surface, where the ice is clearest and so the ice above the array can partially attenuate the atmospheric muon background. IceCube fulfilled its goal of discovering astrophysical neutrinos consistent with those produced in hadronic interactions at cosmic ray accelerators in 2014 [22], with later confirmation in 2015 with an independent analysis channel [23], though the astrophysical sources remain unknown.

The following chapter describes the IceCube experiment. The neutrino detection principle employed by the experiment is discussed, then the data acquisition and

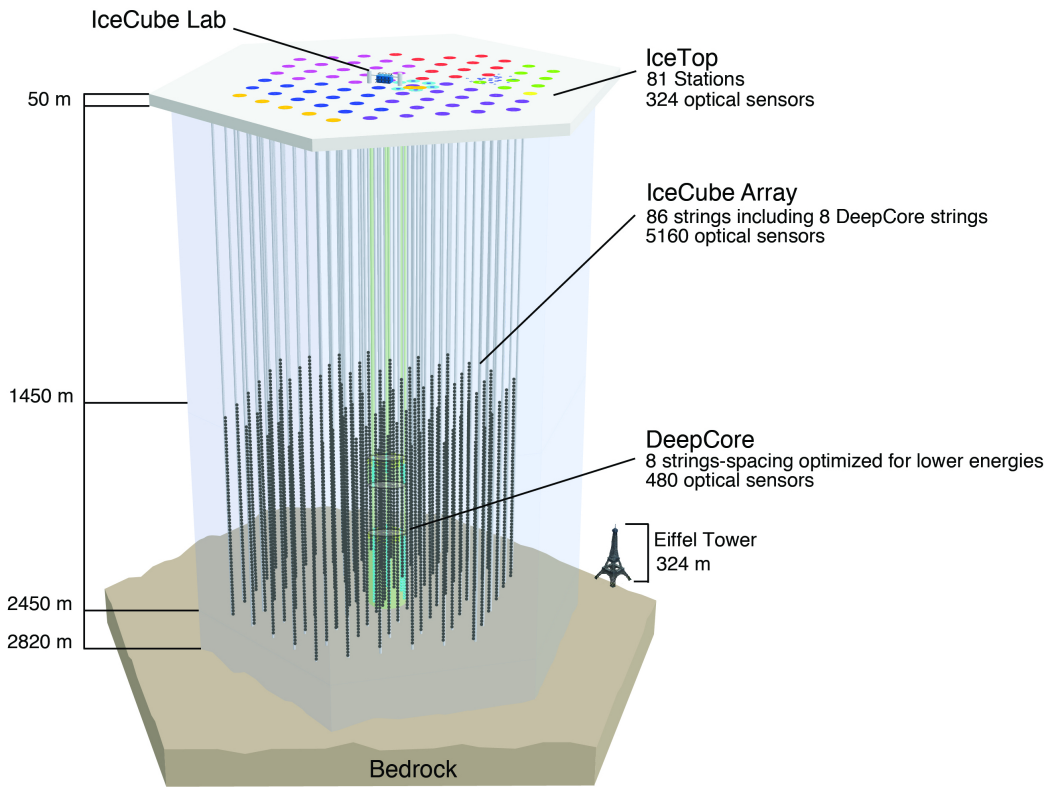

Figure 3.1: The IceCube detector.

processing techniques to transform the Cherenkov radiation signal into a digitized neutrino event sample are detailed.

3.1 Neutrino Detection

Neutrinos of all flavors can interact with other fermions through the weak force. In a dense material such as water or ice, this interaction is typically a deep inelastic weak scattering with a quark within the water molecule's oxygen and hydrogen nuclei. In the exchange of a $W^{\pm}$ boson, called a charged-current (CC) interaction, the neutrino is converted to the charged lepton of the same flavor while the quark is typically converted to the complementary quark modeled in the Cabibbo-Kobayashi-Maskawa quark-mixing matrix. The neutrino can also exchange a Z^0 boson with a quark, called the neutral-current (NC) interaction, leaving all particles unchanged

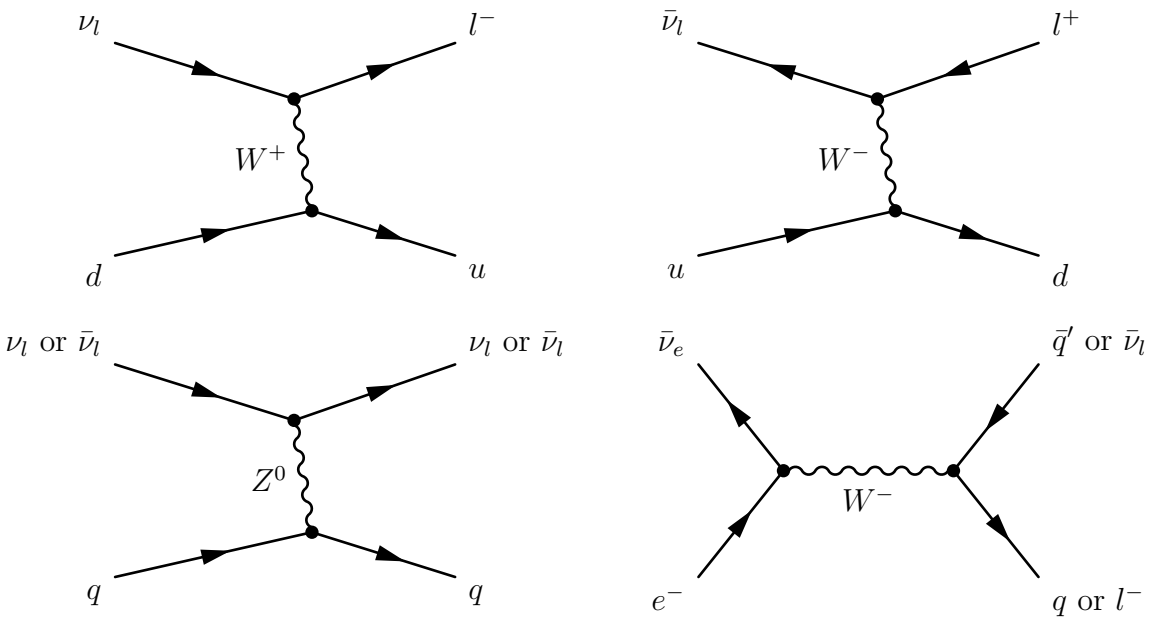

Figure 3.2: Feynman diagrams of neutrino detection channels in IceCube. The top row shows CC interactions of neutrinos and anti-neutrinos, and the bottom left diagram shows the NC interaction. The resonant scattering of electron neutrinos with electrons in a material, called the Glashow resonance, is shown at the bottom right.

though exchanging energy. Electron anti-neutrinos at an energy of $E_\nu = 6.3\,\text{PeV}$ additionally can interact with electrons in a material to produce an *on-shell* W^- boson, which then decays to leptons or quarks, known as Glashow resonance scattering [80].

The Feynman diagrams of these interaction modes are shown in Figure 3.2, while the cross-sections of these interactions as a function of neutrino energy are shown in Figure 3.3. The overall cross sections of these processes are $7-10$ orders of magnitude lower than pp cross sections at similar center-of-mass energies. For neutrino energies $E_\nu \lesssim 10^4 - 10^5\,\text{GeV}$, the deep inelastic scattering cross section is proportional to the neutrino energy. Above these energies, the mass of the weak boson propagator suppresses the neutrino-nucleon cross section [81, 82]. The neutrino-electron scattering process is typically subdominant to the neutrino deep inelastic scattering, due to the electron being much less massive than a nucleon constituent quark. At the W^- boson production resonance, however, the cross section is a factor of $\sim$300 higher than the deep inelastic scattering cross section.

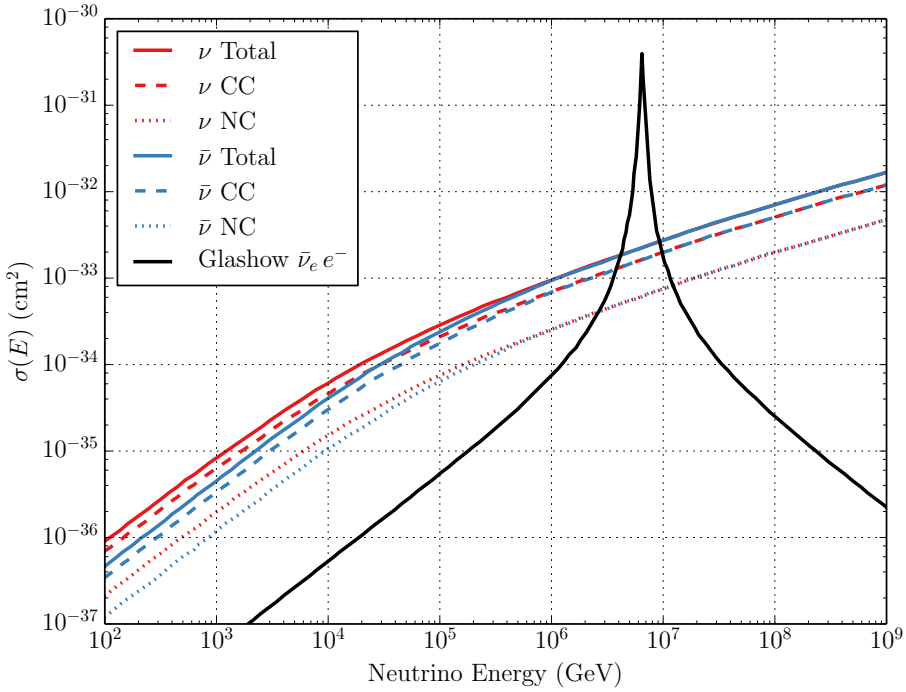

Figure 3.3: Neutrino and anti-neutrino interaction cross sections in deep inelastic scattering. Figure adapted from [81] and [82].

Though the neutrinos themselves are not observable electromagnetically, the charged particle products of their weak interactions are. As these charged particles are relativistic, they will be moving faster than the speed of light in the material, generating light via the Cherenkov mechanism [83]. Cherenkov radiation is induced through the disturbance of a material's electromagnetic field by a moving charged particle with velocity v, which when greater than the speed of light of a certain wavelength λ in the material $v_d(\lambda) = c/n(\lambda)$, the disturbance adds coherently to form a electromagnetic shock wave. The coherent radiation is emitted at a characteristic angle (called the Cherenkov angle) of

$$\cos\theta_C(\lambda) = \frac{v_d(\lambda)}{v} = \frac{1}{\beta n(\lambda)}, \tag{3.1}$$

where $\beta = v/c$. The photon yield as a function of wavelength is given by the Frank-Tamm relation [84]

$$\frac{d^2N}{dxd\lambda} = \frac{2\pi\alpha}{\lambda^2}\left[1 - \frac{1}{\beta^2 n^2(\lambda)}\right] \tag{3.2}$$

where α is the fine structure constant. By this relation, the photon yield is greatest at short wavelengths, limited to where $n(\lambda) > 1$; in ice, Cherenkov radiation is most intense in blue-UV wavelengths at a Cherenkov angle of $\theta_C \simeq 41°$.

The macroscopic event signatures of neutrino interactions are dependent on the interaction products. All deep-inelastic scattering interactions with high energy neutrinos impart enough energy on the nucleon to induce a nuclear recoil, resulting in a hadronic shower of baryons and mesons that propagates $\sim$10 m in ice and radiates light spherically. In NC interactions, the entirety of the visible event is the hadronic shower. The ν_e CC interactions yield an electron or positron, which bremsstrahlung and e^+e^- pair produce. The result is an electromagnetic cascade at the same location as the hadronic shower, similarly propagating $\sim$10 m in ice and radiating spherically. Muons produced in ν_μ CC interactions slowly lose energy as they propagate, allowing them to travel over kilometers in the ice—appearing as long, straight tracks of light—before decaying. Taus produced in ν_τ CC interactions typically decay within the hadronic cascade of the initial interaction, typically to either a hadronic or electromagnetic cascade. At high enough energies, the decay vertex can be distinguished from the interaction vertex, resulting in two distinct spherical cascades possibly connected by a dim track, called a *double-bang* event. Glashow resonance scattering can yield any of these event signatures, depending on the W^- decay products. The propagation ranges of interaction products in ice as a function of product energy are shown in Figure 3.4.

The large range of muons in ice allows ν_μ CC interactions to be detected far outside the instrumented volume of IceCube, greatly increasing the effective volume of the detector. Further, the muons appear as well-localized tracks, yielding recon-

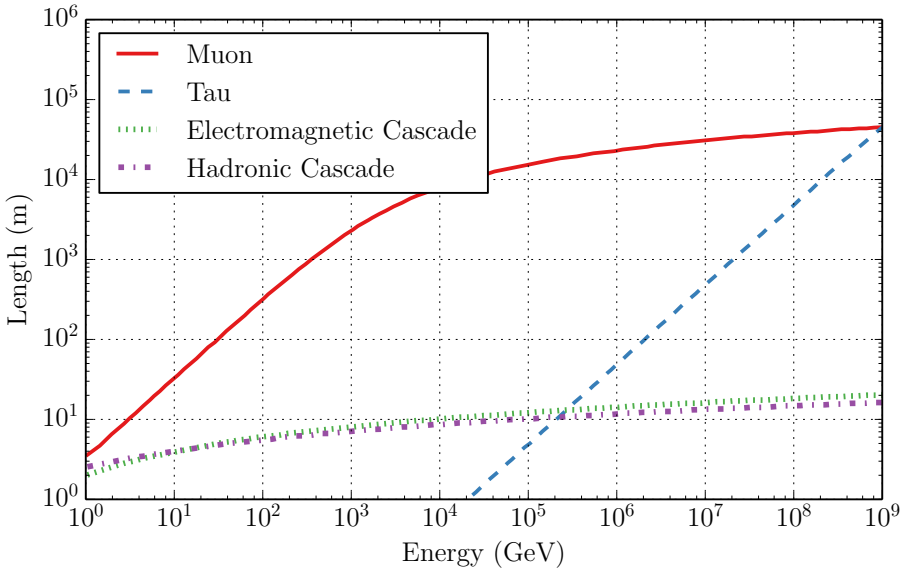

Figure 3.4: Propagation length of neutrino interaction products in ice as a function of product energy. Figure adapted from [85].

structed muon direction resolutions of $\lesssim 1°$, making it an ideal signal for searches of hadronic acceleration in sources such as GRBs. At neutrino energies $\gtrsim 1\,\text{PeV}$, the Earth becomes opaque to neutrinos, attenuating the highest energy neutrinos detectable in searches for tracks from the Northern Hemisphere sky. Sensitivity to this signal, however, is enhanced near the horizon in these searches as the Antarctic ice sheet increases the neutrino interaction volume and the muons can still reach the detector. Searches for tracks from the Southern Hemisphere sky have no such signal attenuation, although IceCube's primary background of atmospheric muons is greatest in this region. This dissertation presents a search for high energy muon neutrino tracks from the Southern Hemisphere sky as a signal from neutrino production in GRBs.

3.1.1 Muon Propagation

Due to the neutrino being highly relativistic in the energy range in which IceCube is sensitive, muons produced in ν_μ CC interactions obtain more than half

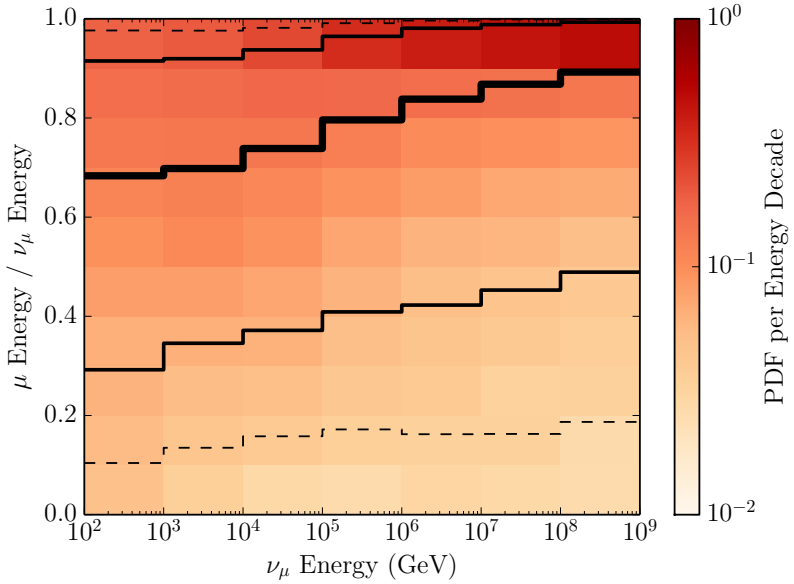

Figure 3.5: Distribution of simulated μ energies from ν_μ CC interactions as a function of ν_μ energy, displayed in terms of the ratio of μ to ν_μ energy and with PDF normalized in decades of ν_μ energy. The median ratio is shown in the thick black line, while the 68% and 90% containment intervals are shown in the thin black and dashed black lines, respectively.

the primary neutrino's energy on average. The average fraction increases with the primary neutrino energy, as demonstrated in Figure 3.5. The muon will also be highly boosted along the neutrino's original direction, with an energy dependent average opening angle of $\Delta\Psi \simeq 0.7^\circ (E_\nu/1\,\mathrm{TeV})^{-0.7}$ [86]. Thus, the reconstructed muon direction is a good proxy of the original neutrino direction.

As the muon propagates in the ice, it loses energy continuously through ionization of water molecules and Cherenkov radiation. At muon energies $\gtrsim 300\,\mathrm{GeV}$, the muon loses energy primarily through stochastic processes, namely pair production, bremsstrahlung, and photonuclear interactions. These stochastic processes appear as electromagnetic or hadronic showers along the muon track. The relative contribution of the stochastic processes and ionization to the average energy loss of the muon per length of track as a function of muon energy is shown in Figure 3.6

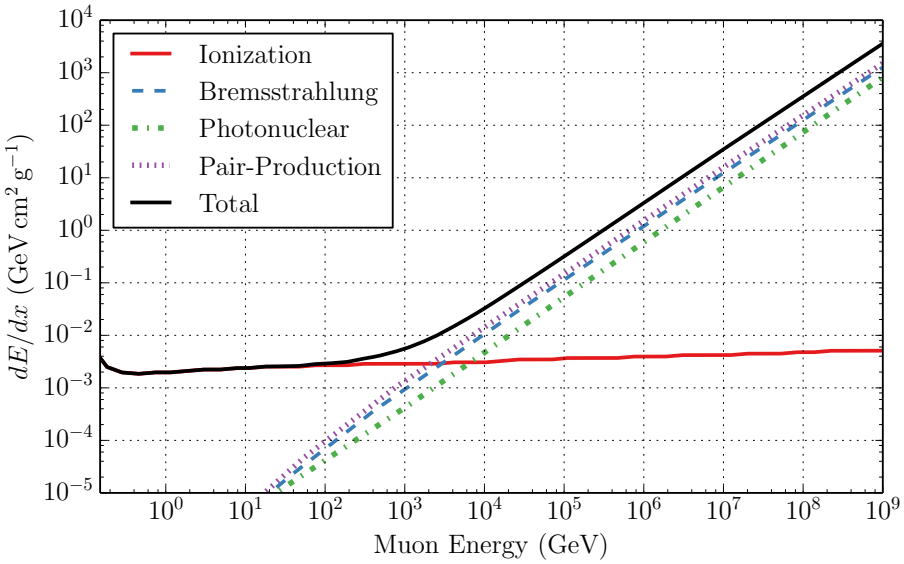

Figure 3.6: Average contributions to the total muon energy loss in a dense material as a function of muon energy. Figure adapted from [87].

Only a fraction of the muon's total energy is deposited within the IceCube detector volume as high energy muons travel for kilometers before decaying. The muon's energy can be estimated from the average energy deposition along its track however. In ice, the muon energy loss can be parameterized by

$$\frac{dE}{dx} = -a - bE \tag{3.3}$$

where a is the average energy loss due to ionization, b is derived from the average energy loss due to stochastic processes. In principle, these parameters are energy dependent, though in the IceCube energy sensitivity range they can be approximated as constants. The Bethe-Bloch formula [88] can be used to find $a \simeq 0.26\,\text{GeV}$ per meter-of-water-equivalent (mwe), while the average stochastic loss parameter can be estimated as $b \simeq 3.6 \times 10^{-4}\,\text{mwe}^{-1}$ when E is in units of GeV.

3.1.2 South Pole Ice Properties

The glacial ice beneath the South Pole is the clearest ice on Earth, allowing the detection of photons hundreds of meters from its source. Though remote, this makes it an ideal medium for a kilometer-scale neutrino detector. The ice is formed through the gradual compression of snow deposited at the South Pole over thousands of years. Bubbles in the ice at depths $\lesssim 1400\,\mathrm{m}$ reduce the ice's clarity to scattering lengths $\lesssim 5\,\mathrm{m}$. Below these depths, the immense pressure compresses and removes the bubbles in the ice, motivating placement of IceCube at depths $\gtrsim 1400\,\mathrm{m}$.

As it is a naturally deposited medium that has formed over thousands of years, detailed measurements of the optical properties of the ice are critical for interpreting and simulating the Cherenkov radiation signal from neutrino interactions. *In-situ* measurements of the scattering length and absorptivity of the ice as a function of light wavelength and depth are made possible through the use of flashing LEDs [89, 90] and a dust-logger that measures the light-scattering properties of the ice surrounding the boreholes during the hot-water drilling [91, 92]. The basic profiles of these measures are shown in Figure 3.7 from flashing LED-based measurements. Within the instrumented region of the detector, light scattering lengths are typically in the range $25 - 70\,\mathrm{m}$.

Dust concentration in the South Pole ice is strongly correlated with its optical properties at depths $\gtrsim 1400\,\mathrm{m}$. Climate variability and volcanic activity are the primary sources of dust deposition in the form of layers in the ice, producing optical properties that vary as a function of depth. The most prominent feature occurs at depths between $2000 - 2100\,\mathrm{m}$—associated with an interglacial period during the Pleistocene era 65,000 years ago—which reduces the light scattering length to $\lesssim 10\,\mathrm{m}$. Dust-logger measurements also indicate the dust layers are tilted, meaning the optical properties also vary as a function of position $(x,\, y)$, which is now accounted for in LED

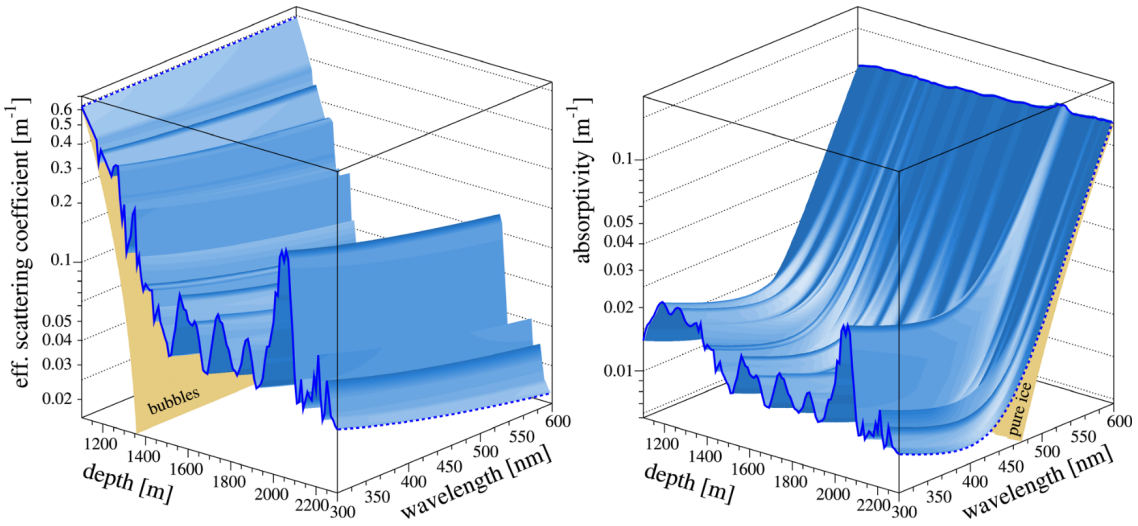

Figure 3.7: Effective scattering coefficient (left) and absorptivity (right) of ice beneath the South Pole as a function of depth and light wavelength. Figure from [89].

flasher measurements. Further, recent measurements have discovered an anisotropy in light scattering as a function of azimuth [93], though its exact origin is unknown.

3.1.3 Background Characteristics

The primary background of IceCube is muons produced in cosmic ray air showers occuring in the atmosphere above the IceCube detector. Atmospheric muons are observed at a rate of $\gtrsim 2\,\text{kHz}$, and are the large majority of recorded events in the IceCube data. Air shower events can be tagged should the air shower pass through the surface array above the IceCube detector, though this is only possible for nearly vertical muons where the geometry of the surface array and in-ice detector overlap.

Single muons from air showers are indistinguishable from muons produced in ν_μ CC interactions outside of the detector volume if coming from the Southern Hemisphere. In high energy air showers, however, many muons are generated that travel together through the detector, called a *muon bundle*. The average energy loss in these bundles typically appear much smoother than a single muon with the same equivalent energy; the single muon loses its energy in large stochastics while the bundle features

many smaller stochastics that smear the appearent energy losses as a function of track length. This difference allows high energy muons produced in ν_μ CC interactions to be distinguishable from high energy muon bundles from air showers in this analysis.

Atmospheric neutrinos produced in cosmic ray air shower meson decays are an additional background of this dissertation. The Earth shields atmospheric muons from the Northern Hemisphere, leaving only atmospheric neutrinos as a background in this portion of the sky. A single muon produced in atmospheric ν_μ CC interactions are indistinguishable from neutrinos produced in GRBs, though two characteristics can be used to statistically separate them: atmospheric ν_μ are produced at lower energies than the expected GRB ν_μ signal, and the atmospheric neutrinos at higher energies from the Southern Hemisphere sky are typically accompanied by a muon bundle.

As this dissertation considers a neutrino signal in GRBs produced coincidently with the prompt gamma-ray emission, a completely unbiased characterization of this atmospheric background can be obtained from IceCube events gathered outside of reported GRB times. Here, data taken more than 2 hours away from any GRBs prompt gamma-ray emission over the entire operation of the detector is used.

3.2 The IceCube Detector

The IceCube detector consists of 5160 Digital Optical Modules (DOMs) placed on 86 vertical *strings* (60 DOMs per string) in the ice $1450\,\mathrm{m} - 2450\,\mathrm{m}$ below the South Pole surface. The strings are configured in a hexagonal array (inter-string distance of 125 m), with a more densely spaced in-fill array of eight strings at the center of the detector (known as *DeepCore*, inter-string distances of $42\,\mathrm{m} - 72\,\mathrm{m}$) for sensitivity to neutrinos with energy $E_\nu \gtrsim 10\,\mathrm{GeV}$ [94]. DOMs are placed on typical IceCube strings with 17 m vertical spacing. DeepCore strings have a denser 7 m vertical spacing configured in two sections: 10 DOMs above and 50 DOMs below

the dust layer between $2000 - 2100\,\mathrm{m}$. Each DOM houses a photomultiplier tube (PMT), digitizing readout electronics, and calibration LEDs within a glass pressure sphere. PMT waveforms are digitized at the DOM, and sent to computers at the surface for processing and filtering. A twisted copper wire pair connects to pairs of DOMs carrying DOM power and communications, with all twisted pairs of a string forming a wire bundle that runs to the IceCube Laboratory (ICL) at the center of the array.

Nearly all IceCube strings, excluding the DeepCore strings, are paired with two surface tanks filled with water, each of which contain two DOMs, making up the *IceTop* surface array [95]. In total, IceTop consists of 81 tank pairs and serves as both a surface veto for atmospheric muons observed in the IceCube detector volume as well as a cosmic ray and gamma-ray air shower detector.

The detector was constructed over seven consecutive austral summers between November 2004 and December 2010. A hot-water drill created 2450 m-deep boreholes in the ice, filled with water. Each hole was then instrumented with a DOM string and allowed to refreeze, permanently placing the DOMs in the ice. After each of these deployment seasons, the detector was fully operational with the following number of strings: 9 (2006-2007, called IC9), 22 (2007-2008, called IC22), 40 (2008-2009, called IC40), 59 (2009-2010, called IC59), and 79 (2010-2011, called IC79). Since May 2011, IceCube has taken data in the full 86-string configuration (years of data called IC86-X, where X is the start year of data set). The top-down geometry of these partially completed detector configurations is summarized in Figure 3.8.

3.2.1 Optical Modules

The basic unit of the IceCube detector, both in construction and data, is the IceCube DOM, an illustration of which is shown in Figure 3.9. Each DOM contains a 25 cm diameter Hamamatsu R7081-02 PMT [96] facing downwards into the ice

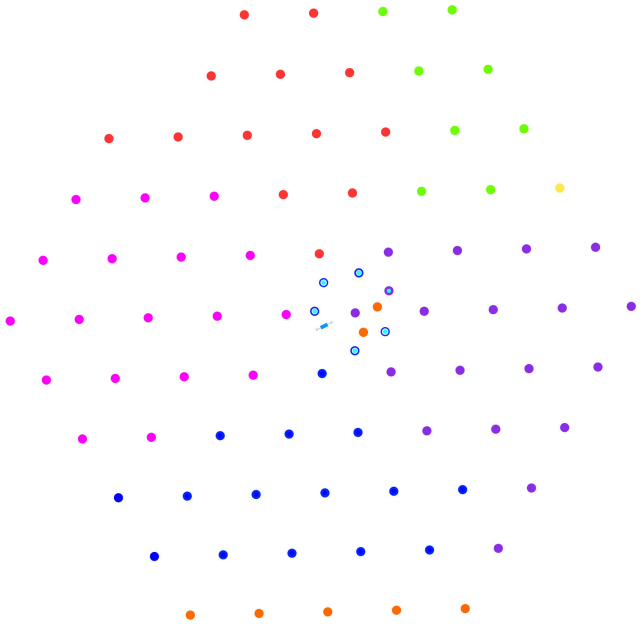

Figure 3.8: Top-down view of the IceCube array. Color indicates the deployment season: yellow – 2004-2005, green – 2005-2006, red – 2006-2007, magenta – 2007-2008, purple – 2008-2009, blue – 2009-2010, and orange – 2010-2011. DeepCore strings are indicated in light-blue.

within a 35.6 cm diameter glass pressure sphere capable of withstanding pressures up to 70 MPa, sufficient for the pressures DOMs experience during and after the string freeze-in. The PMTs are coupled mechanically and optically to the glass with a room temperature vulcanized (RTV) silicone gel. DeepCore DOMs feature a high quantum efficiency (HQE) Hamamatsu R7081MOD PMT that was made available to IceCube during the planning for DeepCore.

The IceCube PMT detects an incident photon when a photoelectron (PE) is ejected by the photon from the PMT's photocathode. A strong electromagnetic field accelerates the PE towards the first dynode, which ejects additional electrons that are accelerated towards the next dynode. Over a series of 10 linear focused dynode stages held at ∼1300 V from cathode to final dynode, an effective gain of 10^7 is achieved, which translates to a ∼8 mV pulse per photon with a width of ∼5 ns. Each PMT is surrounded by a mu-metal grid to reduce curvature of the PE path to the first dynode by the Earth's magnetic field. The Hamamatsu PMTs are sensitive to light in the

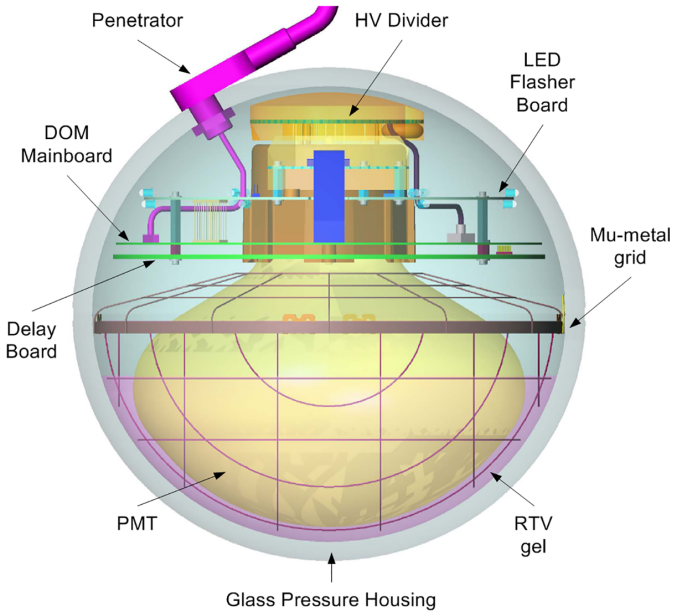

Figure 3.9: Illustration of an IceCube DOM. Figure from [97].

300 − 600 nm photon wavelength range; the maximal quantum efficiency—the fraction of incident photons converted to a PE—of the R7081-02 PMTs is 0.25 at 420 nm, while the HQE R7081MOD PMTs have a 40% higher quantum efficiency than the standard R7081-02 PMT at 390 nm. Thermionic emission at the photocathode and radioactive decays that scintillate in the PMT glass envelope produce noise pulses in the PMT that mimic a signal photon pulse. These noise sources result in a PMT dark count rate of 300 Hz in the $-40°$ to $-20°$ C temperature range relavent to DOM operation in the South Pole ice.

In addition to pulses produced by PEs ejected at the PMT's photocathode, PMT waveforms also can feature prepulses, late-pulses, and afterpulses. Prepulses occur when a photon directly ejects a PE at the PMT's first dynode stage rather than the photocathode, resulting in a low charge ($\sim$1/15 PE), early pulse ($\sim$30 ns before a standard PE pulse); the quantum efficiency of this process is $\sim$0.7% of that of a standard PE. Late-pulses occur when a standard PE is backscattered at the first dynode, occuring in 3.5% of typical PE pulses and resulting in pulses tens of nanoseconds later than a standard PE pulse. Afterpulses are the result of ions being

produced near the last dynode, which are then accelerated to the photocathode and yield a multi-PE pulse hundreds to thousands of nanoseconds after the standard PE pulse.

Each DOM contains all electronics necessary for PMT signal digitization and DOM calibration, powered by ±48 V DC supplied by a penetrating twisted copper wire pair from the string wire bundle. This copper wiring also provides the DOM communication with the ICL. A high voltage module transforms the input power to the ∼1300 V required to power the PMT. The waveforms measured by these PMTs are digitized *in-situ* by the DOMs. The block diagram of the DOM main board electronics that perform this digitization as well as DOM calibration is shown in Figure 3.10, and its components are discussed in Section 3.2.1.1 and Section 3.2.1.2. The PMT is coupled to the electronics board through a toroidal transformer. This transformer effectively acts as a high-pass filter, which can cause the tails of PMT pulses to undershoot the baseline voltage (called pulse *droop*), typically corrected for in software designed to extract photon pulse information.

3.2.1.1 Waveform Digitization

The digitization of photon waveforms produced by DOM PMTs is decentralized from the ICL, and is performed at each DOM individually. Such a system reduces the computational load on the ICL and minimizes the degradation of analog PMT signals over the kilometers of cabling between the DOMs and the ICL.

The signal waveforms from the PMT are digitized by two different systems. A Fast Analog-to-Digital Converter (FADC, called PMT ADC in Figure 3.10) samples waveforms at 40 MSPS—once per clock cycle—to capture long signals up to 6.4 μs in length [97]. An Application Specific Integrated Circuit (ASIC) called an Analog Transient Waveform Digitizer (ATWD) [97, 98] provides more precise waveform digitization, capable of digitizing waveforms at 300 MSPS for 423 ns, though it requires

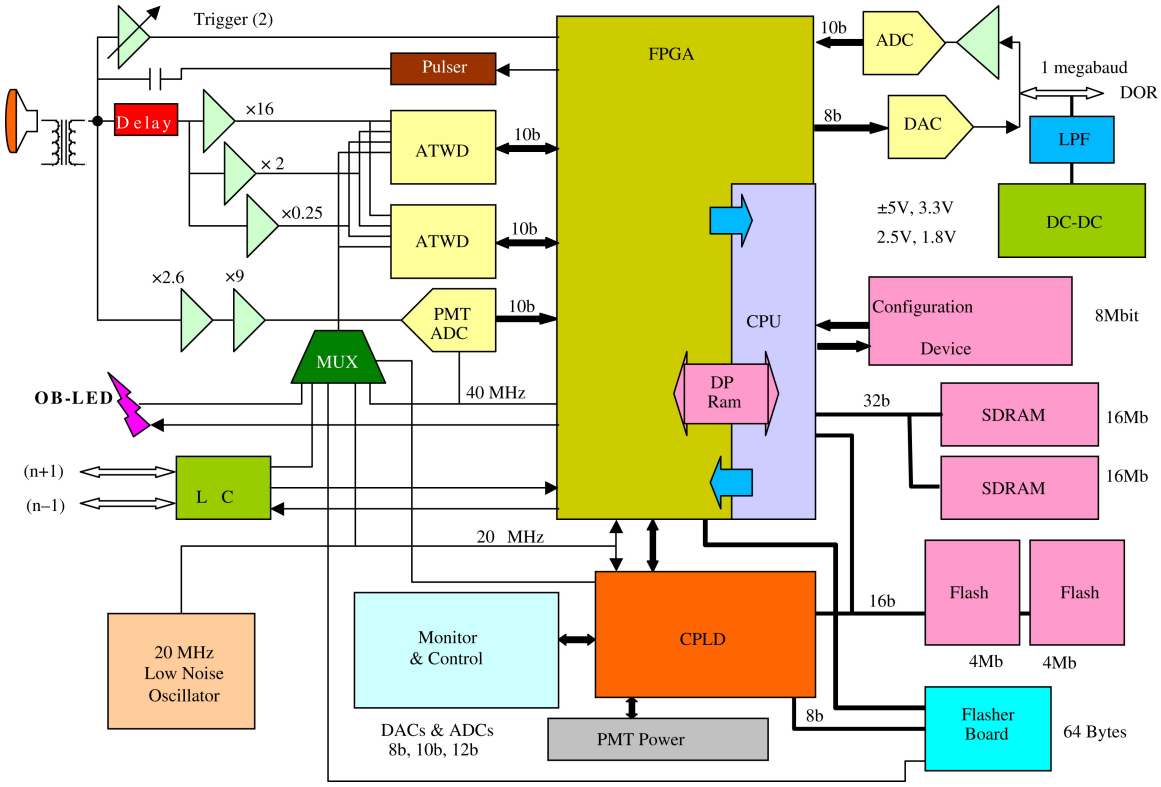

Figure 3.10: Block diagram of the DOM main board. Discussion of all components can be found in [97].

29 μs to fully digitize and capture the waveform. To minimize this DOM dead-time, the DOM main board contains a pair of identical ATWDs operating alternately. The PMT analog signal is first sent through a 75 ns delay line, then split between three wide-band amplifiers of differing gain ($\times$16, $\times$2, and $\times$0.25) before arriving at the ATWDs. The ATWDs preferentially digitize the most sensitive amplification channel first ($\times$16); if this signal saturates one of the ATWD's 128 10-bit sampling capacitors in a given channel (four channels total per ATWD), the next most sensitive amplification channel is digitized ($\times$2), and finally the least sensitive amplification channel ($\times$0.25) is digitized if the $\times$2 amplification channel is also saturated. When digitization is triggered in the ATWD, the beginning of the sampling is synchronized with the clock cycle and thus the FADC sampling. The timing calibration of the ATWD sampling is achieved by digitizing the sinusoidal waveform of the DOM refer-

ence clock in the ATWDs' fourth channel, and is applied during waveform processing at the ICL.

Waveform digitization and capture is controlled by a Field-Programmable Gate Array (FPGA) [97]. The PMT analog signal is sent to high-bandwidth, high-speed discriminator that triggers if a PMT signal exceeds a threshold equivalent to 0.25 PE, with the trigger signal sent to the FPGA. The delayed waveform is then digitized by the ATWD if a *Hard Local Coincidence* (HLC) condition is met, requiring that one of the DOM's four neighboring DOMs on the same string also records a discriminator trigger within 1 μs of its trigger. A DOM trigger without its HLC condition met is referred to as a *Soft Local Coincidence* (SLC) trigger. Though the FPGA does not record full ATWD waveforms for SLC triggers, it does still captures the highest amplitude sample from the FADC within the first 25 samples, and its two neighboring samples, for transmission to the surface.

The digital recording of one or more photons by a DOM forms the fundamental datum of an IceCube analysis, referred to as a DOM *hit*. Hit information—consisting of a timestamp, PMT waveform information, and origin—is communicated to the surface through the FPGA over the twisted copper wire pair, facilitated by a CPU on the main board. This CPU also controls DOM launches, system testing and monitoring. A temperature-compensated crystal oscillator provides a 20 MHz clock reference for the communications DAC/ADC system and the calibration flasher system. Using a phase-locked loop, the FPGA doubles this reference clock to 40 MHz for use in waveform digitization and timing calibration.

3.2.1.2 Calibration

Analyses of collections of DOM hits for physics reconstructions require precise calibration. DOM signal response calibration is required to extract timing and intensity information of the yield of incident photons at the PMT. The calibration of

relative DOM timing and geometry is then required for determination of the topology of the physics event.

The signal response of the electronics in the DOM is calibrated with a variable-voltage electronic pulser on the DOM main board that produces a waveform similar to a single PE (SPE) pulse. The pulser is controlled by the DOM CPU in a program called DOMcal, which was run monthly at the beginning of IceCube operation and now only once per year for in-ice PMTs; DOMcal is still performed monthly for IceTop PMTs. The voltage of the pulser is selected such that it just triggers the discriminator. The input–output voltage mapping is then determined using this pulser for each of the 128 sampling capacitors in each of the ATWD's four channels, as well as the precise determination of the actual gains of each of the $\times 16$, $\times 2$, and $\times 0.25$ amplifiers and sampling timing offsets in the ATWD channels. This calibration is then applied to measured hit data during mass event processing.

The regularization of each PMT's response to an incident photon is achieved by measuring the integrated charge of SPE events. Over a range of high-voltage settings powering the PMT, the mean charge of SPE events is determined. The final high-voltage setting is then chosen to achieve the nominal gain of 10^7 discussed above, with more precise calibration occuring in waveform feature extracting software.

Each DOM features a free-floating 20 MHz clock that must be coordinated relative to all other DOMs in IceCube. A GPS-discplined rubidium clock in the ICL serves as a reference to which all 5160 DOM clocks are coordinated, referred to as *IceCube Time* (ICT). The master clock is accurate to ± 10 ns through GPS disciplining, which is sufficient for astronomical studies. Using a Reciprocal Active Pulsing calibration (RAPcal) procedure, the phase and frequency of DOM clocks is measured relative to the master clock once per second [97]. A fast bipolar 5 ns pulse is transmitted to the DOMs from the ICL where it is measured; a pulse is then transmitted back to the ICL from the DOM with identical hardware (the pulse is *reciprocated*) after a

fixed delay δ, along with the measured digitized waveform of the original pulse. The two pulses are compared at several points in the waveform to determine the timing calibration. By measuring the time between the sending of consecutive pulses at the ICL (ΔT_{ICT}) and receiving them from the DOM (ΔT_{DOM}), the ratio of ICT to DOM clock frequencies is calculated as $\nu_{\mathrm{DOM}}/\nu_{\mathrm{ICT}} = \Delta T_{\mathrm{DOM}}/\Delta T_{\mathrm{ICT}}$. The offset between the clocks is then determined from the total measured round trip time of pair of RAPcal pulses ρ, and the fixed delay: given a one-way cable transit time of $\tau = (\rho - \delta)/2$, the offset between ICT and DOM clocks is calculated as $(T_{\mathrm{ICT}} - \tau) - T_{\mathrm{DOM}}$. The uncertainty in the RAPcal timing calibration for each DOM is roughly $\pm 2\,\mathrm{ns}$.

Precise relative DOM positions are calibrated through several different methods. Deployment data supplies a first order estimation of DOM positions: (1) pressure sensors above the uppermost DOM and below the lowermost DOM on a string convert the column water pressure to an absolute depth of the string, (2) inter-DOM z spacing is directly measured as the string is lowered, (3) borehole locations are manually surveyed relative to the drill tower during installation to give surface (x, y) positions, and (4) NavPack GPS data from the drill tip as a function of drill depth is used to calculate in-ice (x, y) positions. The relative depth of DOMs on different strings are then corrected using data collected from flashing LEDs on the DOM main boards. Large data sets of minimally ionizing muon events yield final calibration of relative DOM positions as muons should appear as straight tracks in the detector as measured by the DOMs. This muon data calibration can also be used to track deformations of the detector due to the yearly movement of the South Pole ice sheet.

3.2.2 Data Acquisition

Digitized measurements by IceCube DOMs are received and recorded at the ICL. After basic processing and filtering, collections of DOM hits are aggregated into prospective physics *events*. These events are stored, and sent over satellite to data

centers in the Northern Hemisphere for use in physics analyses. The data acquisition (DAQ) process is carefully monitored to verify the correct operation of the detector.

3.2.2.1 Hardware

Collections of DOMs communicate with a computer known as a *DOMHub* in the ICL [97]. The DOMHub consists of 8 DOM readout (DOR) cards on a PCI bus backplane (each capable of communicating with 8 DOMs), a low power single board CPU, power source, and hard drive. Thus, a single DOMHub controls either a single string of 60 DOMs, or the 32 DOMs in 8 IceTop stations. The DOR cards control DOM power, establishes proper DOM start-up, performs RAPcal DOM timing calibration, and receives DOM data through the twisted copper wire pair bundle.

The *Stringhub* program runs on the DOMHub CPU to receive DOM hits and convert them into "physics-ready hits" for use by the trigger and event building computer in the ICL [97]. The RAPcal timing calibration is applied by Stringhub to transform all DOM data into ICT, then chronologically orders all DOM hits and checks string-based trigger conditions. The Stringhub program further caches DOM data, sends rough hit infomation to the centralized trigger DAQ computer, and releases DOM data should a multi-string trigger condition be met for event-building.

3.2.2.2 Trigger

Though a number of trigger conditions are checked in the central trigger DAQ system, a simple multiplicity trigger (SMT) is used in this analysis to collect DOM hits into physics events. Here, the trigger searches for eight HLC hits in any in-ice DOMs that occur within a 5 μs window (SMT-8) [99]. This window is allowed to move, and should trigger conditions (including other trigger conditions that look for other kinds of physics signals) be met in overlapping time windows, the trigger windows are combined into a single event. Hits occuring up to 4 μs before the beginning of the

trigger window and 6 μs after the end of the trigger window are also included in the global trigger window. The final collection of hits within this global trigger window are bundled within a data *frame* for use by the Processing and Filtering (PnF) system.

3.2.2.3 Processing and Filtering

Under the SMT-8 condition, atmospheric muons trigger the IceCube detector at a rate $\gtrsim 2\,\text{kHz}$. Constraints on satellite bandwidth dictate full event infomation may only be sent for a subset of the collected data to the Northern Hemisphere data centers. The IceCube PnF system performs basic physics reconstructions on the collected data and yields sets of events consistent with basic signal hypotheses for use in later analyses that can be sent in full over the satellite. The specific reconstructions and filters used in this dissertation will be described in Chapter 4 and Chapter 5, respectively, while the general PnF system is discussed here.

Use of the full DOM waveforms in particle reconstructions is computationally expensive and non-trivial. As a simplifying measure, basic photon arrival infomation is first extracted from the ATWD and FADC waveforms by converting the waveform into a series of PE pulses (called *feature extraction*). Simple and fast algorithms can achieve this by searching for points in the waveform that pass a voltage threshold, however these algorithms have difficulty extracting the pulses from individual photons that pile-up into a single large PMT pulse.

The profile of pulses measured is largely determined by a linear combination of electronic components in the DOM digitization chain, though primarily by the amplifier shaping functions. Response functions measured for SPE events can thus be used as a template to return incident photon pulses using unfolding techniques that simultaneously fit waveforms from the ATWD and FADC channels. Two such algorithms are employed in this dissertation. The first, called *NewFeatureExtractor* (NFE), uses an iterative Bayesian unfolding technique [100] and was applied during initial event

processing for events in IC79 and IC86-2011 data. The second algorithm, called *wavedeform* improves on NFE primarily by improving the ATWD-to-FADC transition in fits to measured DOM waveforms and reducing the overfitting of the waveforms with many small pulses. It is applied during more refined event processing in IC79 and IC86-2011 data, and during initial processing for all subsequent 86-string years. To prevent the waveform from being fit by sums of large positive and unphysical negative pulses, wavedeform stipulates pulses must have non-negative amplitudes that are determined by the Lawson-Hanson Non-Negative Least Squares (NNLS) algorithm [101]. Overfitting of the waveform by many small pulses is prevented naturally in the Lawson-Hanson NNLS method by adding a single pulse in each iteration of the algorithm if it reduces the fit error; adding pulses is terminated when it increases the fit error or if the reduction in the fit error is smaller than a certain threshold. An example waveform feature extraction with wavedeform is shown in Figure 3.11.

The trigger time window typically contains many noise pulses unrelated to the physics event pulses. To improve reconstruction accuracy, the pulses series is cleaned of these noise pulses. Two techniques are used to achieve this. The first uses a simple *time-window cleaning* technique, where only the 6 μs of the trigger window with the most pulses is kept. The second technique yields a series of causally connected pulses (called the r–t condition), removing all pulses not within 150 m and 1 μs of another pulse. The HLC pulses that meet the r–t condition serve as a seed for the algorithm, which is then iterated three times to connect other HLC or SLC pulses under the r–t condition with previously kept pulses (referred to as Seeded r–t cleaning).

Reconstructions are performed on the cleaned pulse series to obtain estimated particle direction and energy, as well as basic light yield topology and fit quality measures. Filters are then applied to these reconstructions to obtain subsets of events that match various signal hypotheses, primarily tracks or cascades in different energy ranges. This dissertation focuses on high-energy muon track events that pass the

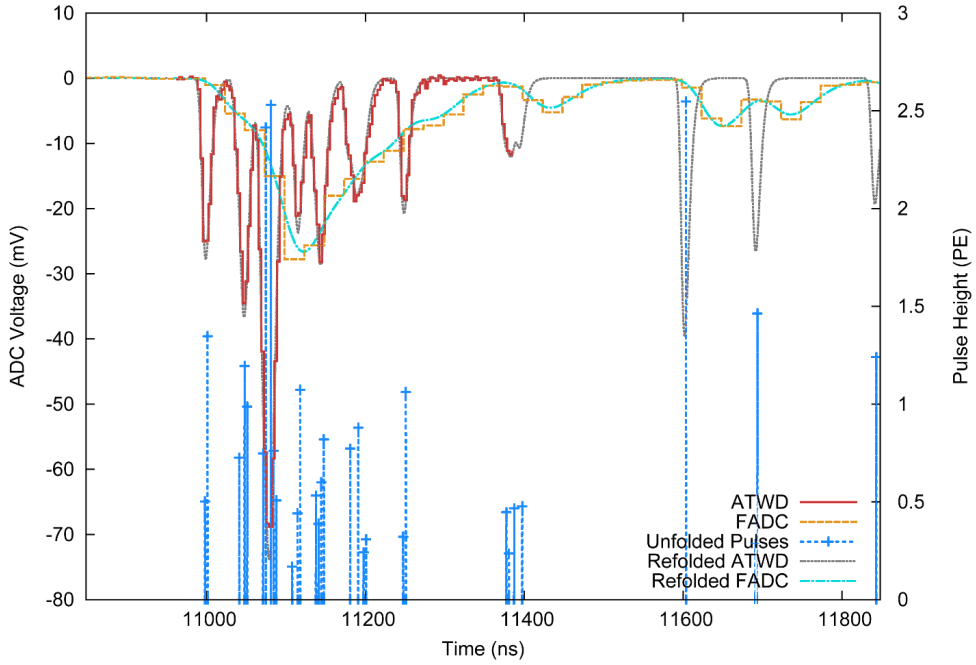

Figure 3.11: Waveform feature feature extraction with the wavedeform algorithm. The ATWD waveform over 420 ns is shown in red, while the FADC waveform is shown in orange. Extracted pulses are shown in blue crosses, with height indicating the pulse charge. Refolded ATWD and FADC waveforms from the extracted pulses are shown in grey and cyan, respectively, with good agreement to the measured waveforms. Figure adapted in [102] from [103].

Muon Filter or the Extremely-High Energy (EHE) Filter, which are discussed in Section 5.4; events collected by a Minimum Bias Filter are used for calibration.

The PnF system performs all processing and filtering by distributing events from the DAQ onto a computer cluster in the ICL for parallel processing. Events are then recompiled chronologically into larger files for further processing and analysis, with files assembled into eight hour *runs*, sent to Northern Hemisphere data centers over communications satellites. Compressed, feature-extracted waveforms and reconstructions are sent for events passing any of the over 20 filters applied, while only basic reconstruction information is sent for events that pass no filters. Waveforms and reconstructions for all events are stored on tapes and hard drives within the ICL as a permanent backup, which are moved to the North each year.

3.2.2.4 Monitoring

Metadata summarizing detector operation is stored in a database called *IceCube Live*, which is visible through a web interface. Additional run statistics are also available, such as IceCube filter pass-rates, DOM launch rates, and DOM operational values. These can be monitored as a function of time to verify continuous and stable detector operation, while anamolous behavior can be quickly determined and corrected. A list of runs where the detector operation is stable is compiled yearly, called the *good run list*. Runs can be excluded for various reasons, such as power outages, DOMHub crashes, calibration is being performed, or new operational software is being commissioned. Further, malfunctioning DOMs can be removed from analysis processing through this monitoring without removing the run from the good run list, should the rest of the detector be operating correctly. Some $\sim$100 habitually malfunctioning DOMs are permanently removed from HLC pulse processing, while $\sim$20 of these DOMs are still available for SLC pulse processing as their only problem is a bad local coincidence connection.

Only GRBs occuring during good detector operation are analyzed in this dissertation. The years of data analyzed had the following good run statistics: the IC79 data had 91% good uptime (118 GRBs analyzed during good runs, 7 GRBs during bad operation excluded); the IC86-2011 data had 93% good uptime (144 GRBs analyzed during good runs, 5 GRBs during bad operation excluded); the IC86-2012 data had 94% good uptime (121 GRBs analyzed during good runs, 4 GRBs during bad operation excluded); the IC86-2013 data had 89% good uptime (135 GRBs analyzed during good runs, 1 GRB during bad operation excluded); and the IC86-2014 data had 98% good uptime (146 GRBs analyzed during good runs, 2 GRBs during bad operation excluded).

Chapter 4

Event Reconstruction and Simulation

The selection of events consistent with a given signal hypothesis within the terabytes of IceCube data requires both the ability to reconstruct physical parameters from the events, and the simulation of the expected signal within IceCube that can be distinguished from background given these reconstructed quantities. In this dissertation, muons produced by ν_μ CC interactions are separated from the atmospheric muon background of the Southern Hemisphere sky. These events are then correlated with a given GRB through reconstructions of an event's direction; energy reconstructions are also used since the GRB neutrino spectrum is expected to be much harder than the atmospheric background. This chapter first describes the reconstructions that are performed on each event's collection of DOM pulses. IceCube event simulation is then discussed, focusing on the simulation of expected neutrino signal and atmospheric muon backgrounds.

4.1 Reconstructions

The direction and energy of a neutrino can be approximated based on the position and timing of photons detected by IceCube DOMs from the secondary particles produced in the neutrino's interaction. Reconstructions are performed in an iterative fashion, starting with simple models to obtain fast estimates for particle properties, then successively improving these estimates by increasing the complexity and accuracy of the models. The underlying particle that produces the detected light can also be revealed by investigating the quality of fit for these reconstructions. Finally, the topology of the light deposition can be parameterized such as to remove backgrounds

from an event sample, though these parameters are described in Chapter 5. Taken together, a sample of high energy muons can be obtained for correlation with GRBs.

4.1.1 LineFit

The simplest and first reconstruction of particle direction performed on an event is *LineFit*, which treats the reconstruction as a simple least-squares fit of pulses in time and space with an infinite muon track [104]. No specific radiative process or scattering and absorptive ice model is assumed to produce the measured photon pulses; one simply tries to minimize the total squared distance of pulses from the fit muon position at the time of the pulse. Let the muon track have a velocity $\vec{v}$, which passes through a point $\vec{x}_0$ at time t_0. The distance of a pulse i at location $\vec{x}_i$ and time t_i from the muon is

$$d_i(t_0, \vec{x}_0, \vec{v}) = \|\vec{v}\,(t_i - t_0) + \vec{x}_0 - \vec{x}_i\|_2. \tag{4.1}$$

Given a set of N such pulses, the track parameters are determined such that they minimize the total squared distance of all pulses:

$$\min_{\vec{v},\vec{x}_0} \sum_{i=1}^{N} d_i(t_0, \vec{x}_0, \vec{v})^2. \tag{4.2}$$

The reference time t_0 is chosen and fixed arbitrarily, as the minimization above is degenerate with respect to a simulataneous fit of $\vec{x}_0$ and t_0. This minimization can be solved analytically for track parameters $\vec{v}$ and $\vec{x}_0$ as

$$\vec{v}_{\mathrm{LF}} = \frac{\langle \vec{x}_i \cdot t_i \rangle - \langle \vec{x}_i \rangle \cdot \langle t_i \rangle}{\langle t_i^2 \rangle - \langle t_i \rangle^2} \tag{4.3}$$

and

$$\vec{x}_{0,\mathrm{LF}} = \langle \vec{x}_i \rangle - \vec{v}_{\mathrm{LF}} \cdot \langle t_i \rangle. \tag{4.4}$$

The original LineFit formulation [104] presented above gives quadratic weight to outlier pulses. As these pulses are more likely to be noise or light that has been significantly scattered from its original trajectory, it would be better for these pulses to be given less weight within the fit. A Huber fit [105, 106] remedies this by introducing a penalty function defined as

$$\phi[d] \equiv \begin{cases} d^2, & d < \mu \\ \mu(2d - \mu), & d \geq \mu, \end{cases} \tag{4.5}$$

which reduces the weight of outliers to being simply linear with respect to distance from the fit track above a certain distance μ. The Huber penalty function of (4.5) is then used in the minimization as

$$\min_{\vec{v},\vec{x}_0} \sum_{i=1}^{N} \phi[d_i(t_0, \vec{x}_0, \vec{v})]. \tag{4.6}$$

The Huber fit features a useful feature in that pulses with $d \geq \mu$ can be labeled as outliers and explicitly removed. The original least squares minimization can then be performed on the remaining pulses. The combined Huber fit and cleaned least squares minimization makes up the *ImprovedLineFit* algorithm, which shows best performance for $\mu = 153\,\mathrm{m}$ and is referred to simply as LineFit for the remainder of this dissertation. LineFit obtains reconstructed track directions with a median opening angle of $\Delta\Psi \sim 3^\circ$ relative to the true neutrino direction for neutrinos with energy $E_\nu = 10\,\mathrm{TeV}$. The median angular resolution of LineFit is shown as a function of simulated neutrino energy in Figure 4.1.

4.1.2 Likelihood-Based Angular Reconstructions

The result of the LineFit track reconstruction serves as a seed for reconstructions that compares the measured photon yield with that expected from light production

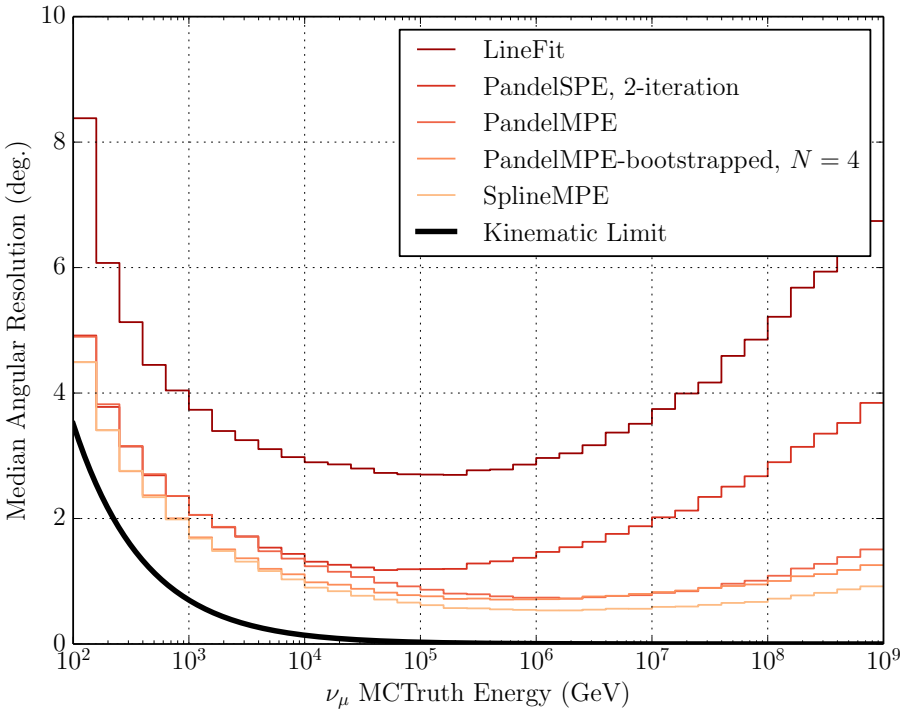

Figure 4.1: The median angular resolution of IceCube direction reconstructions as a function of simulated ν_μ energy weighted to an E^{-2} spectrum. The neutrino sample has been processed to the event selection Level 3, as discussed in Section 5.5. The kinematic limit of these reconstructions due to the deflection of the muon from the original neutrino direction is shown in the black line.

models convolved with scattering and absorption in the ice models. These fits are split into single photoelectron (SPE) and multi-photoelectron (MPE) variants that both attempt to maximize a light yield likelihood with respect to track parameters numerically [104].

The muon track is assumed to effectively travel at the speed of light, meaning the track is simply parameterized by its position at time t_0 and track direction of incidence (zenith θ and azimuth ϕ), denoted here as $\boldsymbol{a} = (\theta, \phi, x_0, y_0, z_0)$. Pulses positions and times are compactly written as $\boldsymbol{x}_i = (x_i, y_i, z_i, t_i)$. Formally, the light yield SPE likelihood is

$$\mathcal{L}_{\text{SPE}}(\boldsymbol{a}) = \prod_{i}^{\text{1st Hits}} p(\boldsymbol{x}_i|\boldsymbol{a}) \tag{4.7}$$

where $p(\boldsymbol{x}_i|\boldsymbol{a})$ is the probability of observing pulse i given the fit track. Here, the SPE likelihood only considers the first pulse measured at each DOM as they are most likely to be signal photons. The MPE variant of this likelihood is similar and considers all pulses measured, which is useful for high-energy events where a DOM can measure many signal photons. The likelihood, however, is modified to account for the total light at each DOM:

$$\mathcal{L}_{\mathrm{MPE}}(\boldsymbol{a}) = \prod_i N_j \cdot p(\boldsymbol{x}_i|\boldsymbol{a}) \left[\int_{t_i}^{\infty} p(\boldsymbol{x}'_i|\boldsymbol{a}) dt'_i\right]^{N_j-1} \tag{4.8}$$

where N_j is the total number of PEs measured at DOM j that measured pulse i, and $\boldsymbol{x}'_i = (x_i, y_i, z_i, t'_i)$. If all DOMs measure a single pulse, the SPE likelihood is recovered.

The optimal track parameters are determined through numerical minimization of $-\ln \mathcal{L}$ using minimizers such as Minuit [107]. Due to noise pulses within the measured pulse series, inherent complexity in the track parameter likelihood-space, and poor initial track parameter seeds, these minimizers typically fail to find the global minimum in one attempt, rather finding local minima. This is practically resolved by iteratively performing fits where the previous fit is used as a seed, and slightly varying the seed direction. The most computationally intensive portion of this minimization is the evaluation of the pulse probabilities $p(\boldsymbol{x}_i|\boldsymbol{a})$, and the integrated probabilities of (4.8). These calculations are simplified by using analytical functions or spline tables for the photon arrival time probability distribution function (PDF).

4.1.2.1 Pandel Function Fits

The Pandel function [108, 109] is a modified Gamma distribution, which is useful in modeling the arrival time PDF of monochromatic light propagating in a

dense material and is defined as

$$p_{\text{Pandel}}(\Delta t) = \frac{\Delta t^{(d_{\text{eff}}/\lambda)-1}}{\Gamma\left(d_{\text{eff}}/\lambda\right)\left(\frac{1}{\tau}+\frac{c_n}{\lambda_a}\right)^{-d_{\text{eff}}/\lambda}} \exp\left[-\Delta t\left(\frac{1}{\tau}+\frac{c_n}{\lambda_a}\right)\right] \tag{4.9}$$

where c_n is the speed of light in the medium, and $\Delta t = t - t_{\text{geo}}$ is the difference between the measured photon arrival time and that expected from unscattered light. This probability is introduced into the likelihood as $p(\boldsymbol{x}_i|\boldsymbol{a}) = p_{\text{Pandel}}(\Delta t_i)$ where $\Delta t_i = t_i - t_{\text{geo},i}$. For the detection of a muon by its Cherenkov radiation, the unscattered arrival time of light at a DOM can be determined through the geometry illustrated in Figure 4.2:

$$t_{\text{geo},i} = t_0 + \frac{\hat{v}\cdot(\vec{x}_i - \vec{x}_0) + d\,\tan\theta_C}{c}. \tag{4.10}$$

The Pandel function features a number of parameters that are tunable to the specific properties of the South Pole ice. The photon arrival times are best modeled with $\lambda = 33.3\,\text{m}$, $\lambda_a = 98\,\text{m}$, and $\tau = 557\,\text{ns}$. The final parameter d_{eff} additionally accounts for the angle η between the light arrival direction and the PMT axis, modeled best as

$$\begin{aligned} d_{\text{eff}} &= a_0 + a_1 d \\ a_0 &= 3.1\,\text{m} - 3.9\,\text{m}\cos\eta + 4.6\,\text{m}\cos^2\eta \\ a_1 &= 0.84 \end{aligned} \tag{4.11}$$

These parameters are determined through fits to average arrival time distributions from simulated light point sources throughout the IceCube detector, with no fit to the depth dependence of the ice properties that is included in the simulation.

Though the Pandel function largely models the photon arrival times well, it features two aspects that are unphysical: it has a pole at $\Delta t = 0$, and evaluates to zero for $\Delta t < 0$. PMT jitter and timing uncertainty, however, can yield early pulses

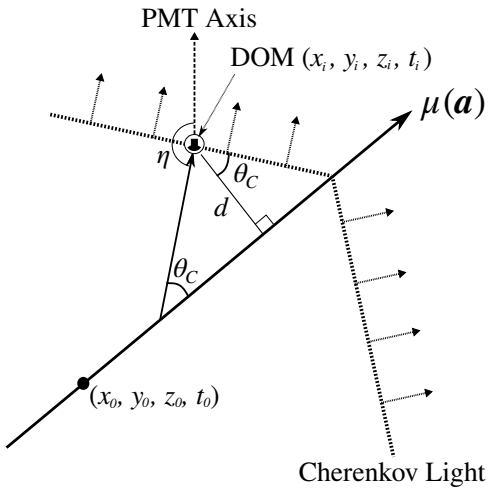

Figure 4.2: Cherenkov light detection geometry, adapted from [104].

from signal photons that should be accounted for in the timing PDF. To address this, the Pandel function is convolved with a Gaussian distribution with a width of a few nanoseconds. The convolved Pandel function is used in both SPE and MPE likelihood fits in this dissertation, referred to as *PandelSPE* and *PandelMPE*, respectively. For neutrinos with energy $E_\nu = 10\,\mathrm{TeV}$, both a 2-iteration PandelSPE and PandelMPE yield reconstructed direction with a median opening angle of $\Delta\Psi \sim 1.3°$; at higher energies, PandelSPE's median angular resolution is degraded, while PandelMPE's is improved to $\Delta\Psi \sim 0.8°$ for neutrino energies of $E_\nu = 10\,\mathrm{PeV}$. The median angular resolution of both methods as a function of neutrino energy is shown in Figure 4.1.

4.1.2.2 Bootstrapped Pandel Fit

The quality of the Pandel function reconstruction can be improved further using a bootstrapping technique [110]. Given a measured sample of pulses X that is derived from a true probability distribution P, one cannot know with certainty how well X reflects P. Bootstrapping involves resampling a new pulse series $\hat{X}_i$ based on the original pulse sample; comparing X and $\hat{X}_i$ then allows one to estimate the

uncertainty in X and iteratively perform reconstructions on X seeding with results of reconstructions based on $\hat{X}_i$.

Though bootstrapping in principle can be applied to any IceCube reconstruction, it is only applied in this dissertation to the PandelMPE reconstruction, called the *PandelMPE-bootstrapped* reconstruction. The Pandel functions in this fit are slightly modified compared to the original PandelMPE fit as they include the depth dependence of the South Pole ice. A first fit is performed on the full measured pulse series. New bootstrapped pulse series are randomly sampled with replacement from the full pulse series, with each pulse selected with probability equal to its charge divided by the total summed charge. Reconstructions are then performed on N bootstrapped pulse series, using the initial fit as a seed. The average of the N bootstrapped reconstructions is used as a seed of a final fit to the original pulse series.

The final PandelMPE-bootstrapped reconstruction shows a $\sim$10% improvement in angular resolution compared to the standard PandelMPE at neutrino energies $E_\nu \lesssim 1\,\text{PeV}$ and $E_\nu \gtrsim 100\,\text{PeV}$, seen in Figure 4.1. These improvements are largely the result of the bootstrapping avoiding local minima in the Pandel likelihood space. The angular uncertainty of the reconstruction can also be estimated based on the point spread function of the N bootstrapped fits, though it is not used in this dissertation because it does not improve this measure compared to other methods discussed in Section 4.1.3.

4.1.2.3 Spline-Parameterized Fit

Though the Pandel function yields reconstructed direction angular resolutions sufficient for astronomical studies, the likelihood-based reconstructions can be improved further by accounting for the depth dependence of the South Pole ice properties. Further, the Pandel function does not well model photon arrival times at DOMs where $d \lesssim \lambda$. These deficiencies are overcome through tabulated photon arrival time

and total photon yield PDFs from muon source simulation as a function of muon depth and direction, orientation relative to the DOM, and distance from the DOM.

Using these photon tables directly in the likelihood features two primary drawbacks: coarse binning can lead to numerical artifacts in the likelihood parameter-space, while finer binning requires unfeasible amounts of computer storage and memory for use in reconstructions. One solution is to store the finely binned tables in a compressed format through B-spline fits, which can be easily loaded and evaluated in likelihood-based fits. The cumulative distribution functions of the photon arrival timing and photon yield distributions are fit using the *photospline* package [111] using a NNLS algorithm that requires the spline to be monotonic and uses a smoothing parameter λ that prevents rapid variation in the fit; the PDF can be determined as the derivative of the spline fit. The splines are then convolved with a Gaussian distribution to accounted for PMT jitter.

In total, the spline fits reduce the computational requirements in memory and storage compared to the photon timing and yield tables by two orders of magnitude. Use of the splines has been implemented within the MPE likelihood, called *SplineMPE*. In this dissertation, the result of the PandelMPE-bootstrapped reconstruction is used as a seed for the SplineMPE reconstruction. SplineMPE improves reconstructed direction angular resolutions at nearly all muon energies compared to PandelMPE, achieving a median angular resolution of $\Delta\Psi \sim 0.6^\circ$ for neutrino energies of $E_\nu = 10\,\mathrm{PeV}$, shown in Figure 4.1.

4.1.3 Angular Uncertainty Estimators

To determine how likely a given event came from a GRB, one needs not only a reconstructed direction, but also an estimate of the uncertainty in this direction. Two methods for determining this uncertainty are used in this dissertation, a fast lower-

bound angular uncertainty estimator and a more computationally intensive mapping of the reconstruction likelihood-space.

4.1.3.1 Cramer-Rao

The first angular uncertainty estimator used in this dissertation is derived from the Cramer-Rao lower bound relation [112], which places a limit on the angular uncertainty based on the per-DOM arrival time PDFs near the fit minimum. Generally, the Cramer-Rao relation places a lower bound on the covariance of pairs of parameters in a likelihood-space with the inverse of the Fisher information matrix:

$$\mathrm{cov}(a_m, a_n) \geq \mathcal{I}^{-1}(\boldsymbol{a}) \tag{4.12}$$

where the Fisher information matrix is

$$\mathcal{I}_{mn}(\boldsymbol{a}) = -\left\langle \sum_i \frac{\partial^2}{\partial a_m \partial a_n} \ln p(\Delta t_i | \boldsymbol{a}) \right\rangle. \tag{4.13}$$

Here, the angular brackets signify the expectation value of the bracket's contents over possible values of Δt_i weighted by the arrival time PDF $p(\Delta t_i|\boldsymbol{a})$. Though the sum in (4.13) would formally be performed over all DOMs, it is implemented to only be performed over hit DOMs as it shows better correlation with angular uncertainties derived directly from the likelihood-space.

The angular uncertainty of a fit is determined by finding the Cramer-Rao variances with respect to zenith $\sigma_{\theta,\mathrm{CR}} = \sqrt{\mathcal{I}^{-1}_{\theta\theta}(\boldsymbol{a})}$ and azimuth $\sigma_{\varphi,\mathrm{CR}} = \sqrt{\mathcal{I}^{-1}_{\varphi\varphi}(\boldsymbol{a})}$. These variances are then converted to a per-event error circle by

$$\sigma_{\mathrm{CR}} = \sqrt{\frac{\sigma^2_{\theta,\mathrm{CR}} + \sigma^2_{\varphi,\mathrm{CR}} \sin^2\theta}{2}}. \tag{4.14}$$

Though the Cramer-Rao relation is useful to determine the angular uncertainty estimates for all likelihood-based reconstructions, it is only determined for the SplineMPE reconstruction for use in this thesis.

4.1.3.2 Paraboloid

The second angular uncertainty estimator used in this dissertation is derived directly from the reconstruction likelihood space [113]. The likelihood is maximized with respect to track initial position $\vec{x}_0$ at 24 fixed angular directions (θ, φ) around the original fit. The likelihood-space scan is fit with a paraboloid as expected for a 2D Gaussian PDF, with the 1σ error contour ellipse determined through Wilks' theorem with two degrees of freedom [114]. The paraboloid can be converted to an approximate per-event error circle by

$$\sigma_{\text{Parab}} = \sqrt{\frac{a^2 + b^2}{2}} \tag{4.15}$$

where a and b are the length of the semi-major and semi-minor axes of the 1σ error ellipse, respectively. The paraboloid error can be determined for any likelihood-based reconstruction, however it becomes computationally expensive for complicated likelihoods like SplineMPE and can fail for significant fractions of events. This makes its application in future near real-time analyses of events from GRBs unrealistic. It is therefore only applied to the PandelMPE reconstruction for use in this dissertation.

4.1.4 MuEX Energy Reconstruction

The energy of a muon can be estimated as it passes through or near IceCube by the amount of light deposited in the detector. This cannot be precisely extrapolated to the energy of the possible ν_μ that produced the muon because the interaction location is likely unknown (unless the interaction was within the IceCube fiducial

volume). The muon energy, however, is useful as a lower bound to the possible neutrino's energy. For events from the Southern Hemisphere sky, this lower bound is much closer to the true neutrino energy compared to those from the Northern Hemisphere as the interaction volume is constrained by the ice surface, on average placing the neutrino interaction vertex closer to the detector. The muon deposited energy therefore can still be used to statistically distinguish low-energy atmospheric muons with the muons produced in high-energy ν_μ CC interactions.

The number of detected photons can be defined as a function of muon energy E. Including the expected number of noise hits detected ρ, the total number of detected photons is expected to follow a Poisson distribution with mean $\lambda = \Lambda E + \rho$, where Λ is the expected photon yield per unit energy. The Poissonian likelihood of observing k photons is then

$$\begin{aligned} \mathcal{L} &= \frac{\lambda^k}{k!} \exp(-\lambda) \\ \implies \ln \mathcal{L} &= k \ln(\Lambda E + \rho) - (\Lambda E + \rho) - \ln(k!). \end{aligned} \tag{4.16}$$

This can be generalized to k_i detected photons at DOM i as

$$\ln \mathcal{L} = \sum_i \left[k_i \ln(\Lambda_i E + \rho_i) - (\Lambda_j E + \rho_j) - \ln(k_j!) \right] \tag{4.17}$$

The likelihood is then maximized with respect to E to determine the muon energy.

The primary difficulty in evaluating the likelihood of (4.17) is the calculation of expected light yields Λ_i. Functionally, the photon density should scale as $1/d$ close to the track, while far from the track the photon density becomes diffusive and scales as $\exp(-d/\lambda_p)/\sqrt{d}$ [115]. The characteristic propagation length λ_p is composed of effective absorption and scattering lengths (λ_a and λ_s, respectively) as $\lambda_p = \sqrt{\lambda_a \lambda_s / 3}$.

The photon density in these two regimes can be modeled analytically by

$$\Lambda(d, E) = \frac{A \cdot l(E)}{2\pi \sin\theta_C} \frac{1}{\sqrt{\lambda_\mu d \tanh \sqrt{d/\lambda_\mu}}} \exp\left(-d/\lambda_p\right) \tag{4.18}$$

where

$$\sqrt{\lambda_\mu} = \frac{\lambda_s}{3\sin\theta_C} \sqrt{\frac{2}{\pi\lambda_p}} \exp\left(\lambda_s/\lambda_a\right). \tag{4.19}$$

Here, A is the effective collection area of the DOM, and $l(E)$ is the average number of photons emitted per meter of muon track, dependent on the muon energy and parameterized empirically. The effective absorption and scattering lengths are also parameterized as a function of depth from simulation.

The likelihood of (4.17) can be improved further to include the possible over-fluctuation of measured light due to large stochastic losses along the muon track. This is achieved by convolving (4.17) with

$$G_\Lambda(x) = \frac{\text{const}}{x} \left[\exp\left(-wy\right) + \left(\frac{y}{\sigma}\right)^2\right]^{-1}, \tag{4.20}$$

a probability distribution determined empirically with $y = \ln(x/\Lambda)$ and skewness parameter w. The algorithm that maximizes this convolved likelihood using the analytical photon yield of (4.18) is called *MuEX*, which determines the muon energy E by numerically minimizing $-\ln\mathcal{L}$ with respect to a given track reconstruction. In this thesis, this is done with respect to the SplineMPE reconstructed track. The strong correlation between the MuEX calculated energy and the simulated neutrino energy is shown in Figure 4.3.

4.1.5 Millipede Energy Unfolding

The stochastic losses of a muon can be explicitly included within the Poissonian likelihood of (4.16) by generalizing it to multiple photon sources rather than just a

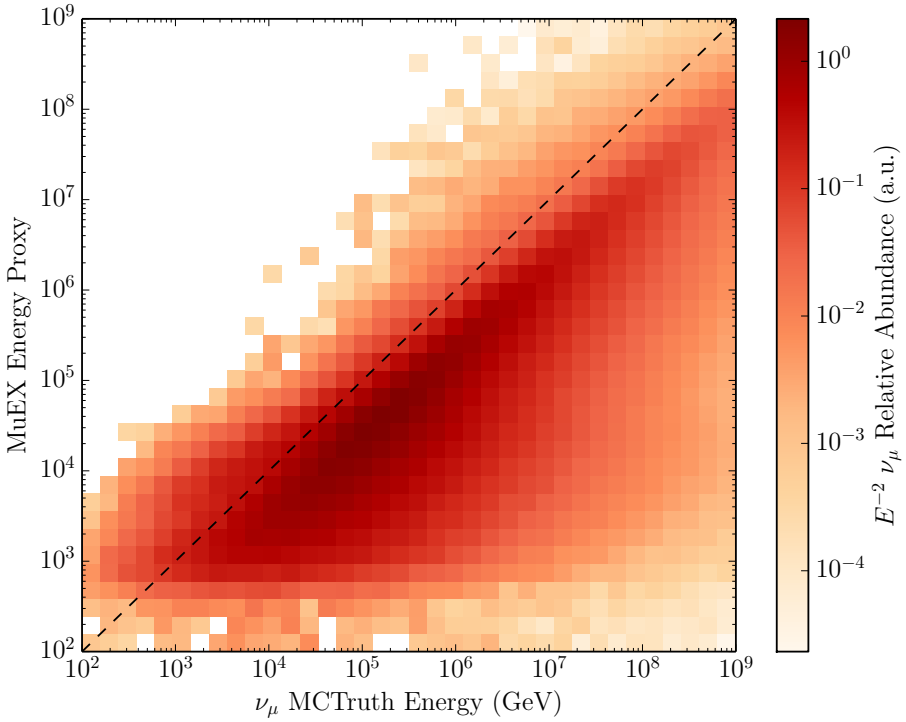

Figure 4.3: The distribution of SplineMPE MuEX reconstructed muon energies as a function of simulated ν_μ energy weighted to an E^{-2} spectrum. The neutrino sample has been processed to the event selection Level 3, as discussed in Section 5.5.

single muon track [115]. These stochastic losses can then be determined by unfolding the energies of discrete sources that maximize the multi-source likelihood. The expected photon yield can be written as a sum of individual stochastic light sources along the muon track as

$$\lambda = \sum_{j}^{\text{sources}} E_j \Lambda_j + \rho = \vec{E} \cdot \vec{\Lambda} + \rho \tag{4.21}$$

This light yield can be then directly inserted into the likelihood of (4.16). Including the observation of all photons at DOMs i and time bins m, the final likelihood becomes

$$\ln \mathcal{L} = \sum_{i,m} k_{i,m} \ln \left(\vec{\Lambda}_{i,m} \cdot \vec{E} + \rho_{i,m} \right) - \left(\vec{\Lambda}_{i,m} \cdot \vec{E} + \rho_{i,m} \right) - \ln \left(k_{i,m}! \right). \tag{4.22}$$

To first order in the Gaussian error regime, this can be solved by

$$k_{i,m} - \rho_{i,m} = \vec{\Lambda}_{i,m} \cdot \vec{E}, \tag{4.23}$$

which can be expressed as a set of linear equations

$$\vec{k} - \vec{\rho} = \mathbf{\Lambda} \cdot \vec{E}. \tag{4.24}$$

The response matrix $\mathbf{\Lambda}$ for a given DOM location, time bin, and muon energy is determined through the spline tables discussed in Section 4.1.2.3. By inverting this equation, one can determine the muon energy losses $\vec{E}$.

The determined muon energy losses can be refined further by directly maximizing the likelihood of (4.22). Solutions with negative energy losses are prevented by using NNLS algorithms to maximize the likelihood, specifically a Non-Monotonic Maximum Likelihood algorithm [116] that can determine muon energy losses to within $\sim 10 - 15\%$, comparable to that achieved for cascade event energy reconstructions [115]. Regularization in the form of a weak ridge penalty on $\|\vec{E}\|$ further prevents large variation in the energy losses along the muon track.

The algorithm that determines the muon energy losses that maximize the multi-source likelihood is called *Millipede*. The number of possible losses is fixed within the algorithm by splitting the muon track into 10 m segments, each of which containing one energy loss. A full reconstruction of the muon track parameters $\boldsymbol{a}$ along with the energy losses $\vec{E}$ is possible within Millipede with standard numerical minimizers, though they are susceptible to finding local minima. Typically this is avoided by manually performing scans of the likelihood space with respect to track direction, where the track direction is held fixed and the likelihood is minimized with respect to vertex position $\vec{x}_0$ and energy losses $\vec{E}$. One can also simply determine the energy losses $\vec{E}$ using a fixed track direction and vertex; Millipede energy losses determined

along the SplineMPE reconstructed track are used in this dissertation. Full Millipede angular scans are also performed on significant events in the final analysis.

4.2 Simulation

The robust simulation of the IceCube detector is critical not only for verifying its proper operation, but also the behavior of reconstructions described in this chapter. Further, simulation of various particle signals forms the basis for physics analyses in IceCube, allowing certain physics signals to be separated reliably from backgrounds based on reconstructed quantities. In this thesis, simulations are focused on the ν_μ neutrino signal and cosmic ray air shower background. Data sets of these simulated events are used to define the event selection of the analysis, evaluate its sensitivity to astrophysical neutrino signals, and describe the expected backgrounds in the final analysis.

4.2.1 Particle Generation

The first step of the IceCube simulation chain produces the incident particles. To do so in a statistically rigorous manner, Monte Carlo simulations randomly generate particle events that are then propagated to a simulated IceCube detector, accounting for standard model particle interactions.

4.2.1.1 Neutrino Simulation

Neutrino events are generated by the *neutrino-generator* package—a port of the *ANIS* neutrino event generator [117]—with energy chosen randomly from a power law spectrum and distributed uniformly over the entire sky. These neutrinos are then propagated to the IceCube detector. Due to the neutrino's small interaction cross section, it is computationally inefficient to continuously generate neutrino events un-

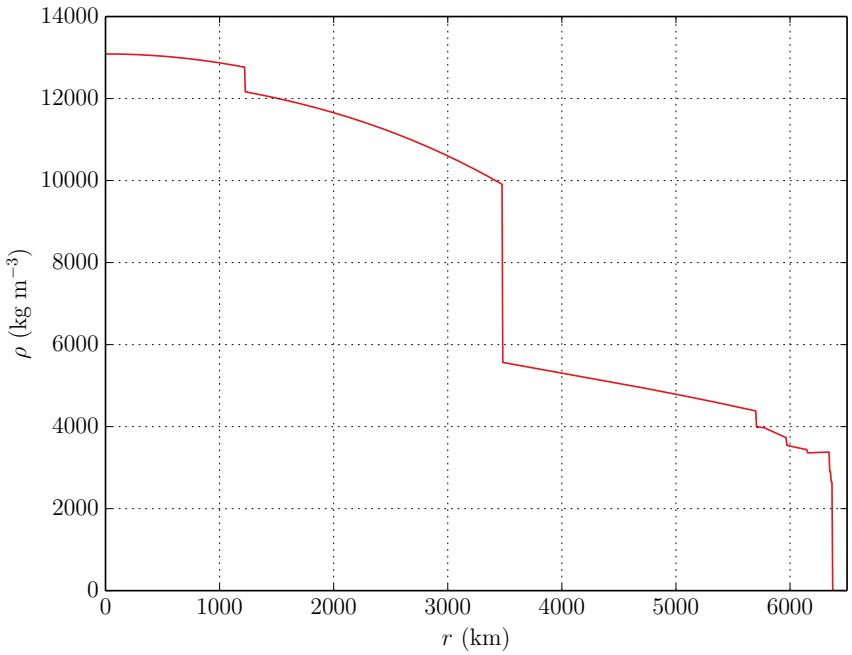

Figure 4.4: Density profile of the Earth as a function of radius from its center, from the Preliminary Reference Earth Model [120].

til one happens to interact near the IceCube detector. Rather, each neutrino is forced to interact at a random vertex near the simulated detector, and assigned a *weight* later that represents its probability of being detected per second and is derived from the neutrino-nucleon cross section and model of the Earth density profile. The neutrino-nucleon cross sections are taken from the HERA parton distribution function v1.5 (HERAPDF1.5) [118] as calculated by Cooper-Sarkar, Mertsch, and Sarkar (CSMS) [82], shown in Figure 3.3. Simulation for the IC79 and IC86-2011 detectors use neutrino cross sections calculated from the CTEQ5 parton distribution function [119]. Neutrinos are propagated through the Earth accounting for absorption, scattering, and NC regeneration, with the Earth's density profile taken from the Preliminary Reference Earth Model [120], shown in Figure 4.4.

Having propagated the neutrino to the interaction vertex and calculated the final neutrino energy at this vertex, the neutrino is forced to interact by deep-inelastic scattering with a nucleon, with CC or NC interactions chosen with relative proba-

bility determined from the neutrino cross sections at the neutrino interaction energy. Products of this interaction are then generated according to the Standard Model.

Neutrino event weights are determined from the initial neutrino generation area and energy spectrum, as well as the probability of the neutrino interacting at the chosen interaction vertex. This is referred to as an event's *OneWeight* (units of $\mathrm{GeV\,cm^2\,sr}$), and is calculated as

$$\mathrm{OneWeight} = \left(\frac{P_{\mathrm{int}}}{E^{-\gamma}}\right) \Omega A \int_{E_{\mathrm{min}}}^{E_{\mathrm{max}}} E'^{-\gamma} dE', \tag{4.25}$$

where E is the generated neutrino energy, Ω and A are the solid angle and area, respectively, over which the neutrino events are generated, and γ is the spectral index of the neutrino energy generation spectrum from E_{min} to E_{max}. The interaction probability is determined as

$$P_{\mathrm{int}} = 1 - \exp\left[-\left(\frac{L\sigma_{\nu N}}{m_N}\right)\right] \tag{4.26}$$

where L is column depth ($\mathrm{g\,m^{-2}}$) of the neutrino path through the possible interaction volume, $\sigma_{\nu N}$ is the total neutrino-nucleon cross section at the neutrino interaction energy, and m_N is the nucleon mass. For an arbitrary signal spectrum $d\Phi_\nu/dE_\nu$, the weight of a given neutrino event i can be rescaled as

$$\omega_i = \frac{\mathrm{OneWeight}_i}{N_{\mathrm{gen}}} \times \left.\frac{d\Phi_\nu}{dE_\nu}\right|_{E_i}. \tag{4.27}$$

Here, E_i is the generated neutrino energy, and N_{gen} is the total number of simulated neutrinos generated in a given data set. The units of this weight ω_i is $\mathrm{s^{-1}}$, meaning the sum of weights ($\sum_i \omega_i$) of all simulated neutrino events yields the total detected neutrino rate in Hz for a given flux model, with statistical uncertainty calculated as $\sqrt{\sum_i \omega_i^2}$.

Typically neutrino simulation is generated over the entire Earth surface, which reliably describes diffuse neutrino signals. To represent point sources like GRBs with resolved locations, it is useful to downsample the diffuse simulation to just the neutrino events near the source location. In this dissertation, each GRB is simulated with diffuse neutrino events within 11° of the GRB location. The expected number of neutrinos detected from the GRB is then determined from weights calculated with a given model's fluence prediction dF/dE_ν. This is achieved by modifying the diffuse weights of (4.27) as

$$w_i = \frac{\text{OneWeight}_i}{N_{\text{gen}}} \times \frac{1}{4\pi f_s} \times \left.\frac{dF_\nu}{dE_\nu}\right|_{E_i}, \tag{4.28}$$

where f_s is the fraction of the sphere over which the diffuse simulation is downsampled, 0.01 in the case of a 11° sampling radius. The weights of (4.28) are unitless, meaning the total number of detected neutrinos is calculated from the sum of all event weights.

4.2.1.2 Cosmic Ray Simulation

The muons produced in cosmic ray air showers are generated with *CORSIKA* [121], a package that produces extensive air showers induced by cosmic ray primaries in the atmosphere by Monte Carlo simulation. To generate sufficient statistics for atmospheric muons produced by many primary compositions over a wide range of energies, primary energies are chosen randomly from an $E^{-2.6}$ spectrum. The primary composition is chosen randomly from the five most common spectral components: H, He, N, Al, or Fe. Multiple air showers can be randomly combined into a single event to simulate coincident atmospheric muons in the detector. Additionally, air shower events can be combined with neutrino events generated by neutrino-generator to simulate temporal coincidences between signal and background.

A given cosmic ray air shower simulation data set can be weighted to an arbitrary cosmic ray flux model analogously to the neutrino simulation. This weighting accounts for the expected relative probability of the various primary compositions and energies, as well as the probability of coincident events. Simulation of IC79 features an *unweighted* CORSIKA, which generates primary compositions and energies randomly from the Polygonato model [122] and requires no additional weighting to obtain a realistic cosmic ray spectral simulation.

Once the air showers have been generated, muons are tracked from the atmosphere to the simulated IceCube detector volume. These muons are then propagated through IceCube's fiducial volume identically to those produced in ν_μ CC interactions. Atmospheric neutrinos are simulated separately with neutrino-generator simulation weighted to an atmospheric neutrino spectrum, while all other particle species produced in the air shower are expected to be completely attenuated by the ice overburden.

4.2.2 Detector Simulation

Simulated muons are propagated through the ice of the IceCube fiducial volume with the Propagator with Optimal Precision and Optimized Speed for All Leptons (PROPOSAL) package [123], or in older simulation with the Muon Monte Carlo (MMC) package [87]. Energy losses are generated along the muon track according to the expected contributions of Figure 3.6, taking the form of cascades along the muon track. These cascades are simulated by the Cascade Monte Carlo (CMC) package, which can either treat cascades as point-like light sources, or include their longitudinal development by simulating the cascade as a series of smaller cascades along a line. Additionally, CMC accounts for muons produced in the hadronic cascades at a neutrino's interaction vertex and photonuclear stochastic losses, which are then propagated in the ice with PROPOSAL (or MMC). The final muon is visible through

the radiative contributions of these cascades and the bare muons' Cherenkov and ionization radiation.

Photons are produced and propagated to the simulated DOMs either by direct photon propagation or through interpolated photon yield tables. Direct photon propagation is computed on GPUs, accounting for scattering and absorption through a random-walk Monte Carlo within a given ice model. Two programs can perform this direct propagation: Photon Propagation Code (PPC), which parameterizes expected photon production of tracks and cascades, and *CLSim*, which itself can exactly replicate PPC's parameterized photon production or use GEANT4 [124] to directly simulate all particles and their light production processes. Alternatively, spline-interpolated photon yield tables from direct photon propagation simulation can be used. Tables are produced for cascades and bare muon tracks separately, as a function of source depth, source direction, and receiver position for a given ice model. The *Photonics* program [125] reads the spline-interpolated fits to the average photon yield as a function of time and photon wavelength—to account for the wavelength dependence of the PMT's quantum efficiency—to generate photon hits at the simulated DOMs. Finally, a hybrid mode is offered by CLSim, which performs direct photons propagation for the bare muon track photons, and uses Photonics spline-tables for cascades. The result of each photon propagation method is the times of discrete photon hits, accounting for the PMT's quantum efficiency. Noise hits from thermionic emission at the photocathode and correlated noise from radioactive decays inducing scintillation in the DOM glass are simulated as well with the *Vuvuzela* package. The simulation of the IC79 and IC86-2011 IceCube detector use the older *noise-generator* package that does not account for correlated noise.

The PMT response to all photon and noise hits is then simulated through the *PMTResponseSimulator* module. Each hit typically corresponds to a SPE pulse, with amplification determined from the PMT charge response function and exact timing

accounting for PMT jitter; these hits have a small probability of randomly becoming pre-pulses or late pulses. A fraction of normal SPE pulses randomly generate an after-pulse as well. All pulses are then passed to the *DOMLauncher* module to simulate the measurement of the pulses by the DOM electronics and trigger logic. Templates of measured pulses are used to convert the PMT pulses to the amplified pulses measured at the FADC and ATWDs. The pulses passing simulated discriminator trigger conditions are then digitized, accounting for electronic noise, the FPGA clock phase, and uncertainty in the RAPcal timing calibration. Local coincidence conditions are then checked, resulting in HLC or SLC launches that are recorded. Finally, the *trigger-sim* module check for DAQ trigger conditions being met, resulting in trigger windows of launches being formed. At this point, the simulated events can be processed identically to that performed by the PnF system, yielding data sets of simulated events passing the IceCube processing and filtering proceedure.

Chapter 5

Event Selection

The sensitivity of a search to a high-energy ν_μ signal from GRBs is contigent on reducing the terabytes of available IceCube data—overwhelmingly made up of atmospheric muons—to those events consistent with that signal. This data reduction, also known as the analysis event selection, is applied in stages. This process allows more and more computationally expensive reconstructions to be applied progressively to the data, for use either in further event selections or in physics analyses.

The event selection in this dissertation yields a sample of events that reconstruct to having an origin from the Southern Hemisphere sky of IceCube. As past Northern Hemisphere track searches have included the near-horizon declination band from -5° to 0° where atmospheric muons are shielded by the South Pole glacier, this search applies to the remaining portion of the sky, that is at declinations $< -5^\circ$ (typically called *downgoing* events). Here, atmospheric muons produce $\gtrsim 2\,\mathrm{kHz}$ of IceCube SMT-8 triggers, which must be reduced to search for track events consistent with ν_μ CC interactions. An additional irreducible background in this analysis are muons produced in atmospheric ν_μ CC interactions that trigger the detector at a rate of $\gtrsim 20\,\mathrm{mHz}$ ($\gtrsim 7\,\mathrm{mHz}$ from the Southern Hemisphere sky). The atmospheric ν_μ background is much less prominent in quantity compared to atmospheric muons and is spectrally much softer than the prompt ν_μ signal, and is therefore largely negligible in this analysis.

As this analysis is interested in high-energy neutrino signal, the event selection employed primary focuses on removing the low energy atmospheric muon background through energy proxies and direction information. Information about an event's reconstruction quality and light deposition topology allow further reductions in this

background. This chapter first describes the parameters used to separate signal and background events, then summarizes each stage of the complete event selection, from IceCube trigger level data to final event sample.

5.1 Event Quality Parameters

For the best association of an event with a GRB, events with the highest quality reconstructions are desired. Parameterization of an event's reconstruction quality allows one to remove events made up of multiple coincident muons and poorly reconstructed events where the muon clips the detector volume.

The first set of quality parameters are derived from a likelihood-based reconstruction's negative log-likelihood value. As this value is minimized given a certain signal hypothesis, the log-likelihood value gives some indication of the quality of the fit of this hypothesis to the data. To correct this value for the number of degrees-of-freedom (DOF) in the fit—the number of input parameters (the number of hit DOMs, denoted as N_{ch}) minus the number of fit parameters (5, having fit the vertex position and track direction)—the analysis uses a *reduced* log-likelihood of the fit defined as

$$\mathrm{rlogl} \equiv \frac{\mathrm{logl}}{N_{\mathrm{DOF}}} = \frac{\mathrm{logl}}{(N_{\mathrm{ch}} - 5)}. \tag{5.1}$$

The reduced log-likelihood, however, is found to typically correlate with event energy for IceCube reconstructions. Rather than correct for the exact number of degrees of freedom, it is found that the following displays more consistent behavior with event energy in IceCube's range of energy sensitivity, called *plogl*:

$$\mathrm{plogl} = \frac{\mathrm{logl}}{(N_{\mathrm{DOF}} + 1.5)} = \frac{\mathrm{logl}}{(N_{\mathrm{ch}} - 3.5)}. \tag{5.2}$$

The second set of fit quality parameters used in this analysis are the Cramer-Rao and paraboloid angular uncertainty measures discussed in Sections 4.1.3.1 and 4.1.3.2, respectively. Both measures estimate the depth of the likelihood-space near a fit minimum, giving a useful measure of the fit quality.

All these fit quality parameters can be used to trim poorly reconstructed events from the analysis. Further, they can be used to distinguish signal muons from ν_μ CC interactions and atmospheric muon events in machine learning algorithms, as well-reconstructed signal events tend to have smaller rlogl, plogl, or angular uncertainty measures than background events.

5.2 Event Topological Parameters

The second general class of parameters used in the event selection of this analysis are those that quantify characteristics of the deposited light in the IceCube detector. These can be used to generally distinguish high-energy ν_μ CC interaction muons from the much more plentiful atmospheric muon background.

The first set of parameters generally the amount of light measured by the detector for a given event. Counts of the number of hit DOMs (N_{ch}) and hit strings (N_{str}) serve as simple event energy proxies. The total measured charge equivalent of deposited light in the detector from droop corrected and feature extracted waveforms (denoted by Q_{tot}) yields a further proxy of an event's energy, while the average distance of hits from a reconstructed track, weighted by hit charge (denoted as *AvgDistQ*), can give a simple proxy of reconstruction quality.

The next set of parameters are derived from the approximate position of hits within the detector. For this, the center-of-gravity (COG) position of hits weighted by their measured charge is calculated relative to the center of the IceCube detector. Two coordinates of the COG are particularly useful in distinguishing signal high-energy muons and atmospheric muons: the z position and $\rho^2 = x^2 + y^2$ in cylindrical

coordinates. Signal events are more likely to occur deep in the ice (more negative COG z) and closer to the center of the detector (smaller COG ρ^2) than atmospheric muons. These parameters are especially useful when included in machine learning algorithms to distinguish these event classes.

Two additional parameters were introduced to describe where the event has been reconstructed within the IceCube detector. First, background events that happen to pass close to IceCube strings and rows of strings are more likely to be kept in various Q_{tot} and N_{ch} cuts, as they yield more visible light than events further from IceCube strings. There are therefore excesses of background events at azimuths every 30°, corresponding to various string rows. Because of the rotational symmetry of the IceCube detector, an angular measure relative to these string rows, called an *Azimuth Map*, can be calculated as

$$\text{Azimuth Map} = |\text{mod}_{30^\circ}(\phi_{\text{reco}} - \phi_0) - 15^\circ| \tag{5.3}$$

where $\phi_0 = 9.1^\circ$ is a baseline rotation of the IceCube detector in azimuth. Next, Events that exhibit their first light well-within the detector fiducial volume are more likely to be from ν_μ interacting within the detector than from atmospheric muons, as shown in the IceCube starting-event analysis that discovered the astrophysical neutrino flux [22]. A proxy measure of this is the distance of the reconstructed vertex to the detector edge (i.e. the surface created by the outer-most strings, and the shallowest and deepest DOMs on the strings) along the reconstructed track direction, called the *Starting Distance*. By convention, a positive Starting Distance corresponds to a track starting in the detector volume, and negative corresponds to a track starting outside the detector volume; tracks that never enter the IceCube fiducial volume are given a default value of zero so that they can still participate in the analysis.

The next set of event topology paramters are derived from DOM hits that are considered *direct hits* relative to a reconstructed track, as these hits are most likely to have been due to light emitted by the muon rather than noise or scattered photon hits. Direct hits are defined to have time residuals in the window $-15\,\text{ns} < t_{\text{res}} < 250\,\text{ns}$ relative to the expected geometric light travel time from a muon track at the Cherenkov angle given by (4.10). The total number of direct DOM hits is denoted by N_{dir}. Atmospheric muon bundles can be partially distinguished from single high-energy muons by comparing the number of early hits ($t_{\text{res}} < -15\,\text{ns}$, denoted as N_{early}) to N_{dir} as a ratio $N_{\text{early}}/N_{\text{dir}}$; muon bundles are expected to have more early hits caused by light radiated by the additional muons in the event, compared to single muon events. The total length of the track within the detector can also be determined as the longest distance between direct hit DOMs measured parallel to the reconstructed track, denoted by L_{dir}, which roughly corresponds to the event's "lever-arm" in the track reconstruction.

Several secondary measures can be calculated from these direct hits. First, the N_{dir} and L_{dir} parameters can be combined into a *direct ellipse* parameter, defined as:

$$\text{DirectEllipse} = \left(\frac{N_{\text{dir}}}{10}\right)^2 + \left(\frac{L_{\text{dir}}}{180\,\text{m}}\right)^2. \tag{5.4}$$

Next, the smoothness of the light deposition can be estimated from the direct hits by:

$$\text{Smoothness} = s(i_{\text{max}}) \tag{5.5}$$

where

$$s(i) = \frac{i}{N_{\text{dir}}} - \frac{(\vec{x}_i - \vec{x}_0) \cdot \hat{v}}{L_{\text{dir}}} \tag{5.6}$$

and $i_{\max}$ is the index of the direct hit (ordered along the length of the reconstruction) that maximizes the absolute value of the smoothness function:

$$i_{\max} = \arg\max_{i} |s(i)| \,. \tag{5.7}$$

Here, $\hat{v}$ is the unit vector in the direction of the given reconstruction. Large Smoothness values indicate an event with a large stochastic energy deposition early in the detected muon track, while large negative values correspond to either late stochastic depositions or events composed of multiple coincident muons. Finally, the COG position of the first and last quartiles of direct DOM hits, weighted by the measured hit charge, can be calculated. The distance between these positions along the reconstructed track is referred to as the direct hit *Separation*. Large Separation values can indicate coincident muon events, while small Separation values usually correspond to poorly reconstructed events due to a small reconstruction lever-arm.

A parameter that is helpful in tagging atmospheric muon events is a count of IceTop hits. To reduce the number of noise hits contributing to this count, only *on-time* hits are counted. These are hits with time residual $-50\,\text{ns} < t_{\text{res}} < 500\,\text{ns}$ relative to a cosmic ray air shower-front (assumed to be a plane wave-front coincident with the incoming muon) arriving from a given reconstructed direction. Steeply downgoing atmospheric muon events are expected to be accompanied by many on-time IceTop hits, while more oblique downgoing atmospheric muon and cosmic neutrino events are expected to have very few such hits.

5.3 Muon Bundle Likelihood Parameters

The final class of parameters used in the event selection of this analysis attempt to distinguish high-energy atmospheric muon bundles and high-energy single muons expected from signal. These parameters refine the measure of early light (compared

to the $N_{\text{early}}/N_{\text{dir}}$ measure) and parameterize the stochasticity of the muon energy losses along the reconstructed track length to give an indication that the event is composed of more than one muon.

The time residuals for DOM hits in an event can be used to construct signal and background hit PDFs as a function of hit distance from a reconstructed track and event energy. Background events are selected from data more than two hours from any GRB in the measured IceCube data. Signal events are taken from ν_μ simulation weighted to an E^{-2} spectrum. As this parameter is most useful in the later stages of the event selection, only events reconstructing as being downgoing tracks, passing the Muon Level 3 event selection (discussed in Section 5.5), and passing an IceTop veto (see Section 5.6.1) are considered. Background and signal hit time residuals are histogrammed as a function of distance from the reconstructed track, separating events by reconstructed energy into four separate such histograms (each with equal signal plus background hit statistics, eight histograms total). Normalizing each of these histograms therefore represent per-energy bin time-residual PDFs, denoted by $\mathcal{B}(d, t_{\text{res}}; E_{\text{reco}})$ and $\mathcal{S}(d, t_{\text{res}}; E_{\text{reco}})$ for background and signal, respectively. Background and signal likelihoods can therefore be constructed as

$$\begin{aligned} \mathcal{L}_B &= \prod_i^{N_{\text{hits}}} \mathcal{B}(d_i, t_{\text{res},i}; E_{\text{reco}}) \\ \mathcal{L}_S &= \prod_i^{N_{\text{hits}}} \mathcal{S}(d_i, t_{\text{res},i}; E_{\text{reco}}) \end{aligned} \tag{5.8}$$

for a set of hits i from event with energy reconstruction E_{reco}. The signal-to-background log-likelihood ratio in then simply calculated as $\ln(\mathcal{L}) = \ln(\mathcal{L}_S/\mathcal{L}_B)$. This can be quickly evaluated by pre-calculating per-bin signal-to-background PDF ratios for each reconstruction energy bin, then linearly interpolating all measured bins. The sets of PDFs and PDF ratios obtained for this analysis are shown in Figure 5.1, where SplineMPE has been used as the track reconstruction, and SplineMPE MuEX is the

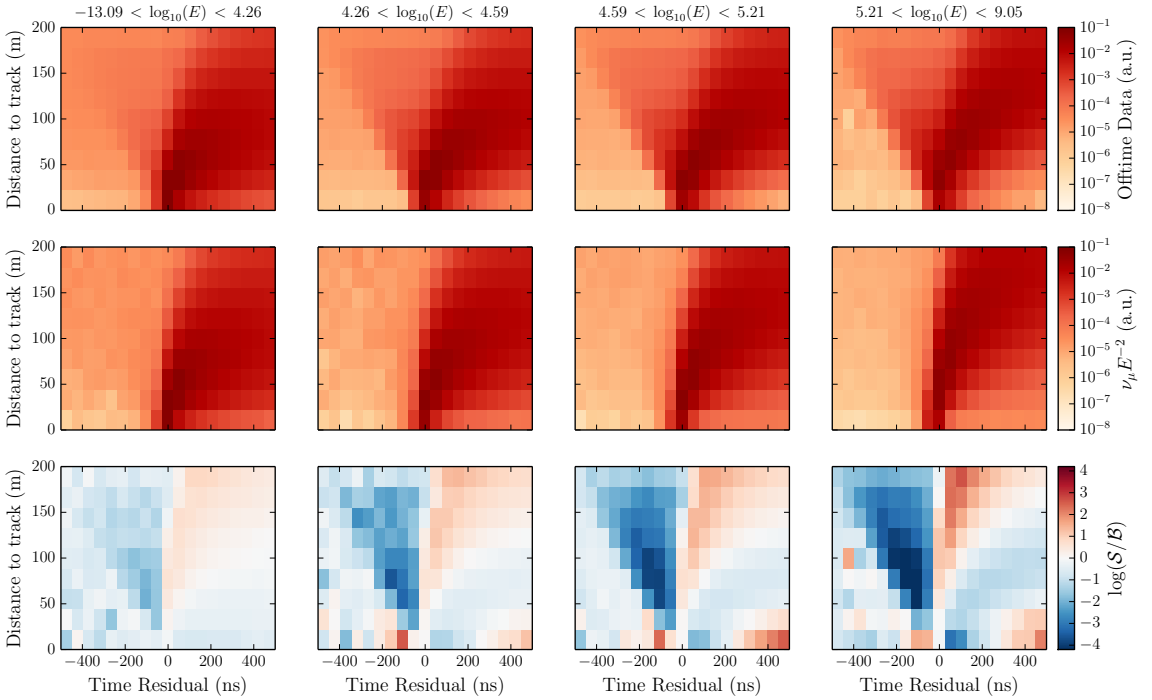

Figure 5.1: Histograms of event hit time residuals as a function of distance from the reconstructed SplineMPE track. The top row is obtained from data more than two hours from any observed GRB, while the middle row is obtained from ν_μ simulation weighted to an E^{-2} spectrum. Each column gives these histograms for events with a certain reconstructed MuEX energy proxy, with energy ranges chosen so equal data plus simulation hit statistics exist in each column. Each histogram is then normalized to yield the log-signal-to-background PDF ratios of the bottom row.

reconstructed energy. The power of this variable is seen in the PDF ratios, where the atmospheric muon bundles in background data at the highest reconstruction energies yield significantly more early DOM hits than a signal muon of comparable energy.

A similar likelihood can be constructed with Millipede reconstructed energy depositions as a function of distance along the reconstructed track. As atmospheric muon bundles are expected to exhibit smoother energy depositions, the Millipede reconstruction should be composed of smaller reconstructed dE/dx values over the entire track length; conversely, single high-energy muons are expected to have large stochastics, and therefore large reconstructed dE/dx over the entire track length. Two simple modifications are made to the hit time residual likelihood to obtain the Millipede dE/dx smoothness likelihood: the index i is over Millipede depositions,

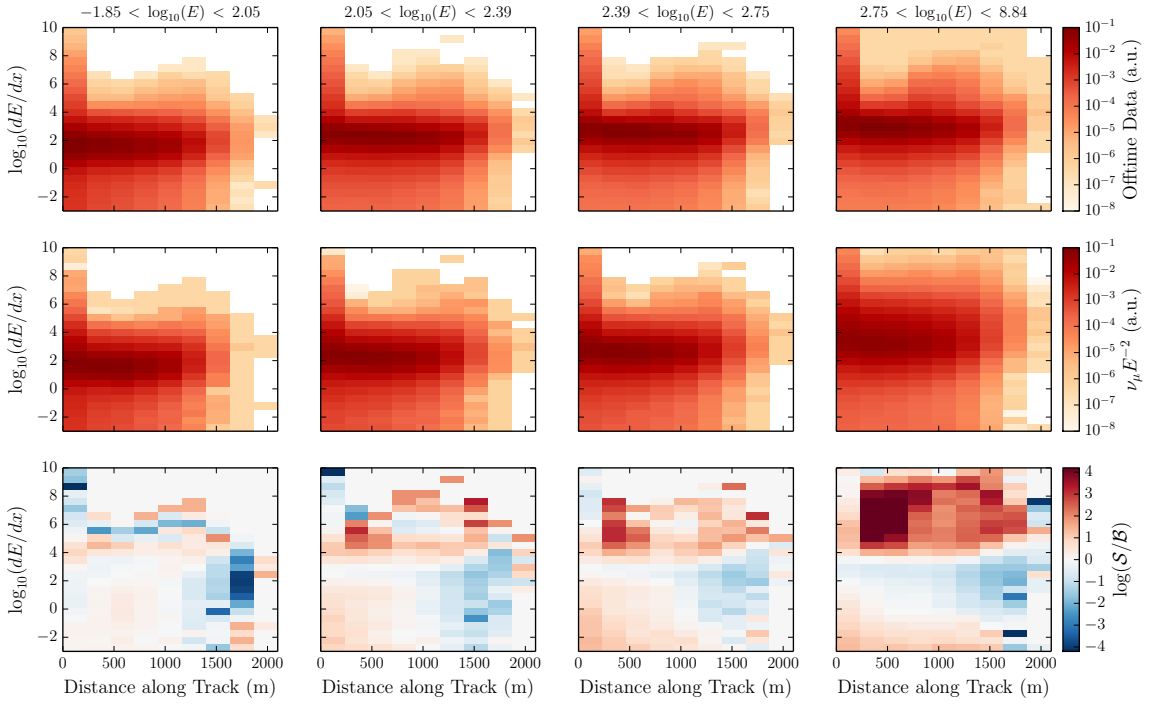

Figure 5.2: Histograms of event Millipede reconstructed dE/dx as a function of distance along the reconstructed SplineMPE track. The top row is obtained from data more than two hours from any observed GRB, while the middle row is obtained from ν_μ simulation weighted to an E^{-2} spectrum. Each column gives these histograms for events with a certain reconstructed Millipede average dE/dx, with energy ranges chosen so equal data plus simulation deposition statistics exist in each column. Each histogram is then normalized to yield the log-signal-to-background PDF ratios of the bottom row.

and the base histograms are constructed in Millipede reconstructed $\log_{10}(dE/dx)$ and distance along the track. The average dE/dx from the Millipede reconstruction over the entire track length is used as the energy proxy of the event to reduce correlations with the SplineMPE MuEX energy reconstruction and hit time residual likelihood. The Millipede dE/dx PDFs for background and signal events, as well as the PDF ratios, are shown in Figure 5.2. As expected, the signal high-energy muon PDFs show a large excess of large reconstructed dE/dx depositions along the entire track, compared to the reconstruction of atmospheric muon bundles. These can then be used to calculate a log-likelihood ratio value, using the same method as the hit time residual likelihood.

5.4 Initial Selection

As discussed in Section 3.2.2.2 and Section 3.2.2.3, the initial IceCube data used in this analysis are events that pass the SMT-8 trigger condition. These events are passed to the IceCube PnF system that apply basic reconstructions to events, and allow basic filtering of events consistent with various signal hypotheses. In this analysis, the Muon Filter, which searches for well-reconstructed track events, and the Extremely-High Energy (EHE) Filter, which looks for events that deposit large amounts of light in the IceCube detector, are employed.

5.4.1 Muon Filter

The Muon Filter passes events most likely to be high-quality muons over the entire sky, while reducing the total rate of events from $\gtrsim 2\,\mathrm{kHz}$ to $\sim 30\,\mathrm{Hz}$ for transfer to the Northern Hemisphere. This is achieved by removing events with very few hit DOMs. Events reconstructed as upgoing then must pass a PandelSPE logl cut, while events reconstructed as downgoing must have sufficient deposited charge in the IceCube detector volume. The net effect of these cuts remove the most poorly reconstructed events and the bulk of low-energy atmospheric muon events from the Southern hemisphere sky.

The exact event requirements to pass the Muon Filter are as follows:

- **IC79**
  - Base cut:

$$N_{\mathrm{ch}} \geq 8 \text{ and } (N_{\mathrm{ch}} \geq 10 \text{ or } \theta_{\mathrm{LF}} > 70^{\circ})$$

  - Zenith cuts:

$$[\theta_{\mathrm{SPE1}} \leq 60^{\circ} \text{ and } \log_{10}(Q_{\mathrm{tot}}) \geq 0.6\cos(\theta_{\mathrm{SPE1}}) + 2.2]$$

$$\text{or } [(\theta_{\text{SPE1}} > 60^\circ \text{ and } \theta_{\text{SPE1}} \leq 78.5^\circ) \text{ and}$$
$$\log_{10}(Q_{\text{tot}}) \geq 3.9\cos(\theta_{\text{SPE1}}) + 0.55]$$
$$\text{or } [\theta_{\text{SPE1}} > 78.5^\circ \text{ and } \text{logl}_{\text{SPE1}}/(N_{\text{ch}} - 2) \leq 8.1]$$

- **IC86-2011** to **IC86-2014**

  - No base cut

  - Zenith cuts:

$$[\theta_{\text{SPE1}} \leq 60^\circ \text{ and } \log_{10}(Q_{\text{tot}}) \geq 0.6\cos(\theta_{\text{SPE1}}) + 2.3]$$
$$\text{or } [(\theta_{\text{SPE1}} > 60^\circ \text{ and } \theta_{\text{SPE1}} \leq 78.5^\circ) \text{ and}$$
$$\log_{10}(Q_{\text{tot}}) \geq 3.9\cos(\theta_{\text{SPE1}}) + 0.65]$$
$$\text{or } [\theta_{\text{SPE1}} > 78.5^\circ \text{ and } \text{logl}_{\text{SPE1}}/(N_{\text{ch}} - 3) \leq 8.7]$$

For events reconstructed as downgoing by the PandelSPE (1 iteration) fit ($\theta_{\text{SPE1}} \leq 78.5^\circ$), the Q_{tot} vs. $\cos(\theta_{\text{SPE1}})$ cut is visualized from the IC86-2011 selection in Figure 5.3, showing its efficacy in removing a significant fraction of atmospheric muon background. The final efficiency of these cuts for truly downgoing ν_μ signal ($\theta_{\text{truth}} < 85^\circ$) with an E^{-2} spectrum is 77% for IC79 and 69% in IC86-2011. The difference in these efficiencies is largely due to the more stringent Q_{tot} vs. $\cos(\theta_{\text{SPE1}})$ cut in IC86-2011.

5.4.2 Extremely-High Energy Filter

The EHE Filter is a simple filter passing events that surpass a deposited light cut. It is included in this analysis primarily to include very bright events that fail to pass the Muon Filter through mis-reconstruction ($\sim$0.13% of E^{-2} ν_μ signal). The EHE Filter calculates the measure of deposited light (i.e. number of photoelectrons, NPE) as the integrated charge of non-droop corrected waveforms in an event that are above its trigger threshold. Events that have NPE $> 10^{3.02}$ PE then pass the EHE

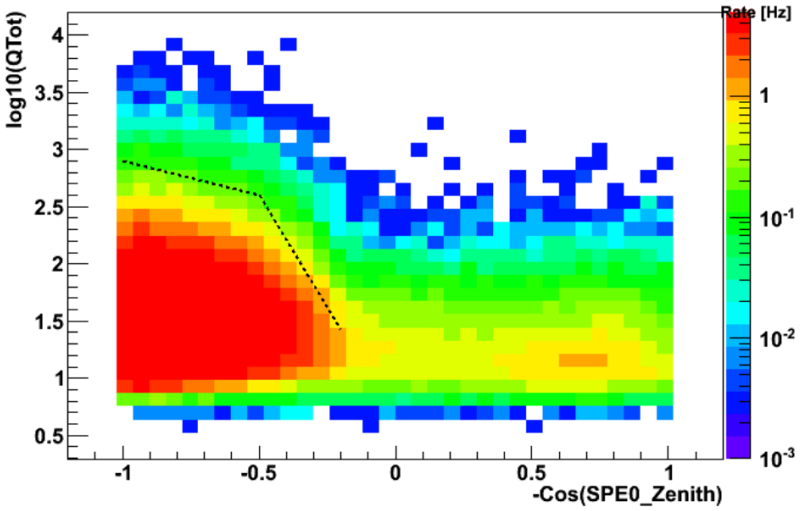

Figure 5.3: The Muon Filter Q_{tot} vs. PandelSPE (1 iteration) Zenith Cut for IC86-2011, relative to simulated atmospheric muons data from CORSIKA.

Filter, yielding 1.7 Hz of data in IC79 and 1.8 Hz of data in IC86-2011 and IC86-2012. For data from IC86-2013 and beyond, only hits within the $[-4.4\,\mu\text{s}, +6.4\,\mu\text{s}]$ time-window around the largest measured charge hit is included in the calculation of NPE, reducing the overall NPE value and passing data rate to $\sim$1 Hz.

5.5 Muon Level 3 Selection

Events passing the Muon and EHE Filters (referred to as Level 2, or L2, data) are transfered to Northern Hemisphere data centers for further processing, applying additional reconstructions like the iterated PandelSPE and PandelMPE fits (called Offline L2 processing). This data is then processed with the Muon Level 3 (L3) Filter. This aims to reduce the total data rate further from $\sim$34 Hz to $\sim$2 Hz—removing more poorly reconstructed and low energy atmospheric muon events—so that IceCube's most advanced reconstructions can be applied to the remaining high-quality muon data set.

The majority of events from the upgoing region consist of multi-muon, edge-clipping, or low energy muons events that are mis-reconstructed to be upgoing. The

Muon L3 processing scheme therefore applies event splitting algorithms to events that pass basic quality cuts to identify and reconstruct individual muons. Additional event cuts are then applied to reduce the data rate to $\sim$2 Hz so that the advanced reconstructions can be performed.

Before event splitting, all events must pass a Q_{tot} vs AvgDistQ cut of

$$Q_{\text{tot}} > 100 \text{ or } \text{AvgDistQ} < 90\,\text{m}$$

where AvgDistQ is measured relative to the best available reconstruction from the Offline L2 processing (PandelMPE, PandelSPE, then LineFit). This cut reduces the measured upgoing data rate from 10 Hz to 3 Hz, while keeping 97% of upgoing E^{-2} ν_μ signal relative to L2. Additionally, many of the events reconstructed as upgoing in the Muon Filter are subsequently reconstructed as downgoing with the additional Offline L2 reconstructions. The IC86-2011 Muon Filter Q_{tot} vs. θ_{reco} is therefore reapplied to the downgoing data, using the best available reconstruction for θ_{reco}. The net effect of these two cuts reduces the downgoing data rate from 24 Hz to 10 Hz, while keeping 89% of downgoing E^{-2} ν_μ signal relative to L2.

Event splitting algorithms are applied on the remaining 13 Hz of data to identify individual muons in coincident muon events. For data from IC79 and IC86-2011, the *TopologicalSplitter* algorithm is applied, which connects causally connected hits into subevents. Iterating through the time-ordered series of hits, hits are considered to be causally connected if they are within 300 m in the $x-y$ plane or 255 m if hits are on the same string, and within 1 μs in time. If more than 5 hits are connected within a 4 μs time window, a *seed* cluster is formed, from which a subevent can be generated with all other causally connected hits. Separate subevents are recombined should they share any single hits, as the full hit series can be causally connected. The final output of the TopologicalSplitter algorithm is a set of subevent hit series that can then be reprocessed individually with all Offline L2 reconstructions. For data in IC86-2012 and beyond, the *HiveSplitter* algorithm, a generalized form of TopologicalSplitter, is

applied. Rather than connect hits with general $x-y$ plane and z measure limits, the set of eligible DOMs that are considered causally connected are derived from the geometry of the IceCube detector. Concentric hexagonal cylinders of strings are formed around a candidate hit; the set of DOMs on these cylinders are then limited in z (TopologicalSplitter has no limit) based on the $x-y$ distance of the strings from the candidate hit. Hits within this set of eligible DOMs and within $1\,\mu$s in time of the candidate hit are then considered causally connected. Subevents are then formed by the same process described for TopologicalSplitter, yielding sets of subevent hits that are reprocessed with Offline L2 reconstructions.

The event splitting algorithms not only split coincident events, but are also capable of cleaning noise and afterpulse hits from an event. In both cases, the quality of event reconstructions can be significantly improved. As some background events that originally reconstructed as upgoing are reconstructed as downgoing after event splitting, the quality cuts and Muon Filter $Q_{\rm tot}$ vs. $\theta_{\rm reco}$ cuts discussed above are reapplied, reducing the measured data rate by an additional $\sim$30%.

Event splitting applied to simulated neutrino signal has only a minor effect, leaving $\sim$93% of E^{-2} ν_μ unaffected. In $\sim$7% of these E^{-2} ν_μ events, the event splitting primarily splits the pulses into signal pulses, and noise and afterpulse hits, which are removed with the quality and $Q_{\rm tot}$ vs. $\theta_{\rm reco}$ cuts. The reconstructions of energy and direction in signal pulse subevents are markedly improved by removing these additional pulses. On the other hand, $\sim$0.2% of E^{-2} ν_μ events are incorrectly split into two physics events; these events are typically low energy muons that can traverse large portions of the detector without depositing detected light, or events that pass through the dust layer. The effect of these falsely split events is minimized by recombining any subevents that yield reconstructions within 5° in arrival direction.

Once event splitting, reconstruction, and recombination algorithms are applied, data is filtered through a final level of cuts to reduce the data to a final rate of $\sim$2 Hz ($\sim$1 Hz reconstructed downgoing). First, all events must pass a base quality cut of:

- **IC79** and **IC86-2011**:

$$(\text{DirectEllipse} > 2 \text{ and } N_{\text{dir}} > 6) \text{ or } \text{logl}/(N_{\text{ch}} - 3) < 7.5 \text{ or } \text{rlogl} < 8.3$$

- **IC86-2012** and beyond:

$$(\text{DirectEllipse} > 2 \text{ and } N_{\text{dir}} > 6) \text{ or } \text{logl}/(N_{\text{ch}} - 3) < 7.5 \text{ or } \text{rlogl} < 9.$$

Here, these parameters are calculated with respect to the best available Offline L2 reconstruction. In the event that LineFit is the best reconstruction, the log-likelihood is set to logl = 1000 so that these events may still participate in the event selection. Events in the downgoing region are then subject to a final Q_{tot} vs. θ_{reco} cut of:

- **IC79** and **IC86-2011**:

$$\log_{10} Q_{\text{tot}} \geq 0.27 + 13.6x - 27.6x^2 + 26.1x^3 - 9.2x^4$$

- **IC86-2012** and beyond:

$$\log_{10} Q_{\text{tot}} \geq 0.15 + 13.9x - 28.1x^2 + 26.5x^3 - 9.3x^4$$

where $x = \cos(\theta_{\text{reco}})$. Any events that fail these cuts, but have $Q_{\text{tot}} > 10^4$, are retained for further analysis.

The final set of events that pass this event selection are processed with advanced reconstructions such as PandelMPE-bootstrapped, SplineMPE, and Millipede. In total, $\sim$65% of truly downgoing E^{-2} ν_μ events that are reconstructed by SplineMPE to within 5° of their true origin (considered *well-reconstructed*) are kept relative to the L2 event selection level, while reducing the data rate by over an order of magnitude. From this sample, only events with SplineMPE reconstruction in the Southern Hemisphere sky ($\theta < 85°$, i.e. declination $< -5°$) are considered for further analysis.

5.6 Analysis Level Selection

The Muon L3 selection successfully reduces the measured downgoing data rate to $\sim$1 Hz. The data, however, is still dominated by atmospheric muons that degrade the sensitivity of the analysis to neutrinos produced in GRBs. These atmospheric muons and muon bundles largely resemble the muons produced in ν_μ CC interactions, making further parameter cuts inefficient in further reducing the background data rate while keeping large fractions of signal muons. The classification of events (i.e. background atmospheric muons or signal ν_μ generated muons) in a large multi-dimensional parameter space can be facilitated with supervised machine learning algorithms.

Supervised machine learning algorithms attempt to build statistical models for discrete or continuous categorization (i.e. regression) outputs based on a set of input parameters from example training data. When used in this event selection, the model supplies a score that represents the likelihood a given event is more likely to be a background atmospheric muon or signal ν_μ CC interaction muon based on the event's input parameterization.

The machine learning algorithm used in this analysis is known as a Boosted Decision Tree (BDT) forest, an algorithm that has been used in particle classification in previous neutrino searches from GRBs [26, 27], as well as IceCube neutrino point source searches [126, 127]. This section describes the training of BDT models to perform the final level of event selection for this analysis.

5.6.1 Preselection (Level 4)

Before training the BDT models, a preselection is applied to the data to reduce the computational load on the BDT training algorithm, and remove additional poorly reconstructed and low energy events. First, an IceTop veto cut is applied. This

removes events with 2 or more on-time IceTop hits, removing ∼9% of background data with only a 0.15% false coincidence rate in signal events (estimated from IceTop hits with time residual $-1550\,\text{ns} < t_{\text{res}} < -1000\,\text{ns}$). Events are then required to pass the following cuts, which attempt to remove further low energy and poorly reconstructed events:

- **IC79**:

$$\text{(SplineMPE rlogl} \leq 9 \text{ or } Q_{\text{tot}} > 10^4\text{) and PandelMPE Paraboloid Error} \leq 7^\circ$$
$$\text{and } (0.1c < \text{LineFit } |\vec{v}| < 1.7c) \text{ and } N_{\text{str}} > 6 \text{ and } N_{\text{ch}} > 20$$

- **IC86-2011** and beyond:

$$\text{(SplineMPE rlogl} \leq 9 \text{ or } Q_{\text{tot}} > 10^4\text{) and PandelMPE Paraboloid Error} \leq 7^\circ$$
$$\text{and } (0.1c < \text{LineFit } |\vec{v}| < 1.7c) \text{ and } N_{\text{str}} > 7 \text{ and } N_{\text{ch}} > 20.$$

Events are also required to have measured values for all parameters used in the BDT model.

An additional cut is applied to IC79, and IC86-2012 and beyond (excluding IC86-2011), where a small fraction of events pass the BDT model selection by having poorly reconstructed, but unreasonably large MuEX values; these events are typically uncontainted, edge-clipping muon events where track reconstructions are poorly constrained by the measured light deposition. Requiring the following removes these events:

- **IC79**:

$$\text{SplineMPE } N_{\text{dir}} > 14 \text{ or SplineMPE MuEX} < 3 \times 10^6$$

- **IC86-2012** and beyond:

$$\text{SplineMPE } N_{\text{dir}} > 15 \text{ or SplineMPE MuEX} < 3 \times 10^6.$$

The data from IC86-2011 was excluded from this cut as the effect of these large MuEX events was much less pronounced in this year of data. As IC86-2011 was analyzed before the other years of data without this cut and its effect would be less useful, it was decided to not re-analyze this data with this addition cut. The final result of all these precuts is to reduce the measured data rate by ∼40% while keeping ∼96% of well-reconstructed E^{-2} ν_μ signal relative to the Muon L3 event level.

5.6.2 Boosted Decision Tree Selection (Level 5)

The straight cuts from trigger level data to L4 sucessfully reduce the data rate to under 1 Hz from the Southern hemisphere sky—over a factor of 10^3 reduction—while keeping ∼45% of all well-reconstructed E^{-2} ν_μ signal muons that trigger the IceCube detector. This sample is still dominated by atmospheric muons that on a per-parameter basis are hard to distinguish from muons produced in cosmic ν_μ CC interactions. The classification of data in a large multivariate parameter-space, however, is a classic problem in machine learning. Decision trees and their extension, boosted decision tree forests (BDT forests, commonly called simply BDTs), have become popular algorithms for particle identification in IceCube, and are now the *de facto* means to separate a desired signal from the atmospheric muon background. Though decision trees and forests can be used in continuous and multivariate regressions, only their application to discrete, binomial categorization problems is discussed. The application of BDT models to reduce the background data rate to ∼2 mHz, where this analysis shows its optimal sensitivity to ν_μ signal, is then described.

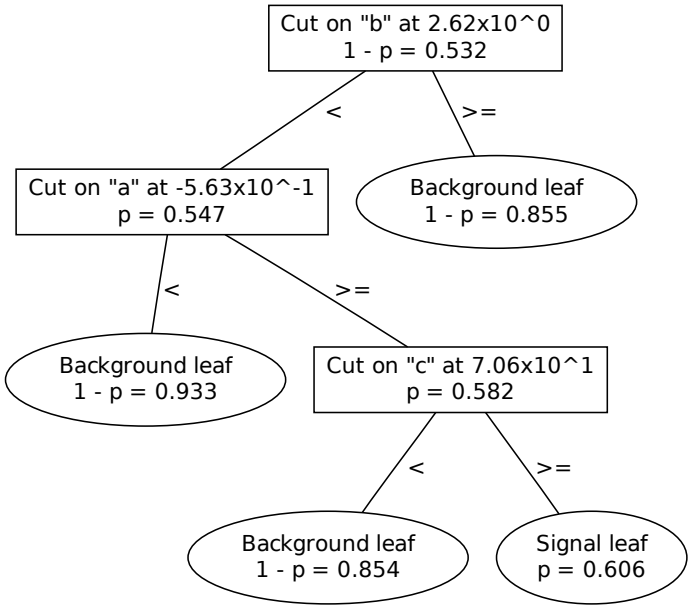

Figure 5.4: An example decision tree presented in [128]. Split nodes are indicated with boxes, while leaf nodes are indicated by ellipses.

5.6.2.1 Decision Trees

Decision trees classify data through a series of splits in single input parameters at each *split* node. The tree of split nodes terminate in *leaf* nodes, each of which considered either a *signal leaf* or *background leaf* (the two categories considered). The category of any input data is simply determined by whether it reaches a signal or background leaf node. An example decision tree is shown in Figure 5.4. The signal purity p at any node is determined as the ratio of total signal weight at that node $\sum_s w_s$ to the total signal and background weight $W = \sum_s w_s + \sum_b w_b$:

$$p = \frac{\sum_s w_s}{\sum_s w_s + \sum_b w_b}. \tag{5.9}$$

A given leaf node is a signal leaf if $p \geq 0.5$; conversely the leaf node is considered a background node if $1 - p > 0.5$.

Decision trees are created through a supervised learning process called *training*. Known signal and background data are split into both *training* and *testing* data samples to create and validate the decision tree, respectively. Starting at a root node, each node is split recursively until typical stopping criterion are reached in the training data sets:

- A specified maximal tree *depth* (i.e. number of sequential cuts).
- A given node has only signal or background events.
- A given node has fewer than a specified minimum number of total events.

The precise cut made at each node is determined to maximize the possible signal and background separation in the tree. The separation at a given node can be scored by the Gini index $S_G(p) = p(1-p)$. For a proposed variable cut that yields a left node with total weight W_L and purity p_L and a right node with total weight W_R and purity p_R, the Gini separation gain is quantified as

$$\Delta S_G = W \cdot S_G(p) - W_R \cdot S_G(p_R) - W_L \cdot S_G(p_L). \tag{5.10}$$

The trained cut at each node is then selected as that which maximizes this Gini separation gain from all possible cut parameters and cut values. To reduce the computational load on this cut determination, the number of cuts considered per parameter is typically limited to a certain number of fixed values.

5.6.2.2 Boosted and Randomized Decision Tree Forests

The power of a given decision tree in classifying testing data is dependent on the tree depth and how closely the training data resembles the underlying data PDFs: shallow trees can misclassify rare events, while deep trees can become *overtrained* to statistical artifacts in the training samples. In both cases, the accuracy of the

single decision tree model in classifying subsequent data is degraded. To mitigate overtraining while increasing tree depth, an ensemble of decision trees, called a *forest*, can be employed to score the signal-ness or background-ness of an event in aggregate. Supposing each tree m in the forest has a relative weight α_m, the score of an event i can be defined as the weighted average of per-tree classifications $s_{i,m}$ as

$$s_i = \frac{\sum_m s_{i,m}\alpha_m}{\sum_m \alpha_m}. \tag{5.11}$$

This score is normalized in the range $[-1, +1]$ by defining the per-event, per-tree score to be -1 if that tree classifies the event as background and $+1$ if the event is classified as signal.

One common means of improving forest classification of rare events is through the technique of *boosting*. This technique artificially increases the weights of misclassified events in one tree for the training of the next tree. The boosting algorithm used in this event selection is *AdaBoost* [129]. For a given tree m that classifies an event i with true class y_i and weight $w_{i,m}$ as $s_{i,m}$, the total error e_m in the tree is be calculated as

$$e_m = \frac{\sum_i w_{i,m} I(s_{i,m}, y_i)}{\sum_i w_{i,m}} \tag{5.12}$$

where the error function has been defined as

$$I(s, y) = \begin{cases} 0, \; s = y \\ 1, \; s \neq y. \end{cases} \tag{5.13}$$

The weight of the tree used in event scoring, also called the boost factor of the tree, is calculated as

$$\alpha_m = \beta \ln\left(\frac{1 - e_m}{e_m}\right) \tag{5.14}$$

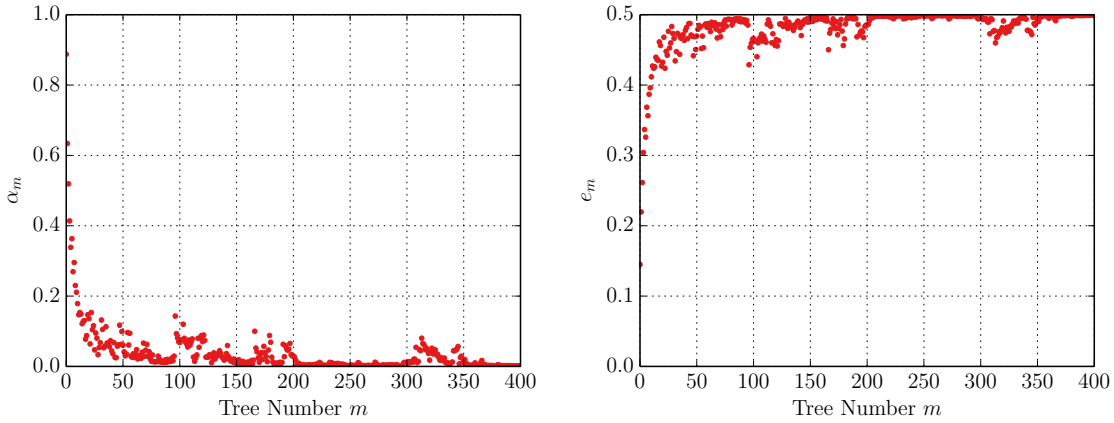

Figure 5.5: IC86-I BDT boost factor (left) and error rate (right) as a function of tree number in the model training. As the trees become more specialized in classifying rare events, they become no better than chance in classifying the bulk of events, resulting in lower tree weight.

where β is a user-specified boost strength, typically in the range (0, 1]. The event weights in the next tree $m + 1$ are boosted by

$$w_{i,m+1} = w_{i,m} e^{\alpha_m I(s_{i,m}, y)}, \tag{5.15}$$

and renormalized such that $\sum_i w_{i,m+1} = 1$. These weights are then used to determine tree cuts using the same method discussed in Section 5.6.2.1. As the weights are never reset to the values in the first decision tree of the sequence, the effect of the boosting is cumulative. Trees trained later in the sequences are thus increasingly specialized in categorizing rare events, while early trees are more successful at categorizing the bulk of signal and background events, demonstrated with the BDT forest boost factors and total errors shown in Figure 5.5.

Overtraining in decision tree forests can be further mitigated by randomization in the decision tree training. This randomization typically comes in two types:

- **Event Sample Randomization**: A random sample of the training events at a fixed total fraction are used to train each decision tree.

- **Cut Parameter Randomization**: At each split node, only a random sample of all input parameters are considered when determining the node split.

Both these types can be used to reduce the prominance of statistical abnormalities in the training data, to which a single decision trees can become overtrained, as each decision tree is trained under constrained conditions. Further, this randomization can be used to reduce overtraining in BDTs. When randomization is used in decision tree forests, each tree is given equal weight in event scoring; in BDTs, randomization has no additional effect in tree weighting.

The final method to reduce overtraining in a decision tree is a technique called *pruning*, which removes split nodes that do not add significantly to the signal and background separation of the tree. Pruning occurs when the child nodes of some split node are destroyed, and the split node itself becomes a leaf node. First, *same split* pruning is applied to every tree. This pruning finds split nodes that yield two leaf nodes, and removes the split if the two leaf nodes are of the same class; this is repeated in the decision tree until no such splits remain. Additionally, *cost complexity* pruning can be applied to decision trees. The pruning cost of a split node can be calculated as $\rho = \Delta S_G/(n_{\text{leaf}} - 1)$ where n_{leaf} is the number of leaf nodes in the subtree below the split node. The pruning cost is calculated for all split nodes, with pruning occuring on the smallest ρ split node if ρ is below a user-specified threshold. As the pruning changes the number of leaf nodes in the tree, the pruning costs of the remaining nodes are recalculated after each pruning occurs.

5.6.2.3 Boosted Decision Tree Forest Validation

Having trained a BDT on an sample of training signal and background events, one must evaluate the amount of overtraining that may have occured. One method involves comparing BDT event score distributions in both training and testing data sets through a Kolmogorov-Smirnov (KS) test [130, 131], which quantifies discrepan-

cies in these distributions by calculating the probability that two distributions are the result of the same underlying PDF (null hypothesis). Given two distributions with sizes m and n, the maximum difference in their normalized cumulative distributions functions $F(s)$ is found:

$$D_{m,n} = \max_s \left| F_m^1(s) - F_n^2(s) \right|. \tag{5.16}$$

The null hypothesis is rejected at the α level when $\sqrt{mn/(m+n)}D_{m,n} = L(\alpha)$, where $L(\alpha)$ is the limiting cumulative distribution function

$$L(\alpha) = 1 - 2\sum_{k=1}^{\infty}(-1)^{k-1}e^{-2k^2\alpha^2}. \tag{5.17}$$

BDT models trained in this dissertation are required to have a KS test p-value is $> 5\%$ for both signal and background samples.

5.6.2.4 Analysis Boosted Decision Tree Forest Training

The final event sample of the analysis is obtained by training a randomized BDT model on L4 data for each season of analysis, and removing all data below a selected BDT score value, which effectively removes the most background-like events. The background training and testing data samples are taken from IceCube data recorded more than 2 hours from the gamma-ray emission of any GRB in the analyzed sample; from this data, a 5% random sample from the entire year of data forms the training sample, and a 25% random sample forms the testing sample. The signal sample is taken from well-reconstructed ν_μ simulation (the SplineMPE reconstruction is within 5° of the true ν_μ direction); the sample is split in half to obtain the training and testing samples. The signal sample is weighted to an astrophysical E^{-2} spectrum to reduce bias in the selection sensitivity to any particular GRB neutrino emission spectrum.

A total of 18 input parameters are used in the BDT model. These parameters are based on those used in IceCube Southern Hemisphere sky point source event selection BDTs [127], though modified for use in prompt ν GRB search. Primarily, this means including zenith and energy reconstruction values in the BDT model, which are powerful in separating low-energy background atmospheric muons from signal muons from ν_μ CC interactions. These parameters were excluded in the point source BDT due to artifacts that appeared in their background energy and space PDFs, as a function of reconstructed zenith. As the search for prompt neutrinos from GRBs is more constrained in space and time than the point source analysis, and the energy and space PDFs in the final analysis are generalized for the entire Southern Hemisphere sky, these artifacts do not appear, allowing these parameters to be included in the BDT models.

The precise input parameters used in the BDT model are listed below. Distributions of these parameters are shown only for the IC86-2011 year, as the the other years are nearly identical. Simulated data does not feature IceTop simulation, and thus can only be compared to IceCube data without the veto applied. Atmospheric μ simulation from CORSIKA is weighted to the Gaisser-H4a spectrum [132], while atmospheric ν_μ simulation is weighted to the Honda et al. (2007) model [133]. Signal ν_μ is weighted to an E^{-2} spectrum, defining $dN/dE = (E/\mathrm{GeV})^{-2} \times 10^{-8}\,\mathrm{GeV}^{-1}\,\mathrm{cm}^{-2}\,\mathrm{s}^{-1}\,\mathrm{sr}^{-1}$ in the following figures.

- COG ρ^2 (`cog_rho2`):

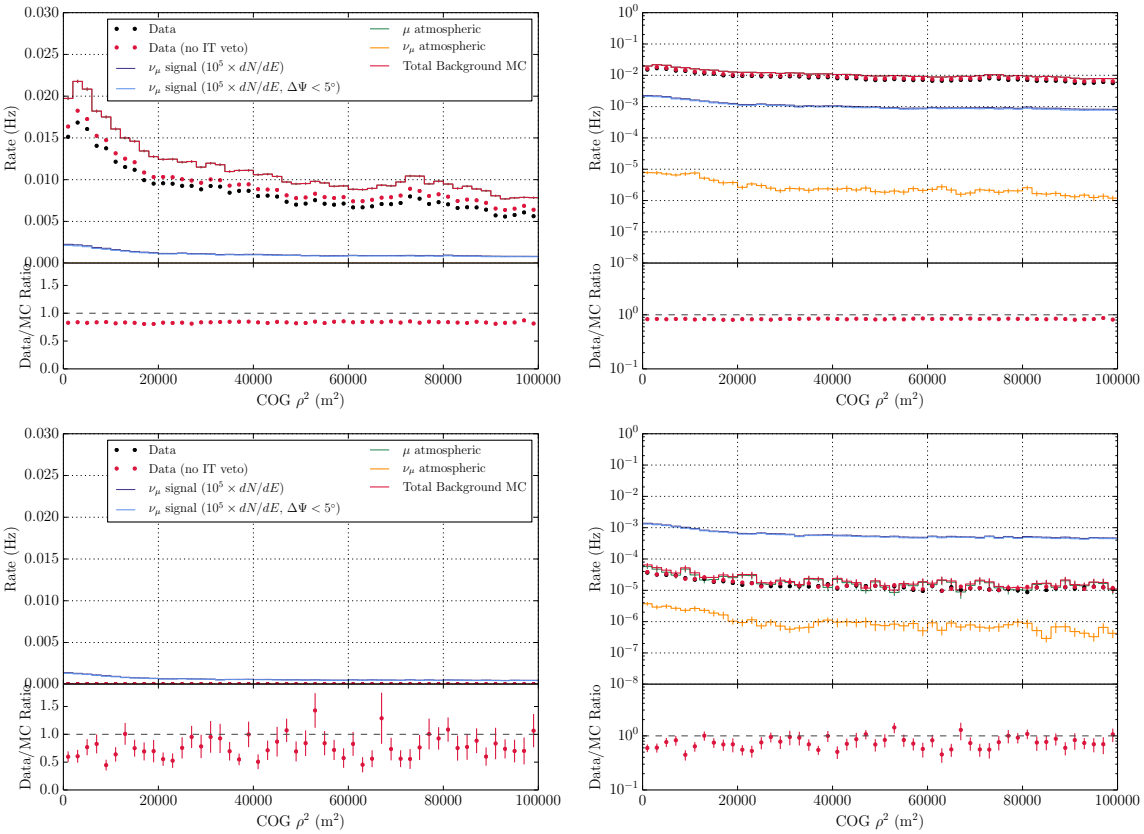

Figure 5.6: IC86-2011 COG ρ^2 distributions for IceCube data and simulation at the L4 (top) and final event sample level (bottom), in both linear (left) and log (right) scales. The ratio of IceCube data without the IceTop veto to total background simulation is shown below each plot.

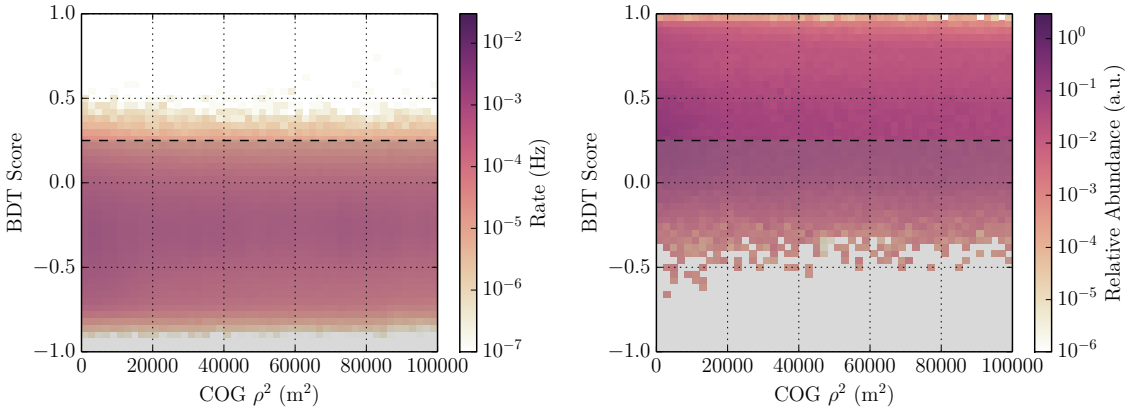

Figure 5.7: IC86-2011 COG ρ^2 vs. BDT score distributions for IceCube data (left) and simulated ν_μ weighted to an E^{-2} spectrum. The final BDT score cut is indicated by the dashed line.

- COG z (`cog_z`):

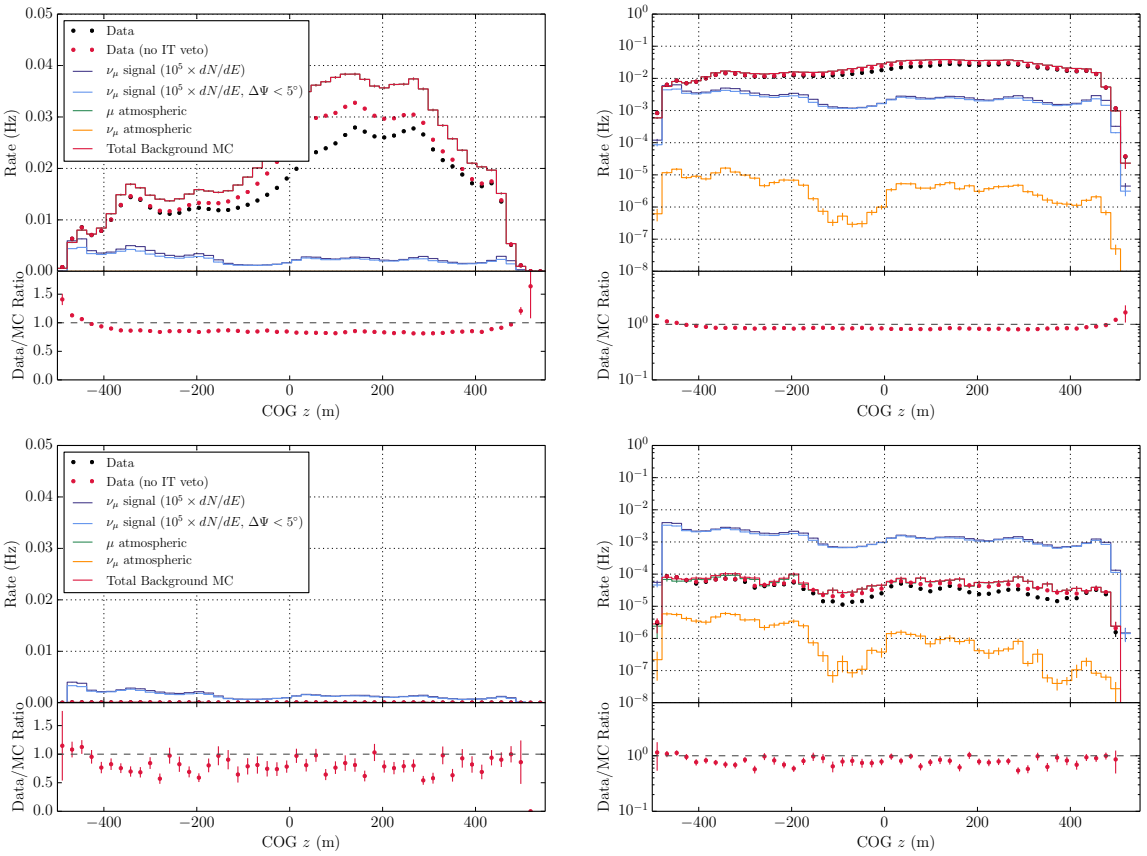

Figure 5.8: IC86-2011 COG z distributions for IceCube data and simulation at the L4 (top) and final event sample level (bottom), in both linear (left) and log (right) scales. The ratio of IceCube data without the IceTop veto to total simulation is shown below each plot.

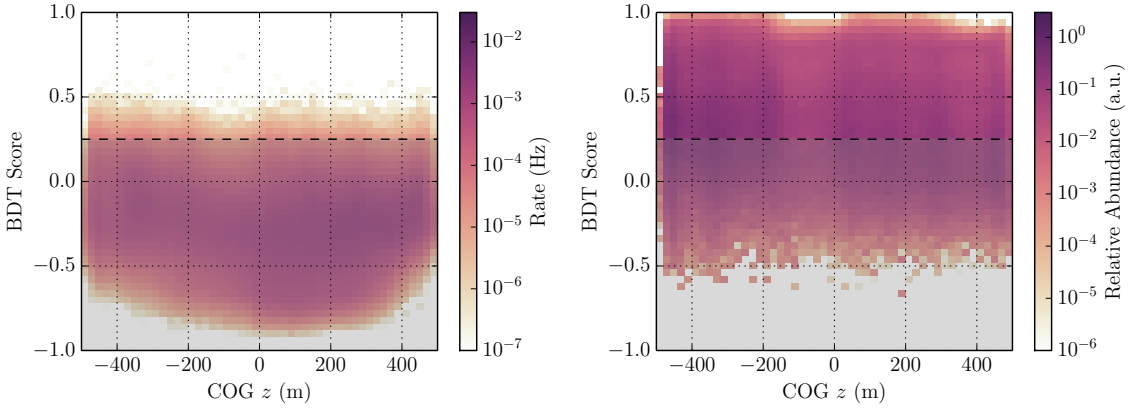

Figure 5.9: IC86-2011 COG z vs. BDT score distributions for IceCube data (left) and simulated ν_μ weighted to an E^{-2} spectrum. The final BDT score cut is indicated by the dashed line.

- cos(SplineMPE Zenith) (`cos_splinempe_zenith`):

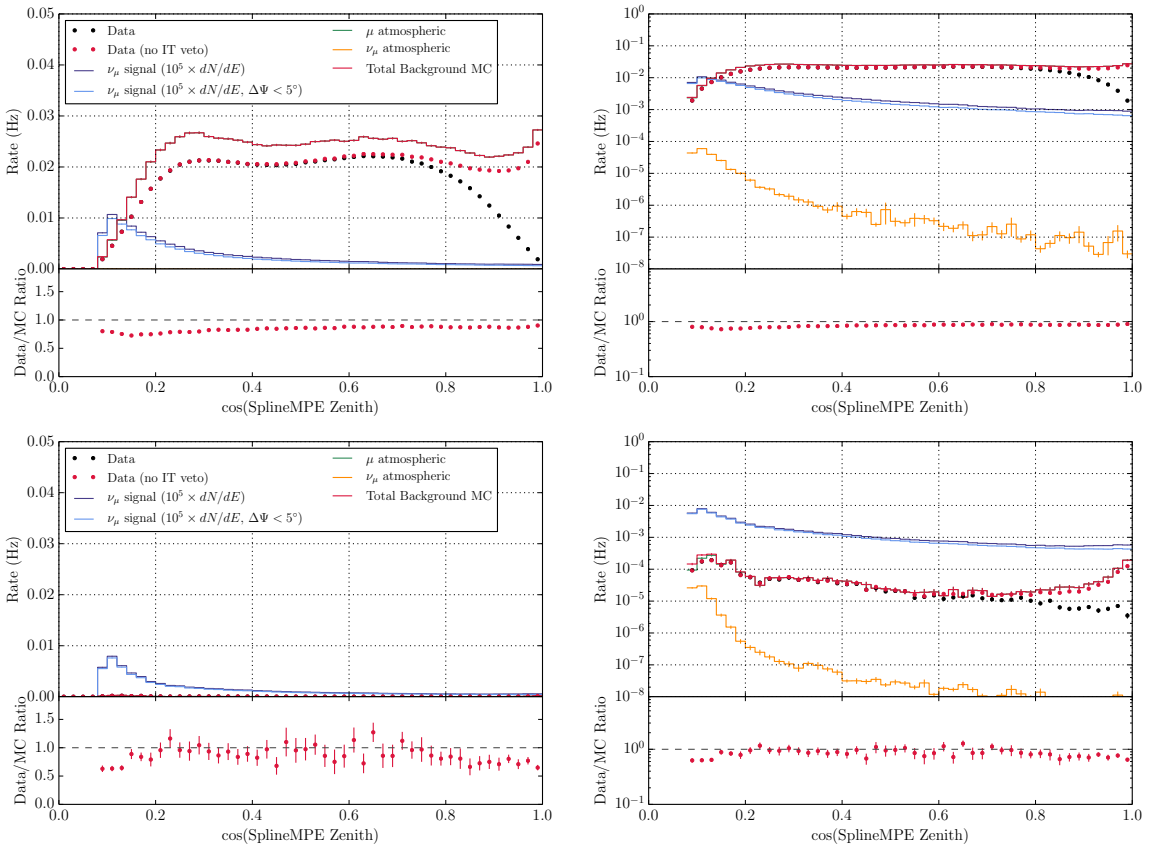

Figure 5.10: IC86-2011 cos(SplineMPE Zenith) distributions for IceCube data and simulation at the L4 (top) and final event sample level (bottom), in both linear (left) and log (right) scales. The ratio of IceCube data without the IceTop veto to total simulation is shown below each plot.

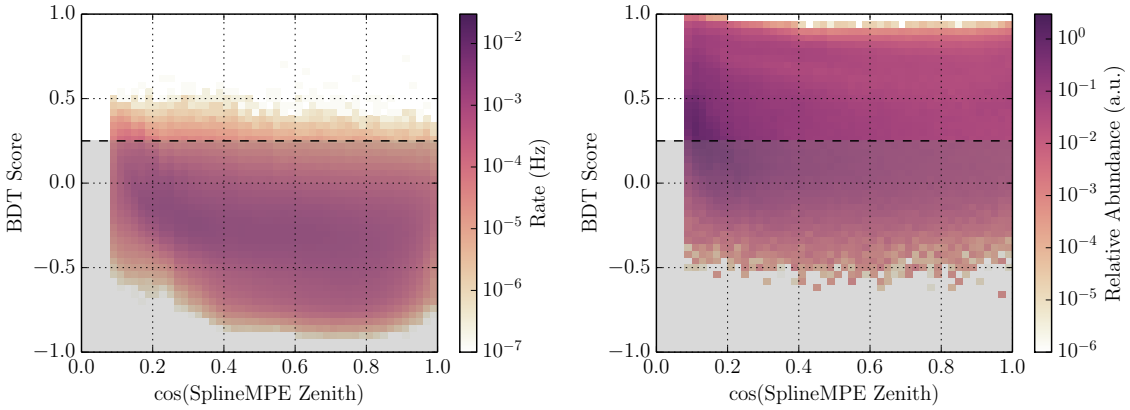

Figure 5.11: IC86-2011 cos(SplineMPE Zenith) vs. BDT score distributions for IceCube data (left) and simulated ν_μ weighted to an E^{-2} spectrum. The final BDT score cut is indicated by the dashed line.

- LineFit $|\vec{v}|$ (`lf_v`):

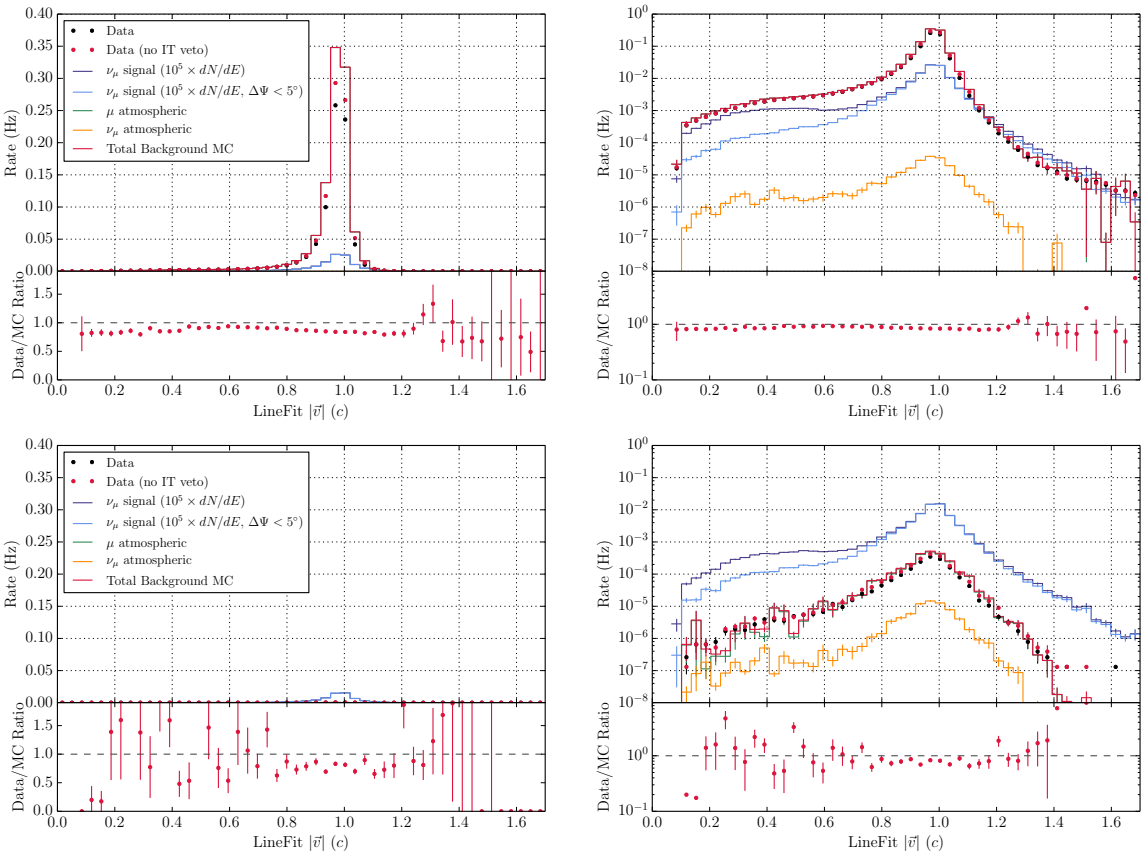

Figure 5.12: IC86-2011 LineFit $|\vec{v}|$ distributions for IceCube data and simulation at the L4 (top) and final event sample level (bottom), in both linear (left) and log (right) scales. The ratio of IceCube data without the IceTop veto to total background simulation is shown below each plot.

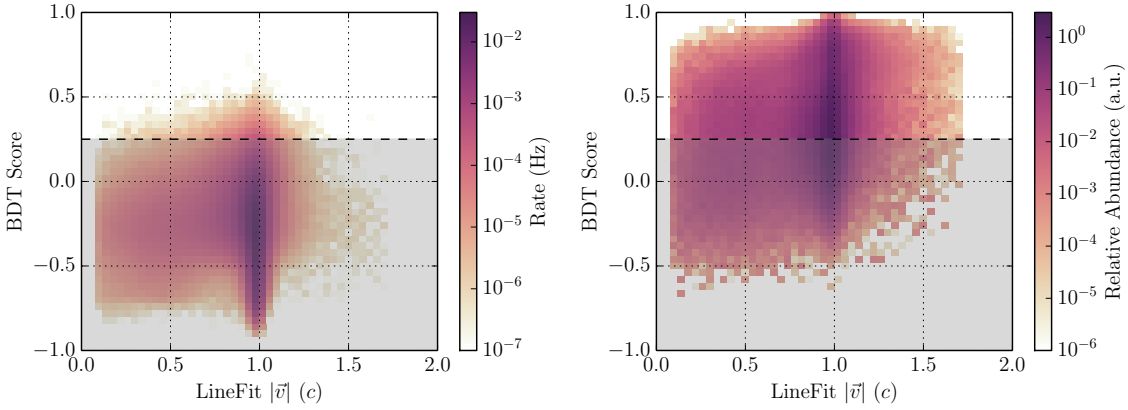

Figure 5.13: IC86-2011 LineFit $|\vec{v}|$ vs. BDT score distributions for IceCube data (left) and simulated ν_μ weighted to an E^{-2} spectrum. The final BDT score cut is indicated by the dashed line.

- $\log_{10}$(SplineMPE MuEX) (`log10_splinempe_muex_energy`):

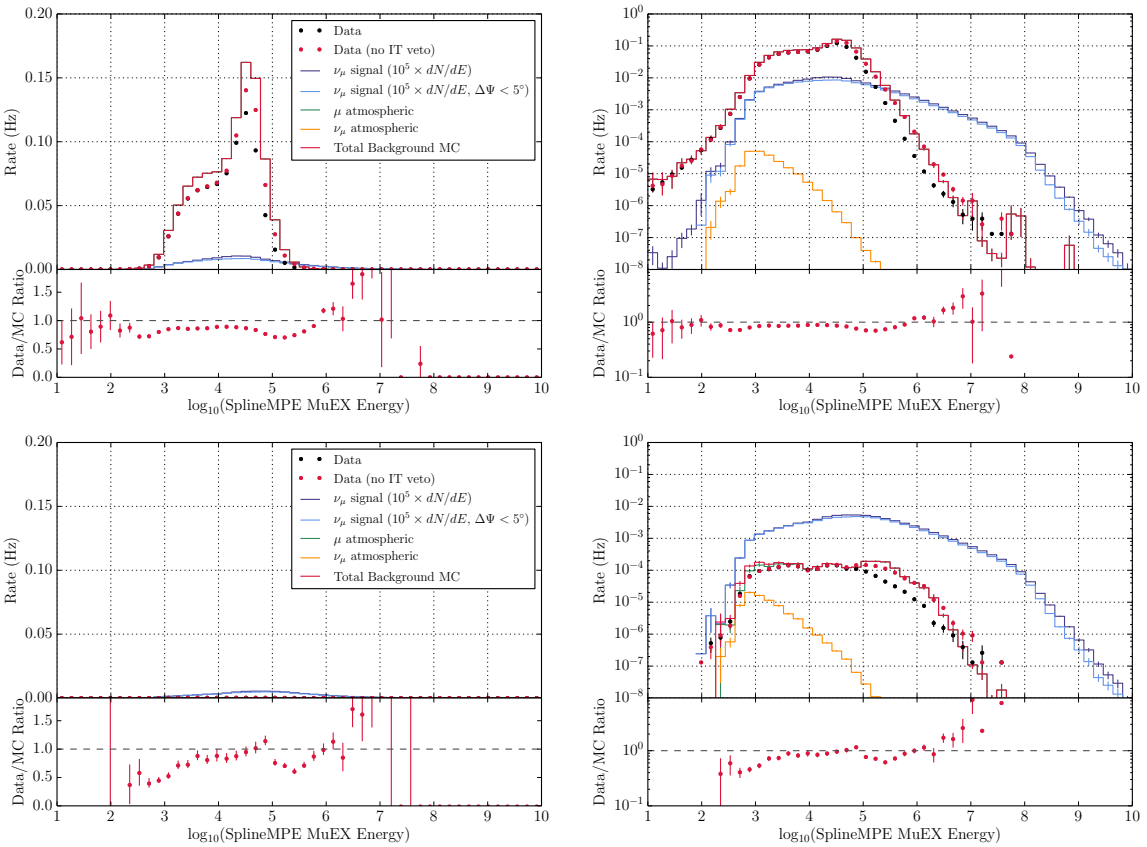

Figure 5.14: IC86-2011 $\log_{10}$(SplineMPE MuEX) distributions for IceCube data and simulation at the L4 (top) and final event sample level (bottom), in both linear (left) and log (right) scales. The ratio of IceCube data without the IceTop veto to total background simulation is shown below each plot.

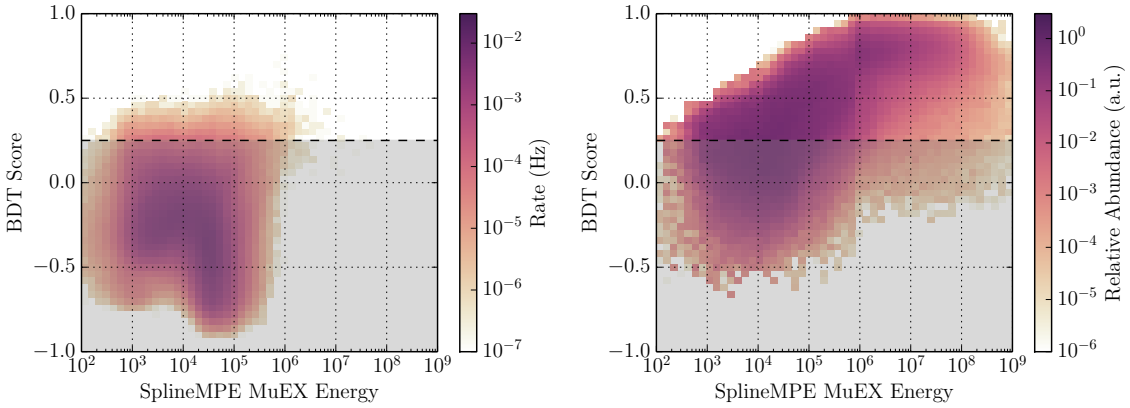

Figure 5.15: IC86-2011 $\log_{10}$(SplineMPE MuEX) vs. BDT score distributions for IceCube data (left) and simulated ν_μ weighted to an E^{-2} spectrum. The final BDT score cut is indicated by the dashed line.

- Millipede dE/dx Smoothness Likelihood rlogl (`milli_llh_rlogl`):

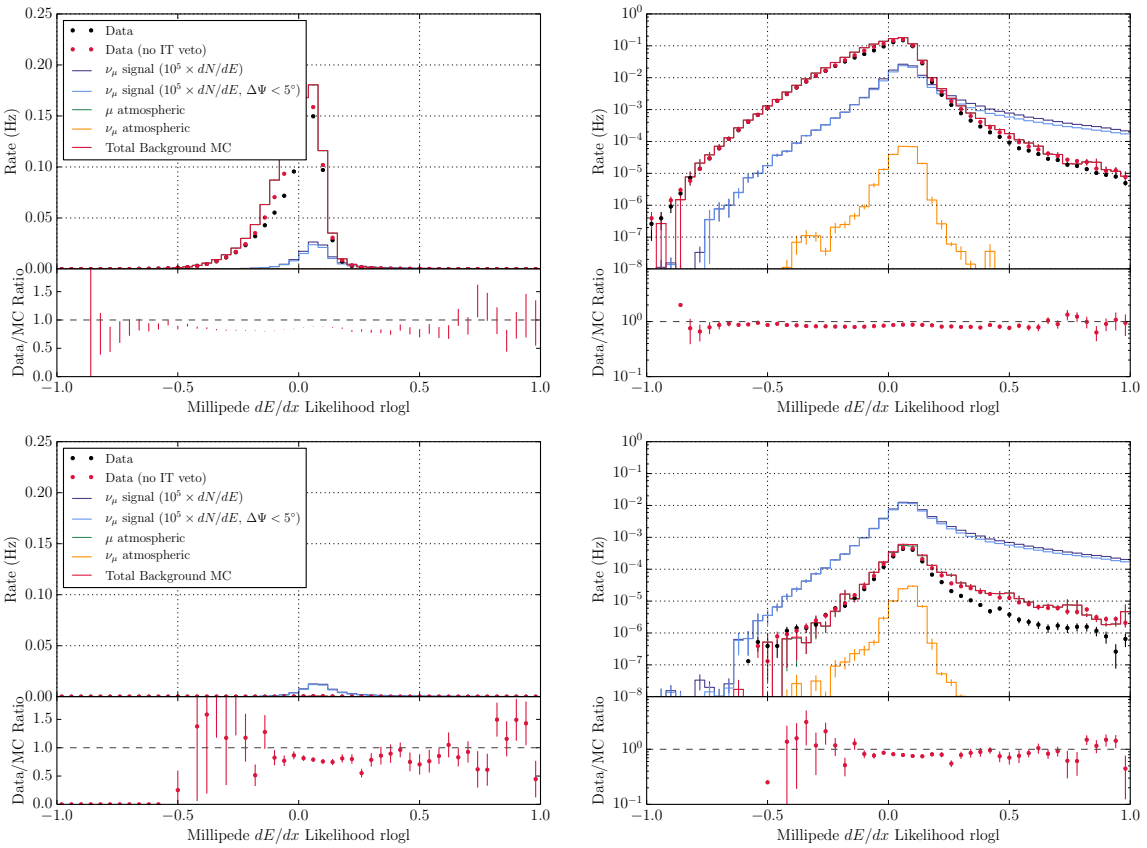

Figure 5.16: IC86-2011 Millipede dE/dx smoothness likelihood rlogl distributions for IceCube data and simulation at the L4 (top) and final event sample level (bottom), in both linear (left) and log (right) scales. The ratio of IceCube data without the IceTop veto to total background simulation is shown below each plot.

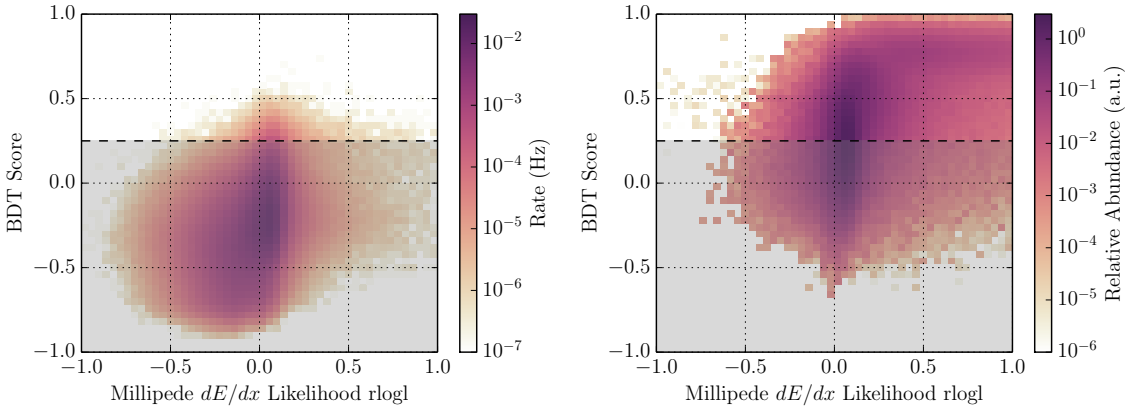

Figure 5.17: IC86-2011 Millipede dE/dx smoothness likelihood rlogl vs. BDT score distributions for IceCube data (left) and simulated ν_μ weighted to an E^{-2} spectrum. The final BDT score cut is indicated by the dashed line.

- Millipede $(dE/dx)_{\text{max}} - (dE/dx)_{\text{median}}$ (`millipede_max_madE`):

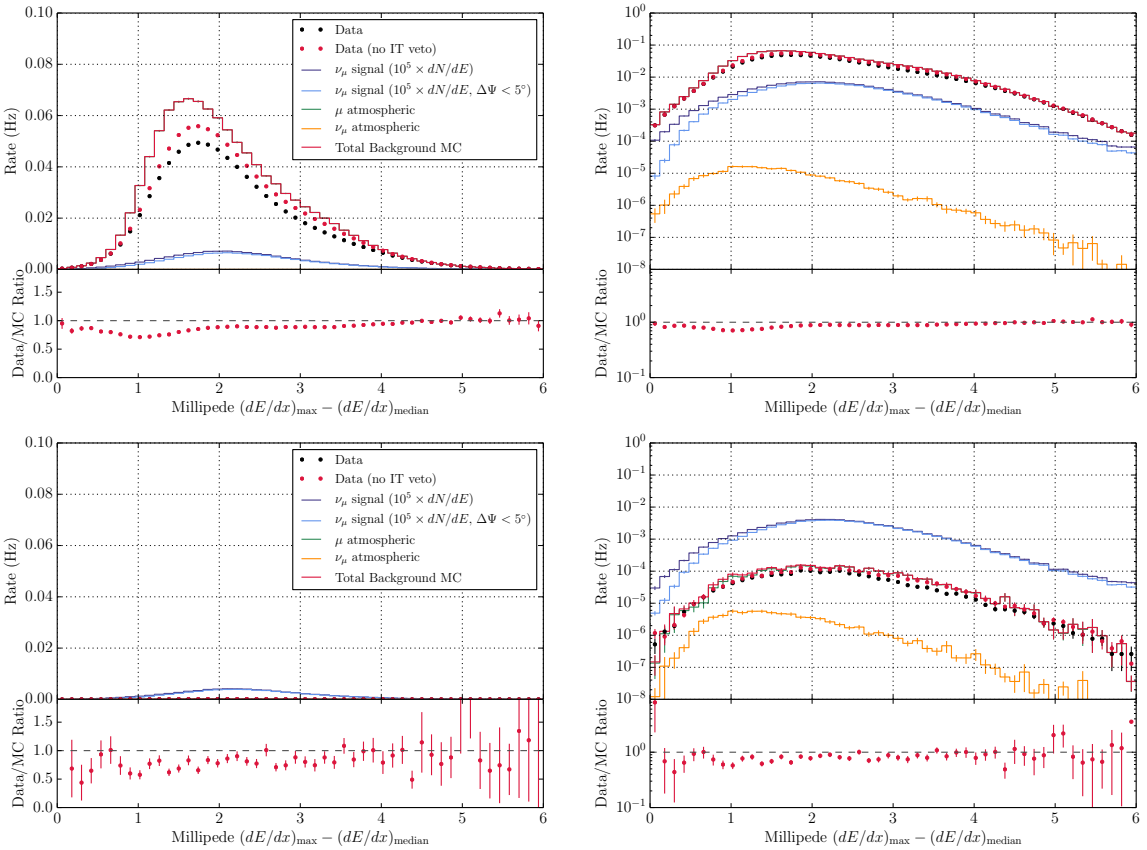

Figure 5.18: IC86-2011 Millipede $(dE/dx)_{\text{max}} - (dE/dx)_{\text{median}}$ distributions for IceCube data and simulation at the L4 (top) and final event sample level (bottom), in both linear (left) and log (right) scales. The ratio of IceCube data without the IceTop veto to total background simulation is shown below each plot.

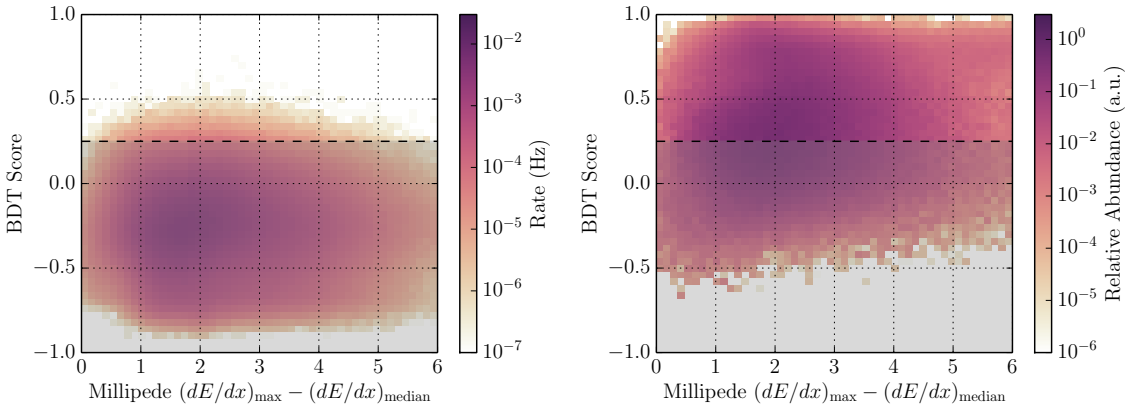

Figure 5.19: IC86-2011 Millipede $(dE/dx)_{\text{max}} - (dE/dx)_{\text{median}}$ vs. BDT score distributions for IceCube data (left) and simulated ν_μ weighted to an E^{-2} spectrum. The final BDT score cut is indicated by the dashed line.

- PandelMPE Paraboloid Angular Uncertainty (`mpeparab_err`):

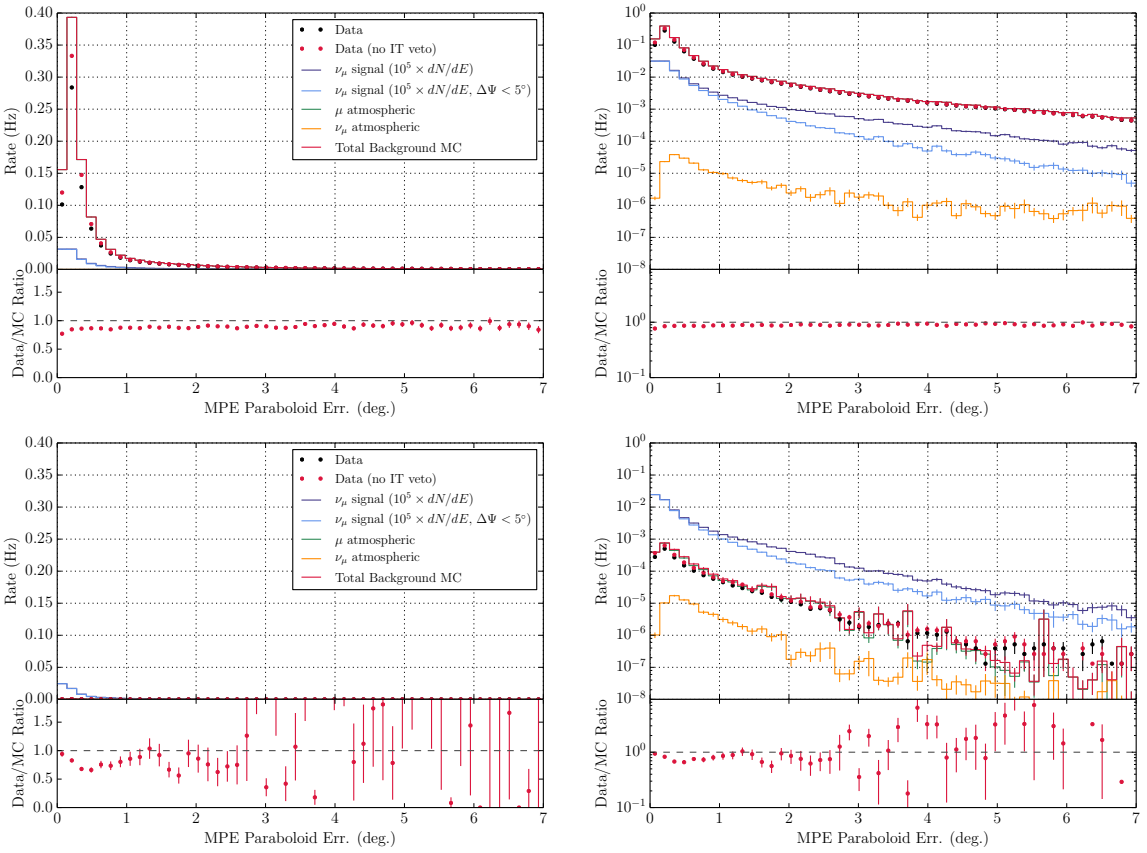

Figure 5.20: IC86-2011 PandelMPE Paraboloid angular uncertainty distributions for IceCube data and simulation at the L4 (top) and final event sample level (bottom), in both linear (left) and log (right) scales. The ratio of IceCube data without the IceTop veto to total background simulation is shown below each plot.

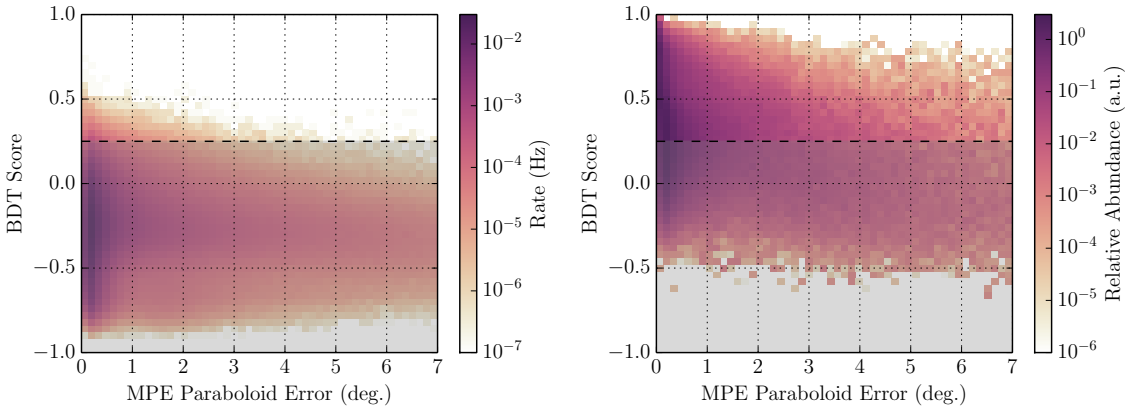

Figure 5.21: IC86-2011 PandelMPE Paraboloid angular uncertainty vs. BDT score distributions for IceCube data (left) and simulated ν_μ weighted to an E^{-2} spectrum. The final BDT score cut is indicated by the dashed line.

- SplineMPE $N_{\text{early}}/N_{\text{dir}}$ (`n_early_n_dir_e`):

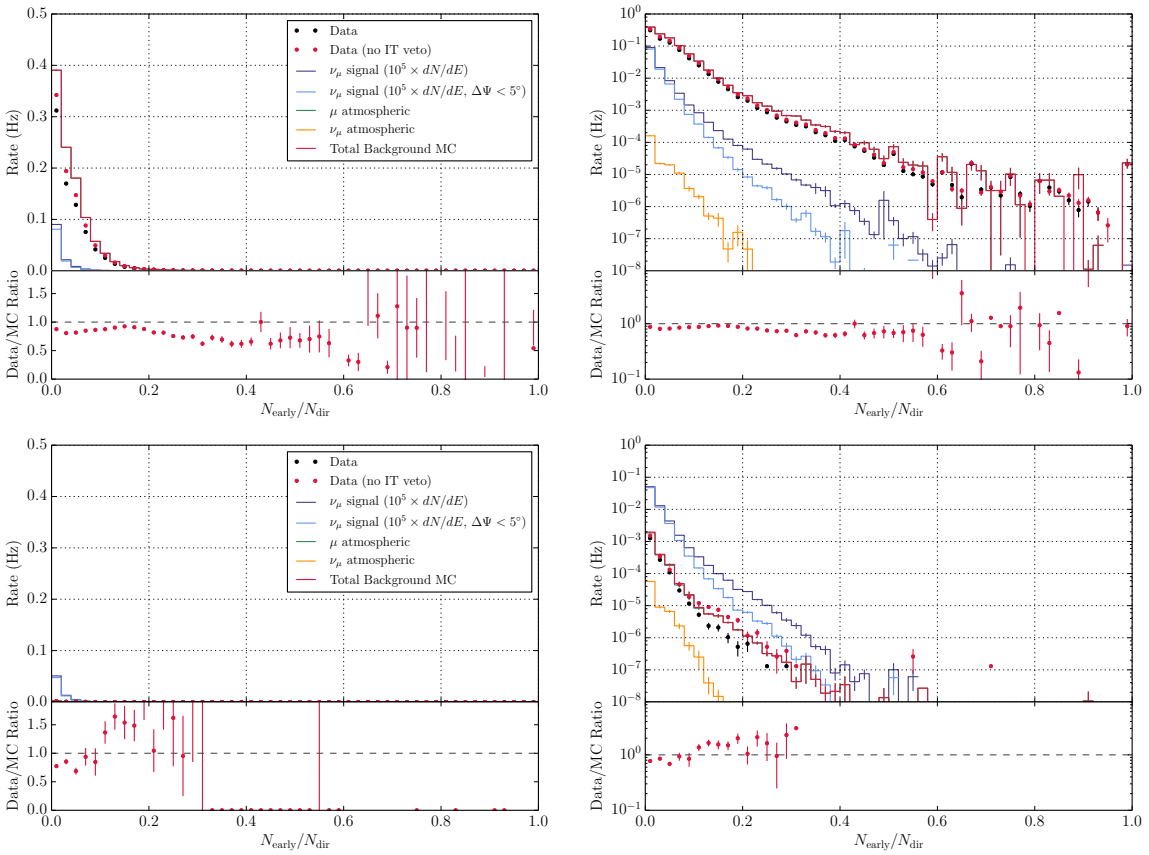

Figure 5.22: IC86-2011 SplineMPE $N_{\text{early}}/N_{\text{dir}}$ distributions for IceCube data and simulation at the L4 (top) and final event sample level (bottom), in both linear (left) and log (right) scales. The ratio of IceCube data without the IceTop veto to total background simulation is shown below each plot.

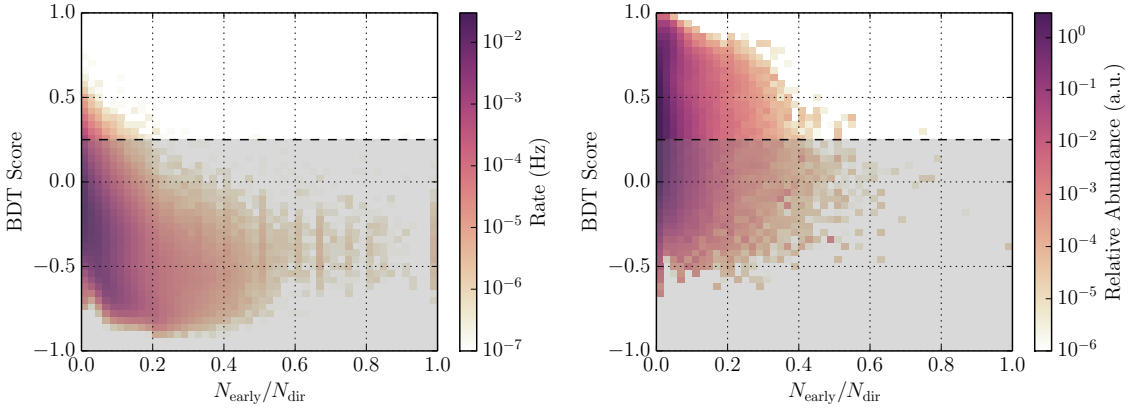

Figure 5.23: IC86-2011 SplineMPE $N_{\text{early}}/N_{\text{dir}}$ vs. BDT score distributions for IceCube data (left) and simulated ν_μ weighted to an E^{-2} spectrum. The final BDT score cut is indicated by the dashed line.

- SplineMPE Azimuth Map (`splinempe_az_map`):

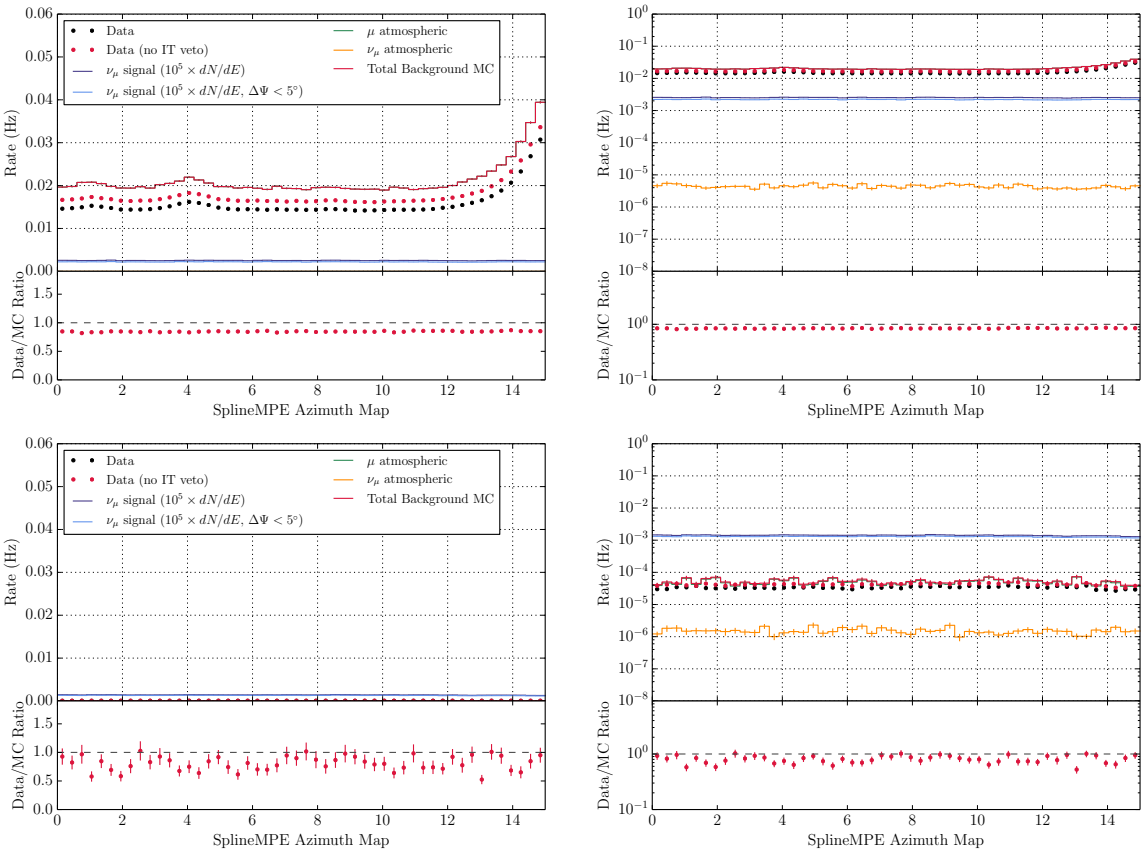

Figure 5.24: IC86-2011 SplineMPE Azimuth Map distributions for IceCube data and simulation at the L4 (top) and final event sample level (bottom), in both linear (left) and log (right) scales. The ratio of IceCube data without the IceTop veto to total background simulation is shown below each plot.

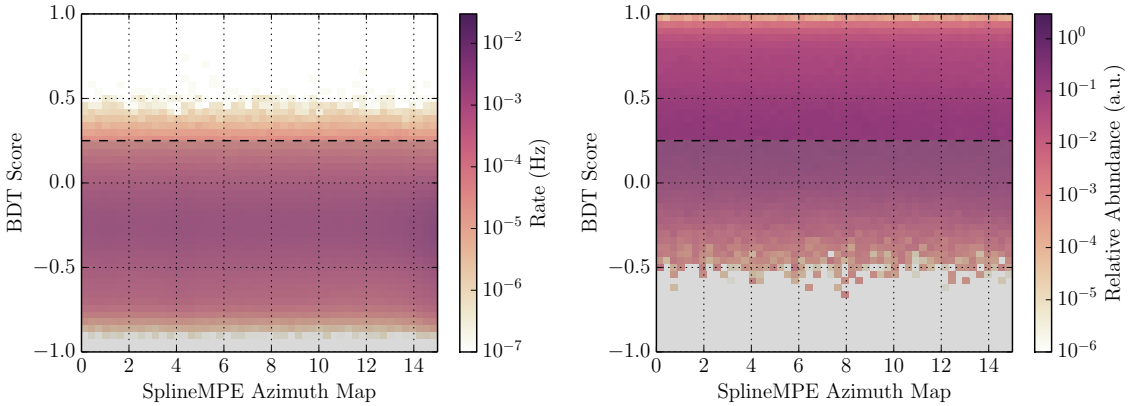

Figure 5.25: IC86-2011 SplineMPE Azimuth Map vs. BDT score distributions for IceCube data (left) and simulated ν_μ weighted to an E^{-2} spectrum. The final BDT score cut is indicated by the dashed line.

- SplineMPE Cramer-Rao Angular Uncertainty (`splinempe_cr_err`):

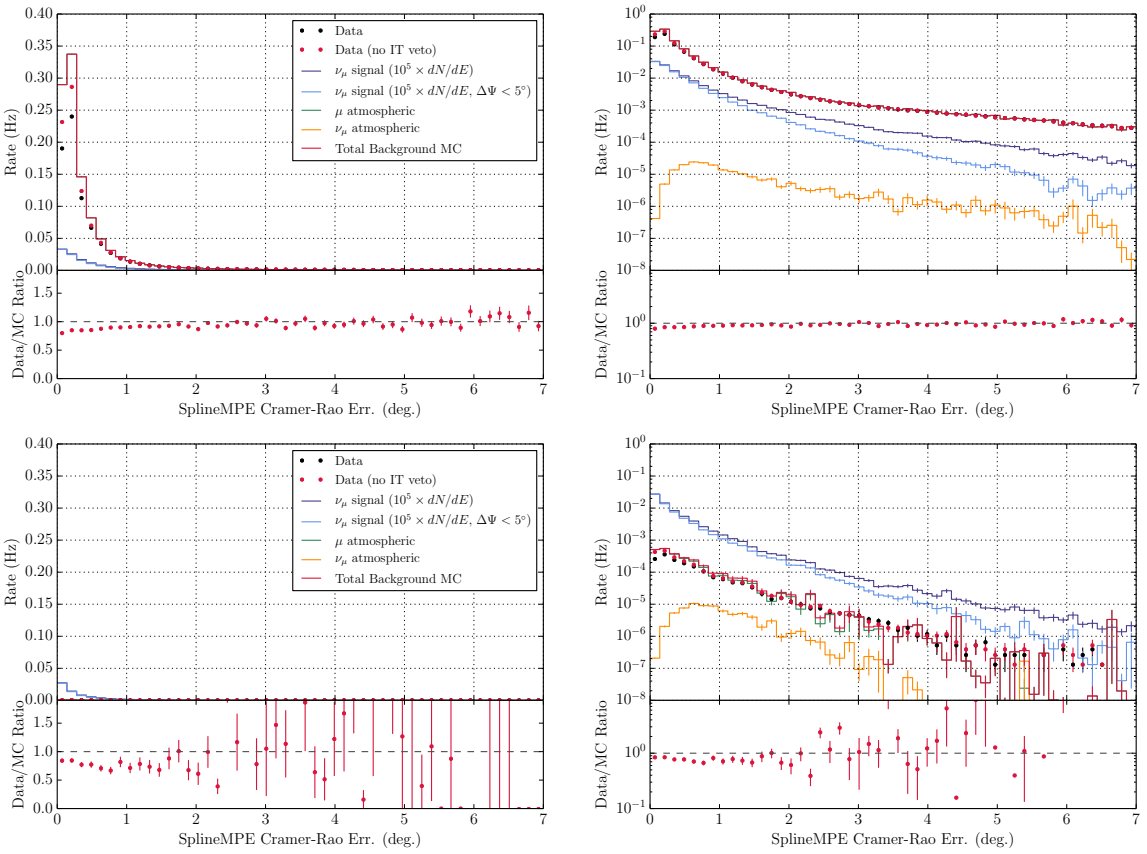

Figure 5.26: IC86-2011 SplineMPE Cramer-Rao angular uncertainty distributions for IceCube data and simulation at the L4 (top) and final event sample level (bottom), in both linear (left) and log (right) scales. The ratio of IceCube data without the IceTop veto to total background simulation is shown below each plot.

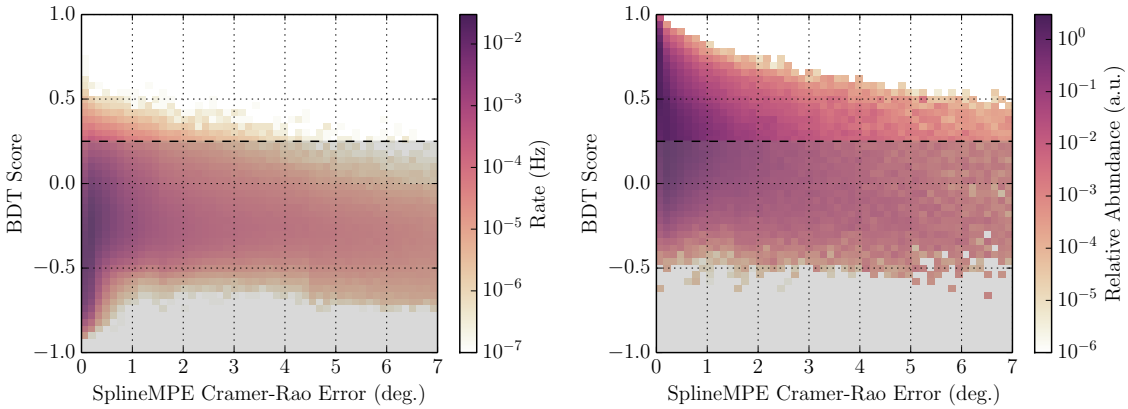

Figure 5.27: IC86-2011 SplineMPE Cramer-Rao angular uncertainty vs. BDT score distributions for IceCube data (left) and simulated ν_μ weighted to an E^{-2} spectrum. The final BDT score cut is indicated by the dashed line.

- SplineMPE L_{dir} (`splinempe_l_dir_e`):

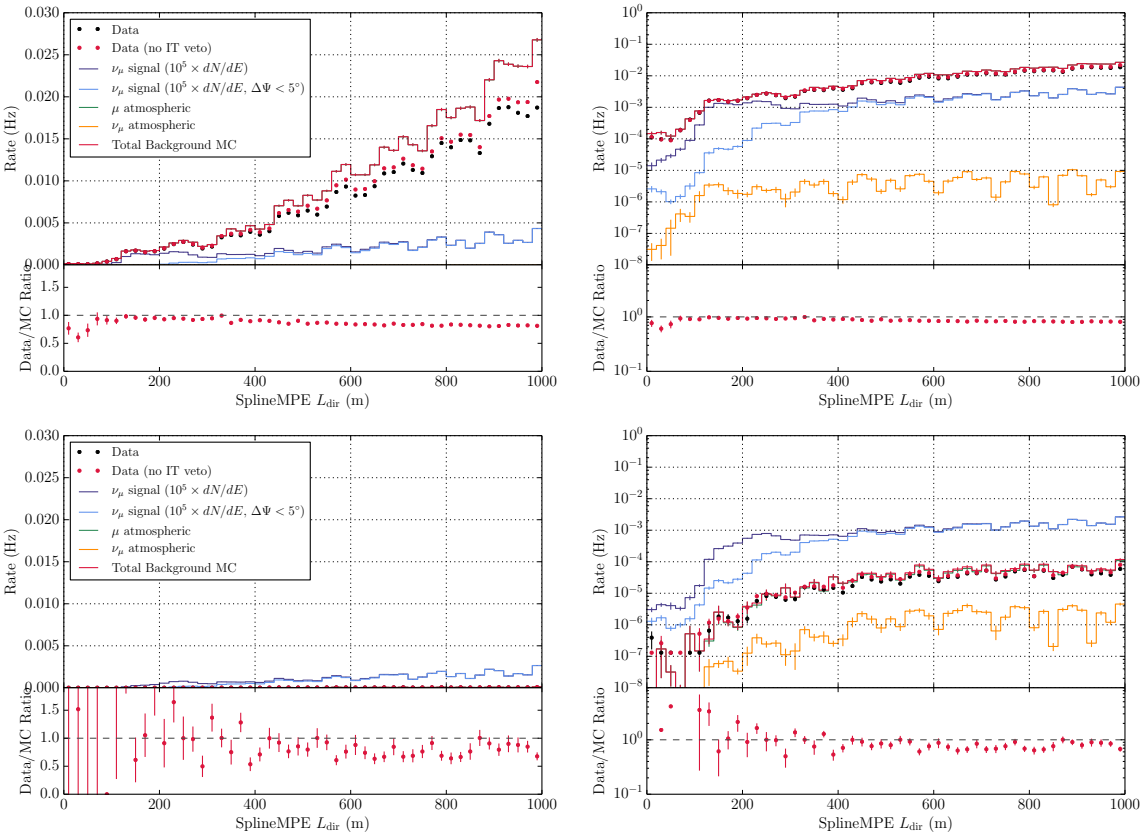

Figure 5.28: IC86-2011 SplineMPE L_{dir} distributions for IceCube data and simulation at the L4 (top) and final event sample level (bottom), in both linear (left) and log (right) scales. The ratio of IceCube data without the IceTop veto to total background simulation is shown below each plot.

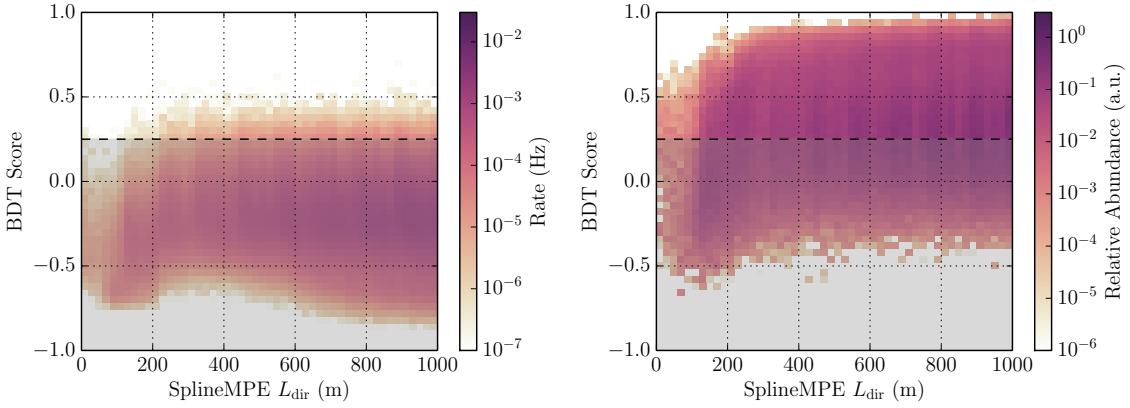

Figure 5.29: IC86-2011 SplineMPE L_{dir} vs. BDT score distributions for IceCube data (left) and simulated ν_μ weighted to an E^{-2} spectrum. The final BDT score cut is indicated by the dashed line.

- SplineMPE N_{dir} (`splinempe_n_dir_e`):

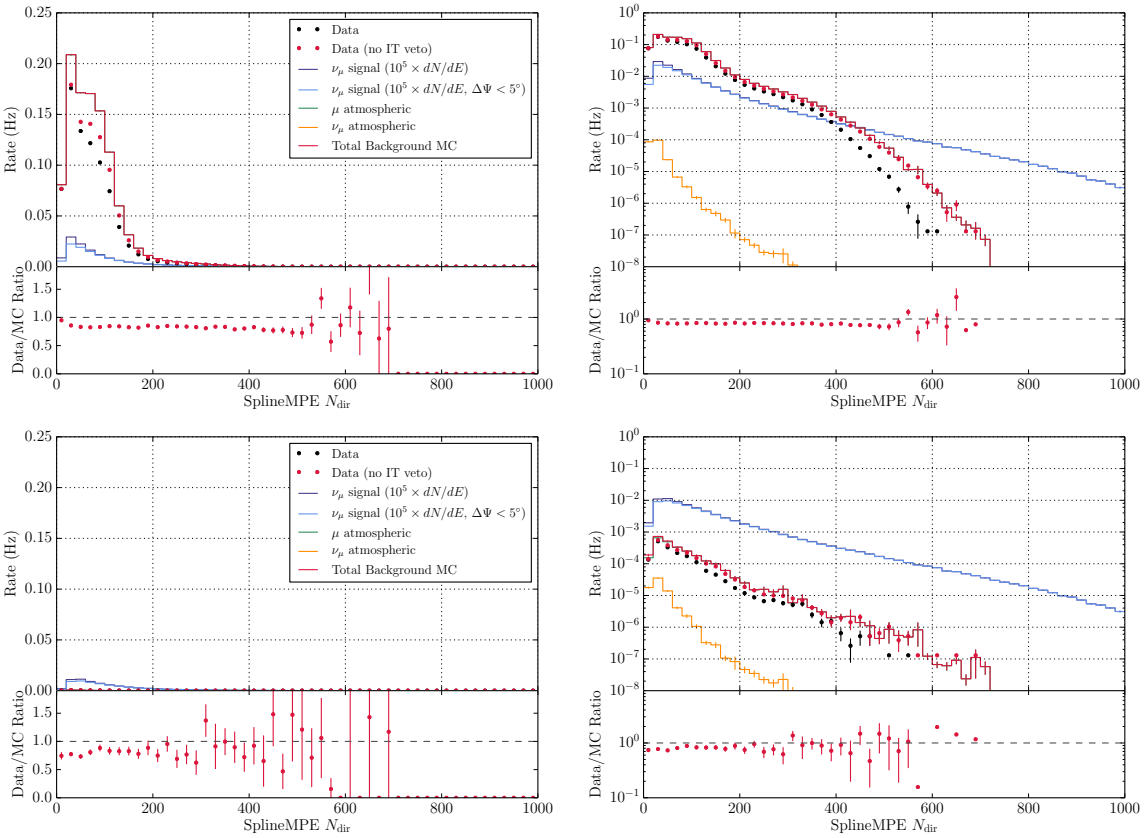

Figure 5.30: IC86-2011 SplineMPE N_{dir} distributions for IceCube data and simulation at the L4 (top) and final event sample level (bottom), in both linear (left) and log (right) scales. The ratio of IceCube data without the IceTop veto to total background simulation is shown below each plot.

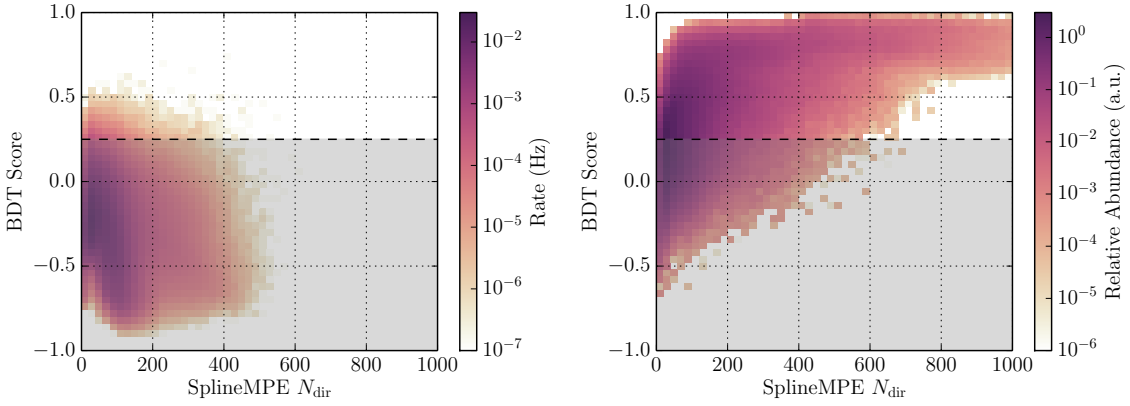

Figure 5.31: IC86-2011 SplineMPE N_{dir} vs. BDT score distributions for IceCube data (left) and simulated ν_μ weighted to an E^{-2} spectrum. The final BDT score cut is indicated by the dashed line.

- SplineMPE plogl (`splinempe_plogl`):

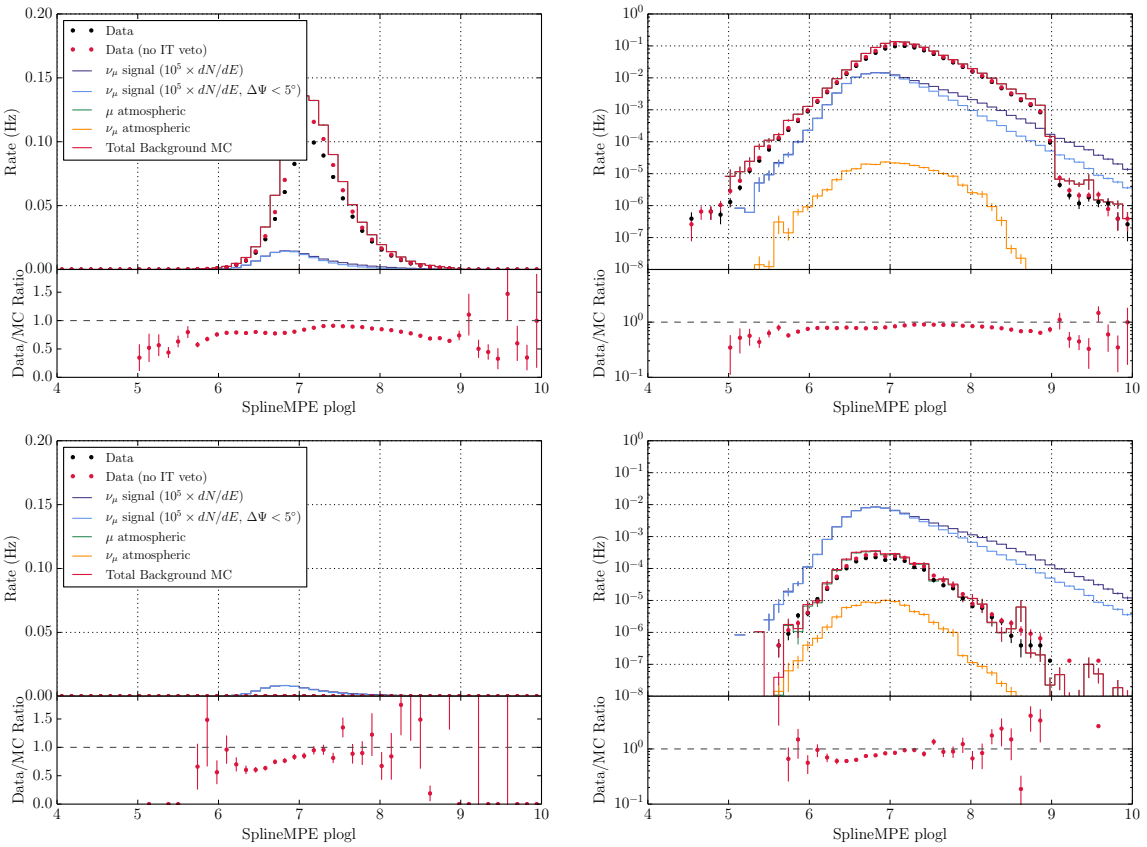

Figure 5.32: IC86-2011 SplineMPE plogl distributions for IceCube data and simulation at the L4 (top) and final event sample level (bottom), in both linear (left) and log (right) scales. The ratio of IceCube data without the IceTop veto to total background simulation is shown below each plot.

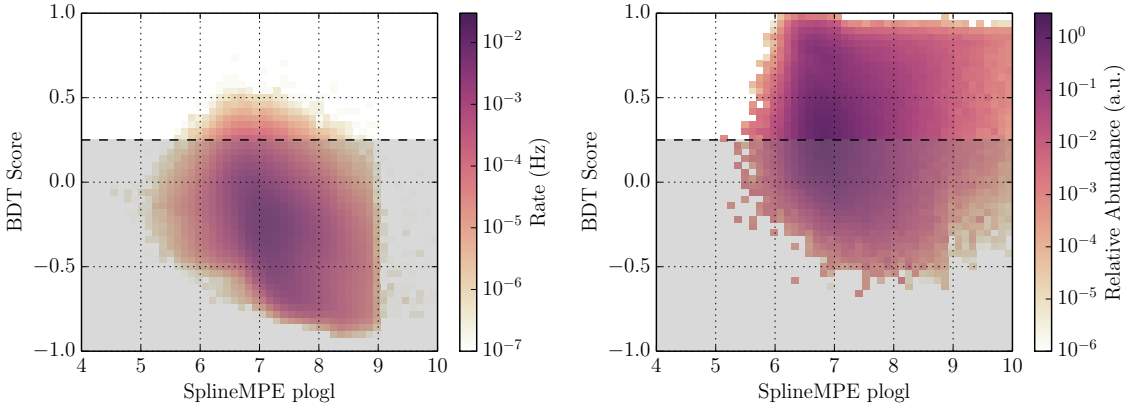

Figure 5.33: IC86-2011 SplineMPE plogl vs. BDT score distributions for IceCube data (left) and simulated ν_μ weighted to an E^{-2} spectrum. The final BDT score cut is indicated by the dashed line.

- SplineMPE Smoothness (`splinempe_s_dir_e`):

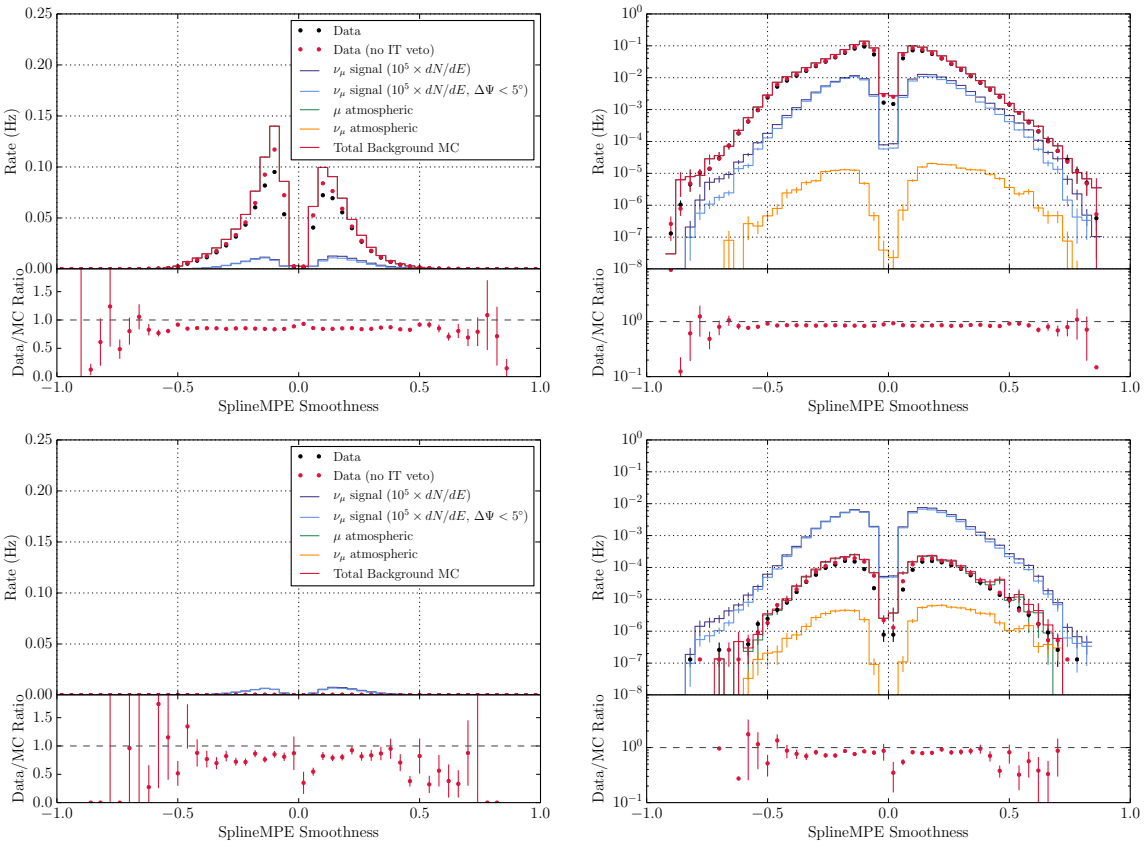

Figure 5.34: IC86-2011 SplineMPE Smoothness distributions for IceCube data and simulation at the L4 (top) and final event sample level (bottom), in both linear (left) and log (right) scales. The ratio of IceCube data without the IceTop veto to total background simulation is shown below each plot.

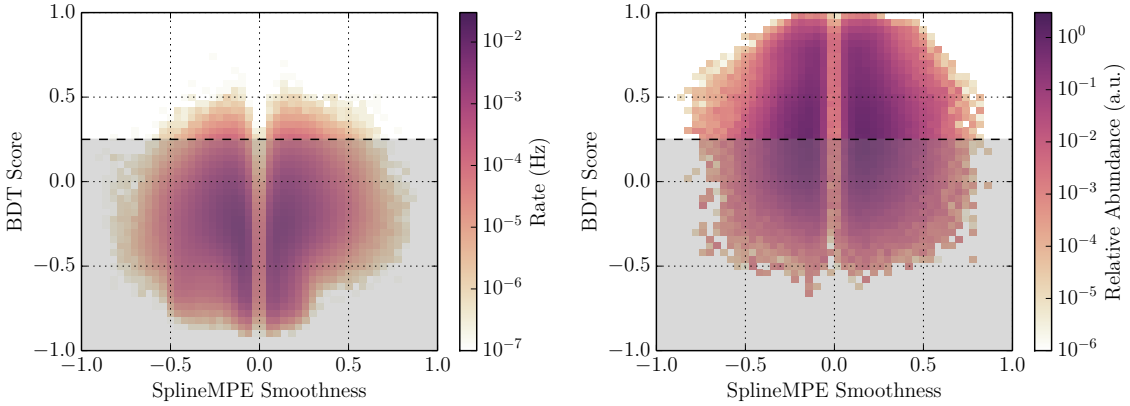

Figure 5.35: IC86-2011 SplineMPE Smoothness vs. BDT score distributions for IceCube data (left) and simulated ν_μ weighted to an E^{-2} spectrum. The final BDT score cut is indicated by the dashed line.

- SplineMPE Separation (`splinempe_sep`):

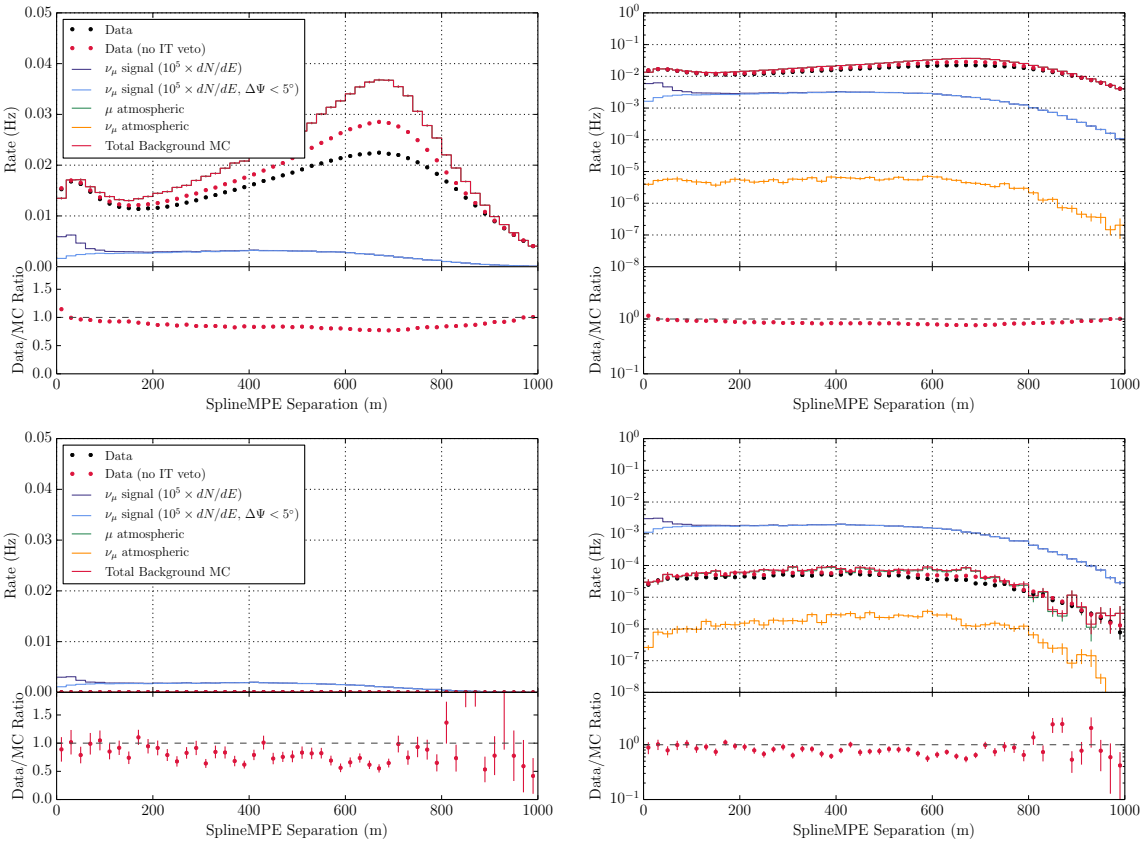

Figure 5.36: IC86-2011 SplineMPE Separation distributions for IceCube data and simulation at the L4 (top) and final event sample level (bottom), in both linear (left) and log (right) scales. The ratio of IceCube data without the IceTop veto to total background simulation is shown below each plot.

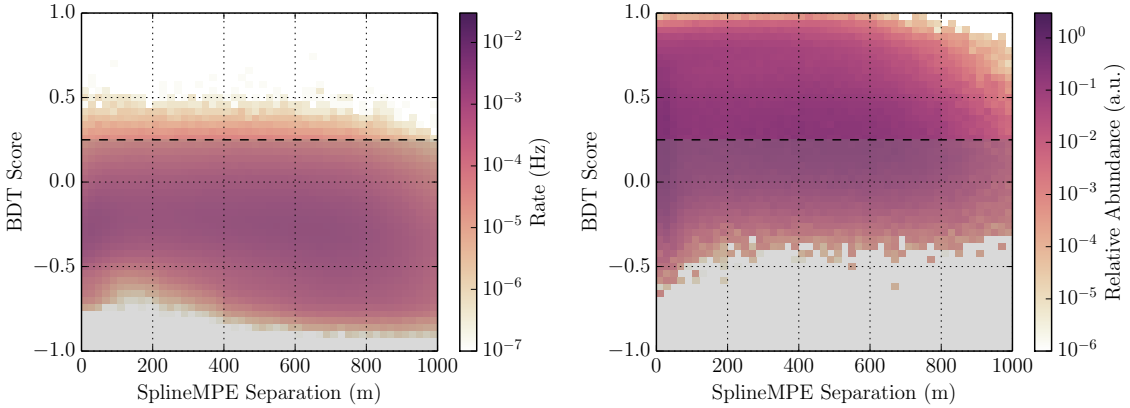

Figure 5.37: IC86-2011 SplineMPE Separation vs. BDT score distributions for IceCube data (left) and simulated ν_μ weighted to an E^{-2} spectrum. The final BDT score cut is indicated by the dashed line.

- SplineMPE Starting Distance (`splinempe_start_dist`):

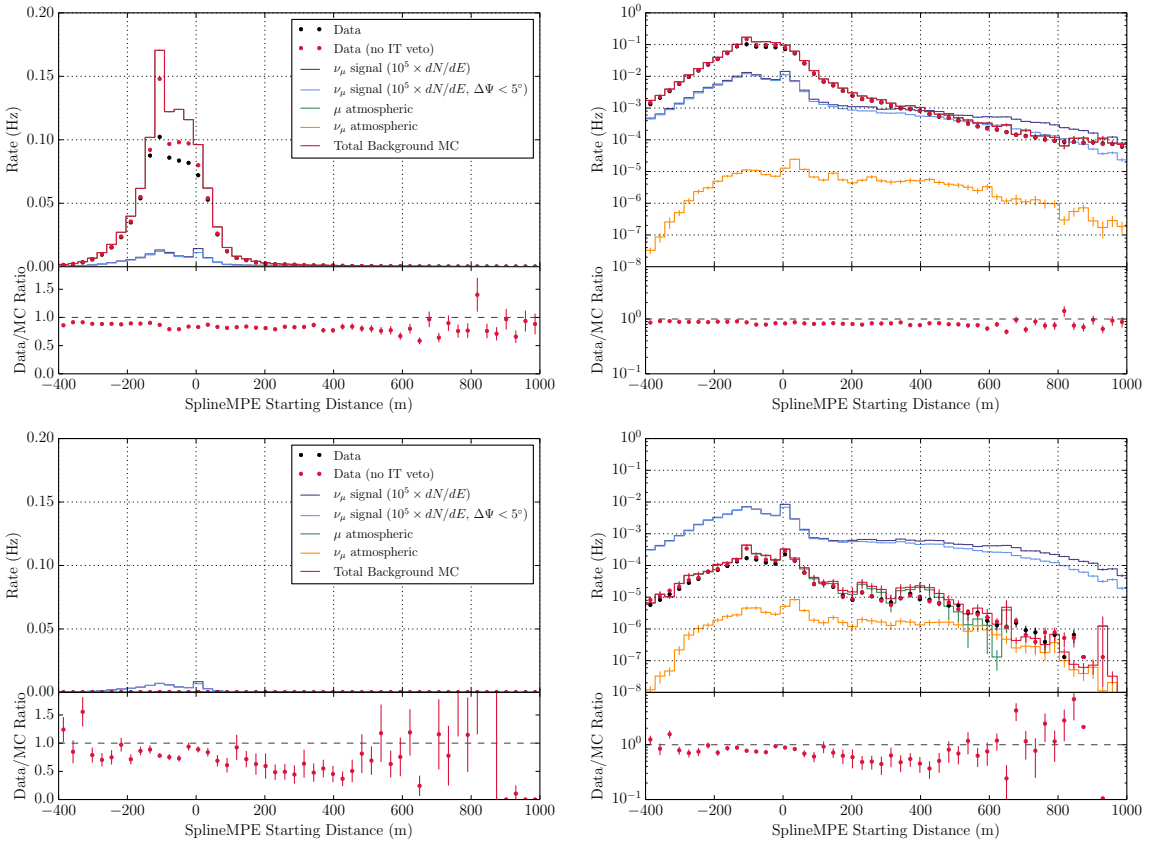

Figure 5.38: IC86-2011 SplineMPE Starting Distance distributions for IceCube data and simulation at the L4 (top) and final event sample level (bottom), in both linear (left) and log (right) scales. The ratio of IceCube data without the IceTop veto to total background simulation is shown below each plot.

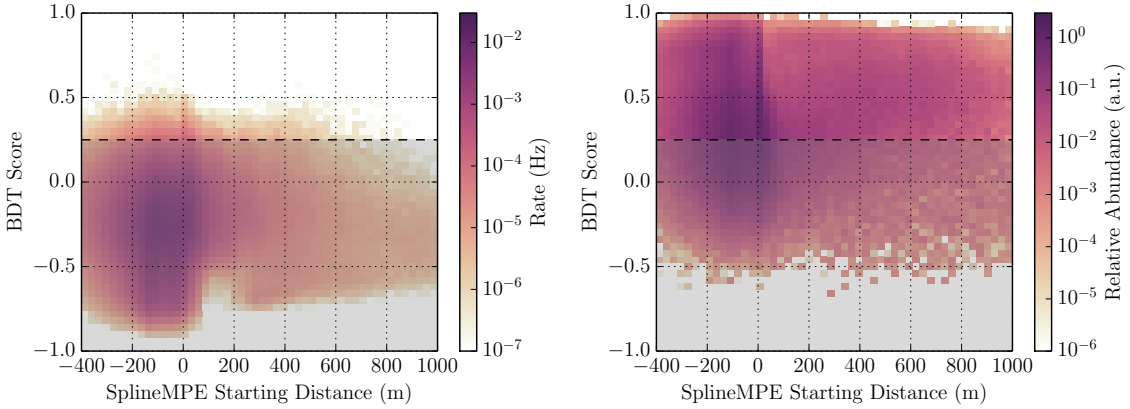

Figure 5.39: IC86-2011 SplineMPE Starting Distance vs. BDT score distributions for IceCube data (left) and simulated ν_μ weighted to an E^{-2} spectrum. The final BDT score cut is indicated by the dashed line.

- SplineMPE Time Residual Likelihood rlogl (`tres_llh_rlogl`):

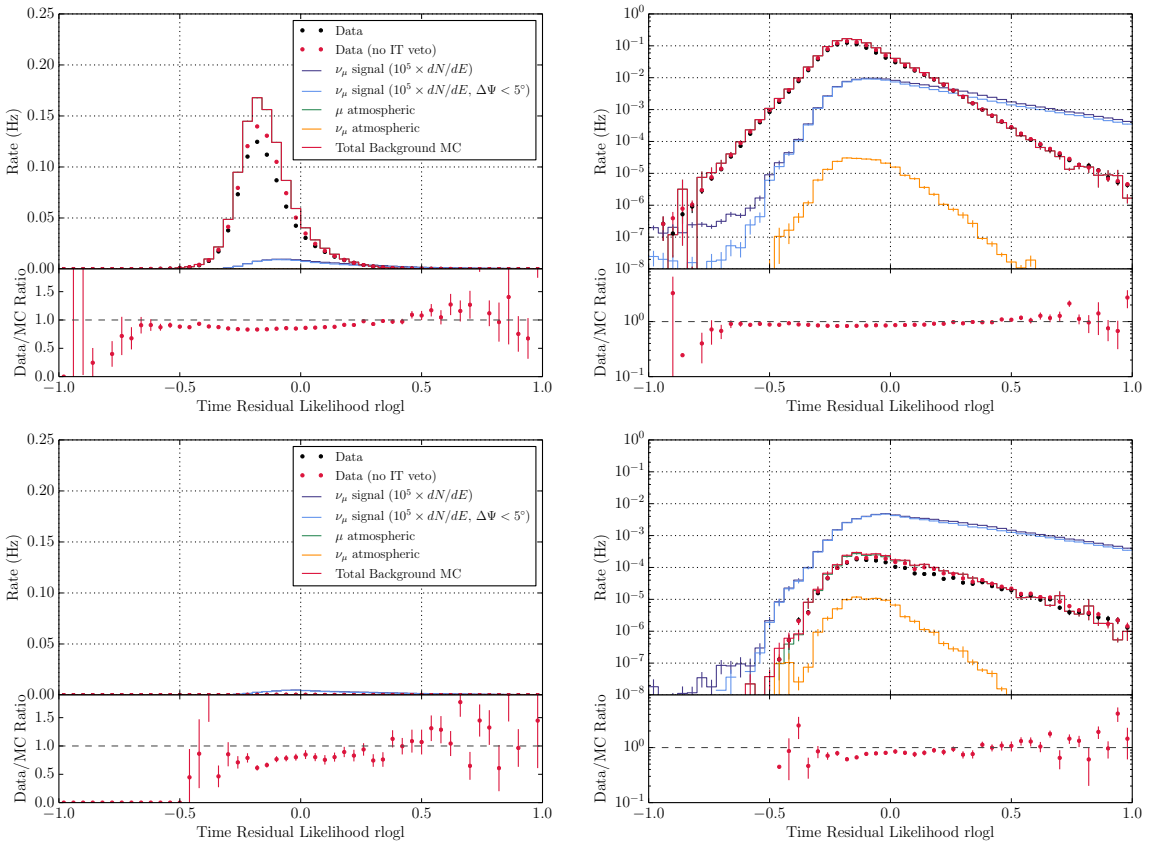

Figure 5.40: IC86-2011 SplineMPE Time Residual Likelihood rlogl distributions for IceCube data and simulation at the L4 (top) and final event sample level (bottom), in both linear (left) and log (right) scales. The ratio of IceCube data without the IceTop veto to total background simulation is shown below each plot.

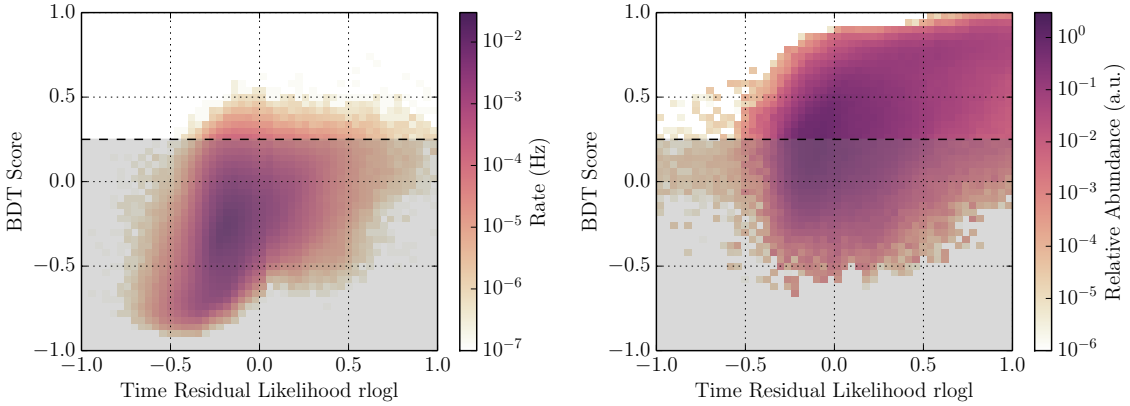

Figure 5.41: IC86-2011 SplineMPE Time Residual Likelihood rlogl vs. BDT score distributions for IceCube data (left) and simulated ν_μ weighted to an E^{-2} spectrum. The final BDT score cut is indicated by the dashed line.

The correlations between these parameters at the Preselection L4 event level for both background and signal are shown in Figure 5.42.

BDT models were trained separately for the IC79, IC86-2011, and IC86-2012 years of data, where the IceCube detector, processing, and simulation were slightly different. The IC86-2012 model was applied to all subsequent years of data, as the processing and filtering for these years are the same, and individual BDTs trained for these additional years showed no improvement in their event selection and sensitivity. The BDT models were trained with the following BDT parameters:

- **IC79**
  - Number of trees: 400
  - Maximum tree depth: 5
  - Event sample random fraction: 0.3
  - Number of cuts per parameter: 20
  - $\beta = 0.5$
  - $\rho = 25\%$
- **IC86-2011, IC86-2012**
  - Number of trees: 400
  - Maximum tree depth: 5
  - Event sample random fraction: 0.3
  - Number of cuts per parameter: 20
  - $\beta = 0.5$
  - $\rho = 15\%$

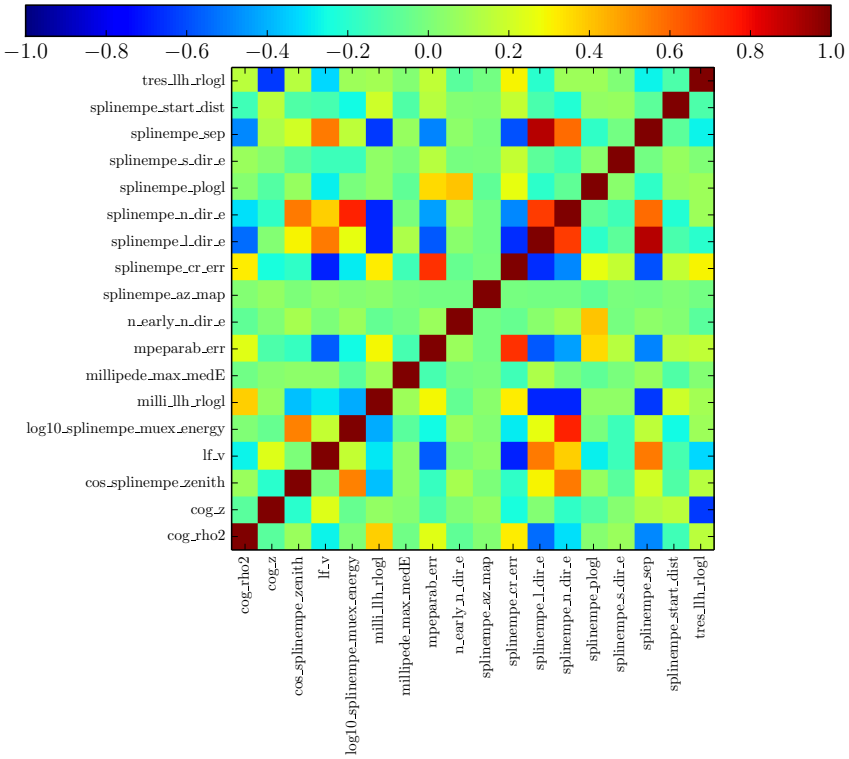

(a) Background

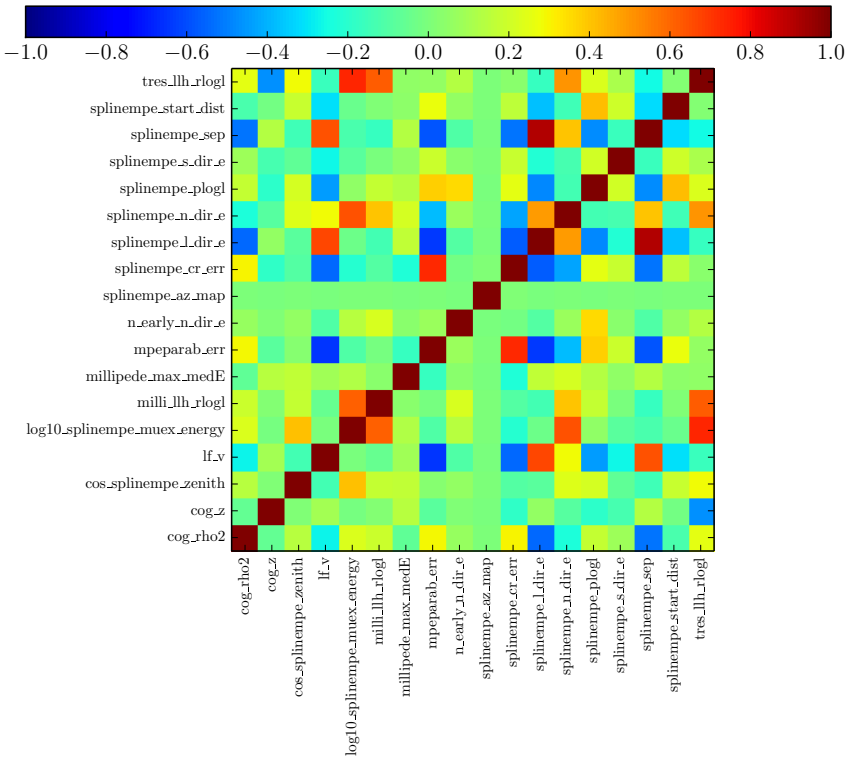

(b) Signal

Figure 5.42: BDT input parameter correlations in data.

Figure 5.43: BDT input parameter correlations in well-reconstructed E^{-2} ν_μ signal.

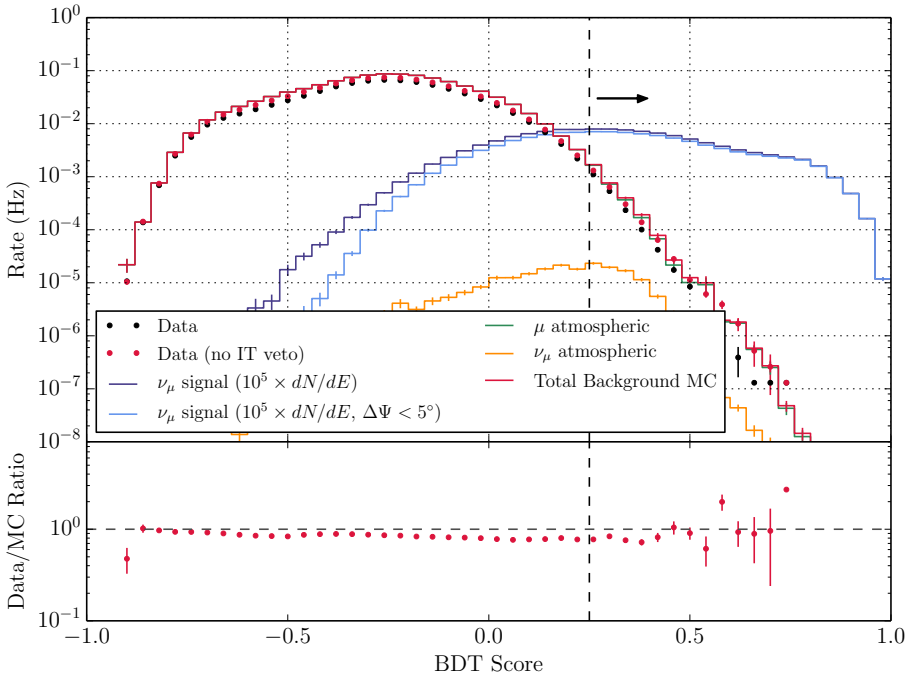

Figure 5.44: IC86-2011 BDT score distributions, with the ratio of IceCube data without the IceTop veto to total background simulation shown below. The final BDT score cut is indicated with the vertical dashed line.

No parameter randomization per-split node was employed in the training as the event sample randomization appeared sufficient to reduce overtraining to an acceptable level.

In the following, only the IC86-2011 BDT and final event sample is shown in detail, as its characteristics are nearly identical to those of the IC79 and IC86-2012 final event samples. The BDT score distributions for the IC86-2011 BDT for IceCube data, and simulated signal and background are found in Figure 5.44. These show good separation of ν_μ signal and measured background, as well as good agreement between simulated background and measured data where no IceTop veto has been applied. The validation of this BDT is shown in Figure 5.45, demonstrating good agreement between training and testing samples.

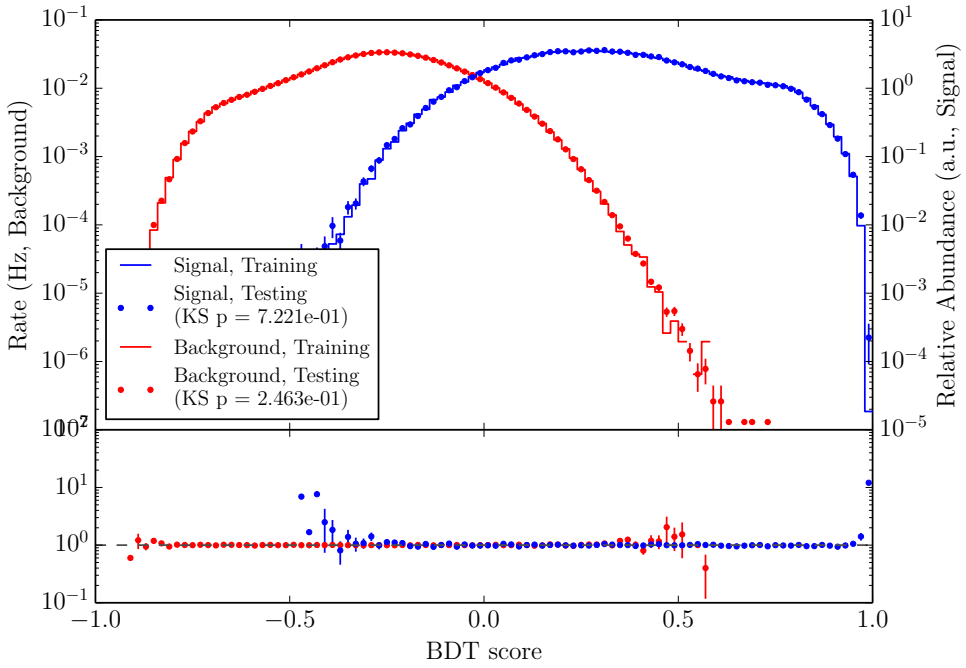

Figure 5.45: IC86-2011 BDT overtraining validation comparing signal and background BDT score distributions for training and testing samples.

In a BDT forest, the relative importance of parameters can be calculated to determine which parameters are primarily used to separate signal and background. One can also verify that all parameters provided to the BDT are actually used; if a parameter be rarely used, this parameter should likely be removed from the BDT training as it yields little but noise to the signal–background separation. These importance measures are calculated as the fraction of nodes the parameter is used in by the BDT, using various relative node weighting schemes. The importance of the various input parameters in the IC86-2011 are summarized below, showing that all parameters contribute to the BDT signal–background separation, and indicating the most used parameters.

The fraction of nodes a parameter is used, weighted by the separation in that node, gives the relative importance of parameters that yield the largest separtion in background and signal:

```
1. n_early_n_dir_e              : 0.323049
```

```
 2. log10_splinempe_muex_energy : 0.112650
 3. tres_llh_rlogl              : 0.090970
 4. splinempe_n_dir_e           : 0.088404
 5. splinempe_cr_err            : 0.065855
 6. splinempe_start_dist        : 0.065806
 7. cos_splinempe_zenith        : 0.050520
 8. splinempe_plogl             : 0.042824
 9. splinempe_sep               : 0.038330
10. splinempe_s_dir_e           : 0.023712
11. cog_z                       : 0.025079
12. lf_v                        : 0.017497
13. milli_llh_rlogl             : 0.017071
14. splinempe_l_dir_e           : 0.015372
15. millipede_max_medE          : 0.014421
16. cog_rho2                    : 0.005576
17. mpeparab_err                : 0.002842
18. splinempe_az_map            : 0.002521
```

The fraction of nodes a parameter is used, weighted by the tree weight, gives the relative importance of parameters in the earliest trees with the easiest to classify events:

```
 1. log10_splinempe_muex_energy : 0.124259
 2. cos_splinempe_zenith        : 0.110984
 3. tres_llh_rlogl              : 0.109488
 4. splinempe_n_dir_e           : 0.076866
 5. splinempe_plogl             : 0.074733
 6. cog_z                       : 0.071039
 7. n_early_n_dir_e             : 0.069840
```

```
 8. splinempe_cr_err            : 0.068447
 9. splinempe_start_dist        : 0.055357
10. splinempe_sep               : 0.040866
11. splinempe_s_dir_e           : 0.035958
12. mpeparab_err                : 0.031791
13. millipede_max_medE          : 0.027832
14. splinempe_l_dir_e           : 0.025098
15. lf_v                        : 0.023778
16. cog_rho2                    : 0.022112
17. milli_llh_rlogl             : 0.019620
18. splinempe_az_map            : 0.011932
```

The fraction of nodes a parameter is used, weighted by both tree weight and separation per node, indicates the most important parameters overall in signal and background separation:

```
 1. tres_llh_rlogl              : 0.210792
 2. log10_splinempe_muex_energy : 0.147532
 3. cos_splinempe_zenith        : 0.147015
 4. n_early_n_dir_e             : 0.075595
 5. splinempe_cr_err            : 0.072320
 6. splinempe_start_dist        : 0.068038
 7. milli_llh_rlogl             : 0.066229
 8. splinempe_plogl             : 0.042500
 9. splinempe_n_dir_e           : 0.040800
10. cog_z                       : 0.031896
11. splinempe_s_dir_e           : 0.019691
12. splinempe_sep               : 0.018970
13. lf_v                        : 0.018329
```

```
14. splinempe_l_dir_e           : 0.013718
15. millipede_max_medE          : 0.010431
16. cog_rho2                    : 0.008188
17. splinempe_az_map            : 0.004329
18. mpeparab_err                : 0.003627
```

The fraction of nodes a parameter is used in gives the relative importance of parameters in classifying the rarest events:

```
 1. n_early_n_dir_e             : 0.159594
 2. tres_llh_rlogl              : 0.105457
 3. log10_splinempe_muex_energy : 0.093252
 4. splinempe_n_dir_e           : 0.087959
 5. splinempe_sep               : 0.079835
 6. splinempe_start_dist        : 0.061869
 7. splinempe_plogl             : 0.056217
 8. cos_splinempe_zenith        : 0.051755
 9. splinempe_cr_err            : 0.047079
10. millipede_max_medE          : 0.044757
11. cog_z                       : 0.040705
12. cog_rho2                    : 0.033167
13. mpeparab_err                : 0.032121
14. splinempe_s_dir_e           : 0.028451
15. milli_llh_rlogl             : 0.023062
16. lf_v                        : 0.021149
17. splinempe_l_dir_e           : 0.019093
18. splinempe_az_map            : 0.014477
```

The final BDT score cut that is used to obtain the final event sample is determined so as to optimize the analysis to discover a neutrino signal from GRBs,

as discussed in Chapter 6. It is found that the optimal score cut reduces the background data rate to $\sim$2 mHz, similar to that in the previous prompt ν_μ searches from Northern Hemisphere GRBs [25, 26]. The total efficiency of this selection to well-reconstructed downgoing ν_μ signal is shown in Figure 5.46 as a function of simulated ν_μ energy. This efficiency is shown with respect to the IceCube SMT-8 trigger level data for each stage of the event selection. The final event sample succesfully retains 26.6% of this well-reconstructed E^{-2} ν_μ signal, while reducing the initial $\gtrsim$ 2 kHz data rate by over a factor of 10^6. The event selection is especially efficient for the high-energy signal, where 83.5% of this signal with energy $E_\nu > 1$ PeV is retained. The data at this final event level is still dominated by atmospheric muons, however, with only 4.4% percent of the final data sample consisting of atmospheric ν_μ events. The median angular resolution of the IC86-2011 final event sample is shown in Figure 5.47. For ν_μ signal with energy $E_\nu > 100$ TeV, this median angular resolution for the SplineMPE reconstruction is $\sim$0.5°, allowing good correlations to be made between measured events with a GRB in the energy range to which this analysis is most sensitive.

The effective area of an event selection in a neutrino energy bin $(E_\nu, E_\nu + \Delta E_\nu)$ can be calculated from simulation as

$$A_{\text{eff}}(E_\nu, \Delta E_\nu) = \frac{N_{\text{detected}}(E_\nu, \Delta E_\nu)}{N_{\text{incoming}}(E_\nu, \Delta E_\nu)} A \tag{5.18}$$

where A is the area over which simulated events are injected by the neutrino event generator, and $N_{\text{detected}}(E_\nu, \Delta E_\nu)$ is the number of detected events in this energy bin over a given time interval from the incoming number of events $N_{\text{incoming}}(E_\nu, \Delta E_\nu)$. This measure is spectrum independent, allowing effective areas to be compared across analyses to show relative sensitivities. The measured event rate of the analysis for a given neutrino spectrum as a function of event energy can then obtained by mul-

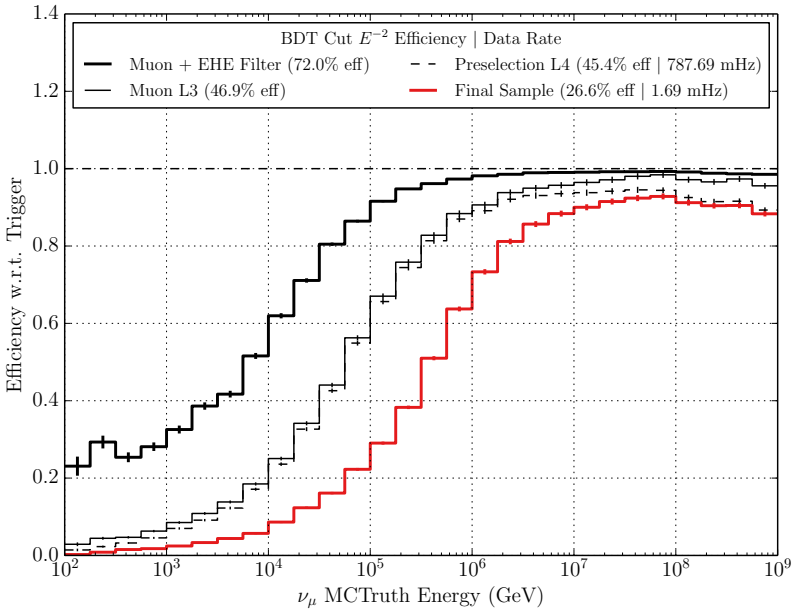

Figure 5.46: The IC86-2011 event selection efficiency relative to the detector trigger at different stages of the event selection as a function of simulated ν_μ energy, for well-reconstructed downgoing events.

tiplying its effective area with the incoming neutrino flux and integrating over the energy bin and analysis solid angle. The effective area of the IC86-2011 analysis final event selection is shown compared to previous prompt ν GRB searches, as well as the Southern Hemisphere sky ν_μ point source analysis, in Figure 5.48. The event selection presented here is demonstrated to be most sensitive of all these analyses to signal above a few PeV, and improves on the point source selection at all ν_μ energies; conversely, because it has had to remove the large low-energy atmospheric muon background from the Southern Hemisphere sky, it has a significantly reduced sensitivity to lower energy ν signal compared to the other prompt ν analyses.

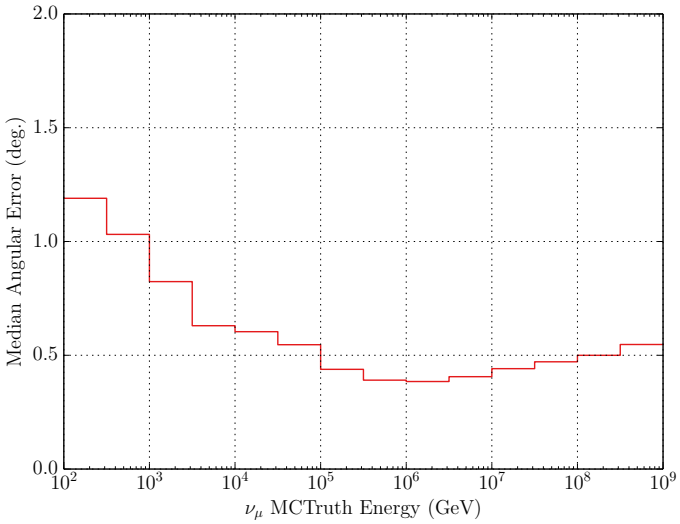

Figure 5.47: IC86-2011 final sample SplineMPE median angular resolution as a function of simulated ν_μ energy, weighted to an E^{-2} spectrum.

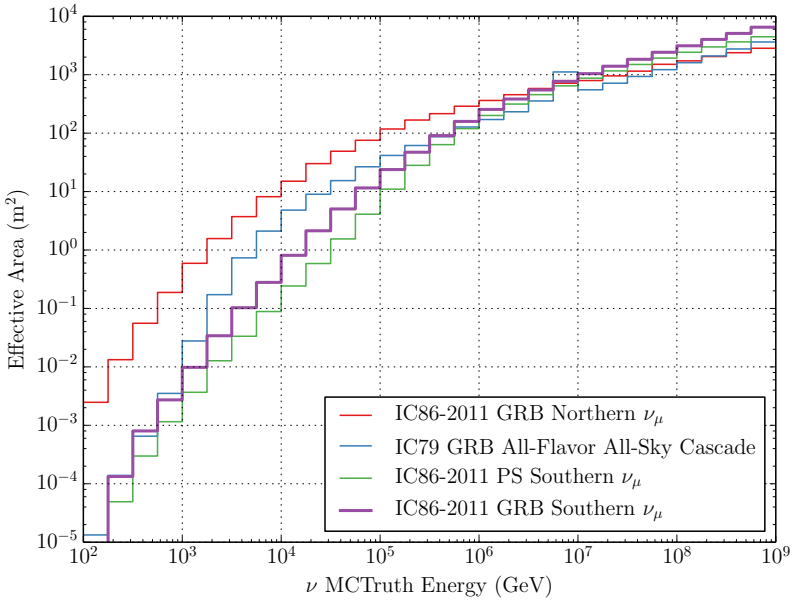

Figure 5.48: IC86-2011 final sample effective area compared to those from previous prompt ν GRB searches and the IceCube Southern Hemisphere sky point source search.

Chapter 6

Unbinned Likelihood Method

Given the final event sample obtained in Chapter 5, the significance of events coincident with GRB must be determined. As this sample consists almost entirely of atmospheric muons and atmospheric neutrinos, the method must be sensitive to small numbers of signal neutrino events while reducing the contribution from background contamination. Moreover, the method should obtain a set of events most likely to have been produced by a GRB and an estimate of the signalness of these events to compare to expectations from background alone.

The unbinned likelihood method employed in this thesis has been used in previous prompt ν GRB searches [25–27], and achieves these goals. Events are scored with respect to their energy, and the spatial and temporal displacement from a GRB to obtain a set of events most likely to have come from a GRB. These event scores are then compiled into a single test statistic that summarizes the amount of signal in the sample compared to the background expectation. From Monte Carlo background-only trials of this test statistic calculation, the final significance of the measured test statistic can be determined.

As the ν emission of GRBs in the numerical models of Section 2.3 is expected to yield less than one neutrino per-search channel, per-year of analyzed GRBs, *stacked* test statistic analyses are used. These combine the event scores from all GRBs in an analyzed sample into a single test statistic, searching for significant coincidences with any GRB in the sample. Effectively, the small ν emission from individual GRBs are added together to attain a statistically significant measurement, where a search from any single GRB would fail to do so. Previous stacked prompt ν searches [25–27], however, have still failed to discover a compelling neutrino signal, setting strong

limits on current GRB ν emission models and motivating modifications to this stacked method.

This chapter first summarizes the unbinned likelihood test statistic method used in this dissertation. The frequentist method for determining the background expectation of the analysis and its sensitivity to a given signal hypothesis are then described. Next, modifications to the stacked search test statistic are discussed, establishing a per-GRB test statistic can be calculated that is sensitive to ν emission that is dominated by a single GRB in a given GRB sample. Finally, the signal sensitivity optimization of the analysis is presented.

6.1 Prompt GRB Test Statistic

The test statistic calculated in this dissertation's unbinned likelihood analysis provides a way of comparing observed events under signal and background hypotheses. Events are first scored with respect to their signal and background likelihoods, then a final value is derived by fitting a best signal rate to the observed events.

Suppose in a given GRB analysis N events are observed, given an expected signal plus background rate of $n_s + n_b$. The Poisson probability $P(N|n_s + n_b)$ for this measurement is

$$P(N|n_s + n_b) = \frac{(n_s + n_b)^N}{N!} e^{-(n_s+n_b)}. \tag{6.1}$$

Each event i has properties $\mathbf{x}_i$, which can be scored with respect to a signal PDF $\mathcal{S}(\mathbf{x}_i)$ and background PDF $\mathcal{B}(\mathbf{x}_i)$. Let $\{\mathbf{x}_i\}$ be the set of properties for all observed events. The likelihood of a certain expected event rate is then derived from the product of the Poisson probability and average per-event signal–background probabilities based on their PDFs, yielding

$$\mathcal{L}\left(n_s, n_b|\{\mathbf{x}_i\}\right) = P(N|n_s + n_b) \prod_{i=1}^{N} \left[p_s \mathcal{S}(\mathbf{x}_i) + p_b \mathcal{B}(\mathbf{x}_i)\right] \tag{6.2}$$

where $p_s = n_s/(n_s+n_b)$ and $p_b = n_b/(n_s+n_b)$. The null (background-only) hypothesis likelihood is simply the likelihood function setting $n_s = 0$. One can estimate the background data rate n_b from data that is not time-coincident with a GRB, fixing $n_b \leftarrow \langle n_b \rangle$ as the expected background rate in the GRB search time window.

The test statistic is defined as the natural logarithm of the ratio of signal plus background likelihood to the null hypothesis likelihood, which is maximized with respect to a fit number of signal events $\hat{n}_s$. Through simple algebra, one can derive the test statistic to be:

$$\mathcal{T} \equiv \ln \left[\frac{\mathcal{L}\left(\hat{n}_s | \{\mathbf{x}_i\}, \langle n_b \rangle\right)}{\mathcal{L}\left(0\right)} \right] = -\hat{n}_s + \sum_{i=1}^{N} \ln \left[\frac{\hat{n}_s \mathcal{S}(\mathbf{x}_i)}{\langle n_b \rangle \mathcal{B}(\mathbf{x}_i)} + 1 \right]. \tag{6.3}$$

The calculation both yields a set of events most likely to have come from a GRB (events with the large signal-to-background PDF ratios), as well as a quantity estimating the amount of signal in the final event sample ($\hat{n}_s$). The test statistic, itself, is used as the final significance measure of the analysis.

In current GRB analyses, a *stacked* test statistic is calculated where events coincident with any GRB in the entire sample are combined in the final measure. The total events observed N is then all such coincident events, and $\langle n_b \rangle$ is the total expected background during the entire GRB sample search time window. Each detection channel c (Northern Hemisphere track, Southern Hemisphere track, and All-Sky cascade) and season s (IC40, IC59, etc.) is treated separately, obtaining a final $\mathcal{T}_{c,s}$ for each configuration. As each configuration constitutes an independent observation, a combined total likelihood is simply the product of individual configuration likelihoods. One can therefore obtain a final combined test statistic $\mathcal{T}$ as a sum of individual configuration test statistics:

$$\mathcal{T} = \sum_{c,s} \mathcal{T}_{c,s} \tag{6.4}$$

where each configuration test statistic $\mathcal{T}_{c,s}$ is maximized independently with respect to $(\hat{n}_s)_{c,s}$

6.1.1 Probability Distributions

The signal and background PDFs used in the unbinned likelihood have yet to be defined. In general terms, signal events are expected to occur in spatial and temporal coincidence to a GRB, which should be reflected in signal space and time PDFs. Further, the GRB neutrino energy spectrum is expected to be harder than the background atmospheric muon spectrum, allowing energy PDFs to be used for further signal and background separation. For simplicity, each of these space, time, and energy PDFs is treated as independent, yielding total signal and background probabilities for a given event i of

$$\mathcal{S}(\mathbf{x}_i) = \mathcal{S}_{\text{space}}(\vec{x}_i) \times \mathcal{S}_{\text{time}}(t_i) \times \mathcal{S}_{\text{energy}}(E_i) \tag{6.5}$$

$$\mathcal{B}(\mathbf{x}_i) = \mathcal{B}_{\text{space}}(\vec{x}_i) \times \mathcal{B}_{\text{time}}(t_i) \times \mathcal{B}_{\text{energy}}(E_i). \tag{6.6}$$

where t_i is the time of the event, and $\vec{x}_i$ and E_i are the event's reconstructed direction and energy, respectively.

6.1.1.1 Space

The background space PDF is characterized entirely from data at the final event level not temporally coincident with a GRB. This data shows little dependence on reconstructed azimuth, as demonstrated in Figure 6.1. Thus, the background space PDF is defined as a function of reconstructed zenith normalized to the solid angle of the Southern Hemisphere search, shown in Figure 6.2 for every year of analysis separately. In these, it is seen that background is most likely to occur near the

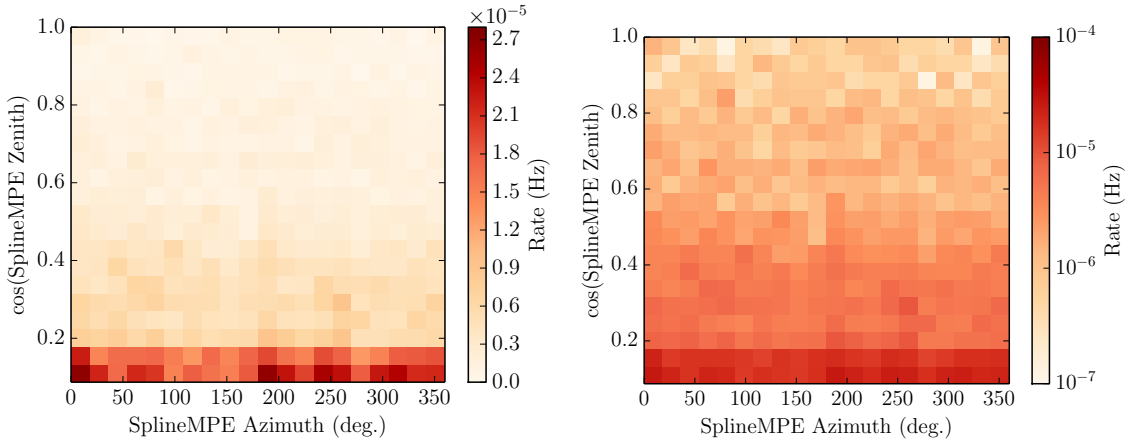

Figure 6.1: IC86-2011 background space distribution at final event level for linear (left) and log (right) scales.

horizon. For fast evaluation of the background space PDF at arbitrary reconstructed zeniths, a spline is fit to the binned background data.

For the signal space PDF, a Kent distribution is used:

$$\mathcal{S}_{\text{space}}(\vec{x}_i) = \frac{\kappa}{4\pi} e^{\kappa \cos(\Delta\theta_{i,\text{GRB}})} \tag{6.7}$$

where $\Delta\theta_{i,\text{GRB}}$ is the opening angle between the reconstructed direction of the event and the measured GRB direction. The concentration parameter κ is

$$\kappa = \frac{1}{\sigma_{\text{GRB}}^2 + \sigma_i^2} \tag{6.8}$$

where σ_{GRB} is the measured uncertainty of the GRB direction, and σ_i is the uncertainty in the reconstructed event direction. This angular probability distribution is essentially a normal distribution that has been mapped to the surface of a sphere through Bessel functions. At small angular uncertainty (large κ), the Kent distribution reduces to the normal distribution. At large angular uncertainty (small κ), the two distributions diverge, both in shape and normalization. The Kent distribution for a number of angular uncertainties is shown in Figure 6.3.

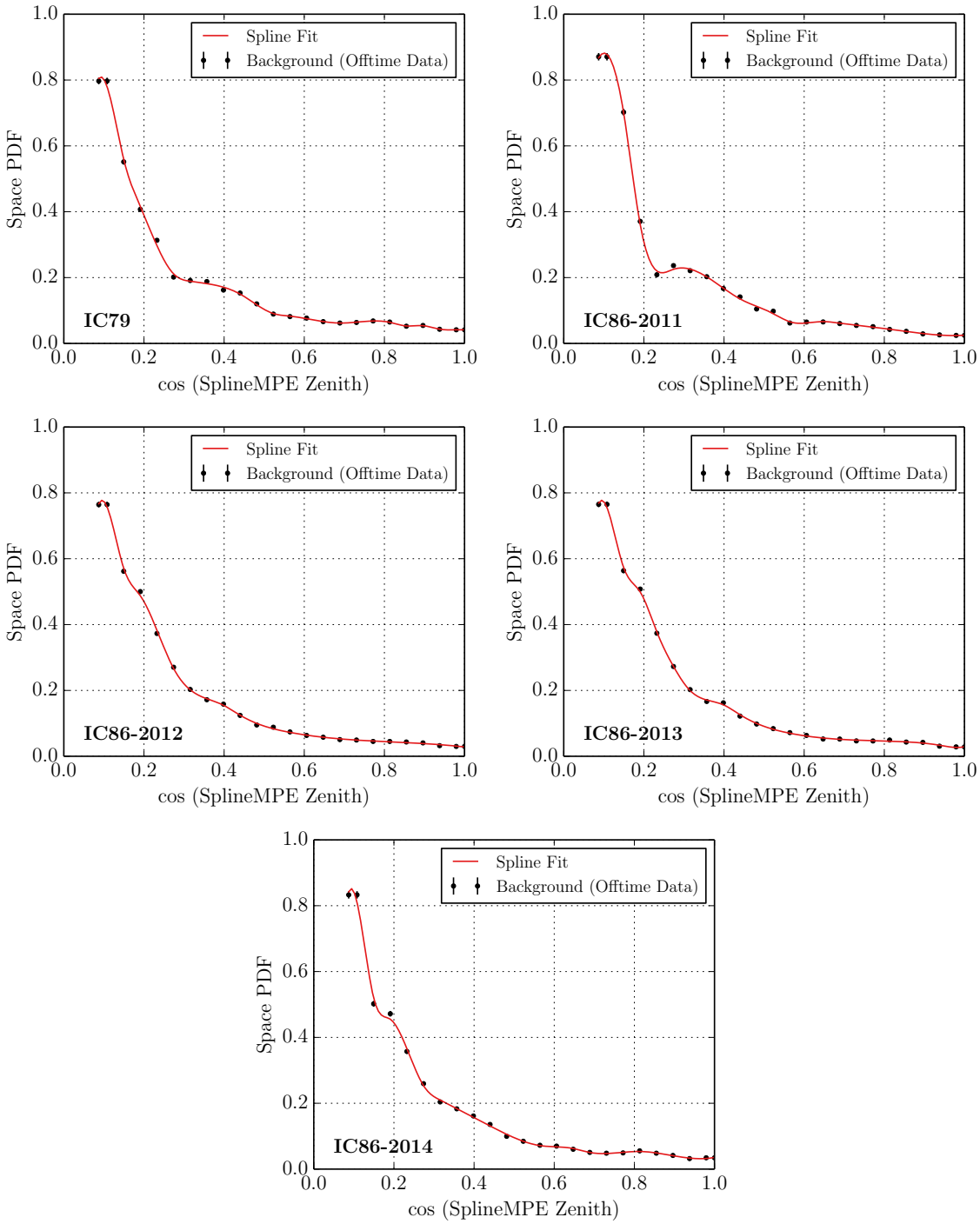

Figure 6.2: The background space PDFs at the final event level for all years of analysis. The spline fits to the binned data are shown in the red lines.

The per-event angular uncertainty σ_i is obtained from the SplineMPE Cramer-Rao reconstruction. All of IceCube's angular uncertainty estimators show a *pull*—a

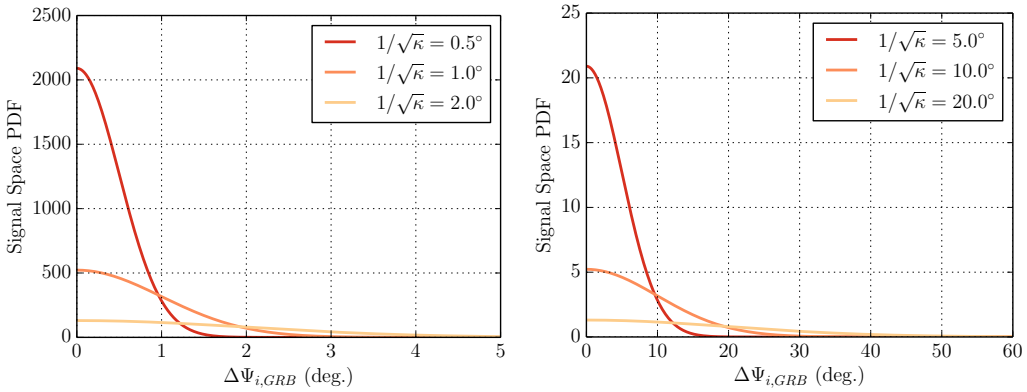

Figure 6.3: The signal space PDF for a number of combined event and GRB angular uncertainties. Note the different scales in the two plots (left: *small* angular uncertainties, right: *large* angular uncertainties).

systematic offset of the estimate compared to the actual angular uncertainty, calculated as the ratio of the true angular offset between the reconstructed and true ν direction to the estimated angular uncertainty—with respect to energy that must be corrected. Approximately 3% of the final E^{-2} ν_μ sample are found to be poorly reconstructed corner clipping events with very large pull ratios and SplineMPE MuEX energies between 10^4 and 10^5, whose pull cannot be correct with a simple correction as a function of reconstructed energy. These events are be kept at the final BDT cut level despite poor track reconstructions for two primary reasons. First, these have a moderate reconstructed muon energy which is selected in signal for by the BDT. Second, and most importantly, their cascade-like light deposition is late relative to the expected geometric arrival time and far from the reconstructed track, biasing these events to very signal-like Time Residual Likelihood values according to Figure 5.1. To correctly estimate their angular uncertainty, a 2D pull correction is constructed in SplineMPE MuEX energy and SplineMPE L_{dir}. This is possible because these corner clipping events have very short tracks in direct hits. The pull in bins of SplineMPE MuEX energy and SplineMPE L_{dir} for the IC86-2011 simulated data can be found in Figure 6.4, with the poorly reconstructed sub-population found at the lower left.

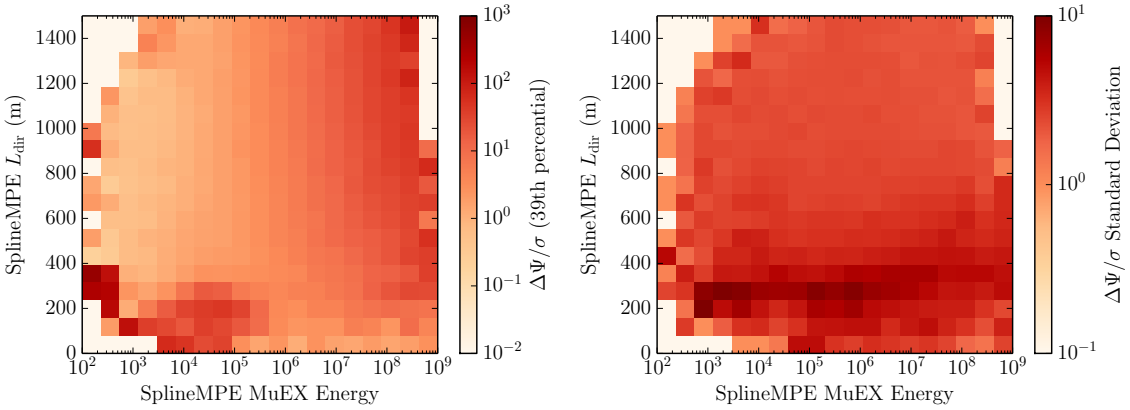

Figure 6.4: The 39th percentile of the pull ratio in IC86-2011 simulated E^{-2} ν_μ data (left) and the standard deviation of this pull ratio (right), in bins of SplineMPE MuEX energy and SplineMPE L_{dir}.

Using a spline fit to the per-bin SplineMPE MuEX energy and SplineMPE L_{dir} pull ratios of Figure 6.4 the SplineMPE Cramer-Rao angular uncertainty is corrected to the 39th percentile in the pull, which corresponds to the 1σ error circle in a 2D normal distribution. The final ratio in IC86-2011 E^{-2} ν_μ simulated data of the true reconstructed angular separation to the pull-corrected SplineMPE Cramer-Rao angular uncertainty is shown in Figure 6.5 as a function of SplineMPE MuEX energy, which is well centered at a ratio of 1.

6.1.1.2 Time

The models investigated in this dissertation assume that neutrinos are produced coincident with the gamma-ray emission of a GRB. For generality, the signal time PDF is constant for the entire gamma emission duration (T_{100}). To also include the possibility of slightly early or late neutino emission, normal tails are added to the signal time PDF at the ends of the T_{100} range. The standard deviation of these tails σ_T is equal to the T_{100} of the burst, with minimum and maximum possible values of 2 s and 30 s, respectively. The normal tails are cut off at $4\sigma_T$, setting the signal time PDF to zero beyond these times. The background time PDF is constant over the time

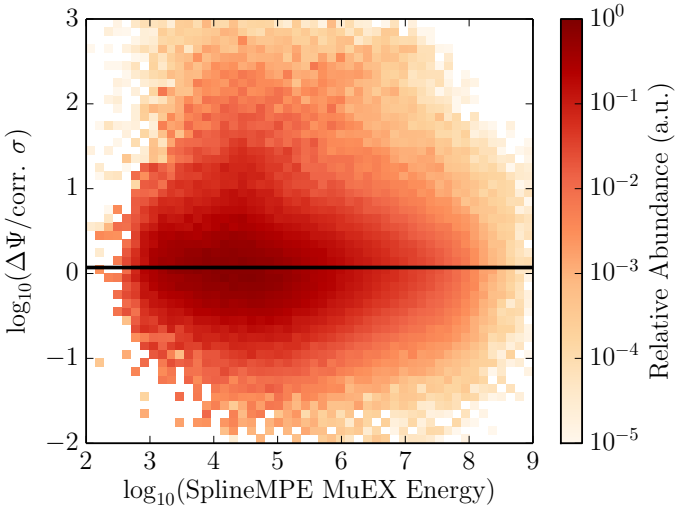

Figure 6.5: The corrected pull ratio in IC86-2011 simulated E^{-2} ν_μ data as a function of SplineMPE MuEX energy.

scales of a GRB. For times where the signal time PDF is non-zero, the background time PDF therefore has a value of $1/(T_{100} + 8\sigma_T)$. The time PDF ratio for several different T_{100} values are shown in Figure 6.6.

6.1.1.3 Energy

The reconstructed SplineMPE MuEX energy corresponds to the muon's energy as it enters the IceCube detector, meaning it can only be interpreted as a lower bound to the neutrino energy. It is still well correlated with the neutrino energy, however, as shown in Figure 4.3. This reconstructed energy can therefore be used in the signal and background energy PDFs.

The energy PDFs for background are derived directly from data not temporally coincident with GRBs at the final events level. In the Northern Hemisphere ν_μ search, these PDFs were extrapolated with ν_μ simulation of atmospheric neutrinos, the dominant source of background for that analysis. The primary background of this analysis is atmospheric muons, however, and though CORSIKA simulation can match the data well, it does not include a simulation of the IceTop veto, a critical

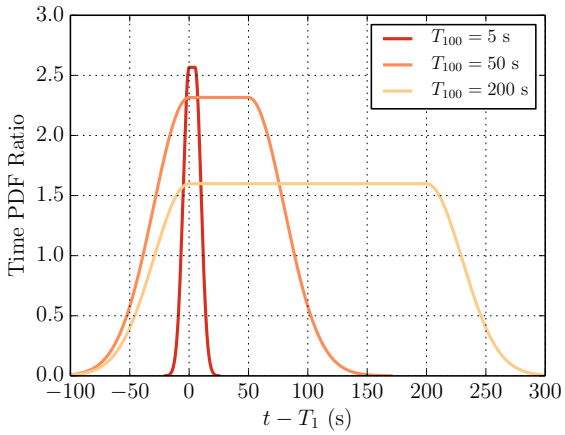

Figure 6.6: The signal-to-background time PDF ratio for a number of GRB T_{100} values.

element of reducing background in this analysis. Therefore, only off-time data can be used to define the background energy PDF.

Simulated ν_μ events at the final event level, weighted to a generic astrophysical E^{-2} spectrum, are used for the signal energy PDF. This is the expected energy spectrum for a wide class of astrophysical particle accelerators, and is useful for sensitivity to a wide range of peak emission energies for GRB models.

The ratio of the signal to background energy PDFs is shown in Figure 6.7 for every year of analysis, showing signal events attain larger PDF ratio values at large energies. Displayed with it is a smoothing spline fit to the binned ratios, allowing fast evaluation of ratio for an arbitrary MuEX energy value. At energies where there is no simulation or data, the ratio is taken to be that of the nearest measured ratio.

6.2 Frequentist Method

The final significance of the measured test statistic is evaluated using frequentist statistics. The consistency of the background-only hypothesis (the null) to the final test statistic is calculated through a p-value, equivalent to the fraction of experiments expected to yield a test statistic as large or larger than that actually observed.

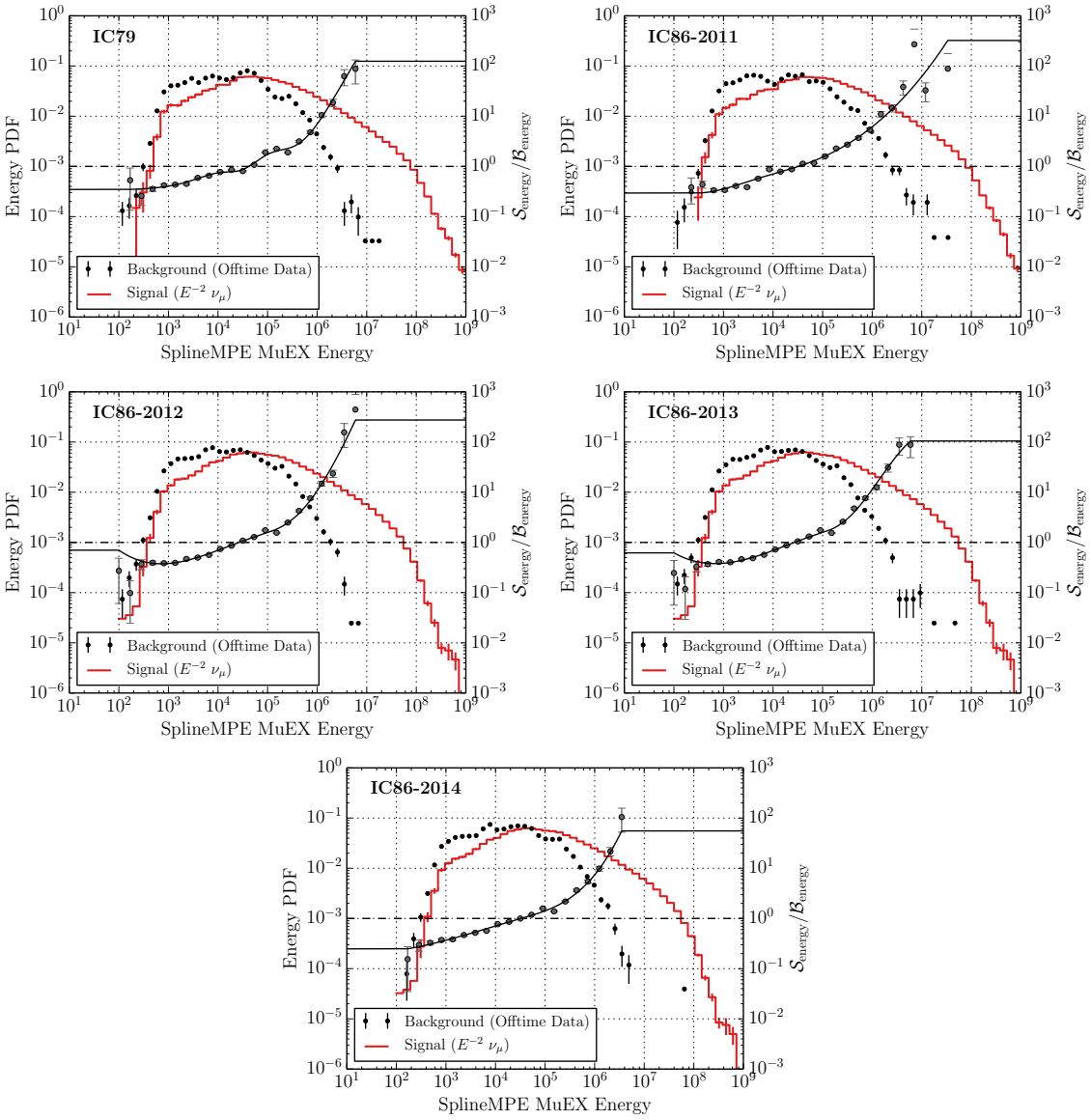

Figure 6.7: The energy PDF ratio (grey circles) for every year of analysis, with the background and signal energy PDFs shown in the black points and red lines, respectively. The ratios are fit with a spline, shown in the black line, where if there is no simulation or data the ratio is taken to be that of the nearest spline fit ratio.

Discovery of a signal from GRBs therefore amounts to rejection of the null at the 5σ level ($p = 2.87 \times 10^{-7}$) under the typical particle physics convention. The following section first describes how the background-only test statistic distribution is characterized. Then, the method for determining the sensitivity and discovery potential of

this analysis to a neutrino signal from GRBs is described. Finally, the optimization of the analysis as a function of BDT score cut is discussed.

6.2.1 Background Characterization

The background-only test statistic distribution is characterized through Monte Carlo simulated trials, where background events are generated and injected randomly with respect to GRB times and test statistic values are calculated. The total number of events injected for each GRB g, denoted by $\langle n_b \rangle_g$, is determined from the background data rate multiplied by the length of the search window $T_{100,g} + 8\sigma_{T,g}$. To account for the yearly variation in the atmospheric muon rate, a sinusoidal function is fit to the measured data rate as a function of date, shown in Figure 6.8. The exact number of events injected N_g in each trial for a given GRB g is then drawn from the Poisson distribution

$$P\Big(N_g|\langle n_b \rangle_g\Big) = \frac{\Big(\langle n_b \rangle_g\Big)^{N_g}}{N_g!} \exp\Big(-\langle n_b \rangle_g\Big). \tag{6.9}$$

The times of these events are randomly sampled uniformly within the GRB's search window, and uniformly in azimuth in the range $[0, 2\pi)$.

The energy, zenith, and angular uncertainty characteristics of these injected events are then drawn from distributions defined from background data. First, the SplineMPE MuEX value of each event is drawn directly from the background MuEX distribution. The SplineMPE reconstructed zenith distribution is then characterized in 10 bins of SplineMPE MuEX energy of equal statistics; the event zenith values are then drawn randomly from the distribution corresponding to their selected MuEX value. Each MuEX bin is then divided into 10 bins according to SplineMPE reconstructed zenith of the background data, each bin with equal statistics. The SplineMPE Cramer-Rao angular uncertainty distribution is then characterized from

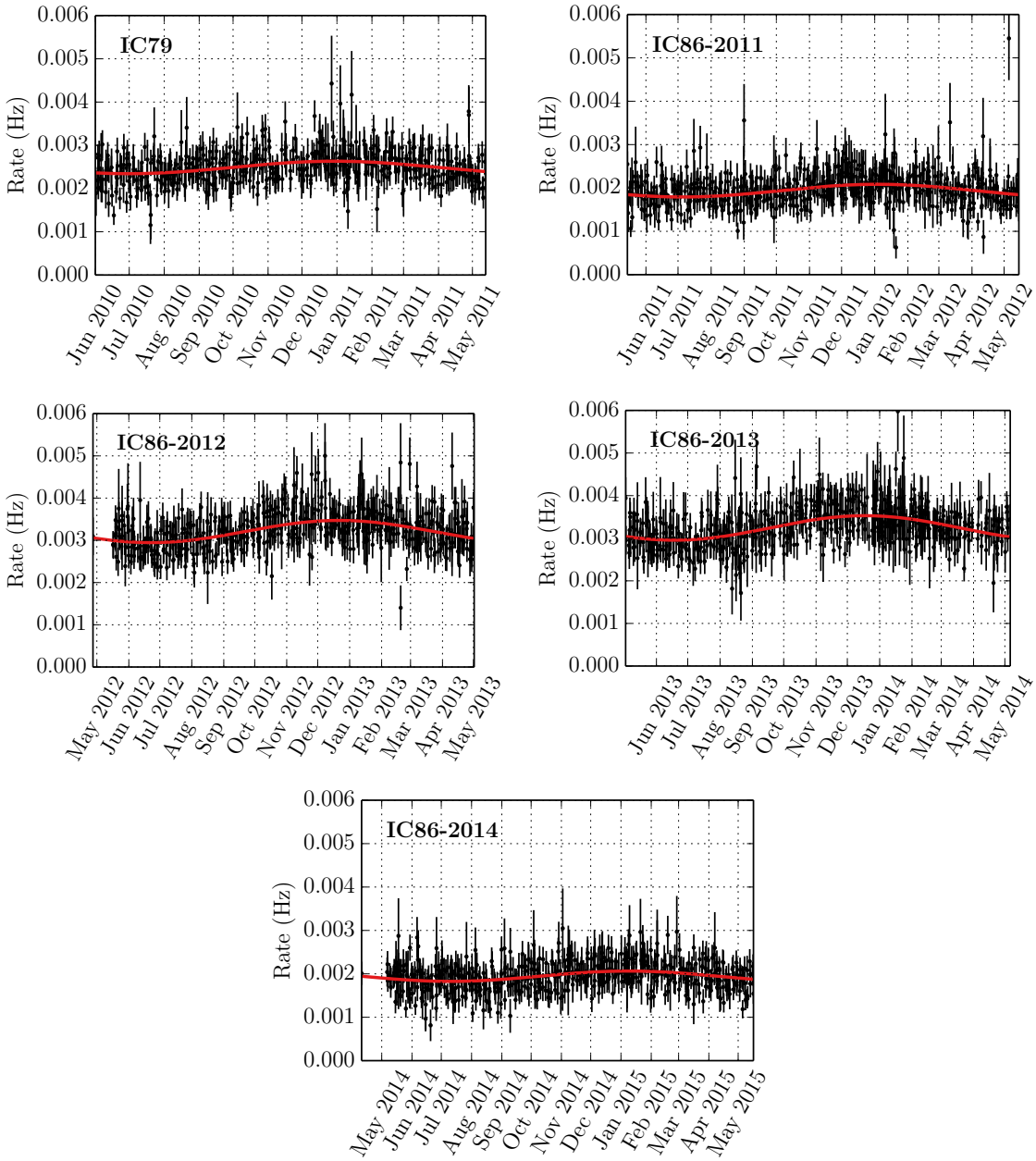

Figure 6.8: Background data rate at the final event level in runs without a GRB, as a function of date. The seasonal variation is fit with a sinusoidal function, shown in red.

background data for each of these MuEX–SplineMPE zenith bins. Finally, the angular uncertainty of each event is randomly sampled from these SplineMPE Cramer-Rao distributions corresponding to the event's MuEX energy and SplineMPE zenith.

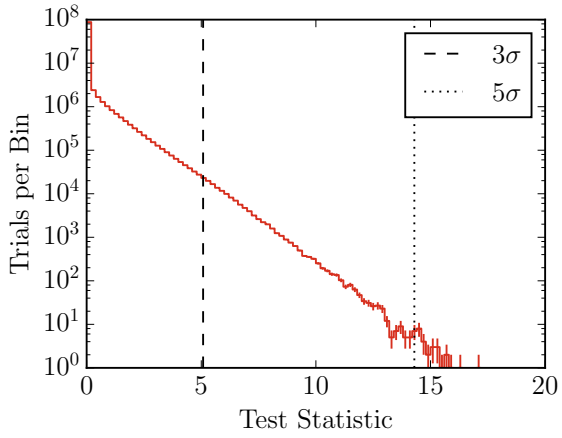

Figure 6.9: IC86-2011 background-only stacked test statistic distributions at the final event selection level, with various test statistic discovery thresholds indicated. Note that the median test statistic is zero.

Once events have been randomly generated and injected for all GRBs in the sample, a test statistic is calculated for that trial. Here, a stacked test statistic is calculated for each season analysis separately, where all coincident events in a season are scored within the sum of (6.3) with respect to their coincident GRB, and the total background rate is calculated as $\langle n_b \rangle = \sum_g \langle n_b \rangle_g$. Performing many such Monte Carlo trials fully characterizes the background test statistic distribution for any desired p-value discovery threshold. An example background-only test statistic distribution for 10^8 trials from the IC86-2011 analysis at the final event level is shown in Figure 6.9, with 3σ and 5σ threshold test statistics indicated.

6.2.2 Randomized Signal Injection

Signal event injection is performed directly using simulated events sampled in a circle of radius 11° around the true GRB location, and reweighted according to (4.28) for investigated models. The weight w_i of each event i corresponds to the rate at which an event will be measured in the analysis; the injection therefore occurs according to a sampling from the Poissonian distribution with mean w_i. Because of the large statistics of the simulated data sets used, the per-event weight will be much

smaller than one ($w_i \ll 1$), meaning the measured rates of zero or one dominate, with the probability of measurement (injection) once being

$$p_i = \frac{w_i^1}{1!} e^{w_i} \approx w_i. \tag{6.10}$$

Each injected event is evaluated in the energy PDF ratio according to their MuEX energy, and in time the events are assumed to occur during the T_{100} of the associated GRB. The background space PDF is evaluated according to their reconstructed SplineMPE zenith. Finally, the space PDF is calculated using the opening angle between their reconstructed SplineMPE direction and the true simulated ν_μ direction that has been smeared with a 2D normal distribution with width equal to the angular uncertainty of their associated GRB. These event scores are then included within the test statistic calculation.

Two useful signal hypotheses are tested with this signal injection: a distributed signal hypothesis and a single source signal hypothesis. In the distributed signal hypothesis, all GRBs in the sample have an associated sample of simulated events that are considered for injection. This situation is analogous to each GRB contributing a small neutrino fluence to a measured neutrino flux, which could be discovered through stacking these separate signals. Conversely, the single source hypothesis considers the simulated events from a single random GRB in the sample for signal injection. This would be analogous to a single GRB in an analysis dominating a measured neutrino flux (e.g. due to its proximity to Earth, or a large measured gamma-ray fluence, etc.).

6.2.3 Analysis Optimization

The analysis can be performed at any arbitrary BDT score cut, though ideally this cut would optimize the sensitivity of the analysis to a given neutrino signal. This amounts to the smallest possible neutrino fluence that yields a discovery-level

final test statistic. Two types of test statistic thresholds in particular are useful. First, the median background-only test statistic can be used to estimate the limits one can set at the end of the analysis should no signal be discovered: the signal fluence that yields a test statistic distribution where 90% of trials have a test statistic greater than the median background-only test statistic corresponds to the median 90% confidence level (CL) Neyman upper limit [134] of the analysis, sometimes called the analysis *sensitivity*. Second, the $X\sigma$ background-only test statistic threshold is used to estimate the *discovery potential* of the analysis: the signal fluence that yields a test statistic distribution that surpasses the $X\sigma$ threshold in either 50% or 90% of trials.

The BDT score cut is chosen such that the median upper limit sensitivity and discovery potentials are optimized, achieved by determining these signal fluence measures in a scan of possible BDT score cuts. At each possible BDT score cut, 10^8 background-only trials are used to characterize the background-only test statistic distribution and obtain discovery thresholds. Trials including signal and background event injection are then performed to determine the sensitivity and discovery potential at each BDT score cut. The optimization scans for the IC86-2011 analysis are shown in Figure 6.10 for a distributed E^{-2} signal. Here, because the median background-only test statistic at these BDT score cuts is zero, the median possible upper limit corresponds exactly to the best possible upper limit of the analysis (i.e. when the final measured test statistic is $\mathcal{T} = 0$).

6.3 Modifications to the Stacked Test Statistic

Previous gamma-ray burst (GRB) analyses have yielded results consistent with background, allowing stringent limits to be placed on GRB neutrino production models [25–27]. These limits now exclude the neutrino fluxes required for discovery in a single year stacked, prompt GRB analysis. Simply performing further stacked analy-

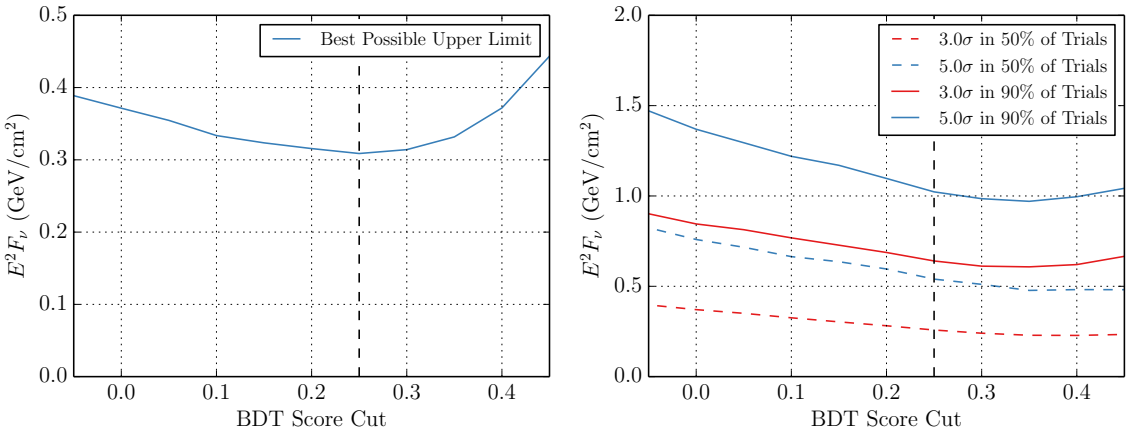

Figure 6.10: Optimization of IC86-2011 stacked analysis to a distributed E^{-2} fluence, with final BDT score cut indicated with the black dashed line. Left: sensitivity optimization, Right: discovery potential optimization.

ses, therefore, will likely prove unfruitful for discovery in the near term should IceCube desire to discover neutrinos from GRBs. It is conceivable, though, that through stacking many years of analysis a signal may slowly emerge. For now, IceCube should be prepared to claim evidence or discovery from the first observation of a high-quality neutrino-candidate coincidence with a GRB, motivating changes to the standard GRB test statistic calculation.

Though stacked GRB analyses treat all GRBs as equally likely to produce a measurable neutrino signal and adds them together to maximize the significance of this signal, the size of the prompt search for neutrino events is entirely ambiguous. One can just as easily treat each GRB individually. Each GRB g can have N_g coincident events with an expected background rate $\langle n_b \rangle_g$. Each GRB's test statistic is then just

$$\mathcal{T}_g = -(\hat{n}_s)_g + \sum_{i=1}^{N_g} \ln \left[\frac{(\hat{n}_s)_g \mathcal{S}(\mathbf{x}_i)}{\langle n_b \rangle_g \mathcal{B}(\mathbf{x}_i)} + 1 \right], \tag{6.11}$$

which is maximized with respect to the number of signal events $(\hat{n}_s)_g$ for that burst.

Such a per-burst test statistic naturally gives high significance to high-energy coincidences, as well as multiplet coincidences with a given burst. Thus, this test statistic may be better suited to claim discovery to a high-significance coincidence

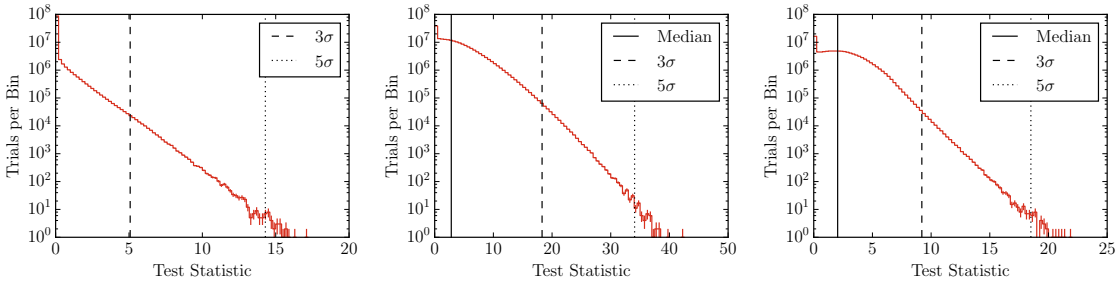

Figure 6.11: Background-only test statistic distributions for different test statistic methods for the IC86-2011 analysis at the final event selection level. Left: *stacked* $\mathcal{T}$ method, Middle: $\sum_g \mathcal{T}_g$ method, and Right: $\max(\{\mathcal{T}_g\})$ method.

with a single GRB. Further, for a real-time search for neutrinos from a GRB, this is exactly the value that must be calculated to determine a single observation's significance. From this per-burst test statistic, one can envision several new tests:

1. Take the maximum per-burst $\mathcal{T}_g$ for discovery (called the $\max(\{\mathcal{T}_g\})$ method for the remainder of the discussion).

2. Take the most significant per-burst p-value given $\mathcal{T}_g$ for discovery (called the *best p-of-p's* method for the remainder of the discussion).

3. A pseudo-stacked $\mathcal{T}$ can be calculated as $\mathcal{T} = \sum_g \mathcal{T}_g$ for discovery (called the $\sum_g \mathcal{T}_g$ method for the remainder of the discussion).

These new tests have been investigated under various signal hypotheses, compared to the classic stacked test statistic (called the *stacked* $\mathcal{T}$ method for the remainder of the discussion). Example distributions for the $\max(\{\mathcal{T}_g\})$ and $\sum_g \mathcal{T}_g$ test statistics are shown in Figure 6.11 compared to the original stacked test statistic for the IC86-2011 analysis at the final event selection level.

6.3.1 $\max(\{\mathcal{T}_g\})$ vs. *Best p-of-p's*

The correlation between the $\max(\{\mathcal{T}_g\})$ and the *best p-of-p's* method was first investigated. These methods both look for the most significant single burst in a sample,

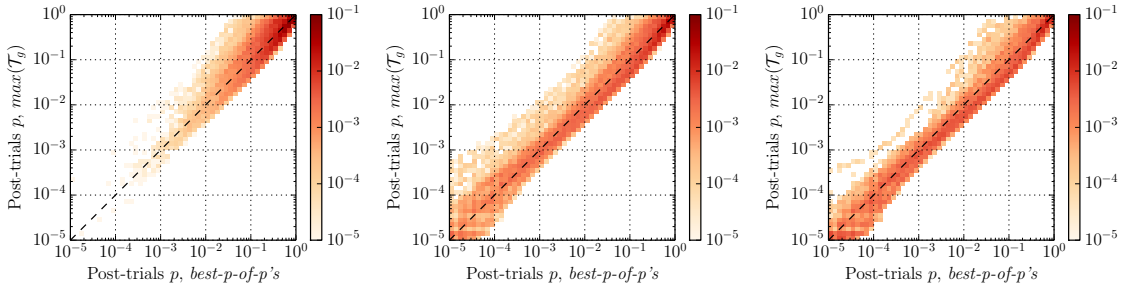

Figure 6.12: Post-trials p-value from the $\max(\{\mathcal{T}_g\})$ and *best p-of-p's* methods in trials of the IC86-2011 analysis at the final event level with different random source signal strengths. Color scale indicates the fraction of trials per bin. Left: background-only trials, Middle: $E^2dN/dE = 0.2\,\mathrm{GeV\,cm^{-2}}$, and Right: $E^2dN/dE = 0.5\,\mathrm{GeV\,cm^{-2}}$.

through slightly different means. The *best p-of-p's* method, however, is much more computationally intensive, as one must both characterize per-burst background-only test statistic distributions, as well as a background-only pre-trials p-value distribution; the $\max(\{\mathcal{T}_g\})$ method simply requires a background-only test statistic distribution. Should these methods be strongly correlated, the more simple to calculate $\max(\{\mathcal{T}_g\})$ is preferred.

The correlation between these methods was investigated by obtaining the post-trials p-value in both methods for a given trial in the IC86-2011 analysis. This was performed in 10^5 trials, for three different signal strengths ($E^2dN/dE = 0$, 0.2, and $0.5\,\mathrm{GeV\,cm^{-2}}$), where signal is injected in a single random burst each trial. The results of these trials are shown in Figure 6.12.

As can be seen, there is a very strong correlation between the post-trials significances of the two methods, especially when a single GRB in the sample produces a detectable neutrino fluence. The $\max(\{\mathcal{T}_g\})$ method actually yields slightly more significant post-trials p-values as seen in the $E^2dN/dE = 0.2$ and $0.5\,\mathrm{GeV\,cm^{-2}}$ signal strength tests. Further, in several small studies, it appeared both methods had nearly the same discovery potential and sensitivity. Thus, only the $\max(\{\mathcal{T}_g\})$ method is investigated further, given its simplicity to calculate.

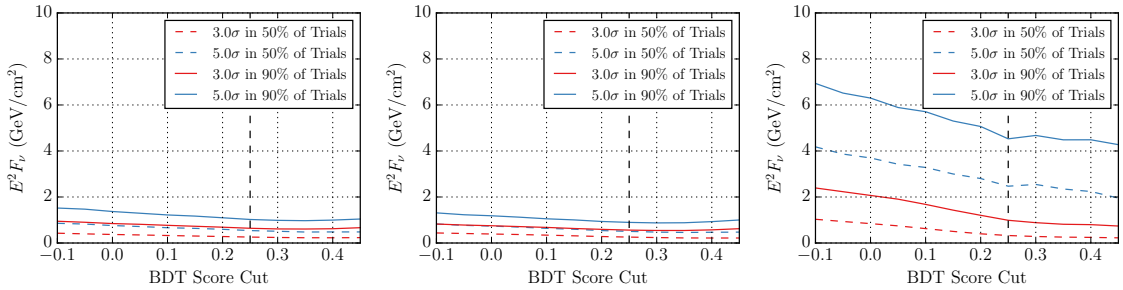

Figure 6.13: Discovery potential optimization for the test statistic methods for a distributed E^{-2} fluence in the IC86-2011 analysis. The y-axis is the total fluence distributed to all GRBs in the sample such that $X\%$ of trials surpass the given significance threshold. Final BDT score cut is indicated by the vertical dashed black line. Left: *stacked* $\mathcal{T}$ method, Middle: $\sum_g \mathcal{T}_g$ method, and Right: $\max(\{\mathcal{T}_g\})$ method.

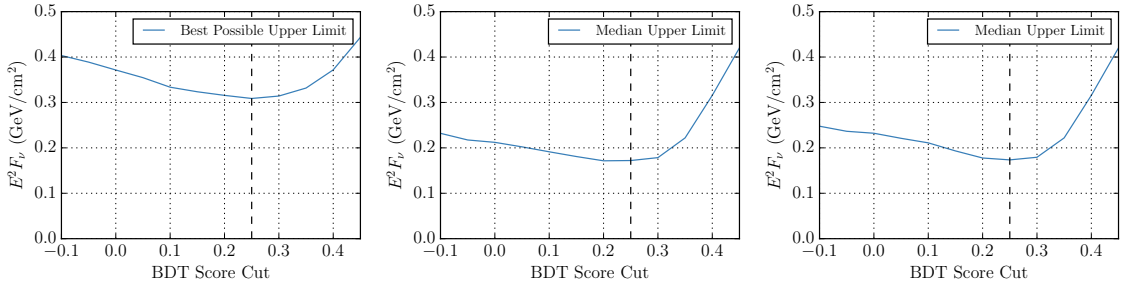

Figure 6.14: Sensitivity optimization for the test statistic methods for a distributed E^{-2} fluence in the IC86-2011 analysis. The y-axis is the total fluence distributed to all GRBs in the sample that surpasses the median test statistic threshold in 90% of trials. Final BDT score cut is indicated by the vertical dashed black line. Left: *stacked* $\mathcal{T}$ method, Middle: $\sum_g \mathcal{T}_g$ method, and Right: $\max(\{\mathcal{T}_g\})$ method.

6.3.2 IC86-2011 Southern Hemisphere Track Analysis Optimization

The sensitivity and discovery potential optimization in the IC86-2011 analysis was investigated for the *stacked* $\mathcal{T}$, $\sum_g \mathcal{T}_g$, and $\max(\{\mathcal{T}_g\})$ methods to an E^{-2} ν_μ signal. At each BDT score cut, background-only test statistic distributions are generated from 10^8 trials to establish discovery thresholds. Discovery potential fluence and median sensitivities in each method are determined for distributed fluence and single source hypotheses, with results shown in Figures 6.13–6.16. The optimal BDT cut of the analysis is indicated by the vertical black dashed line in all optimization figures.

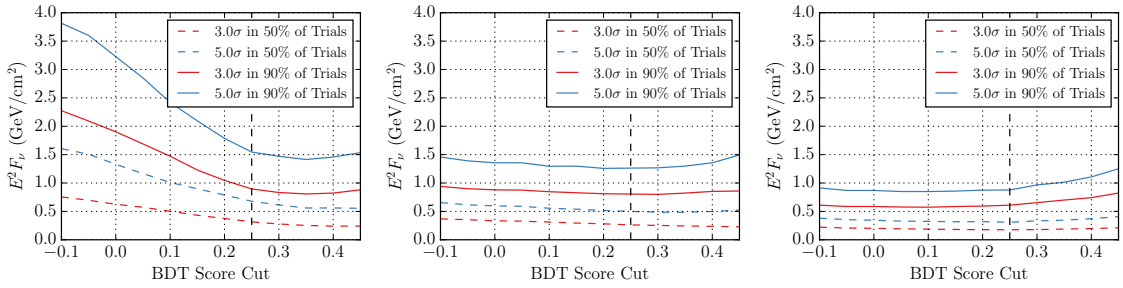

Figure 6.15: Discovery potential optimization for the test statistic methods for a single random E^{-2} source in the IC86-2011 analysis. The y-axis is the fluence of the random source GRB such that $X\%$ of trials surpass the given significance threshold. Final BDT score cut is indicated by the vertical dashed black line. Left: *stacked* $\mathcal{T}$ method, Middle: $\sum_g \mathcal{T}_g$ method, and Right: $\max(\{\mathcal{T}_g\})$ method.

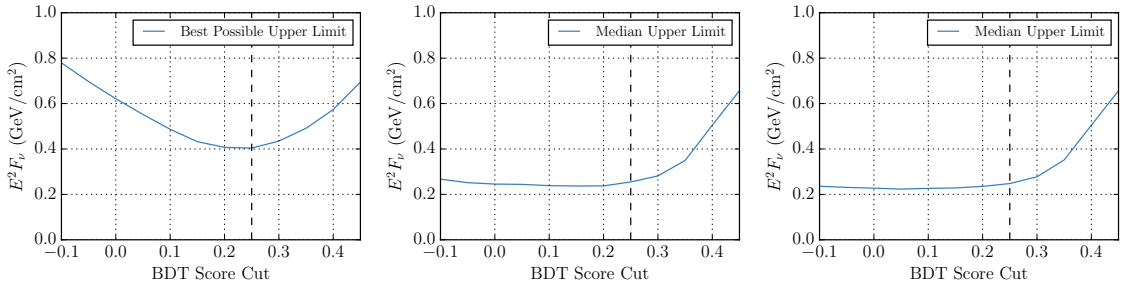

Figure 6.16: Sensitivity optimization for the test statistic methods for a single random E^{-2} source in the IC86-2011 analysis. The y-axis is the fluence of the random source GRB that surpasses the median test statistic threshold in 90% of trials. Final BDT score cut is indicated by the vertical dashed black line. Left: *stacked* $\mathcal{T}$ method, Middle: $\sum_g \mathcal{T}_g$ method, and Right: $\max(\{\mathcal{T}_g\})$ method.

The discovery potential of the *stacked* $\mathcal{T}$ and $\sum_g \mathcal{T}_g$ methods to a distributed fluence are considerably better than that of the $\max(\{\mathcal{T}_g\})$ as demonstrated by Figure 6.13. This is as expected, given the $\max(\{\mathcal{T}_g\})$ method looks for a single high quality coincidence, while the other two methods can combine coincidences with several GRBs for discovery. The method sensitivities shown in Figure 6.14 are slightly surprising, in that the $\max(\{\mathcal{T}_g\})$ method is capable of the best median limits in the Southern Hemisphere hemisphere track analysis. However, in light of its poor discovery potential to a distributed fluence, the $\max(\{\mathcal{T}_g\})$ would likely set poor limits in the case of observing a background up-fluctuation compared to the other two methods. The somewhat poor sensitivity of the *stacked* $\mathcal{T}$ method can be partially

attributed to the large fraction of trials resulting in $\mathcal{T} = 0$, both with and without signal injection. As will be demonstrated in Section 6.3.3, the sensitivity of this method converges with the others when performing the analysis over several seasons of data. The $\sum_g \mathcal{T}_g$ performs well in both discovery potential and sensitivity.

The discovery potentials of the different methods to a single, random source is shown in Figure 6.15. As expected, the $\max(\{\mathcal{T}_g\})$ method has the best discovery potential to single source with a detectable neutrino fluence. This figure also reveals each method's tolerance to background coincidences. The $\max(\{\mathcal{T}_g\})$ prefers loose BDT score cuts, as the background coincidence rate for any given burst is very low. The *stacked* $\mathcal{T}$ method prefers a tighter BDT score cut as the stacking requires a very low total background rate. The $\sum_g \mathcal{T}_g$ method shows much less dependence on the BDT score cut, being a hybrid of the previous two methods.

The $\max(\{\mathcal{T}_g\})$ method has the best sensitivity to a single source as shown in Figure 6.16, with the $\sum_g \mathcal{T}_g$ method showing a similar sensitivity. The *stacked* $\mathcal{T}$ method is seen to be the poorest method in both discovery potential and sensitivity to a single source, though the sensitivity weakness is partially a function of the cutoff of the test statistic at zero.

6.3.3 Method Scaling

As Section 6.3.2 indicates that the new test statistic methods are more sensitive to both distributed fluence and single source hypotheses than the standard *stacked* $\mathcal{T}$ method, it is necessary to investigate how such methods will scale with many years of observation. It is entirely plausible that such gains are limited to low number of observations, but degrade with large numbers of GRB observations.

To test this, discovery potentials and sensitivities were calculated for both the IC86-2011 Southern Hemisphere and Northern Hemisphere track analyses (treated separately) at the optimal BDT score cuts for N_s repeated observations of the same

burst samples. The background and signal event injection of these repeated observations are independent, meaning such a test is analogous to scaling an analysis over N_s years. For the *stacked* $\mathcal{T}$ and $\sum_g \mathcal{T}_g$ methods, the final test statistic value of the trial is calculated through the standard $\mathcal{T} = \sum_{s,c} \mathcal{T}_{c,s}$ formulation; for the $\max(\{\mathcal{T}_g\})$ method, simply the maximum test statistic from any GRB in the repeated burst sample is taken. The background-only test statistic distributions are generated separately for each number of N_s repeated observations, ranging from 1 to 10 in one year increments.

Signal injection under both the distributed fluence and single source hypotheses are performed. In the single source hypothesis, a single random burst in the entire repeated sample is selected (rather than one per-year of observation), representing an increasingly pessimistic guess for the fraction of observable bursts in the sample (i.e. one per $N_s \times N_{\mathrm{GRB}}$ GRBs). For simplicity, only the median upper limit and discovery potential of 3σ in 90% of trials to these source hypotheses are investigated. It is assumed other discovery potentials will scale similarly to this 3σ test case. The results are summarized in Figures 6.17–6.20.

The scaling of the different methods' discovery potential to a distributed E^{-2} fluence is shown in Figure 6.17. In the Southern Hemisphere track search, the *stacked* $\mathcal{T}$ and $\sum_g \mathcal{T}_g$ methods appear to reach equivalence over many years of observation, while in the Northern Hemisphere track search the *stacked* $\mathcal{T}$ is best regardless of the amount of observation. This is likely due to the irreducible atmospheric neutrino background of the Northern Hemisphere track search, which diminishes the effectiveness of the $\sum_g \mathcal{T}_g$ method.

In setting limits to a distributed E^{-2} fluence, the *stacked* $\mathcal{T}$ is seen to be best in both the Southern Hemisphere and Northern Hemisphere track analyses, as shown in Figure 6.18, though the $\max(\{\mathcal{T}_g\})$ is capable of setting comparable limits. Given how poor the $\max(\{\mathcal{T}_g\})$ method's discovery potential is to a distributed E^{-2} fluence,

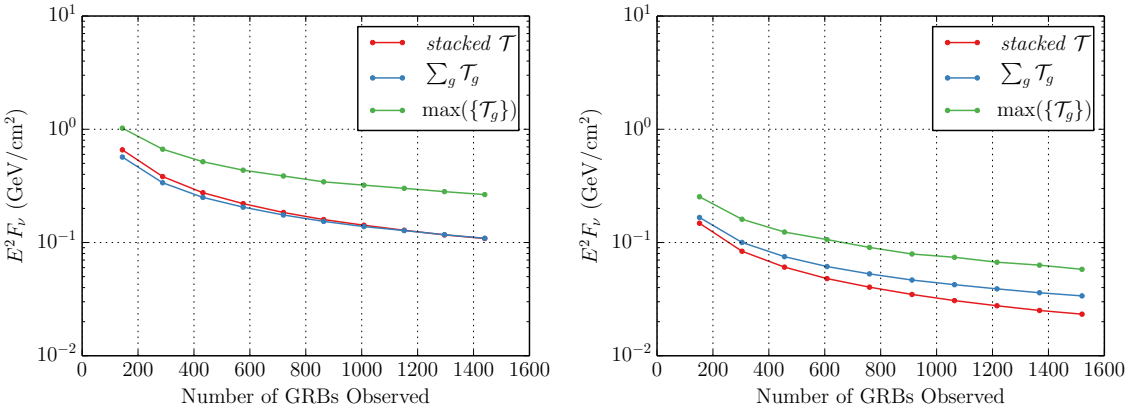

Figure 6.17: Scaling of the discovery potential for 3σ result in 90% of trials for each test statistic method in the IC86 track analyses as a function of total number of GRBs observed, given a distributed E^{-2} signal fluence. The y-axis is the per-year fluence required to reach this discovery threshold. Left: IC86-2011 Southern Hemisphere track analysis, Right: IC86-2011 Northern Hemisphere track analysis.

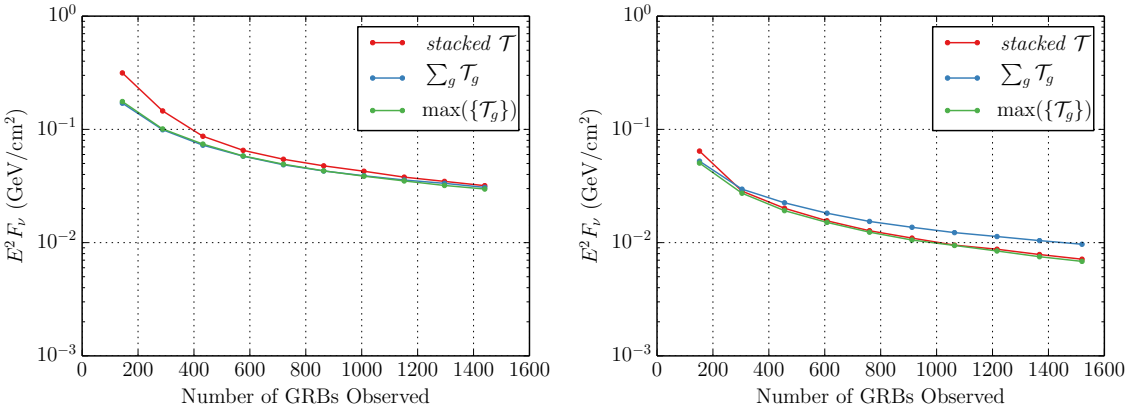

Figure 6.18: Scaling of the median upper limit for each test statistic method in the IC86 track analyses as a function of total number of GRBs observed, given a distributed E^{-2} signal fluence. The y-axis is the per-year fluence required to reach the median background-only test statistic threshold in 90% of trials. Left: IC86-2011 Southern Hemisphere track analysis, Right: IC86-2011 Northern Hemisphere track analysis.

however, it will likely set quite poor limits compared to *stacked* $\mathcal{T}$ limits should an experiment observe an up-fluctuation in background.

The scaling of the discovery potential and median upper limits of the methods to a single, random E^{-2} source are shown in Figures 6.19 and 6.20, respectively. In both Southern Hemisphere and Northern Hemisphere track analyses, the max($\{\mathcal{T}_g\}$) method has the best discovery potential and sensitivity to a single source, as expected.

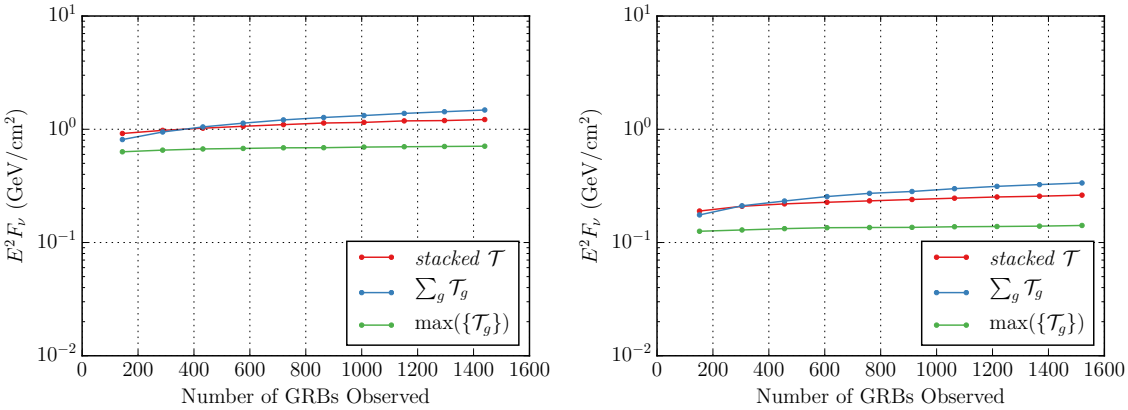

Figure 6.19: Scaling of the discovery potential for 3σ result in 90% of trials for each test statistic method in the IC86 track analyses as a function of total number of GRBs observed, given a single E^{-2} source in the entire GRB sample. The y-axis is the single burst neutrino fluence required to reach this discovery threshold. Left: IC86-2011 Southern Hemisphere track analysis, Right: IC86-2011 Northern Hemisphere track analysis.

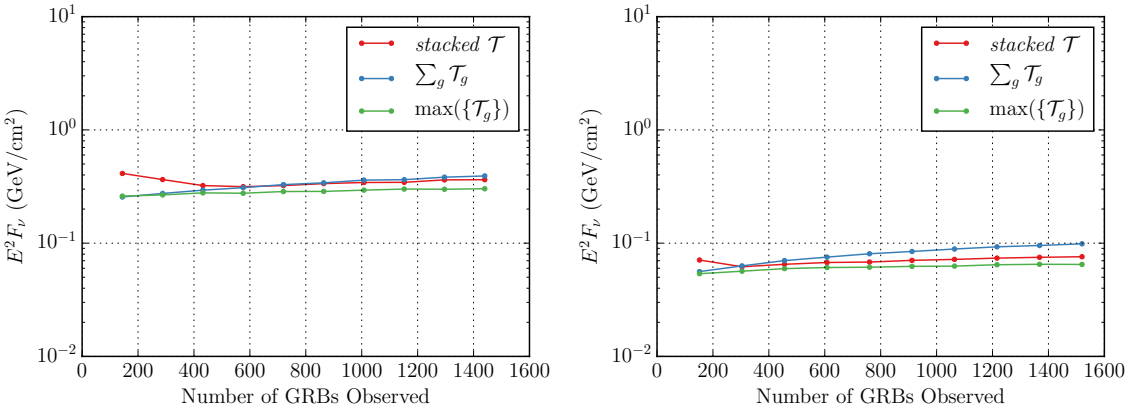

Figure 6.20: Scaling of the median upper limit for each test statistic method in the IC86 track analyses as a function of total number of GRBs observed, given a single E^{-2} source in the entire GRB sample. The y-axis is the single burst neutrino fluence required to reach the median background-only test statistic threshold in 90% of trials. Left: IC86-2011 Southern Hemisphere track analysis, Right: IC86-2011 Northern Hemisphere track analysis.

Over several years of observation, the *stacked* $\mathcal{T}$ method does have comparable median upper limits to a single source.

In both source hypotheses, the $\sum_g \mathcal{T}_g$ shows the poorest scaling in both discovery potential and median upper limits for Southern Hemisphere and Northern Hemisphere track analyses. This is likely due to large amounts of low-significance background

coincidence events that, when summed, degrade the significance of signal events. The *stacked* $\mathcal{T}$ method avoids this problem through an increased estimate of $\langle n_b \rangle$ in the test statistic calculation that reduces the contribution of the low-quality background coincidences to the total test statistic. The $\max(\{\mathcal{T}_g\})$ method also avoids this to an extent by only taking the best coincidence, though its sensitivity is to a single burst.

6.3.4 Summary and Proposed Final Method

Over several years of observation in both track and cascade channels, only a few events have been seen in spatial and temporal coincidence with GRBs in IceCube data. Though these events may be the first signs of a neutrino signal from GRBs, thus far they have been consistent with background, resulting in stringent limits on neutrino production in GRBs. It is conceivable that slowly, a statistically significant signal may start to be built. In the near-term, however, IceCube should be prepared to claim evidence or discovery of neutrino production in GRBs with the observation of the first high-significance coincidence.

The current stacking analysis is inadequate for this purpose, motivating investigation into different test statistic methods reported above. It is seen that by calculating test statistics on a per-burst basis and taking the best test statistic from all bursts, one can significantly improve the discovery potential of a prompt GRB analysis to a population of GRBs whose neutrino production is dominated by a single burst. This method also moves naturally to real-time searches for neutrinos from GRBs with IceCube, allowing IceCube to fully participate in multi-messenger astronomy of GRBs. Model limits for neutrino production in GRBs can then still be performed by calculating the standard stacked test statistic and combining with previous published searches.

A method calculating a stacked test statistic through a sum of per-burst test statistics was also investigated. Though it initially showed promise in studies of

discovery potential and sensitivity for a single Southern Hemisphere track season analysis, it showed poor scaling when moving to observations over multiple seasons of observations, especially in Northern Hemisphere track analyses.

Moving forward, a new optimization procedure is proposed for IceCube prompt GRB neutrino analyses. One should calculate the discovery potential of an analysis to a single-source hypothesis with the $\max(\{\mathcal{T}_g\})$ method, optimizing with respect to BDT score cut. This cut should then be constrained by the optimal cut for discovery and limit setting to a distributed source hypothesis with the standard *stacked* $\mathcal{T}$ method. Any limits to neutrino production in GRBs should be obtained from the *stacked* $\mathcal{T}$ result, as it is more robust to possible up-fluctuations in background compared to the $\max(\{\mathcal{T}_g\})$ method. Both methods are used for discovery as they are optimal in addressing two different source hypotheses, accounting for a trials factor penalty of 2 in reported post-trials p-values. This penalty is seen to degrade the discovery potential of either method by only a few percent.

6.4 Final Analysis Optimization

Using the proposed optimization methodology above, the final IC86-2011 BDT score cut optimization scans are shown in Figure 6.21 to a E^{-2} ν_μ spectrum near the final BDT score cut. Here, one attempts to simultaneously optimize the $\max(\{\mathcal{T}_g\})$ discovery potential to a single GRB neutrino source and the *stacked* $\mathcal{T}$ discovery potential to a distributed neutrino signal. Assuming a final result consistent with background, this discovery potential optimization is also compared to the best possible upper limit of the *stacked* $\mathcal{T}$ method. The final BDT score cut of > 0.25 is chosen. The procedure is replicated for the IC79, IC86-2012, IC86-2013, and IC86-2014 years of analysis to obtain final BDT score cuts for their BDTs: > 0.25 for IC79, IC86-2012, and IC86-2013, and > 0.275 for IC86-2014.

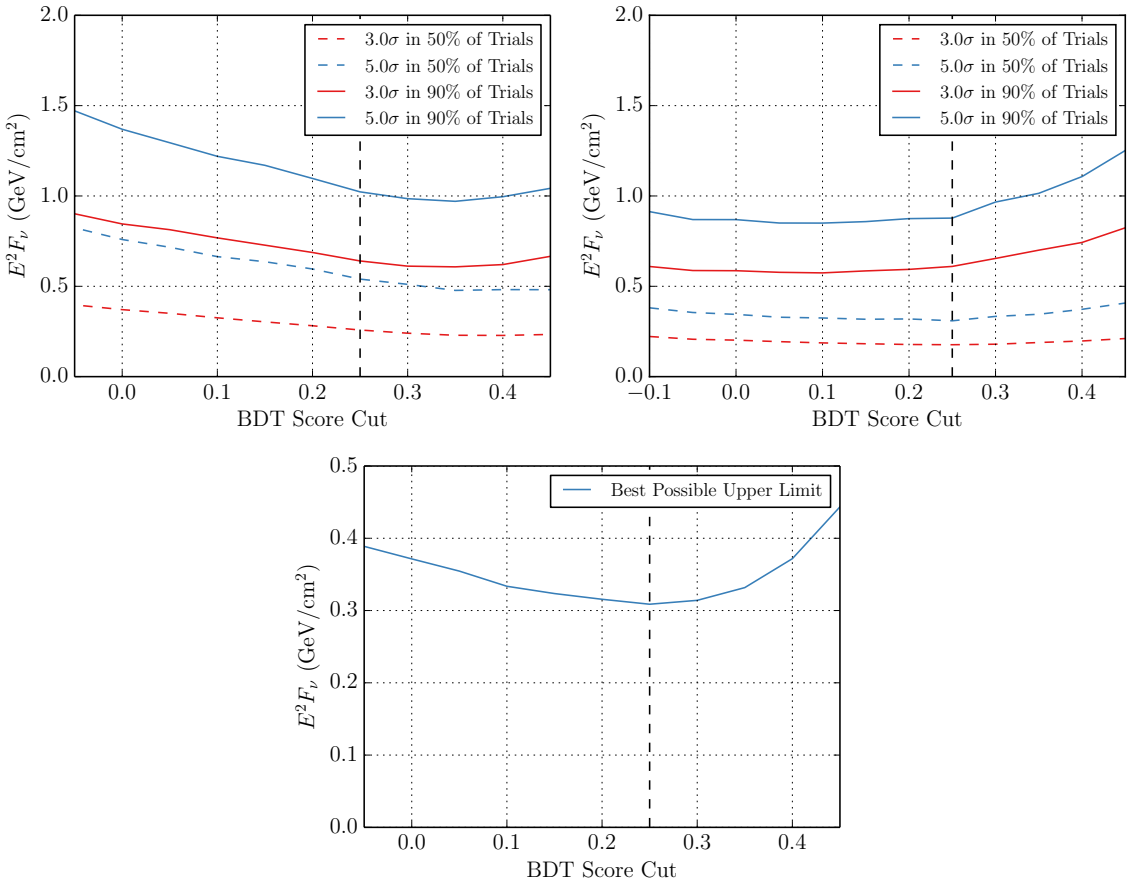

Figure 6.21: IC86-2011 optimization scans using the final proposed procedure. Top Left: discovery potential of the $max(\mathcal{T}_g)$ method to a single random E^{-2} source, Top Right: discovery potential of the *stacked* $\mathcal{T}$ method to a distributed E^{-2} signal, and Bottom: best possible upper limit of the *stacked* $\mathcal{T}$ method to a distributed E^{-2} signal. The final BDT score cuts is indicated with the dashed black line.

Optimization to other source spectrum hypotheses and signal energy PDF weightings were tested, under the same procedure above. It is found that the results are robust to these spectrum changes. Sensitivities of the max($\{\mathcal{T}_g\}$) method to a single source is largely unaffected by changes to the signal energy PDF, while improvements of ∼1% to discovery potential to more realistic GRB neutrino spectra (e.g. the Waxman-Bahcall double broken power law spectrum of [72]) can be achieved by down-weighting low-energy signal events. Discovery potentials and sensitivity to these same spectra assuming a distributed fluence hypothesis can be improved by ∼1% and ∼5%, respectively, with the *stacked* $\mathcal{T}$ method using the same low-energy

signal down-weighting. As these improvements are minimal in actual discovery potentials, the simple E^{-2}-weighted signal energy PDF is retained for consistency with previous Northern Hemisphere track and All-Sky cascade analyses.

Chapter 7

Results

Using the unbinned likelihood described in Chapter 6, events at the final analysis level were associated with 664 GRBs between May 2010 and May 2015 with the IceCube data collected by the detector in its 79-string and full 86-string configurations. The significance of these events were evaluated with both the stacked and per-GRB test statistics. The most significant coincidence occured during a GRB in the IC79 year of analysis, and was the only coincidence to contribute to a non-zero per-year stacked test statistic. This coincidence, however, is consistent with the background-only hypothesis allowing new limits to be placed on neutrino production models in GRBs.

This chapter discusses these results in detail, first describing the coincident event sample and significant events coincident with the analyzed GRBs. The implications of these results for GRB models when combined with previous results from the Northern Hemisphere ν_μ track [26] and All-sky cascade [27] analyses, as well as new results from three additional years of the Northern Hemisphere track analysis, are then described. The systematic uncertainty on these possible limits are first estimated in the context of the Southern Hemisphere track search, and then applied to limits calculated for the GRB neutrino production models presented in Section 2.3.

7.1 Five Year Southern Hemisphere Track Search Results

Events at the final analysis level were searched in coincidence with the 664 GRBs of the five year Southern Hemisphere sample. As a first check of this data, the number of events occuring during the non-zero window of any GRB's time PDF ratio were de-

Table 7.1: Measured number of events N coincident with analyzed GRBs, compared to the expected from off-time background data, $\langle n_b \rangle$. A p-value of these N is calculated relative to a Poisson distribution with mean $\langle n_b \rangle$.

Year	$\langle n_b \rangle$	N	Poisson p-value
IC79	61.0	64	0.321
IC86-2011	68.4	62	0.759
IC86-2012	93.6	93	0.496
IC86-2013	115.0	113	0.546
IC86-2014	60.0	60	0.466

termined (termed *on-time* events, labeled N) and compared to the expected number of background on-time events for a given analysis year $\langle n_b \rangle$, summarized in Table 7.1. In each year, the measured event rate is in good agreement with the expected background rate, given the p-value of a given N relative to a Poisson distribution with mean $\langle n_b \rangle$.

The unbinned likelihood method of Chapter 6 was then applied to this on-time event sample to determine the most significant coincidences temporally and spatially with the GRB sample. All coincidences that yield a non-zero per-GRB test statistic in the five-year sample are summarized in Table 7.2. Here, basic infomation about the GRBs and coincident events are described, including their angular uncertainty σ, angular separation $\Delta\Psi$, the measured gamma-ray fluence of the GRB, and the estimated energy of the coincident event. The significance of the coincidences are then summarized in two ways. Event signal-to-background PDF ratio values used in the test statistic calculation are provided to estimate relative event importance. The significance of the per-GRB test statistic is then given as a p-value calculated from that GRB's expected background-only test statistic distribution, constituting that GRB's pre-trials p-value. In parentheses, the post-trials p-value of this GRB coincidence is given, calculated relative the five-year Southern Hemisphere GRB analysis $\max(\{\mathcal{T}_g\})$ test statistic distribution expected from background.

Table 7.2: Southern Hemisphere track analysis significant events. The duration T_{100}, angular uncertainty σ (Fermi-GBM statistical-only uncertainties indicated by $*$), and total fluence of GRBs with coincident events are described. Coincident events are summarized in terms of their time relative to the GRB start time T_1, their angular uncertainty σ, angular displacement from the GRB location $\Delta\Psi$, and reconstructed muon energy. Event significance is estimated by their signal-to-background PDF ratio value $\mathcal{S}/\mathcal{B}$, while final GRB coincidence significance is given as pre-trials (post-trials) p-values relative to background-only test statistic distributions.

	Time	σ	$\Delta\Psi$	Fluence/Energy	Significance
GRB110105A	$T_{100} = 123.39\,\mathrm{s}$	$^*2.0^\circ$		$2.09 \times 10^{-5}\,\mathrm{erg\,cm^{-2}}$	$p = 0.037$ (0.9999)
Event 1	$T_1 + 102.0\,\mathrm{s}$	0.3°	13.1°	$\gtrsim 15\,\mathrm{TeV}$	$\mathcal{S}/\mathcal{B} = 2.2$
GRB110207A	$T_{100} = 109.32\,\mathrm{s}$	0.0132°		$4.4 \times 10^{-6}\,\mathrm{erg\,cm^{-2}}$	$p = 0.00035$ (0.397)
Event 1	$T_1 + 87.4\,\mathrm{s}$	0.3°	0.9°	$\gtrsim 12\,\mathrm{TeV}$	$\mathcal{S}/\mathcal{B} = 271.6$
GRB111205A	$T_{100} = 80.38\,\mathrm{s}$	0.1°		$1.7 \times 10^{-4}\,\mathrm{erg\,cm^{-2}}$	$p = 0.0023$ (0.982)
Event 1	$T_1 + 150.9\,\mathrm{s}$	18.7°	17.3°	$\gtrsim 482\,\mathrm{TeV}$	$\mathcal{S}/\mathcal{B} = 9.5$
GRB121127A	$T_{100} = 3.51\,\mathrm{s}$	0.08°		$9.34 \times 10^{-7}\,\mathrm{erg\,cm^{-2}}$	$p = 0.00054$ (0.996)
Event 1	$T_1 + 2.42\,\mathrm{s}$	60.1°	79.5°	$\gtrsim 175\,\mathrm{TeV}$	$\mathcal{S}/\mathcal{B} = 0.85$
GRB121231A	$T_{100} = 32.77\,\mathrm{s}$	$^*6.5^\circ$		$2.94 \times 10^{-6}\,\mathrm{erg\,cm^{-2}}$	$p = 0.036$ (0.999)
Event 1	$T_1 + 66.5\,\mathrm{s}$	0.5°	13.9°	$\gtrsim 24\,\mathrm{TeV}$	$\mathcal{S}/\mathcal{B} = 4.1$
GRB130909A	$T_{100} = 33.79\,\mathrm{s}$	$^*17.2^\circ$		$1.98 \times 10^{-6}\,\mathrm{erg\,cm^{-2}}$	$p = 0.01$ (0.912)
Event 1	$T_1 + 14.9\,\mathrm{s}$	0.2°	19.4°	$\gtrsim 53\,\mathrm{TeV}$	$\mathcal{S}/\mathcal{B} = 30.4$
GRB130924A	$T_{100} = 37.1\,\mathrm{s}$	$^*6.0^\circ$		$3.73 \times 10^{-6}\,\mathrm{erg\,cm^{-2}}$	$p = 0.033$ (0.9995)
Event 1	$T_1 + 92.6\,\mathrm{s}$	27.1°	8.0°	$\gtrsim 72\,\mathrm{TeV}$	$\mathcal{S}/\mathcal{B} = 1.3$
Event 2	$T_1 + 6.6\,\mathrm{s}$	0.4°	19.3°	$\gtrsim 2.8\,\mathrm{TeV}$	$\mathcal{S}/\mathcal{B} = 0.85$
GRB131119A	$T_{100} = 34.8\,\mathrm{s}$	$^*7.3^\circ$		$1.85 \times 10^{-6}\,\mathrm{erg\,cm^{-2}}$	$p = 0.025$ (0.995)
Event 1	$T_1 - 23.1\,\mathrm{s}$	0.4°	22.9°	$\gtrsim 16\,\mathrm{TeV}$	$\mathcal{S}/\mathcal{B} = 8.2$
GRB141012A	$T_{100} = 34.64\,\mathrm{s}$	$^*3.1^\circ$		$6.64 \times 10^{-6}\,\mathrm{erg\,cm^{-2}}$	$p = 0.014$ (0.999)
Event 1	$T_1 + 100.54\,\mathrm{s}$	11.5°	22.4°	$\gtrsim 114\,\mathrm{TeV}$	$\mathcal{S}/\mathcal{B} = 2.5$
GRB141013A	$T_{100} = 82.43\,\mathrm{s}$	$^*3.8^\circ$		$8.81 \times 10^{-6}\,\mathrm{erg\,cm^{-2}}$	$p = 0.016$ (0.999)
Event 1	$T_1 + 34.4\,\mathrm{s}$	17.6°	48.0°	$\gtrsim 459\,\mathrm{TeV}$	$\mathcal{S}/\mathcal{B} = 2.4$
Event 2	$T_1 + 97.9\,\mathrm{s}$	1.2°	75.9°	$\gtrsim 1\,\mathrm{TeV}$	$\mathcal{S}/\mathcal{B} = 2.2 \times 10^{-9}$
GRB150222C	$T_{100} = 74.75\,\mathrm{s}$	$^*11.32^\circ$		$3.84 \times 10^{-6}\,\mathrm{erg\,cm^{-2}}$	$p = 0.021$ (0.986)
Event 1	$T_1 + 22.73\,\mathrm{s}$	0.3°	24.5°	$\gtrsim 31\,\mathrm{TeV}$	$\mathcal{S}/\mathcal{B} = 8.3$
Event 2	$T_1 - 61.2\,\mathrm{s}$	0.2°	52.3°	$\gtrsim 50\,\mathrm{TeV}$	$\mathcal{S}/\mathcal{B} = 6.3 \times 10^{-3}$

The most significant coincidence (in both pre-trials and post-trials p-value) is found in the IC79 analysis coincident with GRB110207A, a Swift-localized long GRB. This event occured during the T_{100} of this GRB and had a reconstructed direction within 1° of the GRB, with a moderate reconstructed muon energy of $E_\mu \gtrsim 12\,\mathrm{TeV}$, yielding a signal-to-background PDF ratio of $\mathcal{S}/\mathcal{B} = 271.6$. A visualization of this event in the IceCube detector is shown in Figure 7.1, showing it to be a high-quality through-going track event.

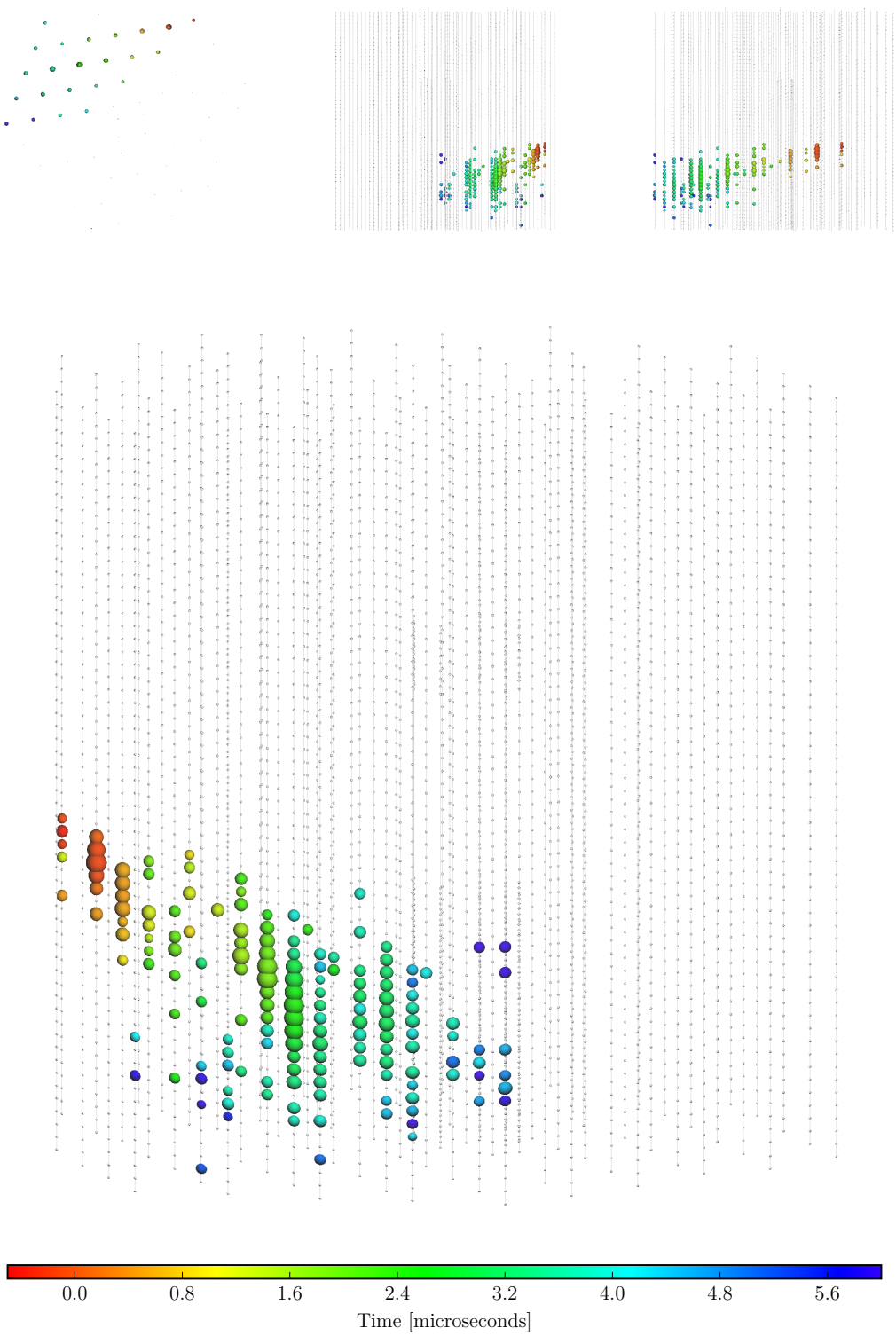

Figure 7.1: IceCube view of event coincident with GRB110207A. Colored DOMS indicate hits, with colorscale defining hit time and size hit intensity. Top: top and side views of event, Bottom: enlarged view of event.

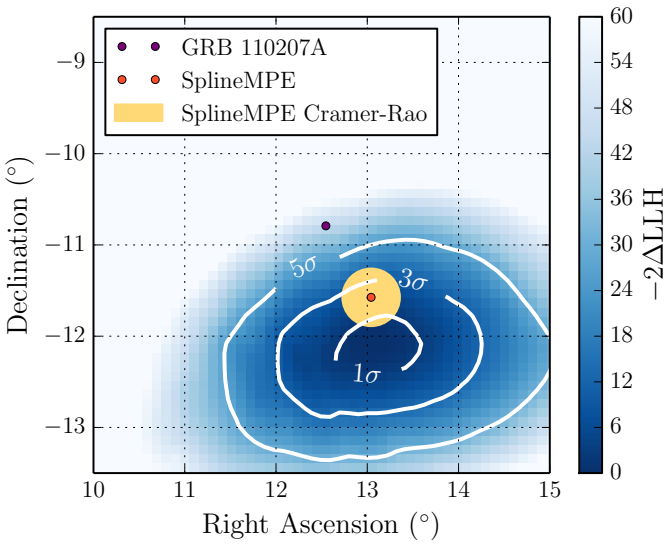

Figure 7.2: SplineMPE Millipede likelihood scan of GRB110207A coincident event. The 1σ, 3σ, and 5σ contours of this likelihood space are calculated by Wilks' theorem with two degrees of freedom [114].

Although the event is within 1° of the GRB location, accounting for angular uncertainty of this event and the GRB, GRB110207A is $\sim 3\sigma$ offset from the event reconstructed direction, reducing the significance of the coincidence. Simulations and reconstructions were performed of muons with similar energy and origin to the measured event, establishing that the reconstructed angular uncertainty of 0.3° is consistent with the median angular resolution of the SplineMPE reconstruction of such muons of 0.24°. Further, a full likelihood scan of the SplineMPE Millipede reconstruction was performed on this event to verify the quality of the SplineMPE reconstructed direction, with results shown in Figure 7.2. It shows that the minimum of the Millipede likelihood space is consistent with the SplineMPE reconstructed direction, while the GRB110207A location is $> 5\sigma$ from the Millipede reconstructed direction, supporting that this event is inconsistent with the GRB location. The post-trials significance of this event is also only $p = 0.397$, making it consistent with the background-only hypothesis. The per-GRB test statistic of this GRB is

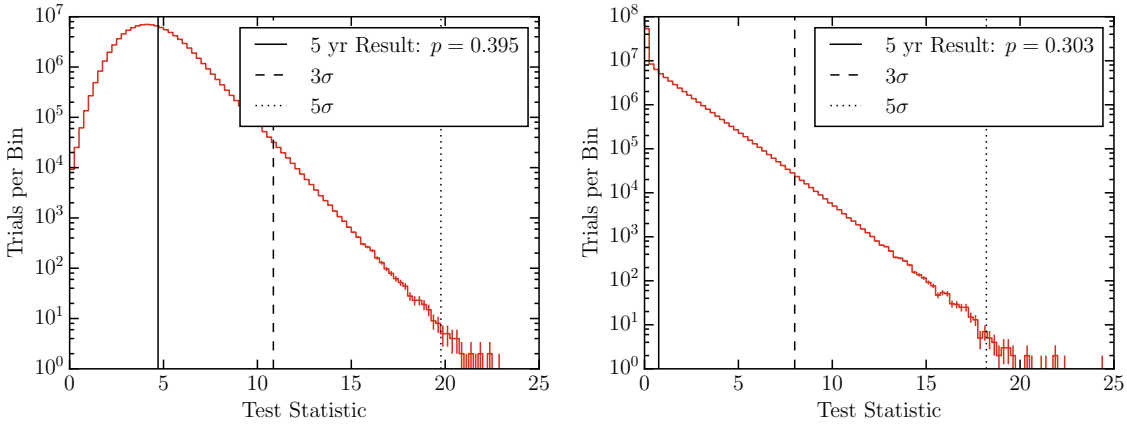

Figure 7.3: Background-only test statistic distributions for the Southern Hemisphere ν_μ track analysis compared to the measured values, and the 3σ and 5σ test statistic thresholds. Left: $\max(\{\mathcal{T}_g\})$ analysis; Right: *stacked* $\mathcal{T}$ analysis.

shown relative to the 5-year background-only test statistic distribution in Figure 7.3. Considered together, this event is concluded to be a background coincidence event.

The remaining coincident events of Table 7.2 are low significance coincidences, as measured by the event signal-to-background PDF ratios and GRB post-trials p-values. These coincidences fall into two categories: track events in coincidence with Fermi GBM poorly localized GRBs, or poorly reconstructed track events in coincidence with a GRB. In sum, the set of per-GRB coincidences observed are taken to be consistent with background.

The stacked test statistic of these coincidences were then calculated on a per-year basis. Only the IC79 year of analysis gave a non-zero stacked test statistic, calculated to be $\mathcal{T}_{\mathrm{ST,IC79}} = 0.7552$. The significance of the combined Southern Hemisphere track test statistic $\mathcal{T}_{\mathrm{ST}} = \sum_s \mathcal{T}_{\mathrm{ST},s} = 0.7552$ is found to be $p = 0.303$. This final combined stacked test statistic is shown relative to the background-only stacked test statistic in Figure 7.3.

7.1.1 Warm Source Population Analysis

The previously published Northern Hemisphere track analysis [26] was recently extended to the IC86-2012, IC86-2013, and IC86-2014 years of IceCube data, following the methodology presented in this dissertation for discovery of neutrino production in GRBs by both the stacked and per-GRB analyses. This analysis found no significant coincident events with GRBs, with results summarized in Appendix B.

Although both the results of both this new Northern Hemisphere track analysis and the Southern Hemisphere track analysis are consistent with the background-only expectation, an *a-posteriori* check can be applied to the per-GRB test statistic ensemble to verify there is not a sub-discovery population of coincidences that when taken together are significant. This check is modeled after a population analysis recently introduced to IceCube's time-integrated neutrino point source search that counts the number of source points above a certain p-value significance for discovery (called a *warm source* analysis). When applied to the per-GRB analysis, one counts the number of GRBs that have a test statistic $\mathcal{T}_g$ above a given threshold test statistic $\mathcal{T}$. A scan of threshold test statistics is performed, searching for significant deviations from the number of sources expected from background.

The background-only expectation is determined by generating ensembles of per-GRB test statistics in Monte Carlo trials of the new Northern Hemisphere track and Southern Hemisphere track searches. Discovery thresholds are defined by calculating the fraction of trials that have N' GRBs having a test statistic greater than $\mathcal{T}'$, scanning over possible values of N' and $\mathcal{T}'$. It should be noted that these thresholds are pre-trials discovery thresholds, as one has not accounted for the scan of possible per-GRB threshold test statistics. As this is simply an *a-posteriori* check, post-trials significances are not calculated.

The results of this warm source population check is found in Figure 7.4. The population of coincidences in the three-year Northern Hemisphere track and Southern

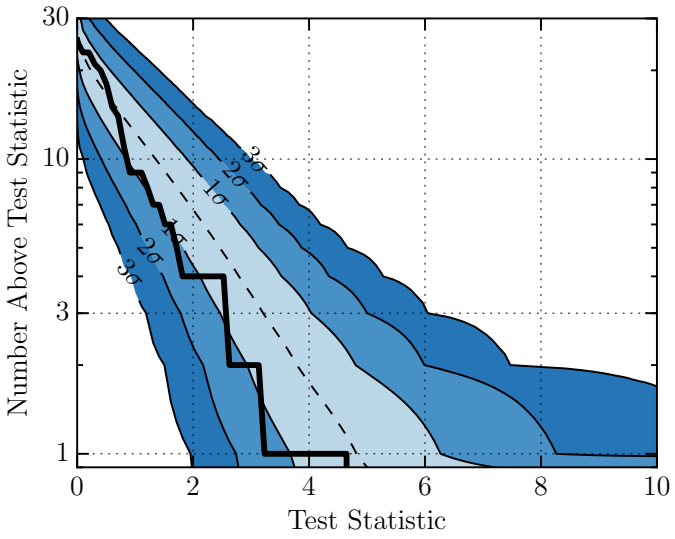

Figure 7.4: Warm source population analysis in Southern Hemisphere and three-year Northern Hemisphere track searches. Results are given by the thick black line, relative to the 1σ, 2σ, and 3σ significance intervals. The median background-only expectation is given by the dashed black line.

Hemisphere track analyses are found to be consistent with background, exhibiting a possible 1σ underfluctuation in per-GRB test statistics over a large range of the test statistic scan. As this check essentially amounts to stacking sub-discovery per-GRB coincidences for discovery, this is not altogether unexpected given the *stacked* $\mathcal{T}$ method results of these analyses are consistent with background.

7.2 Systematic Uncertainties

The result of the prompt neutrino search was consistent with the background-only hypothesis, allowing one to infer upper limits to neutrino production in GRBs given the exposure of the analysis. These limits, however, contain systematic uncertainties that must first be estimated. In general, systematic uncertainties are inherent to the estimation of both signal and background detection in IceCube. As the background of this analysis is characterized directly from large samples of measured IceCube data not temporally coincident with any GRB, systematic uncertainties in

background are negligible. The systematic uncertainty in signal detection sensitivity remains to be estimated.

The systematic uncertainties in signal detection fall into three general categories: uncertainties in the detector environment, detector uncertainties, and particle interaction uncertainties. These uncertainties can influence the expected light yield per event, affecting the resulting event passing rate in the analysis and the quality of event direction and energy reconstructions. Further, uncertainties in the standard model neutrino deep inelastic scattering cross section directly influence the measured signal event rate.

These systematic uncertainties are investigated independently for their effect on possible model limits. Here, each individual detector or particle interaction uncertainty is varied to expected extrema in a single year of the stacked analysis, then a model best possible Neyman upper limit (90% CL for $\mathcal{T} > 0$) is calculated and compared to the baseline best possible upper limit. The total systematic uncertainty is then obtained as a sum in quadrature of all possible limit changes. The IC86-2012 year of analysis has the most robust simulation of these systematic uncertainties, and was thus used to estimate the systematic uncertainty of the entire Southern Hemisphere track analysis. This section describes each individual systematic uncertainty investigated, then summarizes the total estimated systematic uncertainty in the IC86-2012 analysis for models that have limits presented in Section 7.3.

7.2.1 Ice Model

The simulation of photon propagation in the South Pole ice is dependent on the assumed ice properties. As summarized in Section 3.1.2, these properties are typically parameterized in terms of light absorption and scattering coefficients as a function of ice depth. Uncertainties in both these coefficients affect the expected light yield in simulated neutrino events, and therefore signal sensitivities.

The ice model absorption coefficients are estimated to have a systematic uncertainty of $+10\%/-7.1\%$. Increasing the absorption coefficient is expected to lower the total amount of light detected per-event, reducing the estimated energy of an event and lowering the amount of signal passing the energy-proxy selection cuts, reducing the analysis sensitivity to signal neutrino events. Conversely, decreasing the absorption coefficient increases the per-event light yield, improving the analysis sensitivity to signal neutrino events.

The ice model scattering coefficients are also estimated to have a systematic uncertainty of $+10\%/-7.1\%$. The effect of this uncertainty on the analysis sensitivity is somewhat uncertain *a-priori*. An increased scattering coefficient can increase the light yield of downgoing muons in the down-facing DOMs, however this light is late compared to a direct photon, which can degrade event reconstructions. A decreased scattering coefficient alternatively can decrease the light yield of downgoing muons, but the light detected is more direct and unscattered allowing more accurate reconstructions. As this analysis looks at the highest energy downgoing events, it is expected the light yield effect will be second order to the direct–scattered light effects to event reconstructions, meaning higher scattering coefficients yield worse limits while lower scattering coefficients yield better limits.

As the absorption and scattering coefficients in the ice are somewhat correlated, the effects these systematic uncertainties have on model limits are investigated in the following way: the increased absorption and scattering coefficients of $+10\%$ are investigated independently, then the effect of a simultaneous lowering of both absorption and scattering coefficients by -7.1% is investigated. Simulation data sets are generated for each of these variations and processed to the final event selection level to determine their effects on model limits.

The ice model used for final model limits additionally assumes the scattering and absorption coefficients are symmetrical in azimuth, in contradiction to the re-

cent discovery of an anisotropy of these properties in the bulk glacier ice [93]. This anisotropy can be included in photon propagation simulation by implementing an azimuthal dependence to these absorption and scattering coefficients. Model limits are then calculated and compared to the baseline limits to estimate the effect of ignoring the ice anisotropy in the final limits. As the events selected in this analysis are very bright, this anisotropy is expected to yield only a small degradation in final limits through slightly worse resolution in event reconstructions. A simulation data set incorporating the ice anisotropy was processed to the final event selection level to calculate difference in model limits to the baseline.

7.2.2 DOM Quantum Efficiency

The IceCube DOM sensitivity to incident photons was measured in the lab before deployment [96], with uncertainty in the quantum efficiency estimated conservatively at $\pm 10\%$. The DOM efficiency is expected to linearly scale the measured light yield, scaling the reconstructed event energy and final signal event rate. A reduction in DOM efficiency is therefore expected to degrade the analysis model upper limits, while an increase in DOM efficiency is expected to improve analysis model upper limits. Simulation data sets are produced varying the DOM quantum efficiency and processed to the final event selection level. Model limits with these data sets are then compared to the baseline data set limits.

7.2.3 Particle Interactions

Neutrino deep inelastic scattering cross sections determined from the standard model contain uncertainties due to experimental and model uncertainties for neutrino energies $E_\nu > 1\,\mathrm{TeV}$, where this analysis is most sensitive. In the CSMS cross section calculation [82], this total cross section uncertainty is estimated to be $\pm 5\%$ in the neutrino energy range of concern. The neutrino cross section is expected to linearly

scale the measured signal event rate in the Southern Hemisphere, where Earth absorption is not a concern. As there is no simulated data set varying the neutrino cross section, a conservative systematic uncertainty of $\pm 5\%$ is estimated for its effect on model upper limits.

An additional uncertainty exists in the muon photonuclear cross section, which yields an uncertainty in the light deposition topology in through-going muons. The baseline simulation data set take the most up-to-date photon-nucleon cross section parameterized by the Abramowicz, Levin, Levy, and Maor model (ALLM97) [135], a revision to their previously published model (ALLM91) [136] using updated nucleon structure functions. The uncertainties in the ALLM97 model are estimated by comparing it to two previous muon photonuclear cross section models: the ALLM91 model, which reduces the cross section compared to ALLM97 at high and low muon energies, and the Bezrukov and Bugaev model (BB81) [137], which increases the cross section compared to ALLM97 at high and low muon energies. These changes in muon photonuclear cross section model will affect the expected light yield and the effectiveness of the Millipede dE/dx smoothness likelihood included in the event selection. The total effect is expected to be small, though the direction of its effect on model limits is uncertain. Simulation data sets are produced with these alternative photonuclear cross section models and processed to the final event selection level; model upper limits are then calculated and compared to the baseline upper limits.

7.2.4 Total Systematic Uncertainty

The effect of each systematic uncertainty on several model upper limits is summarized in Table 7.3. Model upper limits are calculated in each systematic uncertainty simulation data set for a generic astrophysical E^{-2} neutrino spectrum, and the internal shock (IS) fireball, photospheric fireball, and ICMART numerical models with a bulk Lorentz factor of $\Gamma = 300$. These are then compared to upper limits calculated

Table 7.3: Systematic uncertainties for model limits, calculated as changes in limits relative to baseline limits.

	Change w.r.t. Baseline Limit			
Systematic	E^{-2}	IS Fireball	Photo. Fireball	ICMART
Anisotropic Ice Model	-1.0%	+0.8%	+1.2%	+1.5%
Absorption +10%	+6.4%	+4.4%	+4.7%	+2.6%
Scattering +10%	+9.9%	+7.5%	+9.4%	+6.1%
Absorption/Scattering -7.1%	-7.9%	-7.7%	-8.2%	-8.4%
DOM Efficiency -10%	+6.8%	+4.9%	+5.3%	+2.1%
DOM Efficiency +10%	-4.8%	-4.0%	-4.4%	-4.6%
Neutrino Cross Section	±5%	±5%	±5%	±5%
ALLM91 Nuclear Cross Section [136]	-0.4%	-2.0%	-1.7%	-1.2%
BB81 Nuclear Cross Section [137]	+1.7%	+1.8%	+0.5%	-0.4%
Total	+14.6%	+11.3%	+12.8%	+8.7%

with the the baseline simulation data set. The conservative total upper limit systematic uncertainty is estimated as a sum in quadrature of all positive changes to the baseline model limits. The general magnitude of the total systematic uncertainty of 10–15% in these models is consistent with that in the IceCube Northern Hemisphere GRB track analysis [26], All-sky GRB cascade analysis [27], and general track point source analyses [127].

The largest contributors to the total systematic uncertainty are due to underestimating ice model absorption and scattering coefficients, overestimating the DOM quantum efficiency, or overestimating the neutrino cross section. Uncertainties in the muon photonuclear cross section and excluding anisotropy in the ice model can degrade model limits, though much less in magnitude. For the very highest energy neutrino spectra (i.e. the ICMART model), underestimating the scattering coefficient and overestimating the neutrino cross section are the largest sources of systematic uncertainty.

The total systematic uncertainty is found to be correlated with the "softness" of the signal spectrum; the relatively soft E^{-2} and photospheric fireball model spectra have a higher total systematic uncertainty than the IS fireball and ICMART model spectra that peak at higher neutrino energies. As the Southern Hemisphere event

selection primarily removes low energy data in the event selection, the systematic uncertainties that scale the light yield affect the amount of signal that pass these energy-proxy cut thresholds. Soft model spectra are therefore more greatly effected by these systematic uncertainties as they yield more low energy neutrinos compared to harder model spectra.

The total systematic uncertainty is parameterized for each model investigated as a function of model "softness." In the double broken power law spectra of UHECR-production GRB models, the systematic uncertainty can be parameterized as a function of first neutrino break energy ε_b. In numerical neutrino production models, the systematic uncertainty can be parameterized as a function of bulk Lorentz factor Γ, as this variable pushes the spectral peak to higher or lower energies. Finally, the systematic uncertainty of power law neutrino spectra can be parameterized as a function of spectral index. The results of this parameterization can be found in Figure 7.5, confirming trends indicated in Table 7.3. The splines fit to the systematic uncertainty as a function of model parameters here are applied in all model upper limits presented in Section 7.3 by degrading the calculated limits by the systematic uncertainty amount. As the Southern Hemisphere track systematic uncertainties are slightly larger than previously calculated prompt neutrino analysis uncertainties, this systematic uncertainty is conservative for the combined Northern Hemisphere track, All-sky Cascade, and Southern Hemisphere track analysis.

7.3 Combined Analysis

The results presented Section 7.1 were consistent with the background-only expectation, allowing limits to be placed on neutrino production models in GRBs. These limits can be strengthened when the Southern Hemisphere track result is considered in tandem with the previously published Northern Hemisphere track [26] and All-sky cascade [27] results that were also consistent with the background-only expec-

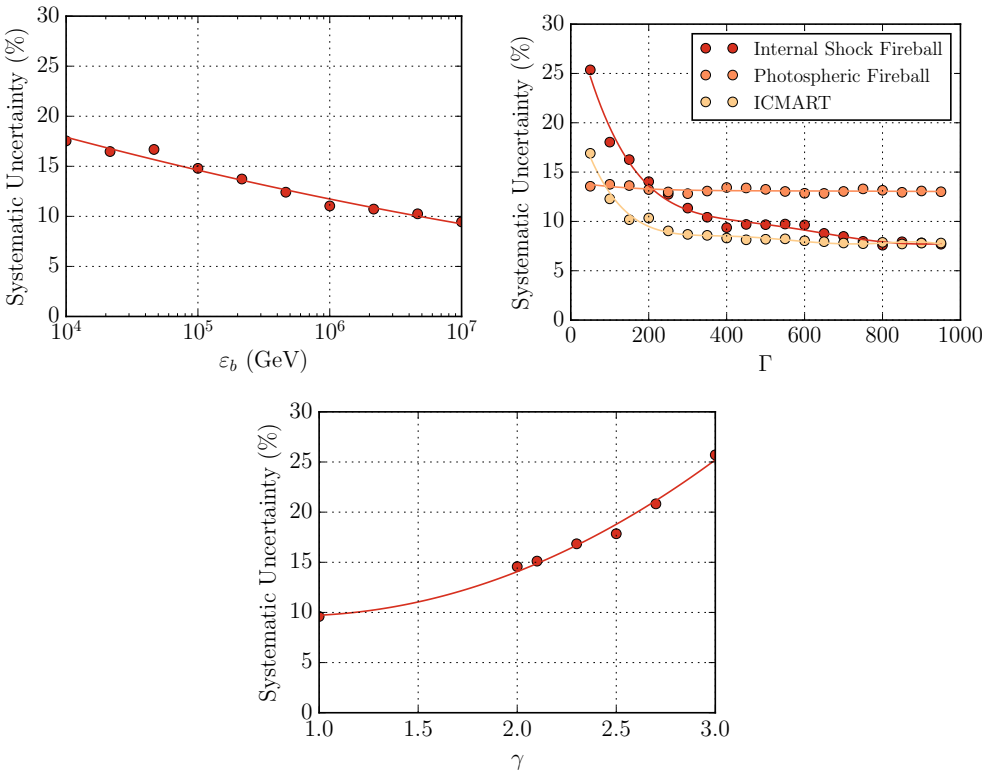

Figure 7.5: Systematic uncertainties as a function of model parameters. Top Left: double broken power law neutrino spectrum as a function of first break energy ε_b; Top Right: numerical neutrino production models as a function of fireball bulk Lorentz factor Γ; Bottom: power law neutrino spectrum as a function of spectral index γ.

tation. Additionally, the Northern Hemisphere track analysis was recently extended to the IC86-2012, IC86-2013, and IC86-2014 years of IceCube data, which found no significant coincident events with GRBs.

A combined stacked analysis test statistic is formed as a sum of per-analysis test statistics following (6.4). The only non-zero values in this sum are as follows (NT: Northern Hemisphere track; AC: All-sky cascade; ST: Southern Hemisphere track): $\mathcal{T}_{\mathrm{NT,IC79}} = 0.1413$, $\mathcal{T}_{\mathrm{AC,IC79}} = 0.0097$, $\mathcal{T}_{\mathrm{AC,IC86\text{-}2011}} = 0.2227$, and $\mathcal{T}_{\mathrm{ST,IC79}} = 0.7552$. The total combined test statistic is therefore $\mathcal{T} = 1.1289$ with significance $p = 0.5877$. As this combined test statistic is found to be consistent with background, one can place upper limits to neutrino production models in GRBs. This section discusses

these limits to a number of model neutrino spectra relevant to GRBs and general neutrino astrophysics.

7.3.1 Combined Analysis Sensitivity

The differential sensitivity of this combined analysis is first calculated. The median Neyman upper limit (90% CL, $\mathcal{T} > \mathcal{T}_{\text{median}}$) is calculated for an E^{-2} signal spectrum in half-decadal neutrino energy bins. Separate upper limits are calculated for each search channel, then for the combined analysis. Each GRB analyzed is assumed to yield an equal measurable neutrino fluence. These upper limits are presented as a per-flavor quasi-diffuse neutrino flux, where the per-GRB signal fluence upper limits are scaled to an assumed 667 GRBs per year that are potentially observable by current satellites, distributed uniformly over the full-sky 4π sr solid angle (discussed generally in Section 2.3.4). The results are found in Figure 7.6, not accounting for the analysis systematic uncertainty.

The Northern Hemisphere track analysis is shown to be the most sensitive, especially at low energies, as it couples the largest search exposure with the most pure neutrino sample. The All-sky cascade and Southern Hemisphere track analyses are much less sensitive at low energies (the All-sky cascade analysis being the more sensitive of the two). At neutrino energies $E_\nu > 1\,\text{PeV}$, the sensitivities of the analyses converge within a factor of a few, with the Southern Hemisphere track analyses becoming most sensitive at the highest energies. As expected, the combined analysis improves on the sensitivity of each individual analysis due to the increased signal exposure. This sensitivity is slightly worse than the pure Northern Hemisphere track analysis for signal energies in the range $1 - 10\,\text{TeV}$, as the Southern Hemisphere track and All-sky cascade analyses have little sensitivity in this energy range, while they increase background contamination.

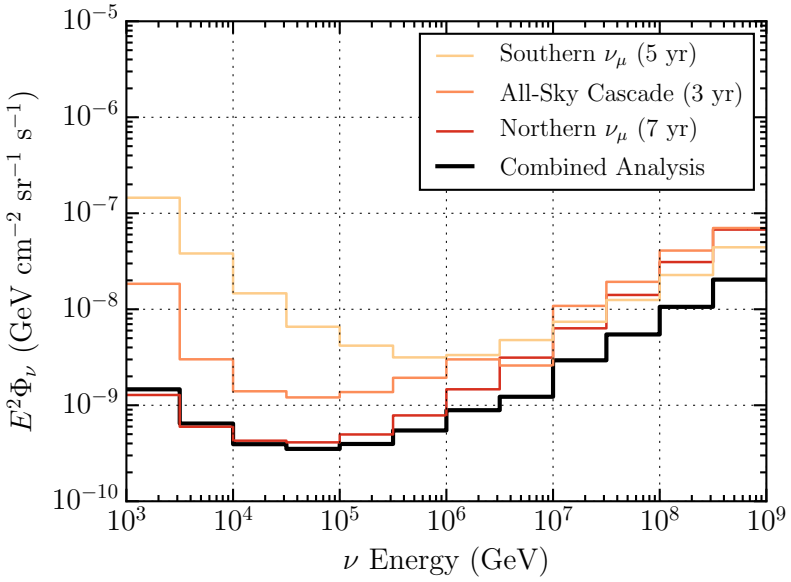

Figure 7.6: Differential median sensitivity of the Northern Hemisphere track, All-sky Cascade, and Southern Hemisphere track stacked GRB analyses to a per-flavor E^{-2} ν quasi-diffuse flux in half-decadal ν energy bins. The Northern Hemisphere track differential sensitivity is calculated combining the most recent three-year analysis with previously published searches [26]. The total combined sensitivity of these analyses is shown in the black line.

7.3.2 GRB Model Limits

The generic double broken power law of (2.33) is constrained as a function of first break energy ε_b and spectral normalization. These limits are presented in Figure 7.7 as excluded regions in this parameter space, where the per-GRB fluence that is limited—assumed to be equal for each GRB in the analyzed sample—is scaled to a per-flavor quasi-diffuse flux. Two models of neutrino production in GRBs where GRBs are assumed to be the sole origin of the measured UHECR flux are provided in this parameter space: the neuton escape model of Ahlers et al. [74] and the proton escape model of Waxman and Bahcall [72], which has been updated with recent measurements of the UHECR flux [73]. Both models are excluded at over the 99% CL, greatly constraining the hypothesis GRBs are significant producers of UHECRs.

Limits are then calculated for the numerical models of neutrino production in GRBs presented in Section 2.3.2, where the expected measurable neutrino fluence

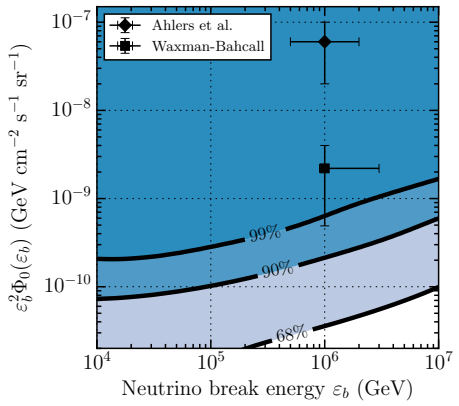

Figure 7.7: Excluded regions of the generic double broken power law neutrino spectrum as a function of first break energy ε_b and per-flavor quasi-diffuse flux normalization from the final combined analysis results. Models of neutrino production assuming GRBs are the sole source of the measured UHECR flux either by neutron escape [74] or proton escape [72] from the relativistic fireball are provided for reference.

is determined from the per-GRB gamma-ray spectrum parameters. First, Neyman upper limits (90% CL) are calculated for the internal shock fireball, photospheric fireball, and ICMART models for canonical parameters for the fireball baryonic loading $f_b = 10$ and bulk Lorentz faction $\Gamma = 300$, presented in Figure 7.8 scaling these model fluences to a per-flavor quasi-diffuse flux. Both the internal shock and photospheric fireball models are strongly constrained. The ICMART model significantly reduces the expected neutrino production in GRBs and remains beyond the sensitivity of the combined analysis.

These limits are extended to arbitrary values for baryonic loading f_b and bulk Lorentz faction Γ in the numerical models. Assuming all GRBs in the analyzed sample have identical values for f_p and Γ, limits are presented in Figure 7.9 as exclusion regions in a scan of f_p and Γ parameter space. Here, the internal shock and photospheric fireball models are shown to be excluded at the 99% CL for canonical model parameters, while the 90% CL exclusion region is extended compared to those published in the All-sky cascade analysis [27]. The primary regions in these models that still cannot be constrained require small baryonic loading and large bulk Lorentz

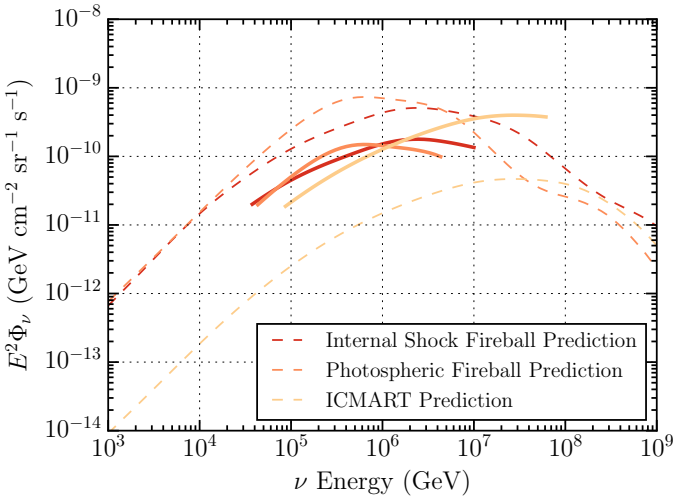

Figure 7.8: Upper limits (90% CL, solid lines) to the predicted per-flavor quasi-diffuse flux of numerical neutrino production models (dashed lines) for canonical parameters $f_p = 10$ and $\Gamma = 300$ over the central 90% energy containment interval of detected neutrinos for these models in the final combined analysis.

factors. The ICMART model is limited in a much smaller interval of possible bulk Lorentz factors ($100 < \Gamma < 400$) as this model is much less well constrained; only regions of large baryonic loading and small bulk Lorentz factors can be meaningfully excluded. These constraints suggest that the baryonic content of GRB fireballs may not be sufficient to account for the measured UHECR flux in internal shock acceleration models. This constraint could be softened should the bulk Lorentz factor be on the high end of the expected range, or if GRBs are better modeled by multi-zone internal shock emission models [64]. The Poyting-dominated models of GRB particle acceleration remain consistent with neutrino and gamma-ray observations of GRBs, and could still produce the observed UHECR flux.

7.3.3 Astrophysical Neutrino Model Limits

IceCube has discovered and measured an astrophysical neutrino flux whose origin has not yet been determined. Assuming GRBs produce a neutrino spectrum consistent with IceCube's spectral measurements, one can limit the fraction of this

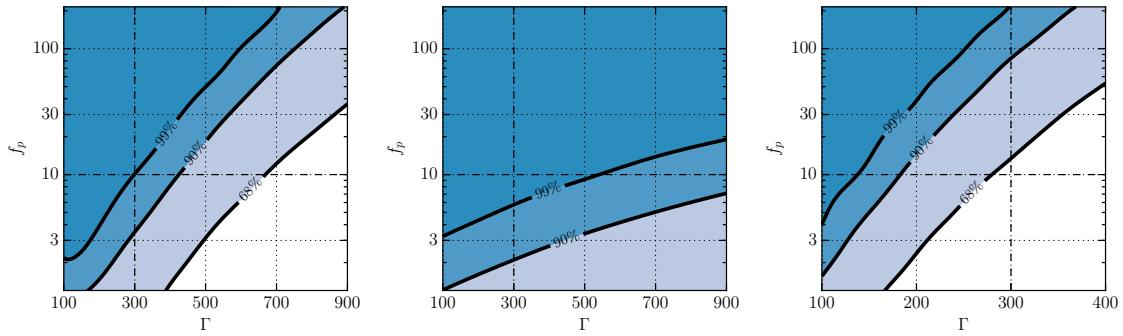

Figure 7.9: Excluded regions in f_p and Γ parameter space for three numerical models of neutrino production in GRBs from the final combined analysis. Canonical model parameters $f_p = 10$ and $\Gamma = 300$ are indicated by the dashed black lines. Left: Internal Shock Fireball Model, Middle: Photospheric Fireball Model, and Right: ICMART Model (shown with a restricted x-axis where model is constrained).

spectrum to which GRBs contribute. Two types of spectra are considered here: a simple power law, and a broken power law of the form

$$F_\nu(E_\nu) = f_\nu \times \begin{cases} \varepsilon_b^{-1} \times E_\nu^{-1} \times \left(\frac{\varepsilon_b}{100\,\mathrm{TeV}}\right)^{2-\gamma}, & E_\nu \leq \varepsilon_b \\ E_\nu^{-2} \times \left(\frac{E_\nu}{100\,\mathrm{TeV}}\right)^{2-\gamma}, & \varepsilon_b < E_\nu, \end{cases} \tag{7.1}$$

which is chosen to be normalized relative to a reference energy of 100 TeV, and ε_b is the spectral break energy. As the astrophysical neutrino spectrum has been measured at high energies, the existence or location of a low energy cutoff has not been established. The broken power law approximates such a cutoff spectrum, which transitions to the measured power law spectrum.

Assuming each GRB contributes an equal fluence to the measured astrophysical neutrino spectrum, one can place limits on this fluence for arbitrary spectral index γ, and break energy in the case of the broken power spectrum. Scaling these per-GRB fluence limits to a per-flavor quasi-diffuse neutrino flux, the contribution of GRBs to the measured flux is constrained. As a function of γ and per-flavor quasi-diffuse flux normalization, exclusion regions are displayed in Figure 7.10. These limits are presented for a power law spectrum, as well as broken power law spectra with

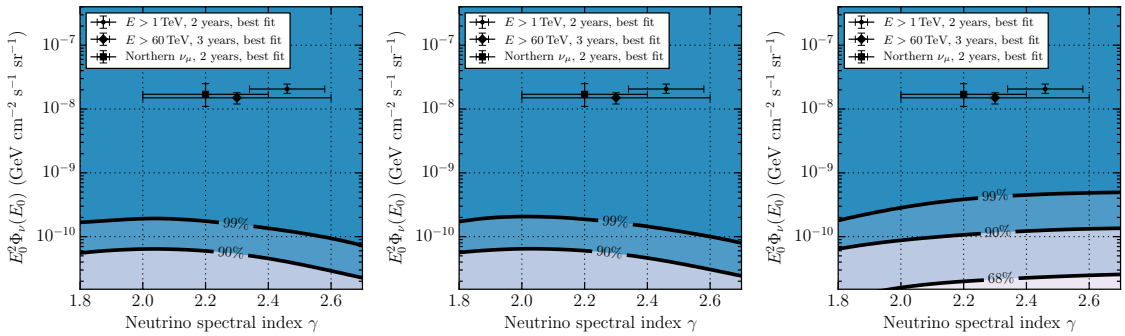

Figure 7.10: Excluded regions of the power law neutrino spectrum as a function of spectral index γ and per-flavor quasi-diffuse flux normalization Φ_0 derived from the final combined analysis. Astrophysical neutrino spectra measured by IceCube are given for reference [22, 23, 138]. Left: power law spectrum; Middle: broken power law spectrum, with $dN/dE \propto E^{-1}$, $E < 1\,\text{TeV}$; Right: broken power law spectrum, with $dN/dE \propto E^{-1}$, $E < 60\,\text{TeV}$.

$\varepsilon_b = 1\,\text{TeV}$ and $\varepsilon_b = 60\,\text{TeV}$, relative to the astrophysical neutrino flux measured in a 2-year contained event analysis for neutrinos with energy $E_\nu > 1\,\text{TeV}$ [138], a 3-year contained event analysis for $E_\nu > 60\,\text{TeV}$ [22], and a 2-year analysis of uncontained Northern Hemisphere ν_μ tracks [23]. The break energies are chosen such that they match the low-energy sensitivity cutoffs of the starting event analyses.

The exclusion regions of the power law and low-energy broken power law spectra are largely consistent with each other, estimating $\lesssim 0.4\%$ of the measured astrophysical neutrinos flux could have been generated in potentially observable GRBs at the 90% CL. Should the measured astrophysical neutrinos flux have a cutoff at $\sim$60 TeV, these constraints are weakened, estimating $\lesssim 1\%$ of the flux is produced in potentially observable GRBs at the 90% CL.

Chapter 8

Conclusions

Previous neutrino searches during the prompt gamma-ray emission period of GRBs in IceCube data have been extended for the first time to the ν_μ CC channel in the Southern Hemisphere sky. Combining the sub-degree reconstruction of ν_μ origin from muon tracks in a region of the sky without Earth attenuation for neutrino energies $E_\nu > 1\,\mathrm{PeV}$, this is IceCube's most sensitive search to GRB neutrino production at the very highest energies. Given the inherently low backgrounds of a prompt neutrino search, the observation of a single high energy ν_μ track could constitute a discovery.

The Southern Hemisphere track search was performed in five years of IceCube data, with both the partially completed 79-string configuration of the detector and four years of the complete detector. High energy tracks were searched in coincidence with 664 GRBs that occured during clean operation of the detector using an unbinned likelihood method. Events in coincidence with GRBs were analyzed on both a per-GRB and on a per-year stacked basis. The per-GRB analysis is optimized to discover high-quality coincidences with a single GRB, sensitive to samples of GRBs where one GRB dominates the measurable neutrino fluence. The stacked analysis is optimized to a distributed neutrino fluence hypotheses, where the coincidences with several GRBs in a sample can be combined for discovery.

The most significant single coincidence was found with GRB110207A, though it is found to be consistent with background, being $> 3\sigma$ (possibly $> 5\sigma$) in space from the precise GRB location. This coincidence is the only one in the analysis to yield a non-zero per-year stacked test statistic, which is not found to be significant. A number of other events are found in coincidence with other GRBs in the sample,

but they either occur relative to a poorly localized GRB or are poorly reconstructed themselves, meaning they cannot be meaningfully associated with the observed GRBs.

Limits to neutrino production in GRBs were then obtained combining the Southern Hemisphere track non-discovery with previously published Northern Hemisphere track [26] and All-sky cascade [27] searches in coincidence with GRBs, as well as with the non-discovery in a recent extension of the Northern Hemisphere track search to three additional years of IceCube data. Neutrino production models where GRBs are assumed to be the sole accelerator of UHECRs are increasingly constrained, excluding current models at the 99% CL. Further, limits are improved for numerical models where neutrino production is directly calculated from a GRB's measured gamma-ray spectrum. The internal shock and photospheric fireball models are excluded at the 99% CL for canonical model parameters, while the ICMART model at canonical model parameters is beyond the sensitivity of the current stacked analysis. It is also established that $\lesssim 1\%$ of IceCube's measured astrophysical neutrino flux [22, 23, 138] can be the result of neutrino emission from potentially observable GRBs.

Several caveats must be made to these conclusions, however. In the generic models, all GRBs in the analyzed sample are assumed to contribute an equal average neutrino fluence to the total quasi-diffuse flux. Further, no variability is allowed burst-to-burst in the baryonic loading f_p and bulk Lorentz factor Γ for numerical model constraints. Multi-wavelength studies of GRB afterglows can be used to constrain Γ on a per-GRB basis [139], with recent results suggesting some GRBs may have bulk Lorentz factors as low as $\Gamma \sim 10$ [140]. Further multi-wavelength studies could yield additional Lorentz factor constraints, allowing more precise neutrino production modeling and constraints to be made.

Recent studies have connected UHECR acceleration in GRBs—assuming a pure proton composition–to the measured GRB gamma-ray spectra with constraints from prompt neutrino and cosmogenic neutrino searches in IceCube in a self-consistent

way [63]. Baerwald et al. find that the non-excluded regions of the internal shock fireball model can still produce the observed UHECR spectrum above the ankle through either direct proton escape or diffusive processes, though they require baryonic loading factors much larger than those considered in this dissertation, where photopion production efficiency is greatly diminished. The bulk Lorentz factor is still required to be large ($\Gamma \gtrsim 400$) in these models, which could be in tension with multi-wavelength constraints should the GRB population in general more closely resemble those low-Γ GRBs observed [140].

Improvements have recently been made to modeling of the standard internal shock fireball model by dynamically simulating the collisions of shells in the relativistic outflow rather than assuming all collisions occur at the same radius from the central engine [64]. Bustamante et al. find that neutrino production in such a model is somewhat decoupled from gamma-ray and UHECR production, with neutrino production occuring primarily near the photosphere while gamma-rays and UHECRs are produced further from the central engine. The result is a reduction to the predicted quasi-diffuse neutrino flux by an order of magnitude compared to the single-zone internal shock model, with a peak differential neutrino flux of $10^{-11}\,\mathrm{GeV\,cm^{-2}\,s^{-1}\,sr^{-1}}$ at neutrino energies between $10^6 - 10^7\,\mathrm{GeV}$, beyond the current sensitivity of this analysis. This predicted neutrino flux is largely insensitive to the fireball's bulk Lorentz factor and less sensitive to the assumed baryonic loading compared to the single-zone internal shock model. Should shell collisions be considered below the GRB photosphere, neutrino production is enhanced and may already be constrained by the results of this dissertation, though this extrapolation is highly uncertain. To meaningfully constrain neutrino production above the photosphere in this model, the IceCube upgrade that increases its fiducial volume by a factor of ten called *IceCube-Gen2* is likely required [141, 142].

These models generally assume a uniform population of GRBs in certain model parameters, which is in some tension with the great variability of characteristics observed GRB-to-GRB. In the near term future, a discovery of neutrino production in GRBs is still possible should nearby a GRB that is especially neutrino-bright occur. The per-GRB analysis introduced in this dissertation is ideal for discovery of such a coincidence. A near real-time framework (full data processing performed in $\lesssim 1$ days) has been introduced to IceCube data processing, making fast per-GRB analyses possible. IceCube would be able to publish information of coincident events to the broader GRB community through the GCN for additional follow-up. This would be especially useful for well-localized track events in coincidence with Fermi-GBM localized GRBs, which could lead to discovery of GRB afterglows or host galaxies. Additionally, such IceCube coincidences can be coupled with searches by LIGO for gravitational waves to constrain GRB source parameters [143], a promising technique in light of LIGO's recent discovery of GW150914 [144] with a possible sub-threshold GRB counterpart observed by Fermi-GBM [145]. Though no significant neutrino coincidence was observed by IceCube with GW150914 [146], such multi-messenger searches have been proven possible.

Continued IceCube searches for neutrinos of all flavors with GRBs may reveal a neutrino flux below its current sensitivity or a discovery-level coincidence with a single GRB. The sensitivity of these searches can further be extended to GRB precursor and afterglow neutrino production with longer time-window searches, for instance with an extension of the previously published expanding time-window search [25] to all neutrino flavors. In the absence of such a discovery, GRBs will be increasingly disfavored as the primary progenitors of UHECRs.

Appendix A

Southern Hemisphere Gamma-Ray Burst Catalog

The analysis presented in this dissertation searches for prompt neutrino emission via tracks in IceCube for the first time in 664 Southern Hemisphere sky GRBs. The properties of these GRBs are summarized in this appendix. The results from this search are combined with previous Northern Hemisphere GRB track searches and an All-sky GRB cascade seach. The properties of these GRBs can be found in previous dissertations [128, 147–149].

Each GRB is named by the convention GRB *YYMMDDL*, where *YY* are the last two digits of the year in which the GRB occurs, and *MM* and *DD* are the month and day in which the GRB occurs, respectively. The letter *L* is assigned alphabetically to the GRBs on a per-day basis starting at "A" so that GRBs which occur on the same day are indentified uniquely.

The positions of these GRBs are given in equatorial coordinates (RA and Dec), as well the angular uncertainty σ of this direction. The redshift z of the GRBs are also given. If no redshift was measured for a particular GRB, average values are used and indicated in the table with $*$: $z = 2.15$ for long GRBs and $z = 0.5$ for short GRBs.

The temporal information of the GRBs are also given. Here, the trigger time of the satellite which detected the GRB is given in Universal Time (UT) in the format *YYYY-MM-DD hh:mm:ss.ss*. The GRB start time T_1 and end time T_2 are then defined relative to this trigger time in units of seconds, with the burst duration calculated as $T_{100} = T_2 - T_1$.

The final set of GRB parameters presented are the gamma-ray spectral fits by the detecting satellite, which defines the E_{min} and E_{max} of the spectrum in units

of keV. The spectral fit is defined by the spectral indices α_γ and β_γ, the gamma-ray break energy ε_γ in units of keV, and the fluence normalization f_γ in units of erg cm^{-2}. As described in Section 2.2.5, when spectral fit parameters are unavailable average values are assigned to the GRB, indicated by $*$. If the GRB is detected solely by Fermi GBM, average values taken from the Fermi GBM two-year catalog are used [44], and indicated by †.

Table A.1: IC79 Southern Hemisphere GRB catalog

	RA (°)	Dec (°)	σ	z	Trigger (UT)	T_1 (s)	T_2 (s)	T_{100} (s)	α_γ	β_γ	ε_γ	$E_{\min}$	$E_{\max}$	f_γ
GRB100604A	248.30	-73.19	3.64°	2.15*	2010-06-04 06:53:34.81	-2.3	11.14	13.44	1.05†	2.25†	205†	8	1000	5.509×10^{-6}
GRB100605A	273.43	-67.60	7.67°	2.15*	2010-06-05 18:35:10.74	-1.02	7.17	8.19	1.05†	2.25†	205†	8	1000	7.565×10^{-7}
GRB100606A	350.63	-66.24	1.08″	2.15*	2010-06-06 19:12:41.00	0.3	672.3	672.0	1.05	3.05	945	20	2000	3.9×10^{-5}
GRB100615A	177.21	-19.48	1.08″	1.398	2010-06-15 01:59:03.00	0	47.4	47.4	1.24	2.27	85.73	8	1000	8.723×10^{-6}
GRB100619A	84.62	-27.00	1.08″	2.15*	2010-06-19 00:21:07.00	-2.9	105.7	108.6	1.6	2.36	135.3	8	1000	1.129×10^{-5}
GRB100620A	80.10	-51.68	1.46°	2.15*	2010-06-20 02:51:29.11	0.19	52.03	51.84	1.05†	2.25†	205†	8	1000	3.716×10^{-6}
GRB100621A	315.31	-51.11	1.08″	0.542	2010-06-21 03:03:32.00	-6	204	210.0	1.7	2.45	95	20	2000	3.6×10^{-5}
GRB100625A	15.80	-39.09	1.08″	0.5*	2010-06-25 18:32:27.80	0	1.3	1.3	0.1	2.6	371	20	2000	0.83×10^{-6}
GRB100628A	225.94	-31.65	0.02°	0.5*	2010-06-28 08:16:40.00	-0.004	0.036	0.04	2.67	4.67	74.1	15	150	2.5×10^{-8}
GRB100702A	245.69	-56.55	0.01°	0.5*	2010-07-02 01:03:47.00	0.036	0.236	0.2	1.54	2.54	1000*	15	150	1.2×10^{-7}
GRB100703A	9.52	-25.71	0.03°	0.5*	2010-07-03 17:43:37.40	0	0.07	0.07	1*	2*	1000*	20	200	7×10^{-7}
GRB100704A	133.64	-24.20	1.08″	2.15*	2010-07-04 03:35:08.00	-62.3	202.3	264.6	0.76	2.53	178.30	10	1000	1.040×10^{-5}
GRB100707A	358.02	-8.66	1.12°	2.15*	2010-07-07 00:46:38.91	-0.5	102.144	102.644	0.95	2.2	264	20	2000	8.8×10^{-5}
GRB100715A	299.27	-54.71	9.32°	2.15*	2010-07-15 11:27:17.64	-1.02	13.82	14.84	1.05†	2.25†	205†	8	1000	2.552×10^{-6}
GRB100718B	121.83	-46.18	5.93°	2.15*	2010-07-18 03:50:09.61	-21.62	11.02	32.64	1.05†	2.25†	205†	8	1000	2.747×10^{-6}
GRB100719A	112.32	-5.86	0.02°	2.15*	2010-07-19 03:30:57.00	-3.9	35.1	39.0	1.69	2.69	200*	15	150	5.3×10^{-7}
GRB100719B	304.87	-67.14	15.41°	0.5*	2010-07-19 07:28:17.62	-1.54	0.06	1.6	1.05†	2.25†	205†	8	1000	3.868×10^{-7}
GRB100722A	238.77	-15.61	1.07°	2.15*	2010-07-22 02:18:37.24	0	7.17	7.17	1.01	2.54	68.1	8	1000	9.5×10^{-9}
GRB100724A	194.54	-11.10	1.08″	1.288	2010-07-24 00:42:19.00	0.1	1.6	1.5	1.92	2.92	1000*	15	150	1.6×10^{-7}
GRB100725A	166.48	-26.67	1.08″	2.15*	2010-07-25 07:12:52.00	-4.8	172	176.8	1.23	2.23	200*	15	150	2.0×10^{-6}
GRB100727A	154.18	-21.39	1.08″	2.15*	2010-07-27 05:42:17.00	-82	29.8	111.8	1.71	2.71	200*	8	1000	2.03×10^{-6}
GRB100728A	88.76	-15.26	0.72″	1.567	2010-07-28 02:18:24.00	-84.3	334	418.3	0.75	3.04	344.3	8	1000	1.291×10^{-4}
GRB100728B	163.49	-45.47	0.36″	2.106	2010-07-28 10:31:54.97	-2.05	14.2	16.25	0.8	2.2	104	8	1000	2.4×10^{-6}
GRB100730A	339.79	-22.23	5.40°	2.15*	2010-07-30 11:06:14.97	-1.54	62.34	63.88	1.05†	2.25†	205†	8	1000	6.058×10^{-6}

Table A.1: IC79 Southern Hemisphere GRB catalog *(continued)*

	RA (°)	Dec (°)	σ	z	Trigger (UT)	T_1 (s)	T_2 (s)	T_{100} (s)	α_γ	β_γ	ε_γ	$E_{\min}$	$E_{\max}$	f_γ
GRB100805C	112.72	-35.93	3.75°	2.15*	2010-08-05 20:16:29.53	0	58.43	58.43	1.05†	2.25†	205†	8	1000	1.061×10^{-5}
GRB100814A	22.47	-18.00	1.08″	2.15*	2010-08-14 03:50:08.51	-1.5	238	239.5	0.64	2.02	106.4	10	1000	1.98×10^{-5}
GRB100816B	102.12	-26.66	1.06°	2.15*	2010-08-16 00:12:41.41	-21.76	40.64	62.4	1.05†	2.25†	205†	8	1000	2.530×10^{-5}
GRB100819A	279.60	-50.04	3.86°	2.15*	2010-08-19 11:56:35.26	-4.86	7.68	12.54	1.05†	2.25†	205†	8	1000	3.322×10^{-6}
GRB100820A	258.79	-18.51	2.14°	2.15*	2010-08-20 08:56:58.47	-0.77	8.19	8.96	1.05†	2.25†	205†	8	1000	2.993×10^{-6}
GRB100825A	253.44	-56.57	6.34°	2.15*	2010-08-25 06:53:48.67	-1.28	2.05	3.33	1.05†	2.25†	205†	8	1000	1.378×10^{-6}
GRB100826A	279.59	-22.13	1.60°	2.15*	2010-08-26 22:58:29.73	0	130.56	130.56	1.31	2.1	606	20	10000	3.0×10^{-4}
GRB100904A	172.91	-16.18	0.02°	2.15*	2010-09-04 01:33:43.00	-14.5	23	37.5	1.67	2.67	200*	15	150	1.3×10^{-6}
GRB100907A	177.29	-40.63	6.90°	2.15*	2010-09-07 18:01:11.64	-1.54	3.84	5.38	1.05†	2.25†	205†	8	1000	7.333×10^{-7}
GRB100910A	238.10	-34.62	1.02°	2.15*	2010-09-10 19:37:43.96	1.34	15.17	13.83	0.92	2.26	143	10	1000	1.48×10^{-5}
GRB100916A	151.96	-59.38	3.48°	2.15*	2010-09-16 18:41:12.49	-0.26	12.54	12.8	1.05†	2.25†	205†	8	1000	1.784×10^{-6}
GRB100917A	289.25	-17.12	0.02°	2.15*	2010-09-17 05:03:25.00	-2.1	76	78.1	1.67	2.67	200*	15	150	8.6×10^{-7}
GRB100918A	308.41	-45.96	1.00°	2.15*	2010-09-18 20:42:18.01	18.43	104.45	86.02	1.05†	2.25†	205†	8	1000	8.924×10^{-5}
GRB100922A	356.98	-25.19	15.03°	2.15*	2010-09-22 14:59:43.01	-1.02	3.33	4.35	1.05†	2.25†	205†	8	1000	4.246×10^{-7}
GRB100925A	254.74	-15.24	0.03°	2.15*	2010-09-25 08:05:05.00	0	10	10.0	1*	2*	200*	10*	10000*	1.00×10^{-5}*
GRB100926A	222.75	-72.35	3.81°	2.15*	2010-09-26 14:17:03.94	-24.06	8.19	32.25	1.05†	2.25†	205†	8	1000	6.973×10^{-6}
GRB100926B	43.58	-11.10	12.00°	2.15*	2010-09-26 16:39:54.52	-3.07	34.82	37.89	1.05†	2.25†	205†	8	1000	1.374×10^{-6}
GRB100928A	223.04	-28.54	0.02°	2.15*	2010-09-28 02:19:52.00	0.9	4.4	3.5	1.79	2.79	200*	15	150	3.5×10^{-7}
GRB100929C	183.03	-24.94	7.79°	0.5*	2010-09-29 21:59:45.82	-0.13	0.19	0.32	1.05†	2.25†	205†	8	1000	7.614×10^{-7}
GRB101002A	323.35	-27.47	16.36°	2.15*	2010-10-02 06:41:26.95	-4.35	2.82	7.17	1.05†	2.25†	205†	8	1000	4.396×10^{-7}
GRB101011A	48.29	-65.98	0.72″	2.15*	2010-10-11 16:58:35.00	-0.4	84.2	84.6	0.49	2.49	296.6	8	1000	5.24×10^{-6}
GRB101013A	292.08	-49.64	1.60°	2.15*	2010-10-13 09:52:42.88	0.58	15.94	15.36	1.05†	2.25†	205†	8	1000	6.410×10^{-6}
GRB101014A	26.94	-51.07	1.00°	2.15*	2010-10-14 04:11:52.62	1.41	450.82	449.41	1.27	2.07	181.40	10	1000	2.072×10^{-4}
GRB101017A	291.39	-35.15	1.44″	2.15*	2010-10-17 10:32:41.69	0	117	117.0	1.18	3.18	600	20	2000	6.7×10^{-5}
GRB101017B	27.47	-26.55	4.92°	2.15*	2010-10-17 14:51:29.48	-1.02	46.85	47.87	1.05†	2.25†	205†	8	1000	1.775×10^{-6}

Table A.1: IC79 Southern Hemisphere GRB catalog *(continued)*

	RA (°)	Dec (°)	σ	z	Trigger (UT)	T_1 (s)	T_2 (s)	T_{100} (s)	α_γ	β_γ	ε_γ	$E_{\min}$	$E_{\max}$	f_γ
GRB101021A	0.87	-23.71	1.33°	2.15*	2010-10-21 00:13:25.36	-51.46	69.31	120.77	1.05†	2.25†	205†	8	1000	2.230×10^{-5}
GRB101023A	317.96	-65.39	1.08″	2.15*	2010-10-23 22:50:12.00	-11	137.3	148.3	1.07	2.5	200	20	2000	6.6×10^{-5}
GRB101024A	66.51	-77.27	1.08″	2.15*	2010-10-24 11:39:33.60	-7.68	16.77	24.45	1.4	3.4	56.25	10	1000	1.2×10^{-6}
GRB101025A	240.19	-8.49	24.35°	2.15*	2010-10-25 03:30:18.64	-1.79	12.54	14.33	1.05†	2.25†	205†	8	1000	2.788×10^{-7}
GRB101030A	166.38	-16.38	1.08″	2.15*	2010-10-30 15:56:30.72	-69.63	46.8	116.43	1.82	2.82	200*	15	150	2.0×10^{-6}
GRB101031A	184.12	-7.47	15.87°	0.5*	2010-10-31 14:59:32.73	-0.06	0.32	0.38	1.05†	2.25†	205†	8	1000	2.217×10^{-7}
GRB101102A	284.68	-37.03	7.85°	2.15*	2010-11-02 20:10:07.43	-1.79	41.73	43.52	1.05†	2.25†	205†	8	1000	1.722×10^{-6}
GRB101104A	161.02	-7.08	8.53°	0.5*	2010-11-04 19:26:14.05	-0.51	0.77	1.28	1.05†	2.25†	205†	8	1000	8.934×10^{-7}
GRB101116A	32.00	-81.20	7.26°	0.5*	2010-11-16 11:32:26.74	-0.13	0.45	0.58	1.05†	2.25†	205†	8	1000	3.044×10^{-7}
GRB101117A	57.19	-26.87	1.75°	2.15*	2010-11-17 11:54:45.75	-2.05	48.13	50.18	1.05†	2.25†	205†	8	1000	8.241×10^{-6}
GRB101117B	173.00	-72.66	0.36″	2.15*	2010-11-17 19:13:23.00	-0.1	8.6	8.7	1.5	2.5	200*	15	150	1.1×10^{-6}
GRB101126A	84.77	-22.55	1.00°	2.15*	2010-11-26 04:44:27.48	0	43.84	43.84	1.05†	2.25†	205†	8	1000	3.101×10^{-5}
GRB101127B	70.95	-11.32	6.55°	2.15*	2010-11-27 02:27:30.90	-5.12	55.55	60.67	1.05†	2.25†	205†	8	1000	3.085×10^{-6}
GRB101128A	145.47	-35.20	5.70°	2.15*	2010-11-28 07:44:04.24	-2.82	5.38	8.2	1.05†	2.25†	205†	8	1000	8.356×10^{-7}
GRB101129A	155.92	-17.64	0.03°	2.15*	2010-11-29 15:39:30.76	0	2	2.0	0.4	2.4	1210	20	5000	3.5×10^{-6}
GRB101130A	61.80	-16.75	0.20°	2.15*	2010-11-30 09:39:26.18	0	65.792	65.792	0.6	2.6	190	20	1000	3.1×10^{-6}
GRB101201A	1.96	-16.20	0.02°	2.15*	2010-12-01 10:01:49.74	0	112.64	112.64	1.5	3.5	275.70	10	1000	2.41×10^{-5}
GRB101204A	167.54	-20.42	1.08″	2.15*	2010-12-04 23:53:29.00	0	10	10.0	1.3	2.3	200*	15	150	1.2×10^{-6}
GRB101205A	322.10	-39.10	11.10°	2.15*	2010-12-05 07:24:24.86	-3.84	4.1	7.94	1.05†	2.25†	205†	8	1000	3.905×10^{-7}
GRB101206A	164.08	-38.11	3.50°	2.15*	2010-12-06 00:52:17.53	0	34.82	34.82	1.05†	2.25†	205†	8	1000	5.841×10^{-6}
GRB101208B	280.94	-59.02	1.41°	2.15*	2010-12-08 11:57:01.20	-0.64	1.41	2.05	1.05†	2.25†	205†	8	1000	3.843×10^{-6}
GRB101214A	0.69	-28.27	5.56°	2.15*	2010-12-14 17:57:03.97	-1.41	0.83	2.24	1.05†	2.25†	205†	8	1000	2.371×10^{-7}
GRB101214B	181.13	-31.06	5.73°	2.15*	2010-12-14 23:50:00.97	-0.77	10.75	11.52	1.05†	2.25†	205†	8	1000	1.092×10^{-6}
GRB101216A	284.27	-20.97	2.12°	0.5*	2010-12-16 17:17:52.54	0	1.92	1.92	1.05†	2.25†	205†	8	1000	3.044×10^{-6}
GRB101219B	12.23	-34.57	1.08″	0.5519	2010-12-19 16:27:53.00	10	66.66	56.66	0.33	2.12	70	10	1000	5.5×10^{-6}

Table A.1: IC79 Southern Hemisphere GRB catalog *(continued)*

	RA (°)	Dec (°)	σ	z	Trigger (UT)	T_1 (s)	T_2 (s)	T_{100} (s)	α_γ	β_γ	ε_γ	$E_{\min}$	$E_{\max}$	f_γ
GRB101224B	289.14	-55.25	4.82°	2.15*	2010-12-24 13:52:58.23	-0.13	44.61	44.74	1.05†	2.25†	205†	8	1000	3.892×10^{-6}
GRB101224D	325.17	-38.66	8.29°	2.15*	2010-12-24 23:57:34.94	-9.73	8.96	18.69	1.05†	2.25†	205†	8	1000	1.355×10^{-6}
GRB101227A	186.79	-83.55	7.16°	2.15*	2010-12-27 04:40:28.72	-0.77	94.72	95.49	1.05†	2.25†	205†	8	1000	3.431×10^{-6}
GRB101227B	240.50	-24.50	1.62°	2.15*	2010-12-27 09:45:06.57	0.77	154.11	153.34	1.05†	2.25†	205†	8	1000	1.375×10^{-5}
GRB101227C	150.87	-49.44	2.59°	2.15*	2010-12-27 12:51:46.19	-0.13	28.74	28.87	1.05†	2.25†	205†	8	1000	6.441×10^{-6}
GRB110105A	85.11	-17.12	2.03°	2.15*	2011-01-05 21:02:39.60	-7.68	115.71	123.39	1.05†	2.25†	205†	8	1000	2.092×10^{-5}
GRB110108A	11.62	-9.64	2.67°	2.15*	2011-01-08 23:26:18.52	-1.02	50.43	51.45	1.05†	2.25†	205†	8	1000	2.511×10^{-6}
GRB110118A	226.57	-39.55	4.07°	2.15*	2011-01-18 20:34:18.79	-6.14	28.42	34.56	1.05†	2.25†	205†	8	1000	2.966×10^{-6}
GRB110120A	61.60	-12.00	0.40°	2.15*	2011-01-20 15:59:39.22	-0.7	44.216	44.916	0.6	2.6	680	20	5000	3.1×10^{-5}
GRB110204A	1.82	-17.40	4.03°	2.15*	2011-02-04 04:17:11.37	-3.84	24.83	28.67	1.05†	2.25†	205†	8	1000	3.096×10^{-6}
GRB110205B	359.73	-80.44	9.24°	2.15*	2011-02-05 00:39:04.65	-2.82	3.58	6.4	1.05†	2.25†	205†	8	1000	1.953×10^{-7}
GRB110206A	92.36	-58.81	0.02°	2.15*	2011-02-06 18:08:05.00	0	20	20.0	1*	2*	200*	10*	10000*	1.00×10^{-5}*
GRB110207A	12.54	-10.79	0.01°	2.15*	2011-02-07 11:17:20.29	-1.02	108.3	109.32	1.09	3.09	450	10	1000	4.4×10^{-6}
GRB110207B	179.00	-58.43	9.03°	2.15*	2011-02-07 23:00:26.41	-0.77	6.91	7.68	1.05†	2.25†	205†	8	1000	3.423×10^{-7}
GRB110208A	22.46	-20.59	1.08″	2.15*	2011-02-08 21:10:46.00	-1.5	40.7	42.2	2.08	3.08	200*	15	150	2.7×10^{-7}
GRB110209A	329.70	-21.93	10.63°	2.15*	2011-02-09 03:58:08.30	-3.78	1.86	5.64	1.05†	2.25†	205†	8	1000	6.733×10^{-7}
GRB110212B	311.33	-74.50	4.33°	0.5*	2011-02-12 13:12:33.52	-0.05	0.02	0.07	1.05†	2.25†	205†	8	1000	6.349×10^{-7}
GRB110223B	150.23	-68.30	1.08″	2.15*	2011-02-23 21:25:48.00	-45	20	65.0	1.65	2.65	200*	15	150	6.1×10^{-7}
GRB110227A	148.72	-54.04	11.93°	0.5*	2011-02-27 00:12:28.23	-0.19	1.54	1.73	1.05†	2.25†	205†	8	1000	1.638×10^{-7}
GRB110227C	232.73	-9.94	4.99°	2.15*	2011-02-27 10:04:12.55	-11.26	14.34	25.6	1.05†	2.25†	205†	8	1000	2.421×10^{-6}
GRB110228A	10.27	-45.67	2.56°	2.15*	2011-02-28 00:15:58.91	-30.72	13.76	44.48	1.05†	2.25†	205†	8	1000	5.144×10^{-6}
GRB110305A	260.88	-15.80	1.08″	2.15*	2011-03-05 06:38:01.00	-0.9	12.1	13.0	1.62	2.62	200*	15	150	8.0×10^{-7}
GRB110312A	157.48	-5.26	1.08″	2.15*	2011-03-12 17:55:37.00	24.1	64.9	40.8	2.32	3.32	200*	15	150	8.2×10^{-7}
GRB110316A	46.70	-67.58	17.80°	2.15*	2011-03-16 03:19:41.86	-3.01	-0.06	2.95	1.05†	2.25†	205†	8	1000	1.150×10^{-7}
GRB110318A	338.29	-15.28	0.01°	2.15*	2011-03-18 13:14:19.00	-13	10.6	23.6	0.8	2.74	107.00	10	1000	8.05×10^{-6}

Table A.1: IC79 Southern Hemisphere GRB catalog *(continued)*

	RA (°)	Dec (°)	σ	z	Trigger (UT)	T_1 (s)	T_2 (s)	T_{100} (s)	α_γ	β_γ	ε_γ	$E_{\min}$	$E_{\max}$	f_γ
GRB110318B	211.68	-51.58	1.08″	2.15*	2011-03-18 15:27:09.00	-1.7	3.7	5.4	1.09	2.09	200*	15	150	2.9×10^{-7}
GRB110319A	356.50	-66.01	1.08″	2.15*	2011-03-19 02:16:41.00	-0.3	31.3	31.6	1.31	3.31	21.9	15	150	1.4×10^{-6}
GRB110319B	326.09	-56.77	0.01°	2.15*	2011-03-19 19:34:02.00	-3.5	28.67	32.17	1.39	2.39	200*	15	150	1.0×10^{-6}
GRB110319C	207.96	-51.58	4.94°	2.15*	2011-03-19 15:04:45.46	-2.3	13.04	15.34	1.05†	2.25†	205†	8	1000	1.562×10^{-6}
GRB110321A	13.31	-21.81	11.83°	2.15*	2011-03-21 08:17:42.48	-4.1	26.62	30.72	1.05†	2.25†	205†	8	1000	1.120×10^{-6}
GRB110322A	99.04	-48.90	4.72°	2.15*	2011-03-22 13:23:42.81	-4.1	32	36.1	1.05†	2.25†	205†	8	1000	3.560×10^{-6}
GRB110407B	97.41	-11.95	1.00°	2.15*	2011-04-07 23:56:57.06	0.83	9.86	9.03	1.05†	2.25†	205†	8	1000	2.643×10^{-5}
GRB110410A	30.94	-15.95	3.67°	2.15*	2011-04-10 03:10:52.43	-11.01	50.94	61.95	1.05†	2.25†	205†	8	1000	6.412×10^{-6}
GRB110410B	337.17	-21.96	17.39°	2.15*	2011-04-10 18:31:19.88	-4.74	3.33	8.07	1.05†	2.25†	205†	8	1000	9.522×10^{-7}
GRB110411B	210.30	-64.99	6.28°	2.15*	2011-04-11 15:05:15.35	-3.84	19.71	23.55	1.05†	2.25†	205†	8	1000	3.584×10^{-6}
GRB110420A	2.16	-37.89	0.36″	2.15*	2011-04-20 11:02:24.00	-0.1	16	16.1	1.71	3.71	43	10*	10000*	6.54×10^{-6}
GRB110420B	320.05	-41.28	0.02°	0.5*	2011-04-20 22:42:11.73	-0.06	0.1	0.16	0.12	2.12	296.8	10	1000	2.65×10^{-7}
GRB110424A	293.31	-11.12	12.35°	0.5*	2011-04-24 18:11:36.65	-0.06	0.61	0.67	1.05†	2.25†	205†	8	1000	4.652×10^{-8}
GRB110426A	219.93	-8.72	1.28°	2.15*	2011-04-26 15:06:26.61	14.59	370.95	356.36	2.28	3.28	200*	10	1000	4.54×10^{-5}
GRB110503B	70.51	-10.90	4.29°	2.15*	2011-05-03 03:28:26.12	-0.26	7.68	7.94	1.05†	2.25†	205†	8	1000	1.865×10^{-6}
GRB110505A	16.81	-32.30	3.09°	2.15*	2011-05-05 04:52:56.43	-0.38	3.71	4.09	1.05†	2.25†	205†	8	1000	2.034×10^{-6}
GRB110509A	180.81	-34.00	4.60°	2.15*	2011-05-09 03:24:38.79	-11.01	57.86	68.87	1.05†	2.25†	205†	8	1000	3.761×10^{-6}
GRB110509B	74.65	-26.98	8.30°	0.5*	2011-05-09 11:24:15.58	-0.32	0.32	0.64	1.05†	2.25†	205†	8	1000	5.257×10^{-7}
GRB110511A	214.10	-45.42	10.62°	2.15*	2011-05-11 14:47:12.69	-2.56	3.33	5.89	1.05†	2.25†	205†	8	1000	4.894×10^{-7}

Table A.2: IC86-2011 Southern Hemisphere GRB catalog

	RA (°)	Dec (°)	σ	z	Trigger (UT)	T_1 (s)	T_2 (s)	T_{100} (s)	α_γ	β_γ	ε_γ	$E_{\min}$	$E_{\max}$	f_γ
GRB110517A	296.09	-73.76	8.97°	0.5*	2011-05-17 10:52:35.41	-0.06	0.51	0.57	1.05†	2.25†	205†	8	1000	9.890×10^{-8}
GRB110518A	67.18	-34.20	0.20°	2.15*	2011-05-18 20:38:10.77	0	35.072	35.072	1.29	2.3	229	20	10000	6.5×10^{-5}
GRB110519A	261.64	-23.43	0.01°	2.15*	2011-05-19 02:12:16.00	-4.7	37.8	42.5	2.09	3.09	200*	15	150	4.0×10^{-6}
GRB110520B	71.01	-85.93	12.41°	2.15*	2011-05-20 07:14:26.24	-10.5	1.79	12.29	1.05†	2.25†	205†	8	1000	1.043×10^{-6}
GRB110521B	57.54	-62.34	1.31°	2.15*	2011-05-21 11:28:58.88	0	6.14	6.14	1.05†	2.25†	205†	8	1000	3.608×10^{-6}
GRB110522C	180.57	-26.81	12.50°	2.15*	2011-05-22 15:11:56.61	-0.26	57.86	58.12	1.05†	2.25†	205†	8	1000	3.044×10^{-6}
GRB110523A	219.03	-15.42	4.50°	2.15*	2011-05-23 08:15:54.58	-1.28	43.26	44.54	1.05†	2.25†	205†	8	1000	2.227×10^{-6}
GRB110526A	102.48	-16.42	5.84°	0.5*	2011-05-26 17:09:01.81	-0.13	0.32	0.45	1.05†	2.25†	205†	8	1000	8.457×10^{-7}
GRB110528A	44.79	-6.87	2.48°	2.15*	2011-05-28 14:58:44.30	-1.02	68.61	69.63	1.05†	2.25†	205†	8	1000	4.595×10^{-6}
GRB110609B	317.63	-38.16	4.71°	2.15*	2011-06-09 10:12:06.16	-6.66	26.37	33.03	1.05†	2.25†	205†	8	1000	2.353×10^{-6}
GRB110616A	274.45	-34.02	11.96°	2.15*	2011-06-16 15:33:25.23	-4.61	7.94	12.55	1.05†	2.25†	205†	8	1000	1.295×10^{-6}
GRB110618A	176.81	-71.69	0.50°	2.15*	2011-06-18 08:47:36.38	-3.07	246.632	249.702	1.4	3.4	569	20	5000	1.1×10^{-4}
GRB110618B	147.05	-7.48	2.10°	2.15*	2011-06-18 18:14:16.31	-0.51	89.09	89.6	1.05†	2.25†	205†	8	1000	9.781×10^{-6}
GRB110624A	65.02	-15.95	17.34°	2.15*	2011-06-24 21:44:25.56	-1.28	2.24	3.52	1.05†	2.25†	205†	8	1000	2.781×10^{-7}
GRB110625B	315.33	-39.44	4.60°	2.15*	2011-06-25 13:53:24.57	-0.51	35.07	35.58	1.05†	2.25†	205†	8	1000	3.523×10^{-6}
GRB110702A	5.62	-37.66	4.75°	2.15*	2011-07-02 04:29:28.92	-10.75	23.62	34.37	1.05†	2.25†	205†	8	1000	7.988×10^{-6}
GRB110703A	155.39	-29.30	3.76°	2.15*	2011-07-03 13:22:15.58	-4.22	2.5	6.72	1.05†	2.25†	205†	8	1000	9.739×10^{-7}
GRB110706B	94.15	-50.77	2.04°	2.15*	2011-07-06 11:26:15.76	-2.56	70.66	73.22	1.05†	2.25†	205†	8	1000	6.716×10^{-6}
GRB110708B	170.38	-50.57	0.16°	2.15*	2011-07-08 13:59:46.39	0	47.616	47.616	0.78	2.4	294	20	10000	9.4×10^{-5}
GRB110709B	164.65	-23.45	0.72″	2.15*	2011-07-09 21:32:44.00	-12	850.3	862.3	1	3.0	278	10*	10000*	1.1×10^{-6}
GRB110709D	156.21	-41.79	10.84°	2.15*	2011-07-09 20:40:50.09	-1.79	3.58	5.37	1.05†	2.25†	205†	8	1000	7.974×10^{-7}
GRB110715A	237.68	-46.24	1.44″	0.82	2011-07-15 13:13:49.00	-3	24.432	27.432	1.23	2.7	120	20	10000	2.3×10^{-5}
GRB110716A	329.68	-76.98	3.86°	2.15*	2011-07-16 00:25:19.97	-3.07	4.1	7.17	1.05†	2.25†	205†	8	1000	1.355×10^{-6}
GRB110717A	308.47	-7.85	7.45°	0.5*	2011-07-17 04:19:50.66	-0.02	0.1	0.12	1.05†	2.25†	205†	8	1000	2.512×10^{-7}

Table A.2: IC86-2011 Southern Hemisphere GRB catalog *(continued)*

	RA (°)	Dec (°)	σ	z	Trigger (UT)	T_1 (s)	T_2 (s)	T_{100} (s)	α_γ	β_γ	ε_γ	$E_{\min}$	$E_{\max}$	f_γ
GRB110717B	312.84	-14.84	1.20°	2.15*	2011-07-17 07:39:55.86	5.38	95.75	90.37	1.05†	2.25†	205†	8	1000	4.245×10^{-5}
GRB110720A	198.65	-44.29	2.60°	2.15*	2011-07-20 04:14:32.38	-0.13	11.07	11.2	1.05†	2.25†	205†	8	1000	5.628×10^{-6}
GRB110721A	333.40	-39.00	0.75°	2.15*	2011-07-21 04:47:43.76	0	29.624	29.624	0.94	1.77	372.50	10	1000	3.52×10^{-5}
GRB110725A	270.14	-25.20	9.06°	2.15*	2011-07-25 05:39:42.06	-1.02	19.2	20.22	1.05†	2.25†	205†	8	1000	1.309×10^{-6}
GRB110730A	263.08	-22.78	4.28°	2.15*	2011-07-30 00:11:54.74	-7.94	20.48	28.42	1.05†	2.25†	205†	8	1000	1.257×10^{-6}
GRB110731A	280.50	-28.54	0.36″	2.83	2011-07-31 11:09:30.00	-1.5	80.3	81.8	0.8	2.98	304	10	1000	2.218×10^{-5}
GRB110801B	248.27	-57.06	7.30°	0.5*	2011-08-01 08:01:43.09	-0.13	0.26	0.39	1.05†	2.25†	205†	8	1000	3.537×10^{-7}
GRB110803A	300.42	-11.44	7.49°	2.15*	2011-08-03 18:47:25.43	-156.68	30.21	186.89	1.05†	2.25†	205†	8	1000	2.951×10^{-6}
GRB110807A	278.70	-8.76	0.03°	2.15*	2011-08-07 19:57:46.00	0	10	10.0	1*	2*	200*	10*	10000*	1.00×10^{-5}*
GRB110808A	57.27	-44.20	1.80″	2.15*	2011-08-08 06:18:54.00	-7.4	40.6	48.0	2.32	3.32	200*	15	150	3.3×10^{-7}
GRB110808B	266.18	-37.74	0.07°	0.5*	2011-08-08 15:44:55.24	0	0.5	0.5	1.07	2.5	4238	20	10000	1.6×10^{-5}
GRB110809A	172.17	-13.93	1.84°	2.15*	2011-08-09 11:03:34.00	-4.35	8.19	12.54	1.05†	2.25†	205†	8	1000	3.905×10^{-6}
GRB110817A	336.04	-45.84	1.54°	2.15*	2011-08-17 04:35:12.12	0	5.95	5.95	1.05†	2.25†	205†	8	1000	1.195×10^{-5}
GRB110818A	317.34	-63.98	0.72″	2.15*	2011-08-18 20:37:49.00	-14.2	117.4	131.6	1.33	3.33	256.3	10	1000	8.2×10^{-6}
GRB110819A	139.49	-76.64	3.19°	2.15*	2011-08-19 15:57:54.97	-0.51	15.87	16.38	1.05†	2.25†	205†	8	1000	3.036×10^{-6}
GRB110820B	157.58	-54.60	0.50°	2.15*	2011-08-20 21:27:48.05	0	191.488	191.488	1.22	2.1	481	20	10000	2.5×10^{-4}
GRB110825B	251.31	-80.28	5.18°	2.15*	2011-08-25 06:22:11.44	-16.38	34.69	51.07	1.05†	2.25†	205†	8	1000	2.179×10^{-6}
GRB110828A	110.58	-23.81	1.04°	2.15*	2011-08-28 13:48:14.72	-1.12	43.55	44.67	1.05†	2.25†	205†	8	1000	2.721×10^{-6}
GRB110901A	141.28	-15.79	3.37°	2.15*	2011-09-01 05:31:44.06	-7.68	14.85	22.53	1.05†	2.25†	205†	8	1000	1.506×10^{-6}
GRB110904B	190.40	-28.85	6.11°	2.15*	2011-09-04 03:54:36.02	-1.28	50.18	51.46	1.05†	2.25†	205†	8	1000	3.464×10^{-6}
GRB110905A	278.96	-19.27	0.03°	2.15*	2011-09-05 05:48:40.00	590	963	373.0	1.53	2.53	200*	15	150	7.8×10^{-7}
GRB110906A	296.89	-26.21	0.04°	2.15*	2011-09-06 12:25:13.00	0	94	94.0	1*	2*	200*	10*	10000*	1.00×10^{-5}*
GRB110909A	347.34	-24.22	1.98°	2.15*	2011-09-09 02:46:58.19	-12.29	8.45	20.74	1.05†	2.25†	205†	8	1000	4.920×10^{-5}
GRB110911A	258.58	-66.98	50.00°	2.15*	2011-09-11 01:41:41.57	-4.61	4.35	8.96	1.05†	2.25†	205†	8	1000	5.938×10^{-7}
GRB110918A	32.58	-27.28	0.06°	0.982	2011-09-18 21:27:02.86	0	69.376	69.376	1.2	2	150	20	10000	7.5×10^{-4}

Table A.2: IC86-2011 Southern Hemisphere GRB catalog *(continued)*

	RA (°)	Dec (°)	σ	z	Trigger (UT)	T_1 (s)	T_2 (s)	T_{100} (s)	α_γ	β_γ	ε_γ	$E_{\min}$	$E_{\max}$	f_γ
GRB110920B	209.82	-27.56	1.00°	2.15*	2011-09-20 13:05:43.81	5.12	165.89	160.77	1.05†	2.25†	205†	8	1000	1.723×10^{-4}
GRB110921B	6.09	-5.83	7.31°	2.15*	2011-09-21 10:38:48.20	-68.61	80.9	149.51	1.05†	2.25†	205†	8	1000	5.897×10^{-6}
GRB110921C	17.97	-27.75	1.00°	2.15*	2011-09-21 21:52:45.09	0.9	18.56	17.66	1.05†	2.25†	205†	8	1000	3.631×10^{-5}
GRB110923A	323.40	-10.89	3.69°	2.15*	2011-09-23 20:01:58.13	0	46.4	46.4	1.05†	2.25†	205†	8	1000	4.092×10^{-6}
GRB110924A	234.75	-66.31	0.03°	2.15*	2011-09-24 09:03:20.00	0	10	10.0	1*	2*	200*	10*	10000*	1.00×10^{-5}*
GRB110929A	288.19	-62.21	4.03°	2.15*	2011-09-29 04:28:53.58	-0.51	4.61	5.12	1.05†	2.25†	205†	8	1000	2.197×10^{-6}
GRB110930A	187.31	-53.66	5.05°	2.15*	2011-09-30 13:32:31.19	-6.91	30.98	37.89	1.05†	2.25†	205†	8	1000	6.232×10^{-6}
GRB111001A	340.01	-15.33	15.11°	0.5*	2011-10-01 19:17:58.58	-0.26	0.13	0.39	1.05†	2.25†	205†	8	1000	1.901×10^{-7}
GRB111003A	276.76	-62.32	1.11°	2.15*	2011-10-03 11:10:00.23	0.51	17.15	16.64	0.94	2.94	231.5	10	1000	1.83×10^{-5}
GRB111005A	223.31	-19.72	0.02°	2.15*	2011-10-05 08:05:14.00	-5.23	23.06	28.29	2.03	3.03	200*	15	150	6.2×10^{-7}
GRB111008A	60.45	-32.71	1.08″	5.0	2011-10-08 22:12:58.00	-2.64	68.8	71.44	1.36	3.36	149	20	2000	9.0×10^{-6}
GRB111008B	220.75	-5.67	4.34°	2.15*	2011-10-08 23:49:01.29	-4.1	38.4	42.5	1.05†	2.25†	205†	8	1000	3.034×10^{-6}
GRB111009A	183.04	-56.82	1.08°	2.15*	2011-10-09 06:45:40.17	-0.26	20.48	20.74	1.05†	2.25†	205†	8	1000	1.203×10^{-5}
GRB111010B	183.54	-31.70	7.08°	2.15*	2011-10-10 15:50:21.80	-1.02	7.68	8.7	1.05†	2.25†	205†	8	1000	8.706×10^{-7}
GRB111010D	77.02	-14.96	7.68°	2.15*	2011-10-10 21:34:13.68	-14.66	3.9	18.56	1.05†	2.25†	205†	8	1000	9.588×10^{-7}
GRB111011A	37.96	-12.53	6.77°	0.5*	2011-10-11 02:15:09.90	-0.06	1.41	1.47	1.05†	2.25†	205†	8	1000	4.205×10^{-7}
GRB111015A	220.65	-58.41	1.96°	2.15*	2011-10-15 10:15:12.98	-0.64	92.1	92.74	1.05†	2.25†	205†	8	1000	2.420×10^{-5}
GRB111017A	8.10	-7.01	1.00°	2.15*	2011-10-17 15:45:23.72	0.26	11.33	11.07	0.91	2.7	692.5	10	1000	2.26×10^{-5}
GRB111020A	287.05	-38.01	1.08″	0.5*	2011-10-20 06:33:49.00	-0.04	0.39	0.43	1.37	2.37	1000*	15	150	6.5×10^{-8}
GRB111022A	275.87	-23.67	0.01°	2.15*	2011-10-22 16:07:04.00	-17.69	18.57	36.26	1.01	3.01	64.7	15	150	2.0×10^{-6}
GRB111022C	104.50	-33.11	9.32°	0.5*	2011-10-22 20:29:23.70	-0.13	0.06	0.19	1.05†	2.25†	205†	8	1000	1.260×10^{-7}
GRB111024B	162.74	-44.94	2.57°	2.15*	2011-10-24 17:19:02.88	-6.14	62.46	68.6	1.05†	2.25†	205†	8	1000	1.578×10^{-5}
GRB111025A	325.62	-35.52	2.73°	2.15*	2011-10-25 01:52:45.74	-0.51	51.2	51.71	1.05†	2.25†	205†	8	1000	2.981×10^{-6}
GRB111026A	244.26	-47.44	0.02°	2.15*	2011-10-26 06:47:29.00	-0.09	4.07	4.16	1.69	2.69	200*	15	150	1.7×10^{-7}
GRB111103A	327.11	-10.53	0.01°	2.15*	2011-11-03 10:35:13.00	-0.42	12.14	12.56	0.43	2.43	152.2	10	1000	3.20×10^{-6}

Table A.2: IC86-2011 Southern Hemisphere GRB catalog *(continued)*

	RA (°)	Dec (°)	σ	z	Trigger (UT)	T_1 (s)	T_2 (s)	T_{100} (s)	α_γ	β_γ	ε_γ	$E_{\min}$	$E_{\max}$	f_γ
GRB111103C	201.58	-43.16	10.99°	0.5*	2011-11-03 22:45:05.72	-0.06	0.26	0.32	1.05†	2.25†	205†	8	1000	2.818×10^{-7}
GRB111107A	129.48	-66.52	1.08″	2.893	2011-11-07 00:50:25.48	-1.54	31.83	33.37	1.38	3.38	108	10	1000	1.392×10^{-6}
GRB111107B	315.46	-38.53	3.53°	2.15*	2011-11-07 01:49:46.02	0.19	77.38	77.19	1.05†	2.25†	205†	8	1000	1.041×10^{-5}
GRB111109A	118.20	-41.58	1.44″	2.15*	2011-11-09 02:57:46.00	-5.6	8.4	14.0	1.86	2.86	200*	15	150	2.4×10^{-7}
GRB111109B	133.73	-33.35	7.38°	2.15*	2011-11-09 10:52:32.25	-2.56	2.3	4.86	1.05†	2.25†	205†	8	1000	3.049×10^{-7}
GRB111113B	4.32	-7.52	3.96°	2.15*	2011-11-13 09:50:11.76	-1.02	14.34	15.36	1.05†	2.25†	205†	8	1000	3.103×10^{-6}
GRB111114A	268.08	-20.01	5.72°	2.15*	2011-11-14 05:35:45.35	-1.54	20.48	22.02	1.05†	2.25†	205†	8	1000	1.112×10^{-6}
GRB111117B	27.16	-16.11	6.22°	2.15*	2011-11-17 12:38:00.76	-1.28	22.53	23.81	1.05†	2.25†	205†	8	1000	1.423×10^{-6}
GRB111120A	344.60	-37.34	5.17°	2.15*	2011-11-20 13:20:24.05	-21.25	77.38	98.63	1.05†	2.25†	205†	8	1000	6.728×10^{-6}
GRB111121A	154.76	-46.67	1.08″	2.15*	2011-11-21 16:26:24.00	-0.34	141.08	141.42	0.44	3	1780	20	10000	2.3×10^{-5}
GRB111123A	154.85	-20.64	1.08″	3.1516	2011-11-23 18:13:21.00	-8.7	481.3	490.0	1.68	2.68	200*	15	150	7.3×10^{-6}
GRB111129A	307.43	-52.71	1.08″	2.15*	2011-11-29 16:18:14.00	-6.29	2.88	9.17	2.56	3.56	200*	15	150	1.8×10^{-7}
GRB111203B	242.83	-22.15	13.30°	2.15*	2011-12-03 14:36:45.38	-2.82	19.2	22.02	1.05†	2.25†	205†	8	1000	6.948×10^{-7}
GRB111204A	336.63	-31.38	1.44″	2.15*	2011-12-04 13:37:28.00	33	81	48.0	1.83	2.83	200*	15	150	4.7×10^{-7}
GRB111205A	134.49	-31.97	0.10°	2.15*	2011-12-05 13:10:50.30	0	80.384	80.384	0.82	2.82	998	20	10000	1.7×10^{-4}
GRB111207A	92.92	-39.00	0.03°	2.15*	2011-12-07 14:16:59.00	-1	3	4.0	1*	2*	200*	10*	10000*	1.00×10^{-5}*
GRB111207B	164.88	-17.94	9.98°	0.5*	2011-12-07 12:17:16.20	-0.9	-0.13	0.77	1.05†	2.25†	205†	8	1000	2.621×10^{-7}
GRB111209A	14.34	-46.80	0.72″	0.677	2011-12-09 07:12:08.00	-1900	4400	6300.0	1.31	3.31	310	10*	10000*	4.86×10^{-4}
GRB111210A	191.48	-7.17	1.44″	2.15*	2011-12-10 14:37:03.00	-2.33	0.36	2.69	1.3	2.3	200*	15	150	1.6×10^{-7}
GRB111212A	310.43	-68.61	1.08″	2.15*	2011-12-12 09:23:07.00	-5.77	62.74	68.51	1.67	2.67	200*	15	150	1.4×10^{-6}
GRB111220A	267.60	-56.05	1.39°	2.15*	2011-12-20 11:40:26.24	-6.14	32.9	39.04	1.05†	2.25†	205†	8	1000	5.356×10^{-5}
GRB111221A	10.16	-29.77	1.92°	2.15*	2011-12-21 17:43:30.81	-0.51	26.62	27.13	1.05†	2.25†	205†	8	1000	3.059×10^{-6}
GRB111229A	76.29	-84.71	1.08″	1.3805	2011-12-29 22:37:52.00	-0.97	26.15	27.12	1.85	2.85	200*	15	150	3.4×10^{-7}
GRB111230B	242.61	-22.12	2.02°	2.15*	2011-12-30 19:39:32.14	-0.64	12.1	12.74	1.05†	2.25†	205†	8	1000	3.512×10^{-6}
GRB120102B	341.15	-23.16	3.58°	2.15*	2012-01-02 09:59:01.27	-10.24	9.98	20.22	1.05†	2.25†	205†	8	1000	2.553×10^{-6}

Table A.2: IC86-2011 Southern Hemisphere GRB catalog *(continued)*

	RA (°)	Dec (°)	σ	z	Trigger (UT)	T_1 (s)	T_2 (s)	T_{100} (s)	α_γ	β_γ	ε_γ	$E_{\min}$	$E_{\max}$	f_γ
GRB120107A	246.40	-69.93	0.50°	2.15*	2012-01-07 09:12:12.45	0	27	27.0	0.91	2.11	188.90	10	1000	6.81×10^{-6}
GRB120114B	263.23	-75.64	11.05°	2.15*	2012-01-14 10:23:39.21	-0.13	2.62	2.75	1.05†	2.25†	205†	8	1000	1.487×10^{-7}
GRB120118A	195.40	-61.64	0.03°	2.15*	2012-01-18 06:04:44.00	0	60	60.0	1*	2*	200*	20	200	2×10^{-7}
GRB120118B	124.87	-7.18	1.08″	2.943	2012-01-18 17:00:22.94	-3.33	34.5	37.83	2.08	3.08	200*	15	150	1.8×10^{-6}
GRB120119B	139.65	-61.33	2.00°	2.15*	2012-01-19 05:29:49.01	0	41.73	41.73	1.05†	2.25†	205†	8	1000	5.942×10^{-6}
GRB120119C	65.96	-33.92	4.42°	2.15*	2012-01-19 08:29:29.82	-7.94	8.45	16.39	1.05†	2.25†	205†	8	1000	2.610×10^{-6}
GRB120121A	249.35	-23.96	1.08″	2.15*	2012-01-21 09:42:19.00	-11	18.33	29.33	1.23	2.23	200*	15	150	1.1×10^{-6}
GRB120121B	235.67	-39.34	7.86°	2.15*	2012-01-21 02:25:53.80	-3.33	15.1	18.43	1.05†	2.25†	205†	8	1000	1.955×10^{-6}
GRB120129B	26.52	-8.51	15.04°	0.5*	2012-01-29 07:29:14.05	-0.64	0.64	1.28	1.05†	2.25†	205†	8	1000	8.932×10^{-8}
GRB120130A	150.04	-17.45	3.69°	2.15*	2012-01-30 16:47:10.88	-0.64	27.14	27.78	1.05†	2.25†	205†	8	1000	6.612×10^{-6}
GRB120203A	339.30	-46.59	6.77°	2.15*	2012-02-03 19:29:23.98	-4.86	5.38	10.24	1.05†	2.25†	205†	8	1000	1.100×10^{-6}
GRB120210A	54.65	-58.52	5.51°	0.5*	2012-02-10 15:35:43.28	-0.06	1.28	1.34	1.05†	2.25†	205†	8	1000	6.445×10^{-7}
GRB120211A	87.75	-24.77	1.08″	2.15*	2012-02-11 11:58:28.00	-2.34	64.1	66.44	1.5	2.5	200*	15	150	8.1×10^{-7}
GRB120212A	43.10	-18.02	1.08″	2.15*	2012-02-12 09:11:23.50	-2.05	7.17	9.22	1.83	2.83	200*	10	1000	1.407×10^{-7}
GRB120212B	303.40	-48.10	7.47°	0.5*	2012-02-12 08:27:47.59	-0.83	0.03	0.86	1.05†	2.25†	205†	8	1000	5.087×10^{-8}
GRB120219B	274.85	-31.11	10.94°	2.15*	2012-02-19 13:31:23.11	-1.15	6.98	8.13	1.05†	2.25†	205†	8	1000	5.578×10^{-7}
GRB120220A	206.13	-57.36	7.39°	2.15*	2012-02-20 05:02:21.60	-5.38	15.87	21.25	1.05†	2.25†	205†	8	1000	1.237×10^{-6}
GRB120222B	340.00	-36.41	5.70°	2.15*	2012-02-22 02:51:54.09	-5.12	24.32	29.44	1.05†	2.25†	205†	8	1000	2.451×10^{-6}
GRB120223A	219.61	-7.46	2.74°	2.15*	2012-02-23 22:23:48.94	-0.51	13.82	14.33	1.05†	2.25†	205†	8	1000	3.879×10^{-6}
GRB120224A	40.94	-17.76	1.08″	2.15*	2012-02-24 04:39:56.00	-1.08	8.26	9.34	2.25	3.25	200*	15	150	2.4×10^{-7}
GRB120227B	256.73	-88.86	1.21°	2.15*	2012-02-27 17:24:41.05	0.26	17.66	17.4	1.05†	2.25†	205†	8	1000	2.195×10^{-5}
GRB120304A	127.15	-61.12	1.00°	2.15*	2012-03-04 01:27:48.72	-0.26	9.73	9.99	1.05†	2.25†	205†	8	1000	5.046×10^{-6}
GRB120304B	277.28	-46.22	1.00°	2.15*	2012-03-04 05:57:47.78	-0.26	5.12	5.38	1.05†	2.25†	205†	8	1000	1.144×10^{-5}
GRB120314A	17.89	-48.73	17.82°	0.5*	2012-03-14 09:52:34.67	-1.28	0	1.28	1.05†	2.25†	205†	8	1000	1.642×10^{-7}
GRB120316A	57.02	-56.29	0.47°	2.15*	2012-03-16 00:11:02.00	0	28.16	28.16	0.92	2.92	539	20	10000	2.3×10^{-5}

Table A.2: IC86-2011 Southern Hemisphere GRB catalog *(continued)*

	RA (°)	Dec (°)	σ	z	Trigger (UT)	T_1 (s)	T_2 (s)	T_{100} (s)	α_γ	β_γ	ε_γ	$E_{\min}$	$E_{\max}$	f_γ
GRB120319A	69.85	-45.44	3.67°	2.15*	2012-03-19 23:35:04.21	-4.61	67.84	72.45	1.05†	2.25†	205†	8	1000	2.420×10^{-6}
GRB120323B	211.10	-45.23	3.79°	2.15*	2012-03-23 03:52:49.27	-0.77	3.58	4.35	1.05†	2.25†	205†	8	1000	1.408×10^{-6}
GRB120327A	246.86	-29.41	1.08″	2.81	2012-03-27 02:55:16.00	-15.79	74.58	90.37	1.52	2.52	200*	15	150	3.6×10^{-6}
GRB120328A	241.61	-39.34	1.08″	2.15*	2012-03-28 03:06:19.00	-17.27	20.61	37.88	1.87	2.87	200*	15	150	4.7×10^{-7}
GRB120331A	26.37	-54.84	6.51°	2.15*	2012-03-31 01:19:06.64	-2.82	13.57	16.39	1.05†	2.25†	205†	8	1000	6.774×10^{-7}
GRB120401A	58.08	-17.64	1.44″	2.15*	2012-04-01 05:24:15.00	-92.97	52.72	145.69	1.66	2.66	200*	15	150	9.1×10^{-7}
GRB120402B	223.73	-10.40	2.61°	2.15*	2012-04-02 16:04:00.76	-2.08	18.14	20.22	1.35	2.44	37.2	10	1000	3.4×10^{-6}
GRB120403B	55.28	-89.01	1.44″	2.15*	2012-04-03 20:33:56.00	-3	5.3	8.3	1.51	3.51	182	4	10000*	4.6×10^{-7}
GRB120410A	159.63	-17.00	8.60°	0.5*	2012-04-10 14:02:00.19	-1.02	0.06	1.08	1.05†	2.25†	205†	8	1000	2.907×10^{-7}
GRB120411A	38.07	-7.24	8.45°	2.15*	2012-04-11 22:12:25.65	0	38.91	38.91	1.05†	2.25†	205†	8	1000	1.464×10^{-6}
GRB120412A	29.44	-24.67	13.47°	2.15*	2012-04-12 01:18:42.15	-4.1	5.63	9.73	1.05†	2.25†	205†	8	1000	1.246×10^{-6}
GRB120419A	187.40	-63.02	0.03°	2.15*	2012-04-19 12:56:25.00	0	20	20.0	1*	2*	200*	20	200	2×10^{-7}
GRB120420A	47.89	-52.19	5.44°	2.15*	2012-04-20 05:58:07.26	-0.77	24.83	25.6	1.05†	2.25†	205†	8	1000	2.878×10^{-6}
GRB120426A	111.54	-65.63	0.30°	2.15*	2012-04-26 02:09:14.33	0.22	3.1	2.88	0.61	3.2	140	20	10000	1.9×10^{-5}
GRB120429A	165.98	-8.76	15.40°	0.5*	2012-04-29 00:04:07.26	-0.19	1.47	1.66	1.05†	2.25†	205†	8	1000	2.794×10^{-7}
GRB120429B	133.04	-32.23	5.34°	2.15*	2012-04-29 11:37:03.74	-1.02	14.34	15.36	1.05†	2.25†	205†	8	1000	2.368×10^{-6}
GRB120504B	200.28	-24.20	6.74°	2.15*	2012-05-04 22:40:08.60	-2.3	3.46	5.76	1.05†	2.25†	205†	8	1000	1.667×10^{-6}
GRB120506A	172.22	-33.72	9.33°	2.15*	2012-05-06 03:05:02.12	-0.77	1.54	2.31	1.05†	2.25†	205†	8	1000	2.872×10^{-7}
GRB120510B	186.93	-55.24	3.75°	2.15*	2012-05-10 21:36:26.10	1.79	64.26	62.47	1.05†	2.25†	205†	8	1000	6.014×10^{-6}
GRB120511A	226.93	-60.49	2.07°	2.15*	2012-05-11 15:18:47.92	-0.13	45.12	45.25	1.05†	2.25†	205†	8	1000	1.140×10^{-5}

Table A.3: IC86-2012 Southern Hemisphere GRB catalog

	RA (°)	Dec (°)	σ	z	Trigger (UT)	T_1 (s)	T_2 (s)	T_{100} (s)	α_γ	β_γ	ε_γ	$E_{\min}$	$E_{\max}$	f_γ
GRB120426B	285.49	-13.68	3.83°	2.15*	2012-04-26 14:02:22.36	0	30.98	30.98	1.05†	2.25†	205†	8	1000	3.658×10^{-6}
GRB120521A	148.72	-49.42	1.08″	0.5*	2012-05-21 05:59:42.00	0.02	0.56	0.54	0.98	1.98	1000*	15	150	7.8×10^{-8}
GRB120521B	197.01	-52.76	1.08″	2.15*	2012-05-21 09:07:48.00	-1.39	95.14	96.53	0.34	2.34	213	10	1000	3.11×10^{-6}
GRB120522A	166.00	-62.09	0.08°	2.15*	2012-05-22 03:11:07.38	0	78.086	78.086	0.88	2.88	381	20	10000	2.5×10^{-5}
GRB120524A	358.15	-15.61	10.45°	0.5*	2012-05-24 03:12:54.68	-0.13	0.58	0.71	1.05†	2.25†	205†	8	1000	2.527×10^{-7}
GRB120526A	66.28	-32.23	1.04°	2.15*	2012-05-26 07:16:40.77	3.07	46.72	43.65	1.05†	2.25†	205†	8	1000	1.162×10^{-4}
GRB120528B	77.59	-37.80	0.06°	2.15*	2012-05-28 18:11:48.00	0	26	26.0	0.41	2.41	201	10*	10000*	2.9×10^{-6}
GRB120602A	87.92	-39.35	0.04°	2.15*	2012-06-02 05:00:00.23	0	70	70.0	0.77	2.8	300	20	10000	3.6×10^{-4}
GRB120604A	163.87	-7.40	9.34°	2.15*	2012-06-04 05:16:31.31	-2.82	7.68	10.5	1.05†	2.25†	205†	8	1000	1.235×10^{-6}
GRB120608A	229.98	-26.12	2.52°	0.5*	2012-06-08 11:43:51.83	-0.19	0.77	0.96	1.05†	2.25†	205†	8	1000	4.834×10^{-7}
GRB120611A	324.68	-44.79	5.28°	2.15*	2012-06-11 02:36:00.52	-9.22	40.7	49.92	1.05†	2.25†	205†	8	1000	4.526×10^{-6}
GRB120612A	126.72	-17.57	1.08″	2.15*	2012-06-12 02:05:19.00	16.9	125.4	108.5	1.36	2.36	200*	15	150	1.3×10^{-6}
GRB120612C	39.67	-37.91	10.65°	0.5*	2012-06-12 16:29:44.56	-0.19	0.06	0.25	1.05†	2.25†	205†	8	1000	7.051×10^{-7}
GRB120619A	190.74	-25.02	2.79°	0.5*	2012-06-19 21:13:16.91	-0.26	0.7	0.96	1.05†	2.25†	205†	8	1000	4.242×10^{-7}
GRB120701A	80.34	-58.53	0.01°	2.15*	2012-07-01 07:50:41.00	0	15.4	15.4	1.05	2.05	200*	15	150	1.4×10^{-6}
GRB120701B	182.73	-45.70	14.79°	0.5*	2012-07-01 15:41:48.32	-0.96	0.06	1.02	1.05†	2.25†	205†	8	1000	8.357×10^{-8}
GRB120703A	339.36	-29.72	0.72″	2.15*	2012-07-03 17:25:22.00	-7.27	32.6	39.87	0.98	2.08	238.5	10	1000	9.154×10^{-6}
GRB120707A	291.87	-32.77	2.11°	2.15*	2012-07-07 19:12:17.43	1.52	66.6	65.08	1.17	2.31	174	10	1000	1.1×10^{-4}
GRB120709A	320.23	-51.13	0.50°	2.15*	2012-07-09 21:11:40.37	-0.13	27.832	27.962	0.94	2	643	20	10000	1.8×10^{-5}
GRB120710A	120.39	-31.14	4.76°	2.15*	2012-07-10 02:23:17.05	0	131.84	131.84	1.05†	2.25†	205†	8	1000	5.338×10^{-6}
GRB120711A	94.70	-70.90	0.16°	3	2012-07-11 02:45:55.81	0	46.336	46.336	0.94	2.4	973	10	1000	1.942×10^{-4}
GRB120711C	127.88	-31.83	11.03°	2.15*	2012-07-11 10:42:54.57	-1.28	86.27	87.55	1.05†	2.25†	205†	8	1000	1.862×10^{-6}
GRB120712A	169.59	-20.03	1.08″	4.15	2012-07-12 13:42:27.00	-4.57	18.74	23.31	0.6	1.8	124	10	1000	4.43×10^{-6}
GRB120714A	167.98	-30.63	1.08″	2.15*	2012-07-14 07:46:46.00	-0.74	17.78	18.52	1.62	2.62	200*	15	150	8.2×10^{-7}

Table A.3: IC86-2012 Southern Hemisphere GRB catalog *(continued)*

	RA (°)	Dec (°)	σ	z	Trigger (UT)	T_1 (s)	T_2 (s)	T_{100} (s)	α_γ	β_γ	ε_γ	$E_{\min}$	$E_{\max}$	f_γ
GRB120714B	355.41	-46.20	0.03°	0.3984	2012-07-14 21:18:46.57	-23	154	177.0	1.52	2.52	200*	15	150	1.2×10^{-6}
GRB120719A	204.29	-43.45	1.37°	2.15*	2012-07-19 03:30:00.82	0.77	75.78	75.01	1.05†	2.25†	205†	8	1000	1.355×10^{-5}
GRB120728A	137.09	-54.44	1.08″	2.15*	2012-07-28 22:25:12.74	-1.54	31.23	32.77	1.66	3.66	119.80	10	1000	5.29×10^{-6}
GRB120728B	103.77	-45.89	0.47°	2.15*	2012-07-28 10:25:34.98	0	250	250.0	1	2.9	95	20	10000	1.20×10^{-4}
GRB120801A	245.73	-47.37	2.39°	2.15*	2012-08-01 22:05:21.19	-7.17	472.07	479.24	1.05†	2.25†	205†	8	1000	3.340×10^{-5}
GRB120803A	269.53	-6.73	0.03°	2.15*	2012-08-03 07:22:16.00	0.4	11.4	11.0	0.86	1.86	200*	15	150	3.0×10^{-7}
GRB120804A	233.95	-28.78	1.08″	0.5*	2012-08-04 00:54:14.00	-0.16	0.83	0.99	1.34	3.34	135	15	150	1.45×10^{-6}
GRB120805B	30.13	-21.51	10.11°	0.5*	2012-08-05 16:56:21.72	-0.96	0.9	1.86	1.05†	2.25†	205†	8	1000	1.879×10^{-7}
GRB120807A	241.26	-47.48	1.08″	2.15*	2012-08-07 07:09:37.00	-0.24	24.07	24.31	1.81	2.81	200*	15	150	2.9×10^{-7}
GRB120811A	257.18	-22.73	0.03°	2.15*	2012-08-11 02:35:18.00	-14.16	169.06	183.22	1.95	2.95	200*	15	150	1.1×10^{-6}
GRB120811B	43.66	-31.68	0.23°	0.5*	2012-08-11 00:20:30.29	-0.13	1.33	1.46	0.14	2.14	1130	20	10000	4.6×10^{-6}
GRB120815A	273.96	-52.13	1.08″	2.358	2012-08-15 02:13:58.00	-0.24	11.97	12.21	2.29	3.29	200*	15	150	4.9×10^{-7}
GRB120816A	282.14	-6.94	1.08″	2.15*	2012-08-16 19:18:34.00	-1.97	6.66	8.63	2.54	3.54	200*	15	150	4.3×10^{-7}
GRB120817A	250.69	-38.35	1.08″	2.15*	2012-08-17 06:49:42.00	-2.24	30.77	33.01	1.97	2.97	200*	15	150	6.9×10^{-7}
GRB120817B	8.31	-26.43	0.05°	2.15*	2012-08-17 04:02:29.72	-0.03	4.08	4.11	0.82	2.82	1740	20	10000	4.1×10^{-6}
GRB120817C	259.97	-9.07	7.14°	2.15*	2012-08-17 01:22:09.78	-6.4	30.46	36.86	1.05†	2.25†	205†	8	1000	1.040×10^{-6}
GRB120819A	235.91	-7.31	1.08″	2.15*	2012-08-19 13:10:14.00	4.42	82.88	78.46	1.49	2.49	200*	15	150	1.4×10^{-6}
GRB120820A	186.64	-12.31	4.81°	2.15*	2012-08-20 14:02:21.99	-17.41	90.11	107.52	1.05†	2.25†	205†	8	1000	6.981×10^{-6}
GRB120821A	255.27	-40.52	0.02°	2.15*	2012-08-21 13:23:45.00	0	12	12.0	1*	2*	200*	20	200	3×10^{-7}
GRB120827A	222.74	-71.89	1.67°	2.15*	2012-08-27 05:10:25.01	-1.66	3.39	5.05	1.05†	2.25†	205†	8	1000	3.367×10^{-6}
GRB120830A	88.42	-28.81	0.86°	0.5*	2012-08-30 07:07:03.53	-0.38	0.9	1.28	0.4	2.4	1212.00	10	1000	3.253×10^{-6}
GRB120830B	337.87	-80.04	3.46°	2.15*	2012-08-30 05:04:52.74	0.45	16.51	16.06	1.05†	2.25†	205†	8	1000	7.515×10^{-6}
GRB120831A	144.02	-16.21	8.54°	0.5*	2012-08-31 21:37:31.88	-0.26	0.13	0.39	1.05†	2.25†	205†	8	1000	2.515×10^{-7}
GRB120907A	74.75	-9.31	1.08″	2.15*	2012-09-07 00:24:24.51	-1.92	17.76	19.68	0.75	2.75	154.50	6	10000*	7.8×10^{-7}
GRB120908A	230.64	-25.79	0.29°	2.15*	2012-09-08 22:31:00.02	-4.61	62.34	66.95	1.21	3.21	205.9	10	1000	1.7×10^{-5}

Table A.3: IC86-2012 Southern Hemisphere GRB catalog *(continued)*

	RA (°)	Dec (°)	σ	z	Trigger (UT)	T_1 (s)	T_2 (s)	T_{100} (s)	α_γ	β_γ	ε_γ	$E_{\min}$	$E_{\max}$	f_γ
GRB120908B	268.67	-35.79	1.50°	2.15*	2012-09-08 20:57:30.95	0.58	47.42	46.84	1.05†	2.25†	205†	8	1000	1.270×10^{-5}
GRB120909A	275.74	-59.45	0.72″	3.93	2012-09-09 01:41:09.00	0	149.17	149.17	1.23	3.23	335	10*	10000*	2.3×10^{-5}
GRB120911B	172.03	-37.51	0.30°	2.15*	2012-09-11 06:25:14.00	0	132	132.0	1.01	2.72	1200	10	1000	1.973×10^{-4}
GRB120913B	213.66	-14.51	0.01°	2.15*	2012-09-13 23:55:58.00	-51.7	111.79	163.49	1.19	1.97	163	10	1000	2.9×10^{-5}
GRB120916B	82.04	-19.22	11.13°	0.5*	2012-09-16 02:02:15.91	-0.32	1.02	1.34	1.05†	2.25†	205†	8	1000	8.154×10^{-8}
GRB120918A	181.04	-32.76	0.01°	2.15*	2012-09-18 11:16:10.00	-2.86	23.9	26.76	1	3.0	85.5	15	150	3.7×10^{-6}
GRB120919A	214.77	-45.56	0.09°	2.15*	2012-09-19 07:24:38.60	0	25.78	25.78	0.76	2.15	162	10	1000	1.679×10^{-5}
GRB120919B	302.63	-37.49	0.27°	2.15*	2012-09-19 01:14:23.07	2.05	134.56	132.51	0.9	2.3	250	20	10000	3.1×10^{-5}
GRB120919C	303.53	-66.16	11.89°	2.15*	2012-09-19 19:35:41.80	-3.33	18.69	22.02	1.05†	2.25†	205†	8	1000	1.031×10^{-6}
GRB120920A	27.12	-26.12	7.84°	2.15*	2012-09-20 00:04:32.73	-2.3	26.88	29.18	1.05†	2.25†	205†	8	1000	1.193×10^{-6}
GRB120921A	96.42	-64.77	3.20°	2.15*	2012-09-21 21:03:03.77	-0.26	5.38	5.64	1.05†	2.25†	205†	8	1000	2.478×10^{-6}
GRB120922A	234.75	-20.18	1.08″	3.1	2012-09-22 22:30:28.00	-22.58	215.73	238.31	1.6	2.3	37.7	180	10000*	6.5×10^{-6}
GRB120926B	59.72	-37.20	3.76°	2.15*	2012-09-26 10:13:16.04	-2.3	57.86	60.16	1.05†	2.25†	205†	8	1000	4.383×10^{-6}
GRB120926C	24.61	-45.58	21.32°	2.15*	2012-09-26 18:04:35.10	-1.54	1.54	3.08	1.05†	2.25†	205†	8	1000	1.878×10^{-7}
GRB121001A	276.03	-5.67	1.08″	2.15*	2012-10-01 18:23:02.00	-30	143	173.0	1.34	2.34	200*	15	150	1.7×10^{-6}
GRB121004A	137.46	-11.02	9.44°	0.5*	2012-10-04 05:03:18.19	-0.51	1.02	1.53	1.05†	2.25†	205†	8	1000	3.794×10^{-7}
GRB121014A	166.65	-29.11	0.02°	2.15*	2012-10-14 20:11:56.00	-12.21	67.79	80.0	1.91	2.91	200*	15	150	1.1×10^{-6}
GRB121014B	320.01	-53.43	17.20°	0.5*	2012-10-14 15:19:00.58	-0.58	-0.19	0.39	1.05†	2.25†	205†	8	1000	9.619×10^{-8}
GRB121024A	70.47	-12.29	0.72″	2.298	2012-10-24 02:56:12.00	-8.27	75.73	84.0	1.41	2.41	200*	15	150	1.1×10^{-6}
GRB121027A	63.60	-58.83	1.08″	1.773	2012-10-27 07:32:29.00	-9.34	65.33	74.67	1.82	2.82	200*	15	150	2.0×10^{-6}
GRB121027B	4.31	-47.54	2.61°	2.15*	2012-10-27 00:54:19.37	-65.54	101.38	166.92	1.05†	2.25†	205†	8	1000	7.395×10^{-6}
GRB121028B	52.56	-25.07	7.68°	2.15*	2012-10-28 06:43:13.09	-1.79	9.22	11.01	1.05†	2.25†	205†	8	1000	9.978×10^{-7}
GRB121029A	226.77	-28.20	1.65°	2.15*	2012-10-29 08:24:18.00	-2	20	22.0	0.57	2.82	176	10	1000	7.82×10^{-6}
GRB121102A	270.90	-16.96	0.72″	2.15*	2012-11-02 02:27:00.00	0	37.25	37.25	1.88	2.88	200*	15	150	1.9×10^{-6}
GRB121109A	6.84	-42.57	10.37°	2.15*	2012-11-09 08:06:56.63	-6.91	15.23	22.14	1.05†	2.25†	205†	8	1000	5.336×10^{-6}

Table A.3: IC86-2012 Southern Hemisphere GRB catalog *(continued)*

	RA (°)	Dec (°)	σ	z	Trigger (UT)	T_1 (s)	T_2 (s)	T_{100} (s)	α_γ	β_γ	ε_γ	$E_{\min}$	$E_{\max}$	f_γ
GRB121112A	78.98	-55.44	15.56°	0.5*	2012-11-12 19:20:44.27	-0.13	1.15	1.28	1.05†	2.25†	205†	8	1000	2.232×10^{-7}
GRB121116A	180.88	-74.79	6.98°	0.5*	2012-11-16 11:00:24.60	-0.7	0.64	1.34	1.05†	2.25†	205†	8	1000	2.398×10^{-7}
GRB121119A	311.65	-16.92	8.13°	2.15*	2012-11-19 13:53:14.13	-0.26	2.05	2.31	1.05†	2.25†	205†	8	1000	8.815×10^{-7}
GRB121123A	307.32	-11.86	0.36″	2.15*	2012-11-23 10:02:41.00	-6.34	419	425.34	0.25	3	85	10	1000	2.20×10^{-5}
GRB121123B	30.52	-18.79	1.61°	2.15*	2012-11-23 10:35:55.71	2.3	44.8	42.5	1.05†	2.25†	205†	8	1000	1.423×10^{-5}
GRB121127A	176.44	-52.41	0.08°	2.15*	2012-11-27 21:55:57.29	0	3.51	3.51	0.55	1.55	200*	100	1000	9.34×10^{-7}
GRB121201A	13.47	-42.94	1.08″	3.6	2012-12-01 12:25:42.00	-24	71	95.0	1.9	2.9	200*	15	150	7.8×10^{-7}
GRB121205A	238.59	-49.71	11.72°	2.15*	2012-12-05 12:10:04.71	-0.38	2.43	2.81	1.05†	2.25†	205†	8	1000	1.335×10^{-7}
GRB121209A	326.79	-8.23	1.08″	2.15*	2012-12-09 21:59:11.00	-2.16	44.28	46.44	1.43	2.43	200*	15	150	2.9×10^{-6}
GRB121216A	13.88	-85.44	14.15°	2.15*	2012-12-16 10:03:16.45	-2.05	7.17	9.22	1.05†	2.25†	205†	8	1000	3.850×10^{-7}
GRB121217A	153.71	-62.35	1.08″	0.8	2012-12-17 07:17:47.00	-17.7	783.8	801.5	1.2	3.2	264	10	1000	1.11×10^{-5}
GRB121217B	153.71	-62.35	1.80″	2.15*	2012-12-17 07:30:01.58	-807.42	21.25	828.67	1.05†	2.25†	205†	8	1000	6.767×10^{-6}
GRB121225A	264.86	-66.07	0.17°	2.15*	2012-12-25 09:50:24.00	0	33	33.0	1*	2*	200*	10*	10000*	1.00×10^{-5}*
GRB121225B	308.91	-34.35	1.25°	2.15*	2012-12-25 10:01:03.17	-16	70	86.0	1.08	2.14	277.6	10	1000	7.16×10^{-5}
GRB121226A	168.62	-30.41	0.02°	0.5*	2012-12-26 19:09:43.00	-0.36	0.8	1.16	1.51	2.51	1000*	15	150	1.4×10^{-7}
GRB121229A	190.10	-50.59	1.08″	2.707	2012-12-29 05:00:21.00	0	64	64.0	2.43	3.43	200*	15	150	4.6×10^{-7}
GRB121229B	315.59	-11.94	4.58°	2.15*	2012-12-29 12:47:33.36	0	23.04	23.04	1.05†	2.25†	205†	8	1000	3.508×10^{-6}
GRB121231A	335.47	-17.78	6.46°	2.15*	2012-12-31 10:41:23.25	-5.63	27.14	32.77	1.05†	2.25†	205†	8	1000	2.937×10^{-6}
GRB130102B	309.58	-72.38	0.17°	2.15*	2013-01-02 04:41:42.00	0	30	30.0	2.85	3.85	200*	10*	10000*	3.46×10^{-6}
GRB130114A	310.19	-15.32	10.86°	2.15*	2013-01-14 00:27:04.55	-2.05	6.66	8.71	1.05†	2.25†	205†	8	1000	1.113×10^{-6}
GRB130121A	211.31	-49.49	1.14°	2.15*	2013-01-21 20:01:59.97	1.79	180.48	178.69	1.05†	2.25†	205†	8	1000	4.345×10^{-5}
GRB130127A	251.05	-17.07	8.46°	0.5*	2013-01-27 17:50:23.93	-0.26	0.19	0.45	0.03	2.4	700	10	1000	4.9×10^{-7}
GRB130127B	301.21	-57.21	10.01°	2.15*	2013-01-27 07:09:53.16	-3.84	15.62	19.46	1.05†	2.25†	205†	8	1000	1.022×10^{-6}
GRB130131C	189.63	-14.48	1.00°	2.15*	2013-01-31 12:15:13.39	3.58	151.04	147.46	1.05†	2.25†	205†	8	1000	3.920×10^{-5}
GRB130206A	140.39	-58.19	0.02°	2.15*	2013-02-06 19:36:30.45	-2.56	89.03	91.59	1.1	3.1	132.6	10	1000	3.3×10^{-6}

Table A.3: IC86-2012 Southern Hemisphere GRB catalog *(continued)*

	RA (°)	Dec (°)	σ	z	Trigger (UT)	T_1 (s)	T_2 (s)	T_{100} (s)	α_γ	β_γ	ε_γ	$E_{\min}$	$E_{\max}$	f_γ
GRB130209A	33.59	-27.58	1.00°	2.15*	2013-02-09 23:03:41.79	0.13	10.05	9.92	1.05†	2.25†	205†	8	1000	5.900×10^{-6}
GRB130211A	147.52	-42.33	0.02°	2.15*	2013-02-11 03:36:32.00	-1.56	32	33.56	1.81	2.81	200*	15	150	6.4×10^{-7}
GRB130213A	99.09	-8.10	10.62°	2.15*	2013-02-13 21:43:55.96	-5.63	9.73	15.36	1.05†	2.25†	205†	8	1000	9.874×10^{-7}
GRB130218A	69.31	-69.13	2.28°	2.15*	2013-02-18 06:16:25.56	-6.14	30.98	37.12	1.05†	2.25†	205†	8	1000	9.433×10^{-6}
GRB130219B	169.29	-22.25	2.20°	2.15*	2013-02-19 04:44:07.57	5.38	173.38	168.0	1.05†	2.25†	205†	8	1000	3.186×10^{-5}
GRB130228B	240.75	-55.21	1.28°	2.15*	2013-02-28 05:05:57.05	0	15.42	15.42	1.05†	2.25†	205†	8	1000	1.748×10^{-5}
GRB130306A	279.48	-11.68	0.02°	2.15*	2013-03-06 23:47:25.57	-17.66	370.1	387.76	1.5	3.5	212	20	10000	2.9×10^{-4}
GRB130310A	141.91	-17.43	0.22°	2.15*	2013-03-10 20:09:41.50	4.1	20.1	16.0	1.01	2.27	2100	10	1000	1.4×10^{-5}
GRB130315A	157.54	-51.79	0.01°	2.15*	2013-03-15 12:45:32.00	-3.3	268	271.3	1.81	2.81	200*	15	150	4.9×10^{-6}
GRB130320A	192.68	-14.47	1.51°	2.15*	2013-03-20 07:08:44.82	0	22.784	22.784	0.78	2.78	295	20	10000	2.6×10^{-5}
GRB130320B	195.54	-71.26	0.49°	2.15*	2013-03-20 13:24:11.73	0	384.768	384.768	1	2	340	20	10000	7.8×10^{-5}
GRB130325A	122.78	-18.90	0.25°	2.15*	2013-03-25 04:51:54.30	0.58	10.448	9.868	0.73	2.18	202.20	10	1000	8.25×10^{-6}
GRB130327B	218.09	-69.51	0.17°	2.15*	2013-03-27 08:24:04.75	-1	43.704	44.704	0.56	3.4	334	10	1000	5.176×10^{-5}
GRB130403A	199.90	-46.68	8.26°	2.15*	2013-04-03 20:46:47.41	-7.94	14.85	22.79	1.05†	2.25†	205†	8	1000	1.094×10^{-6}
GRB130404B	146.58	-42.16	1.08°	2.15*	2013-04-04 20:10:04.03	0.32	34.88	34.56	1.05†	2.25†	205†	8	1000	8.355×10^{-6}
GRB130406A	157.78	-62.05	2.09°	2.15*	2013-04-06 06:55:03.46	-0.51	7.42	7.93	1.05†	2.25†	205†	8	1000	2.924×10^{-6}
GRB130406B	109.66	-27.86	7.66°	2.15*	2013-04-06 08:00:36.77	-5.12	83.71	88.83	1.05†	2.25†	205†	8	1000	3.211×10^{-6}
GRB130408A	134.41	-32.36	1.08″	3.758	2013-04-08 21:51:38.00	-2	33.5	35.5	0.7	2.3	272	20	10000	1.2×10^{-5}
GRB130416B	51.21	-18.25	4.86°	0.5*	2013-04-16 18:28:53.30	-0.05	0.14	0.19	1.05†	2.25†	205†	8	1000	9.385×10^{-7}
GRB130420D	117.06	-69.03	4.01°	2.15*	2013-04-20 10:08:09.20	-2.43	24.9	27.33	1.05†	2.25†	205†	8	1000	3.771×10^{-6}
GRB130425A	6.21	-70.18	2.50°	2.15*	2013-04-25 07:51:16.23	-1.86	77.216	79.076	1.29	2.46	167	20	10000	5.9×10^{-5}
GRB130427B	314.90	-22.55	1.08″	2.78	2013-04-27 13:20:41.00	-1.29	32.71	34.0	1.64	2.64	200*	15	150	1.5×10^{-6}

Table A.4: IC86-2013 Southern Hemisphere GRB catalog

	RA (°)	Dec (°)	σ	z	Trigger (UT)	T_1 (s)	T_2 (s)	T_{100} (s)	α_γ	β_γ	ε_γ	$E_{\min}$	$E_{\max}$	f_γ
GRB130418B	216.53	-17.54	8.46°	2.15*	2013-04-18 20:14:45.49	-45.06	124.42	169.48	1.05†	2.25†	205†	8	1000	5.982×10^{-6}
GRB130503A	214.72	-11.55	21.48°	0.5*	2013-05-03 05:08:28.95	-0.86	0.02	0.88	1.05†	2.25†	205†	8	1000	3.858×10^{-8}
GRB130504A	272.46	-16.32	0.02°	2.15*	2013-05-04 02:05:34.00	-31.07	36.84	67.91	0.52	2.52	84.5	15	150	1.0×10^{-6}
GRB130504B	347.95	-5.74	0.23°	2.15*	2013-05-04 07:31:59.72	0	5	5.0	0.42	3.4	1300	10	1000	6.01×10^{-6}
GRB130505B	344.47	-70.47	1.50°	2.15*	2013-05-05 22:55:15.94	0.38	50.62	50.24	1.05†	2.25†	205†	8	1000	9.873×10^{-6}
GRB130507A	319.74	-20.53	3.29°	2.15*	2013-05-07 13:04:37.98	0	60.16	60.16	1.05†	2.25†	205†	8	1000	4.266×10^{-6}
GRB130509A	240.85	-40.22	2.08°	2.15*	2013-05-09 01:52:14.79	0.51	24.83	24.32	1.05†	2.25†	205†	8	1000	9.007×10^{-6}
GRB130509B	133.86	-11.51	8.78°	2.15*	2013-05-09 20:08:43.35	-5.63	23.04	28.67	1.05†	2.25†	205†	8	1000	2.311×10^{-6}
GRB130510A	105.71	-9.87	4.98°	2.15*	2013-05-10 21:03:22.38	-4.1	25.34	29.44	1.05†	2.25†	205†	8	1000	3.211×10^{-6}
GRB130513A	144.78	-5.24	0.02°	2.15*	2013-05-13 07:38:00.00	0	50	50.0	1*	2*	200*	20	200	1×10^{-6}
GRB130514A	296.28	-7.98	1.08″	2.15*	2013-05-14 07:13:41.00	-7.09	258.01	265.1	1.8	2.8	200*	15	150	1.40×10^{-5}
GRB130514B	147.60	-18.97	0.03°	2.15*	2013-05-14 13:26:32.53	-0.51	16.9	17.41	1.72	2.72	200*	15	150	8.8×10^{-7}
GRB130515A	283.44	-54.28	1.44″	2.15*	2013-05-15 01:21:17.88	-0.06	3.192	3.252	1.9	3.9	450	10	1000	10.4×10^{-7}
GRB130515B	312.84	-14.95	5.37°	2.15*	2013-05-15 10:18:30.17	-3.58	16.9	20.48	1.05†	2.25†	205†	8	1000	1.008×10^{-6}
GRB130518B	321.56	-20.15	0.02°	2.15*	2013-05-18 10:50:38.00	0	10	10.0	1.39	2.39	200*	15	150	8.0×10^{-7}
GRB130523B	39.49	-63.07	2.13°	2.15*	2013-05-23 04:45:42.28	-1.28	4.1	5.38	1.05†	2.25†	205†	8	1000	2.710×10^{-6}
GRB130527A	309.28	-24.73	1.08″	2.15*	2013-05-27 14:21:27.00	-1	93.7	94.7	1.04	3.04	1380	20	10000	1.1×10^{-4}
GRB130529A	24.28	-64.15	1.08″	2.15*	2013-05-29 11:15:25.00	-15.02	150.62	165.64	1.56	2.56	200*	15	150	1.4×10^{-6}
GRB130604B	292.18	-24.86	1.21°	2.15*	2013-06-04 00:48:11.32	-0.26	26.62	26.88	1.05†	2.25†	205†	8	1000	1.746×10^{-5}
GRB130605A	134.54	-33.48	0.02°	2.15*	2013-06-05 23:41:42.00	-6.48	9.18	15.66	1.58	2.58	200*	15	150	2.6×10^{-6}
GRB130606B	218.57	-22.13	0.10°	2.15*	2013-06-06 11:55:35.00	-3	72.328	75.328	1.14	2.05	435	10	1000	2.034×10^{-4}
GRB130609B	53.77	-40.17	0.36″	1.3	2013-06-09 21:38:40.00	-7.84	213.25	221.09	0.66	2.6	491	10	1000	6.02×10^{-5}
GRB130610B	176.36	-32.19	0.28°	2.15*	2013-06-10 21:21:19.09	0	16.64	16.64	1.7	3.7	62	20	10000	8.5×10^{-6}
GRB130611A	238.84	-25.23	2.97°	2.15*	2013-06-11 12:54:20.87	0.26	67.07	66.81	1.05†	2.25†	205†	8	1000	7.443×10^{-6}

Table A.4: IC86-2013 Southern Hemisphere GRB catalog *(continued)*

	RA (°)	Dec (°)	σ	z	Trigger (UT)	T_1 (s)	T_2 (s)	T_{100} (s)	α_γ	β_γ	ε_γ	$E_{\min}$	$E_{\max}$	f_γ
GRB130614A	324.18	-33.89	1.22°	2.15*	2013-06-14 23:56:09.06	-1	9.22	10.22	1.45	3.45	101	10	1000	6.1×10^{-6}
GRB130615A	274.83	-68.16	1.44″	2.15*	2013-06-15 09:44:45.00	25.57	386.86	361.29	0.87	2.87	33.2	15	150	2.1×10^{-6}
GRB130617A	74.73	-60.06	9.99°	0.5*	2013-06-17 13:32:49.85	-0.45	0.32	0.77	1.05†	2.25†	205†	8	1000	2.409×10^{-7}
GRB130623A	20.72	-77.78	0.04°	2.15*	2013-06-23 11:42:47.05	-1.79	20.48	22.27	1.03	3.03	26.11	10	1000	2.63×10^{-6}
GRB130626A	273.13	-9.53	0.02°	0.5*	2013-06-26 10:51:03.81	-0.19	1.66	1.85	0.53	2.53	74.5	15	150	5.2×10^{-8}
GRB130627A	184.41	-37.09	1.08″	2.15*	2013-06-27 08:55:05.93	-17.92	31.6	49.52	1.4	3.4	86	10	1000	1.334×10^{-6}
GRB130627B	181.91	-55.71	0.02°	2.15*	2013-06-27 12:00:50.00	-10.5	26	36.5	0.13	2.13	47.6	15	150	6.1×10^{-7}
GRB130701B	97.79	-60.13	1.00°	2.15*	2013-07-01 01:27:06.27	-0.51	19.71	20.22	1.04	3.04	564	10	1000	1.28×10^{-5}
GRB130701C	325.94	-30.89	1.68°	0.5*	2013-07-01 18:15:30.71	-0.06	1.54	1.6	1.05†	2.25†	205†	8	1000	4.917×10^{-6}
GRB130704A	65.56	-14.46	1.00°	2.15*	2013-07-04 13:26:07.25	0.51	6.91	6.4	1.05†	2.25†	205†	8	1000	2.427×10^{-5}
GRB130707A	54.45	-21.04	5.37°	2.15*	2013-07-07 12:07:48.93	-2.05	74.5	76.55	1.05†	2.25†	205†	8	1000	1.046×10^{-5}
GRB130715A	287.37	-31.05	1.00°	2.15*	2013-07-15 21:44:38.38	-30	62	92.0	0.58	2.44	314.60	10	1000	4.7×10^{-5}
GRB130717A	256.59	-13.57	12.10°	2.15*	2013-07-17 17:36:20.11	-3.33	51.97	55.3	1.05†	2.25†	205†	8	1000	1.871×10^{-6}
GRB130719A	89.04	-11.59	0.02°	2.15*	2013-07-19 05:47:49.00	6.2	205.2	199.0	1.63	2.63	200*	15	150	2.3×10^{-6}
GRB130720B	338.03	-9.40	1.00°	2.15*	2013-07-20 13:57:40.49	-13.57	185.6	199.17	1.05†	2.25†	205†	8	1000	9.997×10^{-5}
GRB130722B	119.86	-47.45	10.12°	2.15*	2013-07-22 00:29:51.01	-0.26	81.15	81.41	1.05†	2.25†	205†	8	1000	1.480×10^{-6}
GRB130722C	352.41	-22.31	2.70°	2.15*	2013-07-22 23:46:11.71	-0.77	1.54	2.31	1.05†	2.25†	205†	8	1000	5.988×10^{-7}
GRB130723A	217.77	-16.86	8.16°	2.15*	2013-07-23 02:12:34.12	-0.77	7.42	8.19	1.05†	2.25†	205†	8	1000	8.708×10^{-7}
GRB130725B	214.24	-11.13	0.36″	2.15*	2013-07-25 17:39:38.00	-0.3	12.8	13.1	2.23	3.23	200*	15	150	3.9×10^{-7}
GRB130727A	330.80	-65.54	0.72″	2.15*	2013-07-27 16:45:19.52	-1.08	24.38	25.46	1.1	2.2	118	10	1000	8.9×10^{-6}
GRB130730A	133.75	-60.36	3.44°	2.15*	2013-07-30 05:50:19.74	-8.7	19.2	27.9	1.05†	2.25†	205†	8	1000	2.115×10^{-6}
GRB130802A	80.28	-7.62	12.88°	0.5*	2013-08-02 17:31:52.80	-0.06	0	0.06	1.05†	2.25†	205†	8	1000	3.258×10^{-7}
GRB130804A	280.03	-76.15	0.76°	2.15*	2013-08-04 00:33:15.53	-0.06	3.024	3.084	0.77	2.22	545	10	1000	1.89×10^{-6}
GRB130807A	269.80	-27.62	0.02°	2.15*	2013-08-07 10:25:43.00	-12.18	163.82	176.0	0.31	2.31	75.9	15	150	1.2×10^{-6}
GRB130811A	192.89	-17.04	3.36°	2.15*	2013-08-11 04:28:01.69	-2.3	42.5	44.8	1.05†	2.25†	205†	8	1000	6.382×10^{-6}

Table A.4: IC86-2013 Southern Hemisphere GRB catalog *(continued)*

	RA (°)	Dec (°)	σ	z	Trigger (UT)	T_1 (s)	T_2 (s)	T_{100} (s)	α_γ	β_γ	ε_γ	$E_{\min}$	$E_{\max}$	f_γ
GRB130812A	92.40	-13.29	1.08″	2.15*	2013-08-12 22:22:52.00	-0.3	8.5	8.8	2.52	3.52	200*	15	150	5.9×10^{-7}
GRB130812B	7.41	-79.18	0.34°	2.15*	2013-08-12 10:55:16.11	0	33.024	33.024	1.33	3.33	78	20	10000	1.52×10^{-5}
GRB130816A	197.14	-58.95	1.08″	2.15*	2013-08-16 01:46:55.00	-28.06	8.84	36.9	1.83	2.83	200*	10	1000	1.3×10^{-6}
GRB130816B	170.02	-57.56	1.08″	2.15*	2013-08-16 04:53:38.00	-6.5	6.5	13.0	0.45	2.45	47.3	15	150	2.7×10^{-7}
GRB130819A	124.72	-33.76	4.93°	2.15*	2013-08-19 09:27:34.10	-1.54	81.15	82.69	1.05†	2.25†	205†	8	1000	8.682×10^{-6}
GRB130821A	314.10	-12.00	0.10°	2.15*	2013-08-21 16:10:28.01	3.58	108.08	104.5	0.54	2.01	165	10	1000	6.60×10^{-5}
GRB130830B	350.97	-51.57	10.49°	2.15*	2013-08-30 22:06:33.51	-3.07	33.28	36.35	1.05†	2.25†	205†	8	1000	1.441×10^{-6}
GRB130831B	192.42	-29.18	1.08″	2.15*	2013-08-31 13:48:19.00	-13.9	30.6	44.5	1.88	2.88	200*	15	150	1.4×10^{-6}
GRB130906B	279.39	-53.38	7.60°	2.15*	2013-09-06 10:26:25.30	-3.58	4.61	8.19	1.05†	2.25†	205†	8	1000	8.243×10^{-7}
GRB130907B	236.63	-25.10	7.37°	2.15*	2013-09-07 18:14:46.59	-0.32	2.82	3.14	1.05†	2.25†	205†	8	1000	2.608×10^{-7}
GRB130908A	219.16	-7.20	8.84°	2.15*	2013-09-08 16:14:23.34	-1.79	64.26	66.05	1.05†	2.25†	205†	8	1000	2.924×10^{-6}
GRB130909A	198.18	-20.79	17.24°	2.15*	2013-09-09 19:36:08.90	-14.85	18.94	33.79	1.05†	2.25†	205†	8	1000	1.977×10^{-6}
GRB130919A	207.28	-10.35	0.02°	2.15*	2013-09-19 11:07:24.00	-20.15	108.07	128.22	0.54	2.54	71.7	15	150	1.4×10^{-6}
GRB130919B	297.35	-11.73	5.32°	0.5*	2013-09-19 04:09:40.26	-0.06	0.9	0.96	1.05†	2.25†	205†	8	1000	3.683×10^{-7}
GRB130919D	242.22	-48.29	6.78°	2.15*	2013-09-19 23:38:13.69	-4.1	13.31	17.41	1.05†	2.25†	205†	8	1000	3.362×10^{-6}
GRB130924A	28.77	-7.14	6.04°	2.15*	2013-09-24 06:06:49.08	-21.76	15.36	37.12	1.05†	2.25†	205†	8	1000	3.728×10^{-6}
GRB130925A	41.18	-26.15	1.08″	0.35	2013-09-25 03:56:23.29	-3.84	5271	5274.84	1.42	3.42	181	10*	10000*	5.0×10^{-4}
GRB130928A	306.91	-44.19	3.26°	2.15*	2013-09-28 12:52:35.19	0.51	133.51	133.0	1.05†	2.25†	205†	8	1000	1.953×10^{-5}
GRB130929A	135.02	-47.56	1.08″	2.15*	2013-09-29 09:36:33.00	-1.93	11.5	13.43	2	3.0	200*	15	150	6.9×10^{-7}
GRB130930A	190.66	-35.50	0.03°	2.15*	2013-09-30 19:09:32.00	0	10	10.0	1*	2*	200*	10*	10000*	1.00×10^{-5}*
GRB131002B	75.12	-75.70	1.44″	2.15*	2013-10-02 10:54:28.00	-5.95	41.6	47.55	0.36	2.36	34.0	15	150	6.2×10^{-7}
GRB131006A	325.38	-26.63	18.48°	0.5*	2013-10-06 08:48:21.36	-0.13	0	0.13	1.05†	2.25†	205†	8	1000	1.269×10^{-7}
GRB131008A	328.00	-25.98	2.50°	2.15*	2013-10-08 20:36:02.79	0	36.35	36.35	1.05†	2.25†	205†	8	1000	8.228×10^{-6}
GRB131014A	100.50	-19.10	0.45°	2.15*	2013-10-14 05:09:00.20	0.96	13.288	12.328	0.34	2.58	318	10	1000	1.9×10^{-4}
GRB131018A	98.47	-19.90	1.08″	2.15*	2013-10-18 12:47:48.00	21.1	117.74	96.64	2.24	3.24	200*	15	150	1.1×10^{-6}

Table A.4: IC86-2013 Southern Hemisphere GRB catalog *(continued)*

	RA (°)	Dec (°)	σ	z	Trigger (UT)	T_1 (s)	T_2 (s)	T_{100} (s)	α_γ	β_γ	ε_γ	$E_{\min}$	$E_{\max}$	f_γ
GRB131021A	329.12	-25.35	6.39°	2.15*	2013-10-21 08:26:45.45	-0.77	16.9	17.67	1.05†	2.25†	205†	8	1000	1.397×10^{-6}
GRB131024A	290.48	-64.60	1.08″	2.15*	2013-10-24 12:26:20.00	-111	17	128.0	1.85	2.85	200*	15	150	1.2×10^{-6}
GRB131028B	333.40	-56.94	6.64°	2.15*	2013-10-28 02:17:51.43	-1.28	13.06	14.34	1.05†	2.25†	205†	8	1000	1.456×10^{-6}
GRB131030A	345.07	-5.37	0.72″	1.293	2013-10-30 20:56:18.00	-6.04	143.37	149.41	0.71	2.95	177	20	10000	6.6×10^{-5}
GRB131030B	61.45	-62.80	7.77°	2.15*	2013-10-30 15:40:25.76	-1.28	51.97	53.25	1.05†	2.25†	205†	8	1000	1.650×10^{-6}
GRB131030C	186.29	-5.34	4.28°	2.15*	2013-10-30 18:59:45.77	-2.56	24.83	27.39	1.05†	2.25†	205†	8	1000	3.507×10^{-6}
GRB131102A	74.10	-28.01	14.82°	2.15*	2013-11-02 14:55:44.62	0	62.98	62.98	1.05†	2.25†	205†	8	1000	1.422×10^{-6}
GRB131103A	348.92	-44.64	0.72″	0.5955	2013-11-03 22:07:25.00	-9.5	13.5	23.0	1.97	2.97	200*	15	150	8.2×10^{-7}
GRB131105A	70.97	-62.99	1.08″	1.686	2013-11-05 02:04:44.00	6.8	133.368	126.568	1.2	1.8	203.9	10	1000	2.9×10^{-5}
GRB131110A	69.27	-17.26	29.16″	2.15*	2013-11-10 11:53:11.00	0	90	90.0	1.61	2.61	200*	15	150	3.53×10^{-6}
GRB131113A	157.99	-41.52	1.21°	2.15*	2013-11-13 11:35:37.16	3.39	63.94	60.55	1.05†	2.25†	205†	8	1000	2.304×10^{-5}
GRB131117A	332.33	-31.76	1.08″	4.042	2013-11-17 00:34:04.00	-1	12	13.0	0.4	2.4	44.0	15	150	2.5×10^{-7}
GRB131118A	349.86	-66.83	0.17°	2.15*	2013-11-18 22:58:58.92	0	139.52	139.52	0.88	2.83	230	20	10000	8.40×10^{-5}
GRB131119A	47.96	-24.01	7.35°	2.15*	2013-11-19 18:44:47.87	-2.56	32.26	34.82	1.05†	2.25†	205†	8	1000	1.849×10^{-6}
GRB131120A	278.94	-12.03	0.03°	2.15*	2013-11-20 14:37:56.00	-71.1	64.3	135.4	2.94	3.94	200*	15	150	5.7×10^{-7}
GRB131123A	53.24	-20.88	8.34°	2.15*	2013-11-23 13:01:58.13	0	3.14	3.14	1.05†	2.25†	205†	8	1000	4.084×10^{-7}
GRB131127C	49.40	-5.67	4.07°	2.15*	2013-11-27 11:31:00.59	0.77	60.42	59.65	1.05†	2.25†	205†	8	1000	4.242×10^{-6}
GRB131202A	344.05	-21.66	1.08″	8.2	2013-12-02 15:12:10.85	-4.35	36.98	41.33	1.1	3.1	288.4	10	1000	1.6×10^{-6}
GRB131204A	309.67	-69.67	4.42°	2.15*	2013-12-04 22:28:57.79	-0.51	29.44	29.95	1.05†	2.25†	205†	8	1000	1.648×10^{-6}
GRB131205A	131.63	-60.16	1.08″	2.15*	2013-12-05 09:18:38.00	-18.5	20.41	38.91	1.57	2.57	200*	15	150	2.9×10^{-7}
GRB131209A	136.50	-33.20	0.90°	2.15*	2013-12-09 13:07:56.97	2.82	20.64	17.82	0.41	2.79	267	10	1000	1.44×10^{-5}
GRB131211A	271.34	-40.61	3.56°	2.15*	2013-12-11 12:14:49.96	-12.54	32.26	44.8	1.05†	2.25†	205†	8	1000	4.507×10^{-6}
GRB131214A	183.94	-6.34	1.00°	2.15*	2013-12-14 16:55:55.60	2.05	82.11	80.06	1.05†	2.25†	205†	8	1000	7.217×10^{-5}
GRB131216A	94.67	-41.63	1.44°	2.15*	2013-12-16 01:56:32.11	-1	24.38	25.38	0.64	2.03	359	10	1000	8.60×10^{-6}
GRB131218A	113.78	-64.74	0.02°	2.15*	2013-12-18 21:05:32.00	0	6	6.0	1*	2*	200*	10*	10000*	1.00×10^{-5}*

Table A.4: IC86-2013 Southern Hemisphere GRB catalog *(continued)*

	RA (°)	Dec (°)	σ	z	Trigger (UT)	T_1 (s)	T_2 (s)	T_{100} (s)	α_γ	β_γ	ε_γ	$E_{\min}$	$E_{\max}$	f_γ
GRB131224B	163.72	-14.18	0.03°	2.15*	2013-12-24 03:25:08.00	0	11	11.0	2.09	3.09	200*	15	150	2.6×10^{-7}
GRB131226A	301.31	-64.94	0.01°	2.15*	2013-12-26 05:47:38.01	0	9.42	9.42	0.9	2.9	264	20	10000	1.01×10^{-5}
GRB140104B	218.81	-8.90	0.22°	2.15*	2014-01-04 17:32:13.93	-14	200	214.0	1.23	3.23	280	10	1000	3.2×10^{-5}
GRB140106A	2.34	-8.75	15.81°	2.15*	2014-01-06 08:16:43.36	-0.51	32.51	33.02	1.05†	2.25†	205†	8	1000	2.457×10^{-6}
GRB140109B	24.09	-25.05	37.45°	2.15*	2014-01-09 21:03:26.39	-1.02	2.3	3.32	1.05†	2.25†	205†	8	1000	1.492×10^{-7}
GRB140110A	28.90	-36.26	0.50°	2.15*	2014-01-10 06:18:37.94	-0.26	9.22	9.48	0.59	2.7	1400	10	1000	7.1×10^{-6}
GRB140110B	50.64	-69.29	11.71°	0.5*	2014-01-10 09:52:04.27	-0.77	0	0.77	1.05†	2.25†	205†	8	1000	4.595×10^{-8}
GRB140115A	210.03	-61.41	2.20°	2.15*	2014-01-15 20:43:18.18	0	14.91	14.91	1.05†	2.25†	205†	8	1000	3.953×10^{-6}
GRB140115B	94.86	-48.86	5.18°	2.15*	2014-01-15 21:35:11.51	-1.79	8.7	10.49	1.05†	2.25†	205†	8	1000	3.256×10^{-6}
GRB140118A	331.00	-17.94	0.02°	2.15*	2014-01-18 01:32:02.00	-73.61	30.87	104.48	1.89	2.89	200*	10	1000	6.0×10^{-6}
GRB140129C	183.40	-10.32	9.06°	0.5*	2014-01-29 11:59:01.63	-0.06	0.06	0.12	1.05†	2.25†	205†	8	1000	2.235×10^{-7}
GRB140206B	315.26	-8.51	0.23°	2.15*	2014-02-06 06:36:09.06	0	154.368	154.368	0.97	2.14	296.6	10	1000	0.993×10^{-4}
GRB140211B	115.84	-13.59	3.99°	2.15*	2014-02-11 02:10:41.16	-0.9	2.56	3.46	1.05†	2.25†	205†	8	1000	7.366×10^{-7}
GRB140213A	105.16	-73.14	0.36″	1.2076	2014-02-13 19:21:32.35	0.77	19.39	18.62	1.01	2.41	80	10	1000	2.04×10^{-5}
GRB140221A	107.45	-17.34	0.06°	2.15*	2014-02-21 07:12:50.00	0	10	10.0	1*	2*	200*	10*	10000*	1.00×10^{-5}*
GRB140223A	141.12	-30.40	5.55°	2.15*	2014-02-23 11:53:06.12	-0.77	16.64	17.41	1.05†	2.25†	205†	8	1000	1.979×10^{-6}
GRB140301A	69.56	-34.26	1.08″	2.15*	2014-03-01 15:24:49.00	-13.18	22.82	36.0	1.96	2.96	200*	15	150	4.4×10^{-7}
GRB140302A	253.86	-12.88	1.44″	2.15*	2014-03-02 08:12:58.00	-0.09	106.25	106.34	0.49	2.49	462	10	1000	1×10^{-5}
GRB140304B	354.18	-27.03	3.31°	2.15*	2014-03-04 20:22:30.14	1.02	233.73	232.71	1.05†	2.25†	205†	8	1000	8.321×10^{-6}
GRB140308A	357.56	-33.35	0.15°	2.15*	2014-03-08 03:49:26.03	-10	80	90.0	0.81	2.07	246	20	10000	1.01×10^{-4}
GRB140311D	39.04	-25.23	5.29°	2.15*	2014-03-11 10:52:04.87	-1.02	13.89	14.91	1.05†	2.25†	205†	8	1000	3.699×10^{-6}
GRB140320A	281.86	-11.19	2.88″	2.15*	2014-03-20 02:12:46.11	-1.22	1.09	2.31	1.5	2.5	200*	10	1000	4.0×10^{-7}
GRB140322A	250.30	-69.45	6.60°	2.15*	2014-03-22 10:11:03.47	-2.05	8.45	10.5	1.05†	2.25†	205†	8	1000	2.005×10^{-6}
GRB140323A	356.96	-79.91	1.08″	2.15*	2014-03-23 10:22:53.12	5.06	135.37	130.31	1.09	3	127	20	10000	3.1×10^{-5}
GRB140327A	283.12	-6.15	5.31°	2.15*	2014-03-27 01:33:05.85	-4.86	6.66	11.52	1.05†	2.25†	205†	8	1000	8.785×10^{-7}

Table A.4: IC86-2013 Southern Hemisphere GRB catalog *(continued)*

	RA (°)	Dec (°)	σ	z	Trigger (UT)	T_1 (s)	T_2 (s)	T_{100} (s)	α_γ	β_γ	ε_γ	$E_{\min}$	$E_{\max}$	f_γ
GRB140329A	145.70	-32.23	0.20°	2.15*	2014-03-29 07:04:41.00	0	33.024	33.024	0.83	2.38	244	10	1000	7.07×10^{-5}
GRB140329B	92.35	-41.08	9.18°	0.5*	2014-03-29 06:31:21.77	-0.03	0.03	0.06	1.05†	2.25†	205†	8	1000	2.380×10^{-7}
GRB140330A	325.59	-64.30	0.20°	2.15*	2014-03-30 04:19:54.22	0	34.3	34.3	0.57	2.4	172	10	1000	5.6×10^{-6}
GRB140404C	101.81	-6.95	2.59°	2.15*	2014-04-04 21:36:17.62	-1.02	21.76	22.78	1.05†	2.25†	205†	8	1000	4.547×10^{-6}
GRB140405A	119.10	-26.89	3.92°	2.15*	2014-04-05 00:47:02.52	-0.51	39.42	39.93	1.05†	2.25†	205†	8	1000	2.599×10^{-6}
GRB140408A	290.72	-12.60	1.44″	2.15*	2014-04-08 13:15:54.00	-0.66	7.66	8.32	1.61	2.61	200*	10	1000	1.8×10^{-6}
GRB140412A	144.97	-65.82	1.44″	2.15*	2014-04-12 22:20:49.00	-36.94	12.18	49.12	1.95	2.95	200*	15	150	7.2×10^{-7}
GRB140413A	65.45	-51.18	1.08″	2.15*	2014-04-13 00:09:40.00	-52	120.4	172.4	1.37	3.37	228	10*	10000*	2.9×10^{-5}
GRB140422A	164.54	-62.62	6.85°	2.15*	2014-04-22 04:38:45.41	-4.35	357.12	361.47	1.05†	2.25†	205†	8	1000	4.777×10^{-6}
GRB140426A	174.49	-13.95	12.52°	2.15*	2014-04-26 12:21:32.74	-4.74	32.83	37.57	1.05†	2.25†	205†	8	1000	2.283×10^{-6}
GRB140430B	146.38	-36.88	1.82°	2.15*	2014-04-30 17:11:23.81	-12.8	13.57	26.37	1.05†	2.25†	205†	8	1000	9.178×10^{-6}

Table A.5: IC86-2014 Southern Hemisphere GRB catalog

	RA (°)	Dec (°)	σ	z	Trigger (UT)	T_1 (s)	T_2 (s)	T_{100} (s)	α_γ	β_γ	ε_γ	$E_{\min}$	$E_{\max}$	f_γ
GRB140506A	276.77	-55.64	0.72″	2.15*	2014-05-06 21:07:36.88	-3.97	120.18	124.15	0.9	2	141	10	1000	3.5×10^{-6}
GRB140508B	350.53	-63.78	4.98°	2.15*	2014-05-08 04:17:41.46	-1.02	18.43	19.45	1.05†	2.25†	205†	8	1000	3.335×10^{-6}
GRB140509A	46.59	-62.64	1.08″	2.15*	2014-05-09 02:22:13.00	-3.8	23.1	26.9	1.59	2.59	200*	15	150	1.2×10^{-6}
GRB140511A	329.76	-30.06	8.84°	0.5*	2014-05-11 02:17:11.56	-0.06	1.34	1.4	1.05†	2.25†	205†	8	1000	3.707×10^{-7}
GRB140511B	26.25	-24.91	3.58°	2.15*	2014-05-11 23:53:09.49	-1.02	58.11	59.13	1.05†	2.25†	205†	8	1000	6.746×10^{-6}
GRB140512A	289.37	-15.09	1.08″	0.725	2014-05-12 19:31:49.00	-22.84	186.29	209.13	0.85	2.85	279	20	10000	4.8×10^{-5}
GRB140513A	248.36	-19.50	3.93°	2.15*	2014-05-13 17:22:12.28	-0.51	16.64	17.15	1.05†	2.25†	205†	8	1000	4.106×10^{-6}
GRB140515B	289.35	-11.70	0.06°	2.15*	2014-05-15 13:00:53.00	0	10	10.0	1*	2*	200*	10*	10000*	1.00×10^{-5}*
GRB140518B	244.04	-77.86	13.43°	0.5*	2014-05-18 17:00:43.42	-0.64	0.06	0.7	1.05†	2.25†	205†	8	1000	3.805×10^{-7}
GRB140526B	142.99	-10.95	6.18°	0.5*	2014-05-26 13:42:54.72	-0.06	0	0.06	1.05†	2.25†	205†	8	1000	1.578×10^{-7}
GRB140528A	280.73	-59.08	0.23°	2.15*	2014-05-28 20:05:22.75	1.02	19.64	18.62	0.59	2.8	202	20	10000	2.4×10^{-5}
GRB140529A	228.81	-41.04	0.01°	2.15*	2014-05-29 09:28:06.31	0	8.448	8.448	1.5	3.5	52	20	10000	2.6×10^{-6}
GRB140604A	263.17	-40.41	0.21°	2.15*	2014-06-04 04:50:15.45	0	8.448	8.448	0.54	2.54	795	20	10000	7.2×10^{-6}
GRB140605A	121.79	-53.86	6.08°	0.5*	2014-06-05 09:02:50.65	-0.38	0.13	0.51	1.05†	2.25†	205†	8	1000	8.025×10^{-7}
GRB140608A	151.22	-50.26	1.26°	2.15*	2014-06-08 03:41:00.98	-3.07	63.62	66.69	1.05†	2.25†	205†	8	1000	1.903×10^{-5}
GRB140611A	349.94	-40.11	0.04°	2.15*	2014-06-11 03:51:04.93	0	8.448	8.448	0.68	2.68	1460	20	10000	1.5×10^{-5}
GRB140612A	267.38	-64.11	4.69°	2.15*	2014-06-12 07:03:33.31	-0.26	38.66	38.92	1.05†	2.25†	205†	8	1000	4.105×10^{-6}
GRB140614A	231.17	-79.13	1.08″	4.233	2014-06-14 01:04:59.00	0.51	957	956.49	1.5	2.5	200*	15	150	1.3×10^{-6}
GRB140616A	104.94	-70.51	7.00°	0.5*	2014-06-16 03:57:05.13	-0.03	0.48	0.51	1.05†	2.25†	205†	8	1000	2.808×10^{-7}
GRB140619A	27.11	-39.26	0.72″	2.15*	2014-06-19 11:38:35.00	32.3	446.26	413.96	1.3	3.3	236	20	10000	5.4×10^{-5}
GRB140619B	132.68	-9.66	0.06°	2.15*	2014-06-19 11:24:40.52	-0.26	2.56	2.82	0.06	3.3	1356	10	1000	1.70×10^{-6}
GRB140619C	233.02	-25.60	0.41°	2.15*	2014-06-19 22:46:06.00	0	97.792	97.792	1.05	2.37	169	20	10000	1.1×10^{-4}
GRB140622A	317.17	-14.42	1.44″	0.959	2014-06-22 09:36:04.00	-0.02	0.13	0.15	3.08	4.08	1000*	15	150	2.7×10^{-8}
GRB140626A	77.38	-82.63	1.44″	2.15*	2014-06-26 00:33:01.00	-8.94	9.08	18.02	0.61	2.61	44.7	15	150	3.6×10^{-7}

Table A.5: IC86-2014 Southern Hemisphere GRB catalog *(continued)*

	RA (°)	Dec (°)	σ	z	Trigger (UT)	T_1 (s)	T_2 (s)	T_{100} (s)	α_γ	β_γ	ε_γ	$E_{\min}$	$E_{\max}$	f_γ
GRB140627A	66.49	-16.76	13.59°	2.15*	2014-06-27 09:37:59.92	-3.58	3.84	7.42	1.05†	2.25†	205†	8	1000	9.002×10^{-7}
GRB140628B	226.03	-25.83	13.04°	2.15*	2014-06-28 15:01:36.12	-11.78	0.77	12.55	1.05†	2.25†	205†	8	1000	1.466×10^{-6}
GRB140701A	351.45	-28.66	3.82°	2.15*	2014-07-01 13:36:11.07	-7.68	17.41	25.09	1.05†	2.25†	205†	8	1000	2.648×10^{-6}
GRB140701B	285.44	-32.59	4.33°	2.15*	2014-07-01 19:59:35.26	-1.79	5.12	6.91	1.05†	2.25†	205†	8	1000	2.609×10^{-6}
GRB140706A	49.29	-38.05	1.08″	2.15*	2014-07-06 19:33:33.00	-21.3	39.6	60.9	1.37	3.37	96	10	1000	2.95×10^{-6}
GRB140710B	204.65	-58.59	0.02°	2.15*	2014-07-10 21:37:37.94	-6.66	30	36.66	1.9	2.9	200*	10	1000	2.3×10^{-6}
GRB140710C	2.80	-38.88	6.45°	0.5*	2014-07-10 12:53:05.52	-0.06	0.32	0.38	1.05†	2.25†	205†	8	1000	3.826×10^{-7}
GRB140711A	166.01	-24.60	8.46°	2.15*	2014-07-11 16:35:24.57	-3.07	77.82	80.89	1.05†	2.25†	205†	8	1000	2.391×10^{-6}
GRB140712A	319.28	-10.72	9.23°	2.15*	2014-07-12 16:57:01.35	-2.05	24.58	26.63	1.05†	2.25†	205†	8	1000	2.114×10^{-6}
GRB140712B	83.48	-73.62	1.68°	2.15*	2014-07-12 23:20:51.89	-4.35	23.81	28.16	1.05†	2.25†	205†	8	1000	5.100×10^{-6}
GRB140716A	108.13	-60.15	0.02°	2.15*	2014-07-16 10:27:56.97	0	169.26	169.26	0.8	2.07	92	106	10000*	1.03×10^{-5}
GRB140717A	168.48	-18.94	6.00°	2.15*	2014-07-17 19:50:58.98	-48.13	32.51	80.64	1.05†	2.25†	205†	8	1000	5.786×10^{-6}
GRB140719A	171.60	-50.13	1.08″	2.15*	2014-07-19 05:53:55.20	-31.5	16.5	48.0	1.9	2.9	200*	15	150	4.3×10^{-7}
GRB140720A	175.03	-32.31	28.19°	0.5*	2014-07-20 03:47:25.37	-0.13	0.19	0.32	1.05†	2.25†	205†	8	1000	1.997×10^{-7}
GRB140721A	177.65	-37.73	3.62°	2.15*	2014-07-21 08:03:22.32	-27.39	105.56	132.95	1.05	1.98	129.0	10	1000	4.95×10^{-5}
GRB140730A	56.40	-66.55	1.44″	2.15*	2014-07-30 19:43:51.00	-13.5	29.6	43.1	2.5	3.5	200*	15	150	2.8×10^{-7}
GRB140815A	86.90	-8.67	0.03°	2.15*	2014-08-15 21:55:05.00	0	8	8.0	1*	2*	200*	20	200	3×10^{-7}
GRB140817B	29.05	-44.48	5.17°	2.15*	2014-08-17 05:30:02.36	-10.75	15.36	26.11	1.05†	2.25†	205†	8	1000	2.381×10^{-6}
GRB140825A	88.72	-11.83	0.07°	2.15*	2014-08-25 06:55:25.66	0	10.752	10.752	0.44	3.42	208	20	10000	3.7×10^{-5}
GRB140825C	264.49	-6.92	16.32°	2.15*	2014-08-25 23:30:52.88	-13.06	3.33	16.39	1.05†	2.25†	205†	8	1000	9.949×10^{-7}
GRB140901A	15.82	-32.76	0.21°	0.5*	2014-09-01 19:41:37.57	-0.02	0.16	0.18	0.3	3	1250	10	1000	4.8×10^{-6}
GRB140901B	112.18	-29.21	0.02°	2.15*	2014-09-01 06:17:22.79	0	65	65.0	1.2	3.2	219	10	1000	3.8×10^{-6}
GRB140901C	112.18	-29.21	0.10°	2.15*	2014-09-01 06:17:22.79	-0.51	64.51	65.02	1.05†	2.25†	205†	8	1000	2.929×10^{-6}
GRB140905A	340.50	-25.94	2.82°	2.15*	2014-09-05 10:53:45.72	5.89	115.97	110.08	1.05†	2.25†	205†	8	1000	2.746×10^{-5}
GRB140907B	163.82	-27.00	9.53°	2.15*	2014-09-07 10:18:16.89	-7.42	19.97	27.39	1.05†	2.25†	205†	8	1000	1.346×10^{-6}

Table A.5: IC86-2014 Southern Hemisphere GRB catalog *(continued)*

	RA (°)	Dec (°)	σ	z	Trigger (UT)	T_1 (s)	T_2 (s)	T_{100} (s)	α_γ	β_γ	ε_γ	$E_{\min}$	$E_{\max}$	f_γ
GRB140911A	128.39	-36.56	3.08°	2.15*	2014-09-11 00:17:07.06	-0.26	116.48	116.74	1.05†	2.25†	205†	8	1000	6.784×10^{-6}
GRB140916A	40.40	-39.69	1.08″	2.15*	2014-09-16 10:43:47.00	-6.6	89.5	96.1	2.15	3.15	200*	15	150	1.7×10^{-6}
GRB140916B	60.02	-10.26	5.62°	2.15*	2014-09-16 05:36:49.81	-14.34	16.9	31.24	1.05†	2.25†	205†	8	1000	6.095×10^{-6}
GRB140919A	221.54	-32.18	1.08″	2.15*	2014-09-19 15:15:15.00	-0.7	174.6	175.3	1.8	3.8	103	10	1000	1.20×10^{-5}
GRB140927A	291.79	-65.39	1.08″	2.15*	2014-09-27 05:15:11.00	0.43	8.7	8.27	1.82	2.82	200*	15	150	2.7×10^{-7}
GRB140928A	43.81	-56.08	0.16°	2.15*	2014-09-28 10:29:53.55	-10.75	57.856	68.606	0.05	2.6	671	10	1000	1.02×10^{-5}
GRB140929A	177.45	-58.64	8.79°	2.15*	2014-09-29 16:14:45.29	-4.86	32.26	37.12	1.05†	2.25†	205†	8	1000	1.872×10^{-6}
GRB141003A	321.77	-36.89	7.00°	2.15*	2014-10-03 13:32:13.10	-0.51	8.19	8.7	1.05†	2.25†	205†	8	1000	1.854×10^{-6}
GRB141004B	30.44	-77.30	2.07°	2.15*	2014-10-04 03:36:28.90	0.32	9.79	9.47	1.05†	2.25†	205†	8	1000	4.096×10^{-6}
GRB141011A	257.94	-9.68	0.12°	2.15*	2014-10-11 06:46:17.67	0	3.06	3.06	0.5	2.7	573	10	1000	1.05×10^{-6}
GRB141011B	259.38	-43.00	4.13°	2.15*	2014-10-11 11:12:49.02	0	12.03	12.03	1.05†	2.25†	205†	8	1000	2.885×10^{-6}
GRB141012A	286.82	-49.88	3.06°	2.15*	2014-10-12 18:33:17.68	-25.86	11.78	37.64	1.05†	2.25†	205†	8	1000	6.641×10^{-6}
GRB141013A	315.06	-61.89	3.78°	2.15*	2014-10-13 19:16:59.41	-0.51	81.92	82.43	1.05†	2.25†	205†	8	1000	8.809×10^{-6}
GRB141016A	221.45	-62.49	1.51°	2.15*	2014-10-16 21:31:21.30	0	17.41	17.41	1.05†	2.25†	205†	8	1000	3.579×10^{-6}
GRB141017A	93.63	-58.58	1.08″	2.15*	2014-10-17 18:25:28.00	-1.2	65.1	66.3	0.89	2.89	97	20	10000	4.0×10^{-6}
GRB141022A	241.93	-72.15	0.02°	2.15*	2014-10-22 01:27:42.00	-0.38	12.14	12.52	0.8	2.8	231.5	10	1000	1.2×10^{-6}
GRB141022B	119.39	-75.17	1.00°	2.15*	2014-10-22 02:04:40.21	2.11	11.33	9.22	0.64	2.41	368.1	10	1000	7.87×10^{-5}
GRB141029A	69.41	-16.48	0.17°	2.15*	2014-10-29 04:32:09.00	-20	20	40.0	1*	2*	200*	10*	10000*	1.00×10^{-5}*
GRB141031A	128.61	-59.17	1.08″	2.15*	2014-10-31 07:18:26.00	-22	20	42.0	0.92	1.76	221	10	1000	5.7×10^{-6}
GRB141031D	133.08	-33.68	15.62°	0.5*	2014-10-31 23:57:20.92	-0.06	0.1	0.16	1.05†	2.25†	205†	8	1000	8.351×10^{-8}
GRB141102A	208.61	-47.10	0.04°	2.15*	2014-11-02 12:51:39.26	-0.06	2.56	2.62	0.58	2.58	444	20	10000	1.43×10^{-6}
GRB141102B	223.23	-17.42	15.61°	0.5*	2014-11-02 02:41:16.34	-0.03	-0.02	0.01	1.05†	2.25†	205†	8	1000	7.363×10^{-8}
GRB141104A	279.49	-12.70	0.14°	2.15*	2014-11-04 00:03:19.52	0	27.136	27.136	1.09	2.57	160	20	10000	5.9×10^{-5}
GRB141105A	202.60	-32.00	5.67°	2.15*	2014-11-05 08:35:48.88	-7.42	11.78	19.2	1.05†	2.25†	205†	8	1000	1.837×10^{-6}
GRB141110A	253.13	-34.09	3.80°	2.15*	2014-11-10 05:33:23.56	-27.39	9.22	36.61	1.05†	2.25†	205†	8	1000	2.431×10^{-6}

Table A.5: IC86-2014 Southern Hemisphere GRB catalog *(continued)*

	RA (°)	Dec (°)	σ	z	Trigger (UT)	T_1 (s)	T_2 (s)	T_{100} (s)	α_γ	β_γ	ε_γ	$E_{\min}$	$E_{\max}$	f_γ
GRB141112A	17.40	-45.81	3.78°	2.15*	2014-11-12 12:56:16.22	-12.29	323.59	335.88	1.05†	2.25†	205†	8	1000	2.156×10^{-5}
GRB141114A	6.75	-13.42	3.89°	2.15*	2014-11-14 16:29:16.09	0.51	45.31	44.8	1.05†	2.25†	205†	8	1000	3.593×10^{-6}
GRB141121B	235.89	-35.60	6.96°	2.15*	2014-11-21 09:56:08.48	-2.82	1.02	3.84	1.05†	2.25†	205†	8	1000	8.791×10^{-7}
GRB141122A	9.71	-20.02	10.90°	0.5*	2014-11-22 02:05:26.17	-0.7	0.58	1.28	1.05†	2.25†	205†	8	1000	2.589×10^{-7}
GRB141122B	280.61	-52.52	5.78°	2.15*	2014-11-22 20:59:46.71	-3.58	27.14	30.72	1.05†	2.25†	205†	8	1000	4.027×10^{-6}
GRB141125A	127.91	-29.87	0.43°	2.15*	2014-11-25 03:33:01.00	0	2	2.0	1*	2*	200*	10*	10000*	1.00×10^{-5}*
GRB141128A	321.80	-35.76	8.75°	0.5*	2014-11-28 23:05:53.84	-0.1	0.18	0.28	1.05†	2.25†	205†	8	1000	1.760×10^{-7}
GRB141205B	294.61	-87.58	3.90°	2.15*	2014-12-05 00:25:29.81	-6.91	6.14	13.05	1.05†	2.25†	205†	8	1000	1.603×10^{-6}
GRB141205D	298.77	-7.82	1.73°	2.15*	2014-12-05 18:18:27.66	0	5.44	5.44	1.05†	2.25†	205†	8	1000	6.406×10^{-6}
GRB141209A	90.20	-30.57	3.50°	2.15*	2014-12-09 03:07:59.54	2.3	80.39	78.09	1.05†	2.25†	205†	8	1000	5.548×10^{-6}
GRB141215A	179.06	-52.74	0.20°	2.15*	2014-12-15 13:26:13.65	0	14.48	14.48	0.29	2.8	241	20	10000	2.8×10^{-5}
GRB141221B	126.02	-74.21	3.69°	2.15*	2014-12-21 21:31:48.79	-1.28	31.23	32.51	1.05†	2.25†	205†	8	1000	7.439×10^{-6}
GRB141222A	178.04	-57.35	0.10°	2.15*	2014-12-22 07:08:55.34	0	8.448	8.448	1.49	1.74	2427	10	1000	8.16×10^{-6}
GRB141223A	147.38	-20.71	7.48°	2.15*	2014-12-23 05:45:37.97	-3.58	90.62	94.2	1.05†	2.25†	205†	8	1000	1.821×10^{-6}
GRB141229A	71.48	-18.96	0.06°	2.15*	2014-12-29 11:48:59.84	0	13.82	13.82	1.03	3.03	254	20	10000	4.7×10^{-6}
GRB141230C	246.93	-40.18	10.48°	0.5*	2014-12-30 20:54:05.71	-0.16	0.06	0.22	1.05†	2.25†	205†	8	1000	1.479×10^{-7}
GRB150101B	188.00	-10.96	0.04°	0.093	2015-01-01 15:23:34.47	-0.02	0.06	0.08	1.7	2.7	1000*	10	1000	1.09×10^{-7}
GRB150103A	131.67	-48.89	1.08″	2.15*	2015-01-03 20:02:18.00	6.06	64.68	58.62	0.03	2.03	54.2	15	150	8.2×10^{-7}
GRB150105A	124.32	-14.78	1.00°	2.15*	2015-01-05 06:10:00.46	3.07	76.8	73.73	0.91	2.25	52	10	1000	4.4×10^{-5}
GRB150110C	68.58	-16.87	0.12°	2.15*	2015-01-10 23:41:01.00	-9	31	40.0	1*	2*	200*	10*	10000*	1.00×10^{-5}*
GRB150118B	240.24	-35.75	0.50°	2.15*	2015-01-18 09:48:22.39	0	58.368	58.368	0.98	2.98	695	20	10000	1.87×10^{-4}
GRB150118C	160.08	-27.55	0.10°	2.15*	2015-01-18 22:14:32.66	0	3.064	3.064	0.9	2	415	10	1000	1.2×10^{-6}
GRB150122A	151.23	-32.60	3.30°	2.15*	2015-01-22 23:02:28.32	-0.51	52.74	53.25	1.05†	2.25†	205†	8	1000	3.168×10^{-6}
GRB150123A	111.56	-9.69	0.09°	2.15*	2015-01-23 15:01:50.00	-39	31	70.0	1*	2*	200*	10*	10000*	1.00×10^{-5}*
GRB150126A	350.50	-12.37	0.51°	2.15*	2015-01-26 20:50:35.78	6.4	938	931.6	1.07	2.45	217	10	1000	2.55×10^{-5}

Table A.5: IC86-2014 Southern Hemisphere GRB catalog *(continued)*

	RA (°)	Dec (°)	σ	z	Trigger (UT)	T_1 (s)	T_2 (s)	T_{100} (s)	α_γ	β_γ	ε_γ	$E_{\min}$	$E_{\max}$	f_γ
GRB150127A	296.95	-9.42	1.45°	2.15*	2015-01-27 09:32:44.14	0.26	52.99	52.73	0.99	2.21	1083	10	1000	2.27×10^{-5}
GRB150201A	11.83	-37.62	1.08″	2.15*	2015-02-01 13:46:51.65	0	57	57.0	1.02	2.7	131	10	1000	6.63×10^{-5}
GRB150201C	11.83	-37.62	5.04″	2.15*	2015-02-01 14:09:55.98	-0.51	25.09	25.6	1.05†	2.25†	205†	8	1000	2.383×10^{-6}
GRB150202A	39.23	-33.15	1.08″	2.15*	2015-02-02 23:10:02.00	-1.7	27.1	28.8	1.5	2.5	200*	15	150	6.1×10^{-7}
GRB150203B	156.88	-21.81	2.67°	2.15*	2015-02-03 13:04:30.40	-1.54	22.27	23.81	1.05†	2.25†	205†	8	1000	3.640×10^{-6}
GRB150204A	160.24	-64.04	0.02°	2.15*	2015-02-04 06:31:07.88	-6.144	7.168	13.312	1.4	3.4	350	10	1000	2.2×10^{-6}
GRB150204B	160.24	-64.04	0.02°	2.15*	2015-02-04 06:31:07.88	-4.61	6.4	11.01	1.05†	2.25†	205†	8	1000	1.935×10^{-6}
GRB150206A	10.07	-63.18	0.72″	2.087	2015-02-06 14:30:02.00	-22.3	164.1	186.4	0.48	2.2	242	20	10000	5.52×10^{-5}
GRB150206C	357.94	-61.61	3.70°	2.15*	2015-02-06 06:50:10.69	-1.74	92.26	94.0	1.05†	2.25†	205†	8	1000	2.40×10^{-6}
GRB150214A	342.58	-34.17	10.47°	0.5*	2015-02-14 07:01:22.65	-0.13	0.06	0.19	1.05†	2.25†	205†	8	1000	2.371×10^{-7}
GRB150216A	120.68	-9.52	10.08°	2.15*	2015-02-16 09:57:57.46	-0.77	33.02	33.79	1.05†	2.25†	205†	8	1000	2.294×10^{-6}
GRB150219A	271.25	-41.59	2.16″	2.15*	2015-02-19 12:31:12.26	1.54	62	60.46	0.82	2.17	166.7	10	1000	1.00×10^{-5}
GRB150222A	198.79	-12.15	1.08″	2.15*	2015-02-22 16:56:40.00	-0.14	28.11	28.25	1.61	2.61	200*	15	150	2.2×10^{-6}
GRB150222B	155.90	-41.17	0.06°	2.15*	2015-02-22 10:48:07.41	8.45	73.73	65.28	1.05†	2.25†	205†	8	1000	1.954×10^{-5}
GRB150222C	294.54	-40.94	11.32°	2.15*	2015-02-22 19:58:03.44	-56.32	18.43	74.75	1.05†	2.25†	205†	8	1000	3.842×10^{-6}
GRB150227A	190.30	-29.93	8.15°	2.15*	2015-02-27 16:51:29.54	-1.54	15.87	17.41	1.05†	2.25†	205†	8	1000	2.456×10^{-6}
GRB150228A	231.32	-41.87	2.03°	2.15*	2015-02-28 20:16:18.11	0	4.13	4.13	1.05†	2.25†	205†	8	1000	6.593×10^{-6}
GRB150228B	7.55	-61.73	2.53°	2.15*	2015-02-28 23:32:40.65	0.45	37.06	36.61	1.05†	2.25†	205†	8	1000	1.153×10^{-5}
GRB150301A	244.28	-48.73	0.02°	0.5*	2015-03-01 01:04:28.65	-0.03	0.56	0.59	0.53	2.53	185	10	1000	1.2×10^{-7}
GRB150301B	89.17	-57.97	0.36″	2.15*	2015-03-01 19:38:04.00	-0.34	15.62	15.96	1.1	2	180	10	1000	4.4×10^{-6}
GRB150303A	114.81	-5.54	5.12°	2.15*	2015-03-03 12:22:51.37	-0.26	4.61	4.87	1.05†	2.25†	205†	8	1000	6.250×10^{-7}
GRB150305A	269.77	-42.65	0.03°	2.15*	2015-03-05 09:49:19.00	0	100	100.0	1*	2*	200*	20	200	7×10^{-7}
GRB150305B	225.12	-44.74	11.36°	2.15*	2015-03-05 17:23:13.69	-0.26	15.87	16.13	1.05†	2.25†	205†	8	1000	1.722×10^{-6}
GRB150306A	0.63	-58.55	1.00°	2.15*	2015-03-06 23:49:39.82	0.77	19.71	18.94	1.05†	2.25†	205†	8	1000	2.701×10^{-5}
GRB150312A	285.49	-86.00	10.75°	0.5*	2015-03-12 09:40:45.71	-0.06	0.26	0.32	1.05†	2.25†	205†	8	1000	1.402×10^{-7}

Table A.5: IC86-2014 Southern Hemisphere GRB catalog *(continued)*

	RA (°)	Dec (°)	σ	z	Trigger (UT)	T_1 (s)	T_2 (s)	T_{100} (s)	α_γ	β_γ	ε_γ	$E_{\min}$	$E_{\max}$	f_γ
GRB150313A	251.44	-11.71	0.06°	2.15*	2015-03-13 15:46:42.06	-1.79	3.33	5.12	1.05†	2.25†	205†	8	1000	8.673×10^{-7}
GRB150318A	325.01	-61.46	1.08″	2.15*	2015-03-18 07:04:53.00	-6.6	98.58	105.18	2	3.0	200*	15	150	2.5×10^{-6}
GRB150318B	269.05	-30.22	2.19°	2.15*	2015-03-18 12:29:53.02	0.77	95.49	94.72	1.05†	2.25†	205†	8	1000	4.329×10^{-6}
GRB150322A	125.84	-48.05	2.80°	2.15*	2015-03-22 01:35:03.24	0	15.62	15.62	1.05†	2.25†	205†	8	1000	3.631×10^{-6}
GRB150324A	180.81	-42.72	4.19°	2.15*	2015-03-24 03:56:10.92	1.02	5.63	4.61	1.05†	2.25†	205†	8	1000	4.849×10^{-6}
GRB150324B	295.21	-20.04	1.70°	2.15*	2015-03-24 07:39:08.88	-0.26	12.8	13.06	1.05†	2.25†	205†	8	1000	7.809×10^{-6}
GRB150326B	331.13	-19.65	5.94°	2.15*	2015-03-26 13:00:35.20	-0.77	3.33	4.1	1.05†	2.25†	205†	8	1000	1.361×10^{-6}
GRB150329A	163.00	-12.32	11.73°	2.15*	2015-03-29 06:55:19.12	-2.56	26.37	28.93	1.05†	2.25†	205†	8	1000	1.717×10^{-6}
GRB150403A	311.50	-62.71	0.72″	2.06	2015-04-03 21:54:16.00	-83.15	145.37	228.52	0.72	1.85	311	10	1000	5.73×10^{-5}
GRB150415A	220.63	-19.34	3.59°	2.15*	2015-04-15 00:41:07.53	0	34.56	34.56	1.05†	2.25†	205†	8	1000	3.847×10^{-6}
GRB150418B	312.43	-43.53	9.17°	2.15*	2015-04-18 19:39:29.42	-1.54	2.3	3.84	1.05†	2.25†	205†	8	1000	6.415×10^{-7}
GRB150422A	215.10	-20.86	1.07°	2.15*	2015-04-22 16:52:33.99	1.54	38.4	36.86	1.05†	2.25†	205†	8	1000	2.990×10^{-5}
GRB150422B	156.02	-53.56	10.29°	2.15*	2015-04-22 07:03:30.58	-6.14	24.06	30.2	1.05†	2.25†	205†	8	1000	2.446×10^{-6}
GRB150423B	220.39	-38.84	14.73°	2.15*	2015-04-23 06:50:42.92	-2.56	11.78	14.34	1.05†	2.25†	205†	8	1000	1.264×10^{-6}
GRB150425A	214.23	-55.50	8.18°	2.15*	2015-04-25 14:48:19.54	-0.77	3.58	4.35	1.05†	2.25†	205†	8	1000	8.052×10^{-7}
GRB150426A	17.64	-30.23	1.46°	2.15*	2015-04-26 14:15:31.22	0.83	23.36	22.53	1.05†	2.25†	205†	8	1000	1.085×10^{-5}
GRB150430A	326.48	-27.92	0.02°	2.15*	2015-04-30 00:21:05.65	-4.1	131.7	135.8	0.79	2.21	200*	20	10000	2.95×10^{-5}
GRB150501A	50.00	-15.57	3.25°	2.15*	2015-05-01 00:24:08.14	-0.26	9.47	9.73	1.05†	2.25†	205†	8	1000	1.461×10^{-6}
GRB150508A	45.93	-52.45	10.08°	2.15*	2015-05-08 22:40:42.82	-104.7	9.22	113.92	1.05†	2.25†	205†	8	1000	2.886×10^{-6}
GRB150511A	91.18	-30.35	5.05°	2.15*	2015-05-11 08:41:57.50	-0.26	30.98	31.24	1.05†	2.25†	205†	8	1000	3.352×10^{-6}
GRB150513A	49.04	-22.87	0.01°	2.15*	2015-05-13 20:31:19.00	-54.33	129.36	183.69	0.9	1.69	252	10	1000	1.36×10^{-5}
GRB150514A	74.85	-60.91	0.12°	0.807	2015-05-14 18:35:05.13	0	10.82	10.82	1.34	2.51	73	10	1000	4.9×10^{-6}

Appendix B

Three-Year Northern Hemisphere Track Results

The Northern Hemisphere GRB track search that had been previously published [26] was extended to the IC86-2012, IC86-2013, and IC86-2014 years of data concurrently with the Southern Hemisphere track analysis presented in this analysis. In each year of data, a stacked test statistic was calculated by the usual method. Further, per-GRB test statistics were calculated, using the $\max(\{\mathcal{T}_g\})$ method for discovery. The per-GRB significant event coincidences are summarized in Table B.1. Here, basic infomation about the GRBs and coincident events are described, including their angular uncertainty σ, angular separation $\Delta\Psi$, the measured gamma-ray fluence of the GRB, and the estimated energy of the coincident event. The significance of the coincidences are then summarized in two ways. Event signal-to-background PDF ratio values used in the test statistic calculation are provided to estimate relative event importance. The significance of the per-GRB test statistic is then given as a p-value calculated to that GRB's expected background-only test statistic distribution, constituting that GRB's pre-trials p-value. In parentheses, the post-trials p-value of this GRB coincidence is given, calculated relative the full five-year Southern Hemisphere GRB and three-year Northern Hemisphere GRB analysis $\max(\{\mathcal{T}_g\})$ test statistic distribution expected from background. No per-GRB test statistic is found to be more significant than then the coincidence found in the Southern Hemisphere track analysis with GRB110207A. Further, the stacked test statistics are all zero for each of the three years analyzed. The results are therefore consistent with background.

Table B.1: Three-year Northern Hemisphere track analysis significant events. The duration T_{100}, angular uncertainty σ (Fermi-GBM statistical-only uncertainties indicated by $*$), and total fluence of GRBs with coincident events are described. Coincident events are summarized in terms of their time relative to the GRB start time T_1, their angular uncertainty σ, angular displacement from the GRB location $\Delta\Psi$, and reconstructed muon energy. Event significance is estimated by their signal-to-background PDF ratio value $\mathcal{S}/\mathcal{B}$, while final GRB coincidence significance is given as pre-trials (post-trials) p-values relative to background-only test statistic distributions.

	Time	σ	$\Delta\Psi$	Fluence/Energy	Significance
GRB120612B	$T_{100} = 63.24\,\mathrm{s}$	$^*7.1^\circ$		$2.06 \times 10^{-6}\,\mathrm{erg\,cm^{-2}}$	$p = 0.049$ (1)
Event 1	$T_1 + 47.71\,\mathrm{s}$	5.3°	29.0°	$\gtrsim 0.54\,\mathrm{TeV}$	$\mathcal{S}/\mathcal{B} = 1.4$
GRB120911A	$T_{100} = 28.58\,\mathrm{s}$	0.0003°		$2.34 \times 10^{-6}\,\mathrm{erg\,cm^{-2}}$	$p = 0.0044$ (1)
Event 1	$T_1 + 120.94\,\mathrm{s}$	4.6°	2.9°	$\gtrsim 0.98\,\mathrm{TeV}$	$\mathcal{S}/\mathcal{B} = 3.1$
GRB130116A	$T_{100} = 66.82\,\mathrm{s}$	$^*29.9^\circ$		$9.27 \times 10^{-7}\,\mathrm{erg\,cm^{-2}}$	$p = 0.076$ (1)
Event 1	$T_1 + 69.25\,\mathrm{s}$	0.5°	67.7°	$\gtrsim 2.1\,\mathrm{TeV}$	$\mathcal{S}/\mathcal{B} = 1.5$
GRB130318A	$T_{100} = 137.99\,\mathrm{s}$	$^*9.9^\circ$		$3.41 \times 10^{-6}\,\mathrm{erg\,cm^{-2}}$	$p = 0.021$ (1)
Event 1	$T_1 + 29.83\,\mathrm{s}$	0.6°	18.5°	$\gtrsim 0.46\,\mathrm{TeV}$	$\mathcal{S}/\mathcal{B} = 6.4$
Event 2	$T_1 + 44.58\,\mathrm{s}$	2.5°	48.2°	$\gtrsim 0.32\,\mathrm{TeV}$	$\mathcal{S}/\mathcal{B} = 0.024$
GRB130925B	$T_{100} = 265.47\,\mathrm{s}$	$^*4.1^\circ$		$1.49 \times 10^{-5}\,\mathrm{erg\,cm^{-2}}$	$p = 0.032$ (1)
Event 1	$T_1 + 108.8\,\mathrm{s}$	3.4°	12.6°	$\gtrsim 0.70\,\mathrm{TeV}$	$\mathcal{S}/\mathcal{B} = 16.3$
GRB131029B	$T_{100} = 50.95\,\mathrm{s}$	$^*5.8^\circ$		$4.49 \times 10^{-6}\,\mathrm{erg\,cm^{-2}}$	$p = 0.053$ (1)
Event 1	$T_1 + 50.49\,\mathrm{s}$	2.4°	18.2°	$\gtrsim 0.68\,\mathrm{TeV}$	$\mathcal{S}/\mathcal{B} = 4.9$
GRB131202B	$T_{100} = 86.02\,\mathrm{s}$	$^*2.2^\circ$		$1.24 \times 10^{-5}\,\mathrm{erg\,cm^{-2}}$	$p = 0.0069$ (0.985)
Event 1	$T_1 + 85.18\,\mathrm{s}$	2.1°	7.5°	$\gtrsim 1.7\,\mathrm{TeV}$	$\mathcal{S}/\mathcal{B} = 122.1$
Event 2	$T_1 - 81.68\,\mathrm{s}$	1.2°	73.1°	$\gtrsim 1.4\,\mathrm{TeV}$	$\mathcal{S}/\mathcal{B} = 6.9 \times 10^{-10}$
GRB140404B	$T_{100} = 26.63\,\mathrm{s}$	$^*2.2^\circ$		$8.18 \times 10^{-6}\,\mathrm{erg\,cm^{-2}}$	$p = 0.026$ (1)
Event 1	$T_1 - 38.49\,\mathrm{s}$	5.4°	13.1°	$\gtrsim 1.1\,\mathrm{TeV}$	$\mathcal{S}/\mathcal{B} = 11.0$
Event 2	$T_1 + 92.08\,\mathrm{s}$	0.8°	67.8°	$\gtrsim 0.40\,\mathrm{TeV}$	$\mathcal{S}/\mathcal{B} = 5.7 \times 10^{-9}$
GRB140521B	$T_{100} = 46.59\,\mathrm{s}$	$^*10.1^\circ$		$2.75 \times 10^{-6}\,\mathrm{erg\,cm^{-2}}$	$p = 0.051$ (1)
Event 1	$T_1 + 98.37\,\mathrm{s}$	1.6°	11.5°	$\gtrsim 0.79\,\mathrm{TeV}$	$\mathcal{S}/\mathcal{B} = 7.3$
GRB140603A	$T_{100} = 138.24\,\mathrm{s}$	$^*2.1^\circ$		$1.86 \times 10^{-5}\,\mathrm{erg\,cm^{-2}}$	$p = 0.025$ (1)
Event 1	$T_1 + 41.35\,\mathrm{s}$	1.1°	14.9°	$\gtrsim 1.5\,\mathrm{TeV}$	$\mathcal{S}/\mathcal{B} = 10.1$
Event 2	$T_1 - 33.78\,\mathrm{s}$	1.3°	38.7°	$\gtrsim 2.1\,\mathrm{TeV}$	$\mathcal{S}/\mathcal{B} = 0.026$
Event 3	$T_1 + 28.93\,\mathrm{s}$	0.6°	54.7°	$\gtrsim 0.68\,\mathrm{TeV}$	$\mathcal{S}/\mathcal{B} = 5.5 \times 10^{-5}$
GRB141029B	$T_{100} = 202.44\,\mathrm{s}$	$^*1.0^\circ$		$3.8 \times 10^{-5}\,\mathrm{erg\,cm^{-2}}$	$p = 0.034$ (1)
Event 1	$T_1 - 10.33\,\mathrm{s}$	1.6°	11.7°	$\gtrsim 0.70\,\mathrm{TeV}$	$\mathcal{S}/\mathcal{B} = 6.4$
Event 2	$T_1 - 80.99\,\mathrm{s}$	1.0°	30.2°	$\gtrsim 0.45\,\mathrm{TeV}$	$\mathcal{S}/\mathcal{B} = 0.003$
GRB150428B	$T_{100} = 161.8\,\mathrm{s}$	0.0003°		$3.7 \times 10^{-6}\,\mathrm{erg\,cm^{-2}}$	$p = 0.0020$ (0.931)
Event 1	$T_1 + 71.35\,\mathrm{s}$	2.9°	6.0°	$\gtrsim 3.2\,\mathrm{TeV}$	$\mathcal{S}/\mathcal{B} = 131.9$
GRB150428D	$T_{100} = 32.51\,\mathrm{s}$	$^*6.1^\circ$		$1.53 \times 10^{-6}\,\mathrm{erg\,cm^{-2}}$	$p = 0.024$ (1)
Event 1	$T_1 - 43.69\,\mathrm{s}$	4.4°	15.2°	$\gtrsim 0.54\,\mathrm{TeV}$	$\mathcal{S}/\mathcal{B} = 9.4$
GRB150507A	$T_{100} = 63.49\,\mathrm{s}$	$^*1.4^\circ$		$1.52 \times 10^{-5}\,\mathrm{erg\,cm^{-2}}$	$p = 0.039$ (1)
Event 1	$T_1 + 58.24\,\mathrm{s}$	1.1°	20.4°	$\gtrsim 1.8\,\mathrm{TeV}$	$\mathcal{S}/\mathcal{B} = 2.4$
Event 2	$T_1 - 74.44\,\mathrm{s}$	2.1°	36.3°	$\gtrsim 0.69\,\mathrm{TeV}$	$\mathcal{S}/\mathcal{B} = 0.0023$
Event 3	$T_1 - 12.1\,\mathrm{s}$	3.5°	66.5°	$\gtrsim 2.2\,\mathrm{TeV}$	$\mathcal{S}/\mathcal{B} = 3.1 \times 10^{-6}$
Event 4	$T_1 + 4.6\,\mathrm{s}$	1.6°	67.3°	$\gtrsim 0.84\,\mathrm{TeV}$	$\mathcal{S}/\mathcal{B} = 3.4 \times 10^{-7}$

Bibliography

1. Hess, V. F. Über Beobachtungen der durchdringenden Strahlung bei sieben Freiballonfahrten. *Physik. Z.* **13,** 1084–1091.
2. Matthiae, G. The cosmic ray energy spectrum as measured using the Pierre Auger Observatory. *New J. Phys.* **12,** 075009 (2010).
3. Ackermann, M. *et al.* Detection of the Characteristic Pion-Decay Signature in Supernova Remnants. *Science* **339,** 807–811 (2013).
4. Greisen, K. End to the Cosmic-Ray Spectrum? *Phys. Rev. Lett.* **16,** 748–750 (17 Apr. 1966); Zatsepin, G. T. & Kuz'min, V. A. Upper Limit of the Spectrum of Cosmic Rays. *JETP Lett.* **4,** 78 (Aug. 1966).
5. Abraham, J. *et al.* Measurement of the Depth of Maximum of Extensive Air Showers above 10^{18} eV. *Phys. Rev. Lett.* **104,** 091101 (2010).
6. Abbasi, R. U. *et al.* Indications of Proton-Dominated Cosmic-Ray Composition above 1.6 EeV. *Phys. Rev. Lett.* **104,** 161101 (2010).
7. Abbasi, R. *et al.* Study of Ultra-High Energy Cosmic Ray composition using Telescope Array's Middle Drum detector and surface array in hybrid mode. *Astropart. Phys.* **64,** 49–62 (2015).
8. Hillas, A. M. The Origin of Ultra-High-Energy Cosmic Rays. *Annu. Rev. Astron. Astrophys.* **22,** 425–444 (1984).
9. Anchordoqui, L., Paul, T., Reucroft, S. & Swain, J. Ultrahigh Energy Cosmic Rays: The State of the Art before the Auger Observatory. *Int. J. Mod. Phys. A* **18,** 2229–2366 (2003).
10. Hjorth, J. *et al.* A very energetic supernova associated with the γ-ray burst of 29 March 2003. *Nature* **423,** 847–850 (2003).
11. Stanek, K. Z. *et al.* Spectroscopic Discovery of the Supernova 2003dh Associated with GRB 030329. *Astrophys. J. Lett.* **591,** L17 (2003).
12. Campana, S. *et al.* The association of GRB 060218 with a supernova and the evolution of the shock wave. *Nature* **442,** 1008–1010 (2006).
13. Berger, E. Short-Duration Gamma-Ray Bursts. *Annu. Rev. Astron. Astrophys.* **52,** 43–105 (2014).
14. Berger, E. *et al.* Afterglows, Redshifts, and Properties of Swift Gamma-Ray Bursts. *Astrophys. J.* **634,** 501 (2005).
15. Berger, E. The Afterglows and Host Galaxies of Short GRBs: An Overview. *AIP Conf. Proc.* **836,** 33–42 (2006).
16. Kawai, N. *et al.* An optical spectrum of the afterglow of a γ-ray burst at a redshift of z = 6.295. *Nature* **440,** 184–186 (2006).
17. Greiner, J. *et al.* GRB 080913 at Redshift 6.7. *Astrophys. J.* **693,** 1610 (2009).
18. Tanvir, N. R. *et al.* A γ-ray burst at a redshift of $z \approx 8.2$. *Nature* **461,** 1254–1257 (2009).

19. Salvaterra, R. *et al.* GRB 090423 at a redshift of $z \approx 8.1$. *Nature* **461,** 1258–1260 (2009).

20. Hoffman, K. D. High energy neutrino telescopes. *New J. Phys.* **11,** 055006 (2009).

21. Aartsen, M. G. *et al.* Evidence for High-Energy Extraterrestrial Neutrinos at the IceCube Detector. *Science* **342,** 947 (2013).

22. Aartsen, M. G. *et al.* Observation of High-Energy Astrophysical Neutrinos in Three Years of IceCube Data. *Phys. Rev. Lett.* **113,** 101101 (2014).

23. Aartsen, M. G. *et al.* Evidence for Astrophysical Muon Neutrinos from the Northern Sky with IceCube. *Phys. Rev. Lett.* **115,** 081102 (2015).

24. Abbasi, R. *et al.* Search for Muon Neutrinos from Gamma-ray Bursts with the IceCube Neutrino Telescope. *Astrophys. J.* **710,** 346 (2010).

25. Abbasi, R. *et al.* An absence of neutrinos associated with cosmic-ray acceleration in gamma-ray bursts. *Nature* **484,** 351–354 (2012).

26. Aartsen, M. G. *et al.* Search for Prompt Neutrino Emission from Gamma-Ray Bursts with IceCube. *Astrophys. J. Lett.* **805,** L5 (2015).

27. Aartsen, M. G. *et al.* An All-sky Search for Three Flavors of Neutrinos from Gamma-ray Bursts with the IceCube Neutrino Observatory. *Astrophys. J.* **824,** 115 (2016).

28. Klebesadel, R. W., Strong, I. B. & Olson, R. A. Observations of Gamma-Ray Bursts of Cosmic Origin. *Astrophys. J. Lett.* **182,** L85 (1973).

29. Cline, T. L., Desai, U. D., Klebesadel, R. W. & Strong, I. B. Energy Spectra of Cosmic Gamma-Ray Bursts. *Astrophys. J. Lett.* **185,** L1 (1973).

30. Mazets, E. P., Golenetskii, S. V., Ilinskii, V. N., Gurian, I. A. & Kharitonova, T. V. Investigations of diffuse cosmic gamma radiation in the range 28 keV-4.1 MeV. *ZhETF Pisma Redaktsiiu* **20,** 77–80 (1974).

31. Paciesas, W. S. *et al.* The Fourth BATSE Gamma-Ray Burst Catalog (Revised). *Astrophys. J. Supp. Ser.* **122,** 465 (1999).

32. Costa, E. *et al.* Discovery of an X-ray afterglow associated with the γ-ray burst of 28 February 1997. *Nature* **387,** 783–785 (1997).

33. Metzger, M. R. *et al.* Spectral constraints on the redshift of the optical counterpart to the γ-ray burst of 8 May 1997. *Nature* **387,** 878–880 (1997).

34. Halpern, J. P., Thorstensen, J. R., Helfand, D. J. & Costa, E. Optical afterglow of the γ-ray burst of 14 December 1997. *Nature* **393,** 41–43 (1998).

35. Castro-Tirado, A. J. *et al.* Decay of the GRB 990123 Optical Afterglow: Implications for the Fireball Model. *Science* **283,** 2069–2073 (1999).

36. Fruchter, A. S. *et al.* Hubble Space Telescope and Palomar Imaging of GRB 990123: Implications for the Nature of Gamma-Ray Bursts and Their Hosts. *Astrophys. J. Lett.* **519,** L13 (1999).

37. Bloom, J. S. *et al.* The unusual afterglow of the γ-ray burst of 26 March 1998 as evidence for a supernova connection. *Nature* **401,** 453–456 (1999).

38. Fox, D. B. *et al.* The afterglow of GRB 050709 and the nature of the short-hard γ-ray bursts. *Nature* **437,** 845–850 (2005).

39. Barthelmy, S. D. *et al.* The Burst Alert Telescope (BAT) on the SWIFT Midex Mission. English. *Space Sci. Rev.* **120,** 143–164 (2005).

40. Burrows, D. N. *et al.* The Swift X-Ray Telescope. English. *Space Sci. Rev.* **120,** 165–195 (2005).

41. Roming, P. W. A. *et al.* The Swift Ultra-Violet/Optical Telescope. English. *Space Sci. Rev.* **120,** 95–142 (2005).

42. Meegan, C. *et al.* The Fermi Gamma-ray Burst Monitor. *Astrophys. J.* **702,** 791 (2009).

43. Atwood, W. B. *et al.* The Large Area Telescope on the Fermi Gamma-Ray Space Telescope Mission. *Astrophys. J.* **697,** 1071 (2009).

44. Paciesas, W. S. *et al.* The Fermi GBM Gamma-Ray Burst Catalog: The First Two Years. *Astrophys. J. Supp. Ser.* **199,** 18 (2012).

45. Von Kienlin, A. *et al.* The Second Fermi GBM Gamma-Ray Burst Catalog: The First Four Years. *Astrophys. J. Supp. Ser.* **211,** 13 (2014).

46. Gruber, D. *et al.* The Fermi GBM Gamma-Ray Burst Spectral Catalog: Four Years of Data. *Astrophys. J. Supp. Ser.* **211,** 12 (2014).

47. Winkler, C. *et al.* The INTEGRAL mission. *Astron. Astrophys.* **411,** L1–L6 (2003).

48. Aptekar, R. *et al.* Konus-W gamma-ray burst experiment for the GGS Wind spacecraft. English. *Space Sci. Rev.* **71,** 265–272 (1995).

49. Matsuoka, M. *et al.* The MAXI Mission on the ISS: Science and Instruments for Monitoring All-Sky X-Ray Images. *PASJ* **61,** 999– (2009).

50. Tavani, M. *et al.* The AGILE Mission. *Astron. Astrophys.* **502,** 995–1013 (2009).

51. Feroci, M. *et al.* SuperAGILE: The hard X-ray imager for the AGILE space mission. *Nucl. Instrum. Meth. A* **581,** 728–754 (2007).

52. Yamaoka, K. *et al.* Design and In-Orbit Performance of the Suzaku Wide-Band All-Sky Monitor. *PASJ* **61,** S35–S53 (2009).

53. Takahashi, T. *et al.* Hard X-Ray Detector (HXD) on Board Suzaku. *PASJ* **59,** S35–S51 (2007).

54. Hurley, K. *et al.* The Third Interplanetary Network. *AIP Conf. Proc.* **1279,** 330–333 (2010).

55. NASA. GCN: The Gamma-Ray Bursts Coordinates Network. <`http://gcn.gsfc.nasa.gov`>.

56. Aguilar, J. Online Gamma-Ray Burst catalog for neutrino telescopes. in *Proceedings, 32nd International Cosmic Ray Conference (ICRC 2011).* **8** (2011), 235.

57. IceCube. GRBweb. <`http://grbweb.icecube.wisc.edu`>.

58. Band, D. *et al.* BATSE observations of gamma-ray burst spectra. I - Spectral diversity. *Astrophys. J.* **413,** 281–292 (1993).

59. Guiriec, S. *et al.* Detection of a Thermal Spectral Component in the Prompt Emission of GRB 100724B. *Astrophys. J. Lett.* **727,** L33 (2011).

60. Axelsson, M. *et al.* GRB110721A: An Extreme Peak Energy and Signatures of the Photosphere. *Astrophys. J. Lett.* **757,** L31 (2012).

61. Waxman, E. Cosmological Gamma-Ray Bursts and the Highest Energy Cosmic Rays. *Phys. Rev. Lett.* **75,** 386–389 (1995).

62. Waxman, E. High-Energy Cosmic Rays from Gamma-Ray Burst Sources: A Stronger Case. *Astrophys. J.* **606,** 988 (2004).

63. Baerwald, P., Bustamante, M. & Winter, W. Are gamma-ray bursts the sources of ultra-high energy cosmic rays? *Astropart. Phys.* **62,** 66–91 (2015).

64. Bustamante, M., Baerwald, P., Murase, K. & Winter, W. Neutrino and cosmic-ray emission from multiple internal shocks in gamma-ray bursts. *Nat. Commun.* **6** (2015).

65. Gaisser, T. K. Cosmic Rays and Particle Physics (Cambridge University Press, 1990).

66. Guetta, D., Hooper, D., Alvarez-Muñiz, J., Halzen, F. & Reuveni, E. Neutrinos from individual gamma-ray bursts in the BATSE catalog. *Astropart. Phys.* **20,** 429–455 (2004).

67. Hümmer, S., Baerwald, P. & Winter, W. Neutrino Emission from Gamma-Ray Burst Fireballs, Revised. *Phys. Rev. Lett.* **108,** 231101 (2012).

68. Mücke, A., Engel, R., Rachen, J., Protheroe, R. & Stanev, T. Monte Carlo simulations of photohadronic processes in astrophysics. *Comp. Phys. Commun.* **124,** 290–314 (2000).

69. Lazzati, D. & Begelman, M. C. Non-thermal Emission from the Photospheres of Gamma-ray Burst Outflows. I. High-Frequency Tails. *Astrophys. J.* **725,** 1137 (2010).

70. Zhang, B. & Kumar, P. Model-Dependent High-Energy Neutrino Flux from Gamma-Ray Bursts. *Phys. Rev. Lett.* **110,** 121101 (2013).

71. Zhang, B. & Yan, H. The Internal-collision-induced Magnetic Reconnection and Turbulence (ICMART) Model of Gamma-ray Bursts. *Astrophys. J.* **726,** 90 (2011).

72. Waxman, E. & Bahcall, J. High Energy Neutrinos from Cosmological Gamma-Ray Burst Fireballs. *Phys. Rev. Lett.* **78,** 2292–2295 (1997).

73. Katz, B., Budnik, R. & Waxman, E. The energy production rate & the generation spectrum of UHECRs. *J. Cosmol. Astropart. Phys.* **2009,** 020 (2009).

74. Ahlers, M., Gonzalez-Garcia, M. & Halzen, F. GRBs on probation: Testing the UHE CR paradigm with IceCube. *Astropart. Phys.* **35,** 87–94 (2011).

75. Hirata, K. *et al.* Observation of a neutrino burst from the supernova SN1987A. *Phys. Rev. Lett.* **58,** 1490–1493 (1987).

76. Bionta, R. M. *et al.* Observation of a neutrino burst in coincidence with supernova 1987A in the Large Magellanic Cloud. *Phys. Rev. Lett.* **58,** 1494–1496 (1987).

77. Alexeyev, E., Alexeyeva, L., Krivosheina, I. & Volchenko, V. Detection of the neutrino signal from SN 1987A in the LMC using the INR Baksan underground scintillation telescope. *Phys. Lett. B* **205,** 209–214 (1988).

78. Cleveland, B. T. *et al.* Measurement of the Solar Electron Neutrino Flux with the Homestake Chlorine Detector. *Astrophys. J.* **496,** 505 (1998).

79. Halzen, F. & Learned, J. G. High-energy neutrino astronomy: Towards a 1-km^3 detector. in *Proceedings of the 5th International Symposium on Neutrino Telescopes* (1993); Gaisser, T. K., Halzen, F. & Stanev, T. Particle astrophysics with high energy neutrinos. *Phys. Rep.* **258,** 173–236 (1995).

80. Glashow, S. L. Resonant Scattering of Antineutrinos. *Phys. Rev.* **118,** 316–317 (1960).

81. Gandhi, R., Quigg, C., Reno, M. H. & Sarcevic, I. Ultrahigh-energy neutrino interactions. *Astropart. Phys.* **5,** 81–110 (1996).

82. Cooper-Sarkar, A., Mertsch, P. & Sarkar, S. The high energy neutrino cross-section in the Standard Model and its uncertainty. *JHEP* **2011,** 1–20 (2011).

83. Čerenkov, P. A. Visible Radiation Produced by Electrons Moving in a Medium with Velocities Exceeding that of Light. *Phys. Rev.* **52,** 378–379 (1937).

84. Tamm, I. E. & Frank, I. M. Coherent radiation of fast electrons in a medium. **14,** 107–112 (1937).

85. Bernard, F. Caractérisation des performances d'un télescope sous-marin à neutrinos pour la détection de cascades contenues dans le cadre du projet ANTARES. Ph.D. Thesis (Université de la Méditerranée - Aix-Marseille II, 2000).

86. Learned, J. G. & Mannheim, K. High-Energy Neutrino Astrophysics. *Annu. Rev. Nucl. Part. S.* **50,** 679–749 (2000).

87. Chirkin, D. & Rhode, W. Propagating leptons through matter with Muon Monte Carlo (MMC). 2004. arXiv: `hep-ph/0407075`.

88. Olive, K. A. *et al.* Review of Particle Physics. *Chin. Phys.* **C38,** 090001 (2014).

89. Ackermann, M. *et al.* Optical properties of deep glacial ice at the South Pole. *J. Geophys. Res. Atmos.* **111,** D13203 (2006).

90. Aartsen, M. *et al.* Measurement of South Pole ice transparency with the IceCube LED calibration system. *Nucl. Instrum. Meth. A* **711,** 73–89 (2013).

91. Bramall, N. E., Bay, R. C., Woschnagg, K., Rohde, R. A. & Price, P. B. A deep high-resolution optical log of dust, ash, and stratigraphy in South Pole glacial ice. *Geophys. Res. Lett.* **32,** L21815 (2005).

92. Aartsen, M. *et al.* South Pole glacial climate reconstruction from multi-borehole laser particulate stratigraphy. *J. Glaciol.* **59,** 1117–1128 (2013).

93. Aartsen, M. G. *et al.* The IceCube Neutrino Observatory Part VI: Ice Properties, Reconstruction and Future Developments. in *Proceedings, 33rd International Cosmic Ray Conference (ICRC2013)* (2013). arXiv: 1309.7010.

94. Abbasi, R. *et al.* The design and performance of IceCube DeepCore. *Astropart. Phys.* **35,** 615–624 (2012).

95. Abbasi, R. *et al.* IceTop: The surface component of IceCube. *Nucl. Instrum. Meth. A* **700,** 188–220 (2013).

96. Abbasi, R. *et al.* Calibration and characterization of the IceCube photomultiplier tube. *Nucl. Instrum. Meth. A* **618,** 139–152 (2010).

97. Abbasi, R. *et al.* The IceCube data acquisition system: Signal capture, digitization, and timestamping. *Nucl. Instrum. Meth. A* **601,** 294–316 (2009).

98. Kleinfelder, S. Gigahertz waveform sampling and digitization circuit design and implementation. *IEEE Trans. Nucl. Sci.* **50,** 955–962 (2003).

99. Kelley, J. L. & IceCube Collaboration. Event triggering in the IceCube data acquisition system. *AIP Conf. Proc.* **1630,** 154–157 (2014).

100. D'Agostini, G. A multidimensional unfolding method based on Bayes' theorem. *Nucl. Instrum. Meth. A* **362,** 487–498 (1995).

101. Lawson, C. & Hanson, R. Solving Least Squares Problems (Society for Industrial and Applied Mathematics, 1995).

102. Schatto, K. Stacked searches for high-energy neutrinos from blazars with IceCube. Ph.D. Thesis (Johannes Gutenberg-Universitat Mainz, 2014).

103. Whitehorn, N. A Search for High-Energy Neutrino Emission from Gamma-Ray Bursts. Ph.D. Thesis (University of Wisconsin, Madison, 2012).

104. Ahrens, J. *et al.* Muon track reconstruction and data selection techniques in AMANDA. *Nucl. Instrum. Meth. A* **524,** 169–194 (2004).

105. Boyd, S. & Vandenberghe, L. Convex Optimization, 298–300 (Cambridge University Press, 2009).

106. Aartsen, M. *et al.* Improvement in fast particle track reconstruction with robust statistics. *Nucl. Instrum. Meth. A* **736,** 143–149 (2014).

107. James, F. & Roos, M. Minuit - a system for function minimization and analysis of the parameter errors and correlations. *Comput. Phys. Commun.* **10,** 343–367 (1975).

108. Pandel, D. Bestimmung von Wasserund Detektorparametern und Rekonstruktion von Myonen bis 100 TeV mit dem Baikal-Neutrinoteleskop NT-72. Diploma Thesis (Humboldt-Universität zu Berlin, 1996).

109. Van Eijndhoven, N., Fadiran, O. & Japaridze, G. Implementation of a Gauss convoluted Pandel PDF for track reconstruction in neutrino telescopes. *Astropart. Phys.* **28,** 456–462 (2007).

110. Efron, B. Bootstrap Methods: Another Look at the Jackknife. *Ann. Statist.* **7,** 1–26 (1979).

111. Whitehorn, N., van Santen, J. & Lafebre, S. Penalized splines for smooth representation of high-dimensional Monte Carlo datasets. *Comput. Phys. Commun.* **184,** 2214–2220 (2013).

112. Cramer, H. Mathematical Methods of Statistics (Princeton Univ. Press, 1945); Rao, R. C. Information and the accuracy attainable in the estimation of statistical parameters. *Bull. Calcutta Math. Soc.* **37,** 81–91 (1945).

113. Neunhöffer, T. Estimating the angular resolution of tracks in neutrino telescopes based on a likelihood analysis. *Astropart. Phys.* **25,** 220–225 (2006).

114. Wilks, S. S. The Large-Sample Distribution of the Likelihood Ratio for Testing Composite Hypotheses. *Ann. Math. Statist.* **9,** 60–62 (1938).

115. Aartsen, M. G. *et al.* Energy reconstruction methods in the IceCube neutrino telescope. *J. Instrum.* **9,** P03009 (2014).

116. Sra, S., Kim, D. & Schölkopf, B. Non-monotonic Poisson Likelihood Maximization. Tech. rep. (Max-Planck-Institut für biologische Kybernetik, 2008).

117. Gazizov, A. & Kowalski, M. ANIS: High energy neutrino generator for neutrino telescopes. *Computer Physics Communications* **172,** 203–213 (2005).

118. Chekelian, V. Proton Structure Measurements from HERA to LHC. *Nuclear Physics B - Proceedings Supplements* **234.** 16th International Conference in Quantum ChromoDynamics, 62–65 (2013).

119. Lai, H. *et al.* Global QCD analysis of parton structure of the nucleon: CTEQ5 parton distributions. *Eur. Phys. J. C* **12,** 375–392.

120. Dziewonski, A. M. & Anderson, D. L. Preliminary Reference Earth model. *Phys. Earth Planet. Inter.* **25,** 297–356 (1981).

121. Heck, D., Schatz, G., Thouw, T., Knapp, J. & Capdevielle, J. N. CORSIKA: A Monte Carlo code to simulate extensive air showers. Tech. rep. (1998).

122. Hörandel, J. R. On the knee in the energy spectrum of cosmic rays. *Astropart. Phys.* **19,** 193–220 (2003).

123. Koehne, J.-H. *et al.* PROPOSAL: A tool for propagation of charged leptons. *Comput. Phys. Commun.* **184,** 2070–2090 (2013).

124. Agostinelli, S. *et al.* Geant4 – A Simulation Toolkit. *Nucl. Instrum. Meth. A* **506,** 250–303 (2003).

125. Lundberg, J. *et al.* Light tracking through ice and water – Scattering and absorption in heterogeneous media with Photonics. *Nucl. Instrum. Meth. A* **581,** 619–631 (2007).

126. Aartsen, M. G. *et al.* Search for Time-independent Neutrino Emission from Astrophysical Sources with 3 yr of IceCube Data. *Astrophys. J.* **779,** 132 (2013).

127. Aartsen, M. G. *et al.* Searches for Extended and Point-like Neutrino Sources with Four Years of IceCube Data. *Astrophys. J.* **796,** 109 (2014).

128. Richman, M. A Search For Muon Neutrinos Coincident With Gamma-Ray Bursts Using IceCube. Ph.D. Thesis (University of Maryland, College Park, 2015).

129. Freund, Y. & Schapire, R. E. A Decision-Theoretic Generalization of On-Line Learning and an Application to Boosting. *J. Comput. Syst. Sci.* **55,** 119–139 (1997).

130. Kolmogorov, A. Sulla determinazione empirica di una legge di distribuzione. *G. Ist. Ital. Attuari* **4,** 83–91 (1933); Smirnov, N. V. On the estimation of the discrepancy between empirical curves of distribution for two independent samples. *Bull. Math. Univ. Moscow* **2** (1933).

131. Feller, W. On the Kolmogorov-Smirnov Limit Theorems for Empirical Distributions. *Ann. Math. Statist.* **19,** 177–189 (1948).

132. Gaisser, T. K., Stanev, T. & Tilav, S. Cosmic ray energy spectrum from measurements of air showers. *Frontiers of Physics* **8,** 748–758 (2013).

133. Honda, M., Kajita, T., Kasahara, K., Midorikawa, S. & Sanuki, T. Calculation of atmospheric neutrino flux using the interaction model calibrated with atmospheric muon data. *Phys. Rev. D* **75,** 043006 (2007).

134. Neyman, J. Outline of a Theory of Statistical Estimation Based on the Classical Theory of Probability. *Phil. Trans. R. Soc. A* **236,** 333–380 (1937).

135. Abramowicz, H. & Levy, A. The ALLM parameterization of σ_T $(\gamma * p)$ - an update. 1997. arXiv: `hep-ph/9712415`.

136. Abramowicz, H., Levin, E., Levy, A. & Maor, U. A parameterization of σ_T $(\gamma * p)$ above the resonance region for $Q^2 \geqslant 0$. *Phys. Lett. B* **269,** 465–476 (1991).

137. Bezrukov, L. B. & Bugaev, E. V. Nucleon shadowing effects in photonuclear interactions. *Sov. J. Nucl. Phys.* **33** (1981).

138. Aartsen, M. G. *et al.* Atmospheric and astrophysical neutrinos above 1 TeV interacting in IceCube. *Phys. Rev. D* **91,** 022001 (2015).

139. Racusin, J. L. *et al.* Fermi and Swift Gamma-ray Burst Afterglow Population Studies. *Astrophys. J.* **738,** 138 (2011).

140. Laskar, T. *et al.* Energy Injection in Gamma-Ray Burst Afterglows. *Astrophys. J.* **814,** 1 (2015).

141. Aartsen, M. G. *et al.* IceCube-Gen2: A Vision for the Future of Neutrino Astronomy in Antarctica. 2014. arXiv: 1412.5106.

142. Ahlers, M. & Halzen, F. Pinpointing extragalactic neutrino sources in light of recent IceCube observations. *Phys. Rev. D* **90,** 043005 (2014).

143. Abbott, B. P. *et al.* LIGO: the Laser Interferometer Gravitational-Wave Observatory. *Rep. Prog. Phys.* **72,** 076901 (2009).

144. Abbott, B. P. *et al.* Observation of Gravitational Waves from a Binary Black Hole Merger. *Phys. Rev. Lett.* **116,** 061102 (2016).

145. Connaughton, V. *et al.* Fermi GBM Observations of LIGO Gravitational-wave Event GW150914. *Astrophys. J. Lett.* **826,** L6 (2016).

146. Adrián-Martínez, S. *et al.* High-energy neutrino follow-up search of gravitational wave event GW150914 with ANTARES and IceCube. *Phys. Rev. D* **93,** 122010 (2016).

147. Redl, P. A search for muon neutrinos coincident with Gamma-ray Bursts with the IceCube 59-String detector. Ph.D. Thesis (University of Maryland, College Park, 2011).

148. Meagher, K. Limits on Neutrino Emission from Gamma-Ray Bursts with the 40 String IceCube Detector. Ph.D. Thesis (University of Maryland, College Park, 2012).

149. Hellauer, R. An All-Sky, Three-Flavor Search for Neutrinos from Gamma-Ray Bursts with the IceCube Neutrino Observatory. Ph.D. Thesis (University of Maryland, College Park, 2015).